

PDF hosted at the Radboud Repository of the Radboud University Nijmegen

The following full text is a publisher's version.

For additional information about this publication click this link.

<http://hdl.handle.net/2066/176200>

Please be advised that this information was generated on 2017-12-05 and may be subject to change.

***Mechanisms and functional
interpretations of oscillatory
neuronal activity***

Bart Gips

The work in this thesis was carried out at the Donders Institute for Brain Cognition and Behaviour, Radboud University Nijmegen, with financial support from the Netherlands Organisation for Scientific Research (NWO, ALW Open Competition Grant (822-02-011))

Publication of this doctoral dissertation was financially supported by the Radboud University Nijmegen

ISBN 978-94-6284-112-3

© Bart Gips, 2017.

All rights reserved. Save exceptions stated by the law, no part of this publication may be reproduced, stored in a retrieval system of any nature, or transmitted in any form or by any means, electronic, mechanical, photocopying, recording or otherwise, included a complete or partial transcription, without the prior written permission of the authors, application for which should be addressed to author

Mechanisms and functional interpretations of oscillatory neuronal activity

PROEFSCHRIFT

ter verkrijging van de graad van doctor
aan de Radboud Universiteit Nijmegen
op gezag van de rector magnificus prof. dr. J.H.J.M. van Krieken,
volgens besluit van het college van decanen
in het openbaar te verdedigen op

vrijdag 22 september 2017

om 12.30 uur precies

door

Bart Cornelis Ivo Gips

geboren op 9 augustus 1989

te Amsterdam

Promotoren:

Prof. dr. O. Jensen

Prof. dr. J.P.J.M. van der Eerden

Manuscriptcommissie:

Prof. dr. T. Celikel

Prof. dr. G. Pipa (University of Osnabrück, Duitsland)

Dr. L. Melloni (New York University, Verenigde Staten)

Contents

Chapter 1. General Introduction	5
Chapter 2. A Biologically Plausible Mechanism for Neuronal Coding Organized by the Phase of Alpha Oscillations	19
Chapter 3. A model mechanism for the generation of thalamic alpha oscillations	51
Chapter 4. A model of microsaccade-rhythmic modulation synchronization and coding in early visual cortex.....	79
Chapter 5. Discovering recurring patterns in electrophysiological recordings	113
Chapter 6. General Discussion	149
Bibliography	157
Nederlandse samenvatting.....	179
Author publications	183
Curriculum Vitae	185
Acknowledgements.....	187

Chapter 1.
General Introduction

1.1 Measuring brain activity

Neurons (also known as nerve cells) are the basic units that make up our brain. By exchanging electrical signals, neurons can communicate and our brain works because of it. Therefore, to investigate the brain we can attempt to measure these electrical signals. The signals we measure are the result of currents across the membrane of the neurons, i.e. from the extracellular space into the cell or vice versa. One could capture the electromagnetic fields related to these currents by using sensors outside of the head using techniques such as electroencephalography (EEG) and magnetoencephalography (MEG). In cases of cell cultures, animal studies, and even in some patient studies, one can insert electrodes directly into the nervous tissue to measure the electrical field therein.

Another common way to investigate brain activity is using functional magnetic resonance imaging (fMRI). fMRI measures the change in the blood oxygen level* caused by activation of nervous tissue. This change in local blood oxygenation, called the haemodynamic response, happens on a timescale in the order of seconds and is therefore slow relative to the currents across a membrane of a single neuron (whose dynamics are in the order of milliseconds). It is therefore more useful in signifying a general increase in activity of a brain area on a larger time-scales.

In this thesis we will focus on sub-second phenomena in networks of brain cells. We will therefore investigate different aspects of the electromagnetic signals produced by neurons by simulating the neuronal activity that generates them. From this we hope provide a link between the different experimental modalities. This may help us to elucidate the possible functions of the underlying neural circuitry.

1.2 The case for simulation

In this thesis we will mainly cover work of a somewhat theoretical nature. All the experiments performed were so-called *in silico*. This means that no living cells or even organisms were needed for our measurements. Instead, everything was simulated on a computer. Membranes, synapses and ion-channels are replaced by mathematical models that use differential equations to describe their dynamics. One could attempt to approach these equations analytically, but a model consisting of only a handful of communicating neurons already is too complex for analytical analysis. Therefore, we can choose to run a *simulation* where a computer numerically solves the many coupled differential equations. In this way we are able

* In fact, increased neuronal activity seems to generally lead to a paradoxical *increase* of local blood oxygen concentration. Despite the increased metabolism of the activated brain cells requiring more oxygen, the neural vasculature seems to overcompensate resulting in a net oxygen increase [339], [340].

to calculate all membrane currents and as a result produce data that are very similar to what is experimentally recorded. The most important difference is that we are in full control of the simulated neural tissue. We can sever connections and connect neurons at will without risk of irreversibly damaging any biological structures. Or we could simulate the addition of certain chemicals such as neurotransmitters, neuromodulators or psychoactive medications and investigate their effects on the behavior of the neural network. All of this can be done in an accurate, fully reproducible manner, since all possible variance in the experiments is under the control of the researcher.

One has to keep in mind that, since the simulated neurons are under full control of the investigator, this leads to an enormous flexibility in the parameter space of any model neural network. This also brings with it a lot of pitfalls. It is easy to generate some interesting dynamics in a computer simulation, but who is to say that biological nervous tissue will act the same? How can you be sure that all the parameter values are realistic? And even if they are, can simulations really lead to new insight?

I would like to argue that, yes, they could. With the output from simulations you can predict the behavior of real biological neural circuitry. One could then test for these predictions in an experimental setting to investigate the validity of (aspects of) the model. The experimental findings can then inform a new revised model, which in turn can then make new predictions and so on (Figure 1-1). This iterative process would then converge to increased understanding of the biological neural network we attempted to investigate. In this sense, model simulations can be a valuable extension to theoretical modelling in general. It is important to note that this also implies that most likely in any iteration of this loop, the model will be far from perfect. This should lead to the realization that, even if a model can be criticized because it is thought to over-simplify reality, or because of some other flaw it may have, still it can lead to helpful insight, as it captures important characteristics of the real biological system.

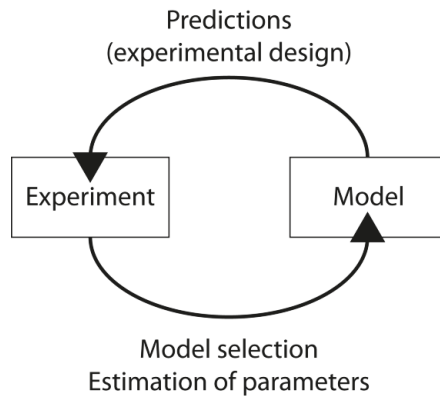


Figure 1-1. The loop between experimentation and theoretical modelling.

1.3 Neuron models: from integrate and fire to ion-channels

How does one go about simulating neural activity? One approach is to try to capture the dynamics of larger populations of neurons to gain insight on a meso or macro scale [1]. Examples of this are the mean field approach [2]–[4] or so-called neural mass models [5]–[7]. These techniques try to capture the neural dynamics as a continuous field or as individual nodes that represent many neurons with similar activity, respectively. In this thesis however, we will instead model individual neurons to simulate the neural circuitry on a micro scale. In this section we will cover some of the most common ways of modelling simple neurons relevant to this thesis.

1.3.1 The leaky integrate-and-fire model

Possibly the simplest successful model for a single neuron’s activity is the leaky integrate and fire neuron (LIF) [8]. As its name may imply, a LIF neuron integrates its inputs and fires an action potential when a certain threshold is reached. It models the evolution of a neuron’s membrane potential as follows:

$$\frac{dV}{dt} \frac{1}{\tau} = V_r - V + IR \quad (1.1)$$

Where V is the membrane potential, V_r the resting potential (often chosen to be around -70mV), I the sum of the imposed and synaptic input currents and R the resistance across the membrane. The value τ is called the membrane time constant

and is equal to $\frac{1}{RC}$, i.e. the inverse of the product of the membrane resistance and capacitance.

This membrane potential will decay towards the resting potential (V_r), when there is no input current I . This decay will happen exponentially with time constant τ . This "leaking" reflects the diffusion of ions through the membrane when the equilibrium (i.e. resting potential) is not yet reached in the cell.

The "fire" component of the LIF name happens when the membrane potential reaches a certain threshold θ and the voltage is reset:

$$\text{if } V \geq \theta, \text{ then } V \leftarrow V_r \quad (1.2)$$

When this happens, the neuron is said to have fired an action potential, this causes the neuron to send synaptic signals to its neighbors (see the section 1.3.4).

1.3.2 The Izhikevich model

A second model proposed by Izhikevich [9] is similar to the LIF model, but slightly more complex, since it uses two coupled differential equations:

$$\frac{dV}{dt} = 0.04V^2 + 5V + 140 - u + I \quad (1.3)$$

$$\frac{du}{dt} = a(bV - u) \quad (1.4)$$

$$\text{if } V \geq 30 \text{ mV, then } \begin{cases} V \leftarrow c \\ u \leftarrow u + d \end{cases} \quad (1.5)$$

Again, V represents the neuron's membrane potential, whereas the added u represents a membrane recovery variable. The membrane potential is reset when it reaches a threshold value (30 mV). This is when an action potential is said to be generated, which leads to synaptic communication (see section 1.3.4). The parameters a , b , c and d can be changed to alter the general behavior of the model. In his work Izhikevich suggests some example values to yield models for different neuron types (e.g. regular spiking, fast spiking, chattering, and bursting neurons, see Figure 1-2). This makes the Izhikevich model very attractive. It is hardly more computationally complex than the simple LIF model, but it is very flexible with only these 4 parameters. In Chapter 4 this model will be used to simulate regular spiking pyramidal cells as well as fast spiking inhibitory neurons.

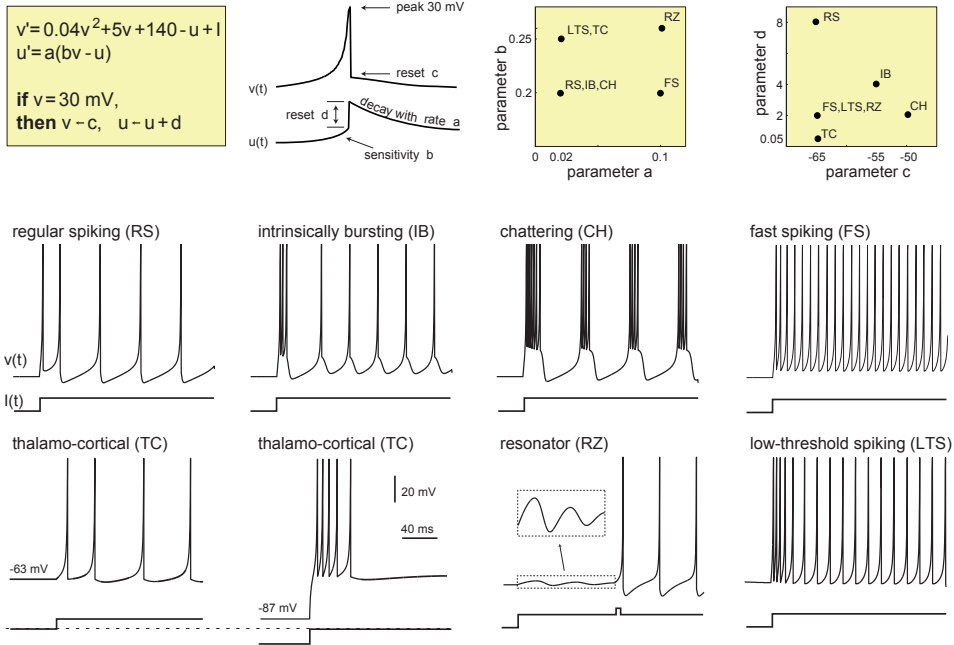


Figure 1-2. Illustration of the Izhikevich model reproducing behavior of different neuron types. Electronic version of the figure and reproduction permissions are freely available at www.izhikevich.com.

1.3.3 Conductance-based models

Finally, we come to the conductance-based models. This is the most complex model-type used in this thesis (applied in Chapter 2 and Chapter 3). This type of model is often named a Hodgkin-Huxley model (HH), after Hodgkin and Huxley who developed the first model of this type in the 1950s to capture the dynamics of the action potential generation in the squid giant axon [10].

This type of model is generally of the form:

$$C_m \frac{dV}{dt} = \Sigma I_i \tag{1.6}$$

Where C_m is the membrane capacitance per area and I_i are all transmembrane currents directed into the cell. These currents have the general form:

$$I_i = g_i(V_i - V) \tag{1.7}$$

Where V_i is the reversal potential of this particular current. The factors g_i are the conductances per unit area for current I_i . These conductances can be constant or, as

is most often the case, may be voltage-dependent and governed by their own dynamics.

The simplest model of this class of models proposed by Hodgkin and Huxley contained 3 of these currents: leak, sodium, and potassium. The leak current has a constant conductance, similar to the leak term in the LIF-model. Whereas the sodium and potassium currents are both voltage-dependent (e.g. see Chapter 2), this makes the generation of action potentials possible. In short: sodium channels start to open more and more when the membrane potential increases causing an increase in sodium conductance and therefore a positive current into the cell. This large positive current causes a spike in the membrane potential, which in turn causes the potassium channels to rapidly open. The potassium reversal potential, however, is negative. This in turn causes a rapid drop of the membrane potential: an action potential (sometimes called a *spike*) is generated. The rapid rise of the membrane potential will cause synaptic currents to flow (see section 1.3.4).

This last observation is an important distinction between the HH model and the previous two models (LIF and Izhikevich): there is no manual resetting when the membrane potential reaches a certain threshold. The entire generation of the action potential is included implicitly in the voltage-dependent dynamics of the sodium and potassium currents.

Other currents can be added to model different ion channels to simulate a wide variety of different neuron types, such as calcium currents that make it possible for the model neurons to generate bursts (e.g. see the thalamic neurons in Chapter 3). These conductance-based models are more realistic than the previous two (LIF and Izhikevich neurons), since they explicitly try to model all trans-membrane currents. This also means that the local field potential (LFP), the potential normally measured by an electrode placed in the extracellular space, can be simulated more realistically from these currents (detailed in Chapter 2). In the case of LIF and Izhikevich neurons the total current is unclear, especially during the generation of action potentials, since this is done implicitly in these cases.

1.3.4 Synaptic interactions

Now we have discussed different ways to simulate the dynamics of a single cell, we will briefly cover the most common way neurons can interact: through synaptic currents.

When an action potential is generated, the neuron is able to send a signal to a neighboring neuron if they are synaptically connected. This leads us to the expression for the total input current:

$$I_{input} = \sum_j I_{s,j} + I_{imp} \quad (1.8)$$

Where the latter term, I_{imp} , is the *imposed* current, i.e. the current that an experimenter may inject into the cell in an experimental setup. The former term sums over all synaptic currents coming from connected neurons j .

The synaptic currents are given by:

$$I_{s,j} = s_j g_j (V_{rev,j} - V) \quad (1.9)$$

In the case of the conductance-based models, these synaptic currents can be directly added to the sum over all incoming currents in equation 1.6. The factor g_j is the synaptic connection strength between sending neuron j and the (receiving) neuron we are simulating. $V_{rev,j}$ is the reversal potential of the synapse between the receiving neuron and the sending neuron j . The character of the synapse (i.e. inhibitory or excitatory) depends on this reversal potential. If reversal potential is below the resting potential of the neuron (e.g. -90 mV) the synaptic activity will tend to hyperpolarize the cell, leading to inhibition[†]. On the other hand, if the reversal potential is above the spiking threshold (e.g. 50 mV) synaptic currents will lead to depolarization and therefore will act excitatory. Lastly, the variable s_j describes the dynamics of the synapse. For the LIF and Izhikevich models these dynamics are often modelled with exponential decay:

$$\frac{ds_j}{dt} = -s_j/\tau_{s,j} \quad (1.10)$$

If neuron j generates an action potential, the variable s_j is set to 1, otherwise it decays back to zero with time constant $\tau_{s,j}$. Since the conductance-based neurons do not have an explicit spiking threshold (i.e. membrane potentials are not “manually” reset) synapses used with these models often also not explicitly reset to a fixed value in the case of an action potential. Instead, their dynamics are somewhat more complex than equation 1.10 and are a function of the presynaptic membrane potential (e.g. see the method section of Chapter 2).

1.4 Local field potentials and spikes

The neural code is thought to be mostly contained in the spatio-temporal patterns of action potentials appearing across a neural network [11]. This is the case, because for information processing to happen in the brain, neurons need to communicate.

[†] A second form of inhibition can be distinguished when the reversal potential is higher than the resting potential, but lower than the spiking threshold. This is often called *shunting inhibition* [341]–[343]. However, this type of inhibition is not covered in this thesis.

Recently this view has been extended somewhat by taking into account the process of dendritic computation [12]. This means that a single neuron could already perform some simple computation besides basic integration and coincidence detection of inputs. Regardless, for any of these computations the neuron will need input and therefore cannot operate in isolation. It needs to communicate with its neighbours.

Synaptic connections between neurons only really become active when the sending neuron generates an action potential[‡] [13], i.e. action potentials are the main signal of interest when investigating neuronal communication and computation.

However, as mentioned in section 1.1, often only more global electrical signals can be measured experimentally. Therefore, there are two important signals we can derive from our simulations: the local, neuron-specific, spike times and the more “global” LFP. The LFP refers to the electric potential measured in the extracellular space in neural tissue. In spite of its name, the sources responsible for generating the local field potential are far from local. Even though the LFP is recorded locally in the extracellular space between the neurons, the activity of neurons far removed from the locus of the electrode still influences its value [14], [15]. However, LFP measurements will still be orders of magnitude more local than the previously mentioned, relatively crude, extracranial recording techniques (i.e. MEG and EEG). As mentioned above, more realistic LFPs can be simulated when using more realistic neuron models. The electrical potential in the extracellular space depends not only on the strength of the total (transmembrane) current of the neurons, but also on the neuron morphology. The shape of a neuron may cause some currents to flow in opposite direction and as a result (partly) cancel each other out (see [16] for a good discussion on simulating LFPs with various degrees of realism). Simulated LFPs are valuable, because they can be directly compared to abundant experimental LFP recordings. Secondly, since they capture the electric fields produced by all simulated neurons, they are a step closer to extracranial MEG and EEG recordings.

Since the neural code is reflected in the patterns of action potentials, the spike times can be analyzed to investigate mechanisms of neural computation. Just like the LFPs, spike times can also be compared to studies with sensitive electrodes placed inside the tissue, but recording individual spiking activity from many neurons at once is still technically challenging. This makes analysis of the precise spike timing in model neural networks theoretically very interesting, although the interpretation may be

[‡] This is ignoring the existence of electrical synapses, also called *gap junctions*. These connections between the neurons are electrical, in essence linking the membrane potentials of two neurons directly. This makes it possible for neurons to affect each other without the generation of action potentials. However, chemical synapses are thought to be far more numerous in the brain (and therefore important)[13].

somewhat speculative in practice. However, recent advances in wide-field optical methods using voltage-sensitive dyes or ion-sensitive indicators (e.g. sensitive to the concentration of Ca^{2+}) come close to making this a possibility for neurons close to the surface of the brain [17]–[19].

1.5 Oscillations

One of the main electrophysiological phenomena of concern in this thesis is the presence of *oscillations* in neuronal activity and therefore in the LFP [20], [21]. These oscillations can be measured with all previously mentioned recording methods, even in extracranial MEG and EEG recordings.

The first oscillatory brain activity was measured by Hans Berger [22] when he measured the electrical potential over the occipital lobe. These oscillatory patterns of around 10 cycles per second have since been known as *alpha oscillations*. Oscillations of other frequencies have subsequently been identified and also named using letters from the Greek alphabet (Table 1-1).

Table 1-1. Different neuronal oscillations and their respective frequency bands.

Name	Alpha	Beta	Gamma	Delta	Theta
Frequency range (Hz)	8-12	13-30	30-70	1-4	4-8

It is generally assumed that activity in these different frequency bands reflects the “state” or “mode” in which the brain operates and that it directly reflects activation of different microcircuits [20], [21]. In this thesis the research is mainly focused on the slow alpha rhythm and the fast gamma rhythm. We will therefore expand on these two rhythms.

The alpha rhythm is measured in humans over the occipital cortex and in the thalamus [23]–[26]. It decreases in strength when the eyes are open, and even more when visual stimuli are presented. In contrast, alpha-band activity is enhanced during non-visual tasks, such as mental calculation and working memory [22], [27]. Because of this, alpha band activity has long been thought to signal a state of cortical idling of the visual system [28]. Over the past decades, however, experiments have shown that alpha activity is modulated when brain areas are actively suppressed in spatial attention tasks [29]–[33]. On the neuronal scale, alpha oscillations have been suggested to selectively inhibit and temporally order neuronal firing [34]–[36]. This last hypothesis will be further investigated in Chapter 2.

Like the slower alpha oscillations, the faster gamma rhythm is also found in occipital, visual, areas[§]. Gamma-band activity is thought to signify local cortical processing [37], since it is thought to be generated by interacting local excitatory and inhibitory neurons [38], [39]. Unlike the alpha rhythm, the exact frequency of the gamma rhythm is variable and may depend on stimulus properties [40]–[46]. The flexibility of the gamma rhythm has led others to give it a functional interpretation. The most prevalent are the theories of binding by synchrony [47]–[50] and of communication through coherence [51]–[53]. These hypotheses are related in such a way that they both suggest that brain areas that perform related processing should synchronize their gamma rhythms. Other theories explicitly take into account the occurrence of action potentials and their timing relative to the ongoing gamma rhythm in the LFP and suggest that action potentials are ordered temporally within gamma cycles [54], [55], or that the gamma mechanism acts as a winner-take-all algorithm to filter out noise [37], [56], [57]. Aspects of all these functional hypotheses will return in Chapter 2 and Chapter 4.

1.5.1 Cross-frequency interactions

Cross-frequency coupling (CFC) is a phenomenon that has gathered a lot of attention recently. In general, CFC is the interaction of two oscillations with different frequencies [58]. The most common interaction that is investigated is *phase-amplitude coupling* (PAC). In this type of cross-frequency interaction, the amplitude of a higher frequency rhythm (generally in the gamma band) varies as a function of the phase of a lower frequency (most commonly in the theta band), in general this means that the high-frequency rhythm's amplitude is modulated rhythmically, following the low-frequency rhythm. Theta-gamma PAC was first shown in the rat hippocampus [59], [60], but later also in auditory cortex of non-human primates [61] and in human cortex and hippocampus [62], [63]. Instead of the low frequency in the theta range, the phase-providing frequency has also been shown to be in the delta [41], [64], [65] and alpha band [66], [67].

CFC may play a role in neural computation, communication and learning [68], multiple theories for the function interpretation of CFC have been offered [35], [69]–[71]. In this thesis we will investigate these functional interpretations by way of

[§] Unlike alpha oscillations, that are mainly reported in occipital cortex and the thalamus, gamma oscillations seem to be a more general cortical phenomenon as well as prominent in the hippocampus [86], [314], [344]. While gamma oscillations in other regions may have similar roles and mechanisms, note that in this thesis the focus is on gamma oscillations found in occipital areas.

simulating the possible neural circuitry that underlies these cross-frequency interactions.

1.6 Aim and Outline of this thesis

This thesis aims to bridge the gap between phenomena observed in electrophysiological recordings, and the neuronal activity that generates them.

As mentioned above, changes in neural alpha oscillations have been shown to correlate with idling and suppression of neural activity, most notably in tasks where attention is involved. It is however not quite clear how these alpha oscillations are precisely generated, and how they could be the result, or the cause, of “idling” or inhibition of processing on a neuronal level.

Similarly, phase-amplitude coupling has often been observed in different experimental contexts, but is not directly clear what it would mean for processing on the level of neurons.

In this thesis we will attempt to shed light on the generation of alpha oscillations by neurons in the thalamus as well as their role in modulating processing of visual information in the cortex. Secondly, we will investigate phase-amplitude coupling found in the visual cortex (specifically delta-gamma and alpha-gamma coupling) and suggest a functional interpretation of this peculiar electrophysiological phenomenon.

The following chapters contain the results from four studies. In these studies, oscillatory neuronal activity was central, mainly in areas of the brain that deal with visual perception.

We aim to find answers to the following questions:

- I. How can occipital alpha oscillations help cortical processing of visual information on a neuronal level?
- II. How can the alpha rhythm be generated and modulated in the Lateral Geniculate Nucleus of the thalamus?
- III. What effects do saccadic eye movements have on oscillatory activity in visual cortex and what are their implications for neuronal processing?
- IV. How can we better investigate waveforms in electrophysiological data?

The following chapters are organized as follows:

Chapter 2 will explore the biological feasibility of a mechanism we proposed in earlier work [35]. It provides a functional role for the phase-amplitude coupling between alpha and gamma oscillations found in occipital cortex.

In **Chapter 3** we present a model mechanism for the generation of the alpha rhythm in the thalamus. We show that feedback inhibition through the reticulate nucleus can be important for generating a stable alpha rhythm. We show how feed-forward input from the retina, or feedback from the cortex can modulate the strength and phase of the alpha oscillations in the thalamus.

In **Chapter 4** the focus is on activity in primary visual areas following saccadic eye movement that results in delta-gamma PAC. After a saccadic eye movement, a strong transient of broad-band activity is visible in the LFP in V1, after which gamma synchrony builds up. We will give different functional interpretations to these two phases of activity surrounding saccadic eye movements.

Chapter 5 covers a novel method for analysis of electrophysiological data such as LFP and EEG or MEG recordings to better investigate signatures of both neuronal oscillations and (non-periodically) repeating transients.

Finally **Chapter 6** consists of a general discussion of the presented work, as well as the questions mentioned above.

Chapter 2.

A Biologically Plausible Mechanism for Neuronal Coding Organized by the Phase of Alpha Oscillations

Adapted from:

B. Gips, J. P. J. M. van der Eerden, and O. Jensen, "A biologically plausible mechanism for neuronal coding organized by the phase of alpha oscillations.," *Eur. J. Neurosci.*, vol. 44, no. 4, pp. 2147–61, Aug. 2016.

2

Abstract

The visual system receives a wealth of sensory information of which only little is relevant for behavior. We present a mechanism in which alpha oscillations serve to prioritize different components of visual information. By way of simulated neuronal networks, we show that inhibitory modulation in the alpha range (~10 Hz) can serve to temporally segment the visual information to prevent information overload. Coupled excitatory and inhibitory neurons generate a gamma rhythm in which information is segmented and sorted according to excitability in each alpha cycle. Further details are coded by distributed neuronal firing patterns within each gamma cycle. The network model produces coupling between alpha phase and gamma (40-100 Hz) amplitude in the simulated local field potential similar to that observed experimentally in human and animal recordings.

2.1 Introduction

The aim of this paper is to propose a physiologically inspired model for a phase-organized code by alpha oscillations. While the alpha rhythm has long been thought to reflect cortical idling or a state of relaxation [22], this view has recently been replaced by the notion that the alpha oscillations play a direct role in the coordination of neuronal processing. For instance the alpha rhythm has been shown to modulate neuronal firing in a phasic manner [36], [72], [73], which may be linked to apparent discrete sampling of the visual environment at a rate in the alpha band (7-13 Hz) [74]. Furthermore, neural activity in higher frequency bands, most notably gamma-band activity in humans and primate visual cortex is modulated coherently with the alpha oscillations [66], [67], [75], [76]. Besides this, extrastriate regions have been found to synchronize in the alpha band in monkeys performing an attention task [77]. These findings have resulted in the proposal that alpha oscillations are important for the temporal ordering of incoming visual information [35].

Neuronal oscillations are readily recorded in various brain regions in both animals and humans [21]. It has been proposed that these oscillations coordinate the timing of neuronal firing and thus neuronal coding. Faster oscillations in the gamma band (30-100 Hz) have been suggested to synchronize the firing of a set of neurons participating in coding for visual features [37], [78]–[80]. Secondly, the phase of slower oscillations at which neurons fire has been shown to carry information (reviewed in [81]). For instance it has been demonstrated that spatial information is represented by the phase of neuronal firing with respect to the hippocampal theta rhythm [82], [83]. Secondly, the theta phase at which a neuron fires in monkey auditory cortex carries information about the stimulus [84]. Furthermore, the phase of the theta oscillations modulates the gamma amplitude in rats and humans [62], [85]–[87] and has been suggested to modulate gamma band activity to encode speech in the human auditory cortex [88]. These observations have resulted in the proposal that slower (theta or alpha band) and faster (gamma band) oscillations create a multiplexing scheme in which multiple visual features are encoded at different phases of the slower rhythm (reviewed in [69]). The faster rhythm then serves to segment the individual items in time.

Though the above examples deal with theta-gamma coupling, we propose to extend this idea to the slow oscillations in visual cortex which are in the alpha range. Therefore, we study a physiologically inspired model network representative of early visual cortex, demonstrating how coupled alpha and gamma oscillations

coordinate neuronal firing [35]. In this framework, inhibitory alpha oscillations not only limit neuronal processing, but they also provide a mechanism for segmenting neural representations of visual images based on neuronal excitation levels. This means that strongly excited neurons fire preferentially at an early alpha phase, while neurons receiving weaker excitation tend to fire at later alpha phases. Neurons that are excited even less do not produce action potentials at all. The level of neuronal excitation can be seen as a combination of bottom-up input (e.g. higher visual contrast causes stronger excitation) and top-down biases (such as attention) [35]. Taken together this translates to a mechanism prioritizing the “most important” over the “less important” visual features. In the literature on hippocampal theta phase precession this temporal ordering is sometimes referred to as “phase coding” (e.g. [83], [89]–[92]), since it is a temporal code organized with respect to the phase of the oscillations. We here present a set of simulations to demonstrate the dynamics of the network model as well as its limitations.

2.2 Materials and methods

2.2.1 Modeling software

All the simulations were conducted using the Neurosim software package version 1.29 developed by Jan van der Eerden at the Donders Institute for Brain, Cognition and Behaviour. Neurosim is a software package written in FORTRAN95 that can be used to simulate neurons and biological neural networks. It solves coupled differential equations to simulate Hodgkin-Huxley type neuron models [10], or even more detailed compartment models to simulate the dynamics of neurons and their interactions. Numerical simulations were computed using a variable step size Runge-Kutta method of order 8 according to the Dormand and Prince algorithm [93]. The relevant output variables were sampled at 10 kHz. All analyses of the simulation output were performed with Matlab (MathWorks, R2012b).

2.2.2 Neuron model

The model neurons used were single-compartment conductance based neuron models, similar to the model first proposed by Hodgkin and Huxley [10]. Two types of neurons were used: 1080 excitatory neurons (E-neurons) and 270 inhibitory neurons (I-neurons). The model network is illustrated in Figure 2-1 and Figure 2-2. The neurons are described using the following equation for the membrane potential [94]:

$$C_m \frac{dV}{dt} = -g_{leak}(V - V_{leak}) - I_{Na} - I_K - I_{K_M} - I_{AMPA} - I_{GABA} - I_{AMPA_{imp}} - I_{GABA_{imp}} - I_{AHP} \quad (2.1)$$

Where V is the membrane potential and C_m is the membrane's specific capacitance (equal to $1 \mu\text{F}/\text{cm}^2$). The currents I_i are voltage-dependent currents flowing through different ion channels i towards the extracellular space. Parameters for the dynamics of I_{Na} , I_K and I_{K_M} are taken to be the mean values as measured by Pospischil and colleagues [94]. The parameters for the synaptic currents (I_{AMPA} and I_{GABA}) were adapted from the work by Jensen and colleagues [95]. The currents representing the directly imposed inputs ($I_{AMPA_{imp}}$ and $I_{GABA_{imp}}$, see equation 1), and the after-hyperpolarization current (I_{AHP}) were only present in the excitatory cells.

A Biologically Plausible Mechanism for Neuronal Coding Organized by the Phase of Alpha Oscillations

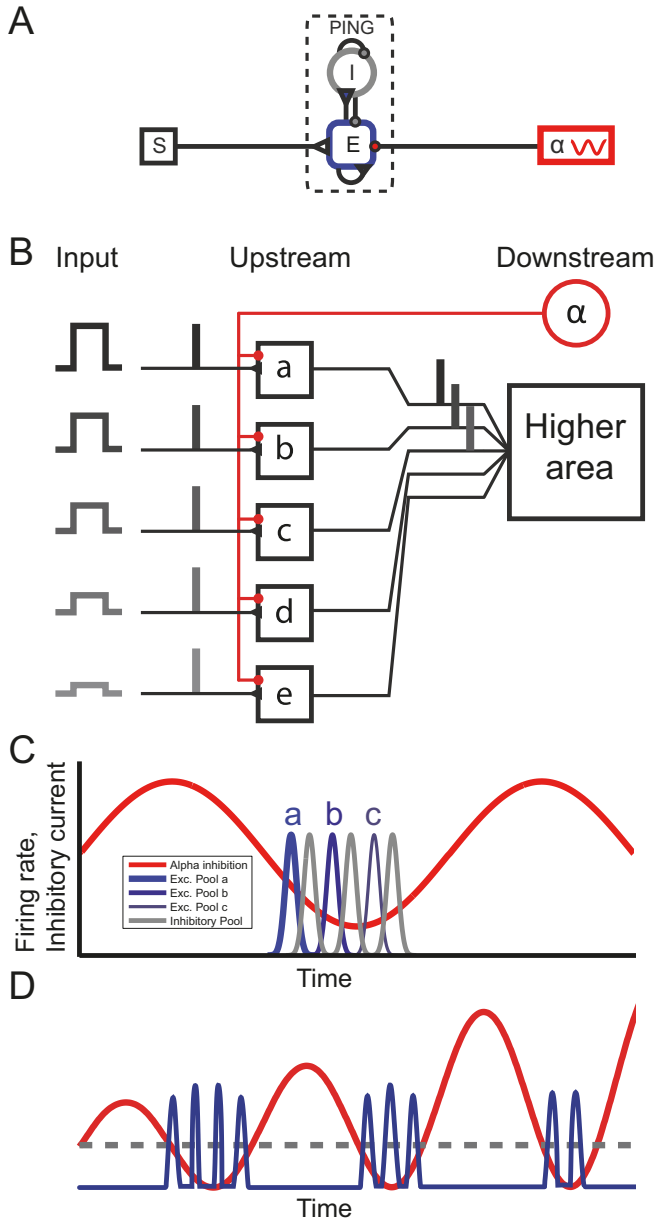


Figure 2-1. (A) An overview of the model. A ‘pyramidal interneuron gamma’ (PING) network composed of pyramidal excitatory (E) and inhibitory (I) neurons is modulated by an inhibitory drive in the alpha band (Greek alpha) and stimulus input (S). (B) Schematic overview of the mechanism. The inhibitory alpha source (red) causes areas a-e to be activated sequentially depending on their input (a-c) or not at all when the input is too low (d, e) (C) The expected result from the simulations. Excitatory neurons with different input levels (a-c)

fire in sequence (blue trace) according to the level of excitability, separated by bursts of inhibitory neuronal firing (grey trace) when the inhibitory alpha drive (red trace) is low. **(D)** Illustration showing how increasing alpha power decreases the duty cycle. The red line corresponds to the alpha inhibition that increases in power over time (from left to right). The blue trace corresponds to gamma activity generated by spiking neurons. The grey dashed line symbolized the threshold at which the inhibition is low enough for the most excited neurons to start firing. Parts of this figure have been reproduced with permission from [35].

2.2.2.1 *Excitatory neurons*

The model used for the excitatory neurons was adapted from the regular spiking model (RS) proposed by Pospischil [94]. An explicit after-hyperpolarization (AHP) potassium current was added (I_{AHP} in equation 1). This brings the individual firing rate of the neurons closer to the alpha frequency as has been measured by others [96], [97]. The AHP-conductance was modeled as a soft switch and causes the E-neurons to stay silent for approximately one alpha period after firing, thereby limiting the firing to one discharge per alpha cycle. This simple model mimics potassium currents whose conductance is strongly modulated by the local calcium concentration (for an explicit model of such calcium modulated currents see supplementary information in [98]).

2.2.2.2 *Inhibitory neurons*

The inhibitory neuron model was adapted from the fast spiking inhibitory neuron model (FS) proposed by Pospischil [94]. The synaptic dynamics (m_{GABA} in Table 2-1) were adapted from the modeling study by Jensen et al. [95]. However, they were sped up, by changing the parameters given in Table 2-1 to bring them more in line with intracellular recordings [99].

Table 2-1. Expressions for the functions of the membrane potential used to describe the dynamics of the (in-)activation variables.

n_{Na}	$\alpha = 0.128 \exp\left[-\frac{V + 44.5}{18}\right]$	$\beta = \frac{4}{\left(1 + \exp\left[-\frac{V + 21.5}{5}\right]\right)}$
m_{Na}	$\alpha = \frac{0.32(V - (13 + V_T))}{1 - \exp\left[-\frac{V - (13 + V_T)}{4}\right]}$	$\beta = -0.28 \frac{V + 21.5}{1 - \exp\left[\frac{V + 21.5}{5}\right]}$
n_K	$\alpha = \frac{0.032(V - (15 + V_T))}{1 - \exp\left[-\frac{V - (15 + V_T)}{5}\right]}$	$\beta = 0.5 \exp\left[-\frac{V + 0.515}{40}\right]$
m_{KM}	$x_\infty = \frac{1}{1 + \exp\left[-\frac{V + 35}{10}\right]}$	$\tau_x = \frac{\tau_{max}}{3.3 \exp[0.05(V + 35)] + \exp[-0.05(V + 35)]}$
m_{AHP}	$x_\infty = \frac{1}{1 + \exp\left(-\frac{V - 20}{5}\right)}$	$\tau_x = \frac{75}{\exp(0.15V) + 1}$
m_{AMPA}	$\alpha = \frac{40}{1 + \exp\left(-\frac{V}{2}\right)}$	$\beta = \frac{1}{2.4}$
m_{GABA}	$\alpha = \frac{5.69}{1 + \exp\left(-\frac{V}{2}\right)}$	$\beta = \frac{1}{1.8}$

2

2.2.3 Explicit description of channel currents

These currents are generally described as:

$$I_i = f_i(m_i, n_i) \cdot g_i \cdot (V - V_i) \quad (2.2)$$

For most currents the variable factor of the conductance is of the form:

$$f_i(m_i, n_i) = m_i^M n_i^N \quad (2.3)$$

But for I_{AHP} the form of the logistic function is used (see Table 2). Where m_i and n_i are the dynamic activation and inactivation variables of the current I_i respectively, V_i corresponds to its reversal potential. The activation and inactivation variables follow first order dynamics. For I_{Na} , I_K , I_{AMPA} and I_{GABA} we use the form:

$$\frac{dx}{dt} = \alpha_x(V)(1 - x) - \beta_x(V)x \quad (2.4)$$

Whereas for I_{KM} we employ:

$$\frac{dx}{dt} = (x_{\infty}(V) - x)/\tau_x(V) \quad (2.5)$$

Where $x = m_i, n_i$ corresponds to the different activation and inactivation variables. The rate functions $\alpha_x(V)$ and $\beta_x(V)$ or $x_{\infty}(V)$ and $\tau_x(V)$ are specific for channels and, except for a possible voltage shift V_T (see Table 2-3), the same for E-neurons and I-neurons. They are given in Table 2-1.

The functions of the activation and inactivation variables describing the variable factor of the conductance (eq. 3) for the different currents, as well as their reversal potentials V_i are shown in Table 2-2.

The parameters that differ between the two neuron models (the maximum conductances g_i in equation 2, and the potential shift V_T and time constant τ_{max} in Table 2-1) are shown in Table 2-3.

Table 2-2. Reversal potentials and conductance variability.

	V_i (mV)	$f(m, n)$
leak	-70	1
Na	50	$m^3 n^2$
K	-90	n^4
K_M	-90	n
AHP	-90	$\frac{1}{1 + \exp\left(\frac{0.368 - m}{0.02}\right)}$
AMPA	0	m
GABA	-80	m

Table 2-3. Parameters specific to the excitatory and inhibitory neurons.

	E-neurons	I-neurons
g_{leak} (mS/cm ²)	0.0205	0.015
g_{Na} (mS/cm ²)	50	46
g_K (mS/cm ²)	4.8	5.1
V_T (mV)	-61.5	-61.84
g_{KM} (mS/cm ²)	0.3	0.07
τ_{max} (ms)	1123.5	824.5
g_{AHP} (mS/cm ²)	0.5	N/A

2.2.4 Spatial configuration of the network and connectivity

The spatial configuration of the network is shown in Figure 2-2A. The excitatory and inhibitory neurons are retinotopically arranged on a triangular grid (with periodic boundaries, providing a toroidal topology, for computational convenience). The most important point here, is that the E- and I-neurons are interconnected to form a PING network [38], [39], [100], [101] to produce a gamma rhythm (Figure 2-1A). After a group of pyramidal excitatory neurons has discharged, their firing triggers the activation of inhibitory neurons. The resulting inhibitory volley hyperpolarizes the network by GABAergic feedback connections for 10-30 ms inhibiting other neurons from firing. After the GABAergic inhibition has decayed, excitatory neurons can fire again. This temporally silencing of the network has been proposed to implement a winner-take-all mechanism [56]. Recent work has demonstrated that this mechanism can account for the visual gamma activity [102], [103].

The connection pattern may influence the firing behavior of the network. In the current work we did not explore this dependency in detail. Rather we chose to mimic local connectivity in early visual cortex [104]–[106]. The neurons are connected according to a Gaussian probability distribution in terms of proximity. This means that the neurons are more likely to connect to neurons nearby than to neurons far away. The E-neurons were considered to be similar to pyramidal cells and the I-neurons were thought to resemble basket cells. This meant that the I-

neurons had a more local connection profile than the E-neurons. From these Gaussian distributions (see equation 6, where D is the distance, in μm , between the sender and target neuron) a number of connections were drawn, equal to the product of the connection fraction \underline{c} and the total number of neurons of the type it was connecting to (i.e. 1080 or 270, see Table 4).

$$P = \frac{1}{\sqrt{2\pi\sigma^2}} \exp\left(-\frac{D^2}{2\sigma^2}\right) \quad (2.6)$$

The connections were generated for every neuron as a receiver, such that every neuron received an equal number of connections, but did not necessarily get the same number of outgoing connections.

In table 4 we show the values used for: 1) the standard deviations (σ) of the Gaussian connection profiles, 2) connection fractions (\underline{c}) that determine from how many neurons a connection is established, and 3) the total maximum synaptic conductance (g_{AMPA} and g_{GABA} in equation 2, summed over all postsynaptic connections to each neuron) are shown in Table 4.

For the connections from E- to I-neurons a uniform distribution was used. This provided that the gamma synchrony was global across the entire simulated network.

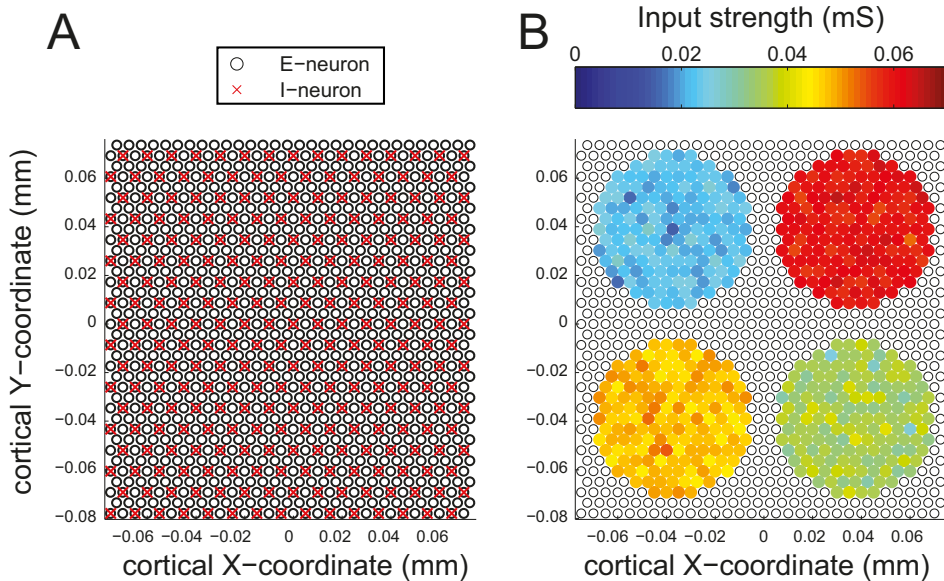


Figure 2-2. (A) Spatial configuration of the network. Black open discs represent the 1080 excitatory neurons; red crosses represent the 270 inhibitory neurons. (B) Spatial configuration of the excitatory input to the network. Inhibitory neurons are omitted for clarity, since they do not receive any direct input currents. Black open discs indicate excitatory neurons not receiving any direct input. Colored discs indicate excitatory neurons

that receive an external input from 4 different circular stimuli of differing strength. Disc color indicates input strength defined as the conductance of a membrane channel.

2.2.5 Direct excitatory and inhibitory input

The E-neurons were supplied with an excitatory input ($I_{AMPA_{imp}}$ in equation 1) without any intrinsic dynamics (i.e. M and N in equation 3 are equal to 0, yielding: $I_{AMPA_{imp}} = g_{AMPA_{imp}}(V - V_{AMPA})$) that is shown in Figure 2-2B. The conductance of the AMPA channels ($g_{AMPA_{imp}}$) for the E-neurons that receive non-zero input (see Figure 2-2B) consisted of a constant term, which was sampled from one of 4 Gaussian distributions with equally spaced means (0.0225, 0.035, 0.0475 and 0.06 mS respectively) with standard deviation of 0.0015 mS (see S 1 Fig) corresponding to the four circular areas of different input strength in Figure 2-2B. This creates four different clusters of neurons, each assumed to code for a different visual feature. The strength of these inputs was chosen such that the network produced realistic firing rates (each neuron firing at around 10 Hz, see S 2 Fig) and oscillations in the gamma band (around 60 Hz, see Figure 2-6A). To this constant conductance, further (temporal) Gaussian white noise was added with a standard deviation of 0.002 mS to make the behavior of the neurons more realistic. The E- neurons also received an inhibitory input ($I_{GABA_{imp}}$ in equation 1; $I_{GABA_{imp}} = g_{GABA_{imp}}(V - V_{GABA})$) representing the thalamic inhibitory drive. This was modeled by changing the conductance ($g_{GABA_{imp}}$) for the GABA channels sinusoidally over time with a frequency of exactly 10 Hz between zero and a maximum value (*alpha inhibition strength*), and is varied across simulations (between 0 mS and 0.2 mS with steps of 0.02 mS and between 0.2 mS and 1 mS with steps of 0.04 mS). The inhibitory neurons did not receive any direct input.

2.2.6 Simulating the local field potential

The local field potential (LFP) $V(\mathbf{r})$ at a position \mathbf{r} in the intracellular space is determined by the transmembrane currents into all neurons. Treating the intracellular liquid as a homogeneous dielectric with resistivity similar to mammalian saline at 20 °C $\rho = 60 \Omega\text{cm}$ [107]

$$V(\mathbf{r}) = \rho \int \frac{I(\mathbf{s})}{4\pi|\mathbf{r} - \mathbf{s}|} d^2s \quad (2.7)$$

Here the local trans-membrane current density $I(\mathbf{s})$ is integrated over the surface positions \mathbf{s} of all neurons. Each neuron is approximated by one or more cylindrical compartments. A compartment j is described by the position \mathbf{r}_j of the center, the

axis \mathbf{L}_j (length $L_j = |\mathbf{L}_j|$, orientation \mathbf{L}_j/L_j), and the radius R_j . A uniform current density I_j is assumed. The integration leads to a sum over all compartments j of all neurons:

$$V(\mathbf{r}) = \sum_j V_j(\mathbf{r}) = \frac{\rho}{4\pi} \sum_j \frac{I_j L_j R_j}{r_{\text{eff}}} \quad (2.8)$$

The parameter r_{eff} takes the relative position ($\mathbf{d}_j = \mathbf{r} - \mathbf{r}_j$) and orientation of each compartment into account:

$$\frac{1}{r_{\text{eff}}} = \int_{\phi=0}^{2\pi} \int_{z=-1/2}^{1/2} \frac{1}{\sqrt{(\mathbf{d}_j - z\mathbf{L}_j)^2 + R_j^2 - 2d_j R_j \cos(\phi)}} dz d\phi \quad (2.9)$$

For infinitely thin cylinders, $R_j \rightarrow 0$, the integration over ϕ is trivial and analytically integrating over z leads to the line source approximation used by Koch and colleagues [108], [109]. For finite R_j the integral over ϕ is a complete elliptic integral of the first kind [110], which is evaluated using a standard numerical algorithm [111]. For the remaining integration over z , a simple approximation is used that is accurate when $d_j^2 \gg L_j^2 - R_j^2$, which usually will be the case.

In the simulations reported in this work, all neurons consisted of one single compartment. All neurons were oriented in parallel and the LFP electrode was positioned in plane with all neurons. Note that in nature inhibitory neurons tend to have neurites oriented isotropically around the soma. This tends to decrease the influence of their activity on the LFP (see e.g. [112]). Since all neurons consisted of only one compartment oriented in the same direction, this attenuating effect on the contribution of inhibitory neurons was not present. Instead, we only took the transmembrane currents of E-neurons into account.

2.2.7 Analysis

The output of the simulations (spike timings and simulated LFP signal) were analyzed using custom scripts written in MATLAB (MathWorks Inc., Natick, MA, USA).

2.2.7.1 Power spectrum estimate

The power spectral density (PSD) of the simulated LFP for alpha and gamma were estimated using Welch's method with 50% overlap (Welch, 1967). A hamming window was used to avoid edge artifacts. For estimating the alpha power, windows of 1 second were used (Figure 2-6B). For the gamma power and frequency, smaller windows of 100 ms were used (Figure 2-6A). This was done to avoid the discrete peaks in the power spectrum at multiples of 10 Hz caused by the higher harmonics

of the alpha modulation. These strong higher harmonics make estimation of peak gamma frequency difficult.

2.2.7.2 Phase-amplitude coupling

For assessing the strength of the phase-amplitude coupling in the simulated LFP, we used the mean vector length as proposed by Canolty and colleagues [62], [113]. We normalized it by the total gamma amplitude summed over time, to normalize the value between 0 and 1.

$$PAC = \frac{|\sum_t A_\gamma(t) * \exp(i\phi_\alpha(t))|}{\sum_t A_\gamma(t)} \quad (2.10)$$

The phase of the lower frequency ($\phi_\alpha(t)$) was estimated by band-pass filtering the LFP signal by multiplying the signal in the frequency domain with a rectangular window with a width of 1 Hz centered around the (positive) frequency of interest (x-axis of Figure 2-7 or fixed at 10 Hz in S2 Fig). Since this filter removes all negative frequencies, the filtering results in a complex signal from which the instantaneous phase angle can be calculated. This is similar to using the Hilbert transform to yield an analytic signal after normal band-pass filtering.

The amplitude envelope $A_\gamma(t)$ of the high frequencies was estimated in a similar way. The signal was band-pass filtered around the frequency of interest (y-axis of Figure 2-7 and S 3 Fig). Since we wanted to quantify modulations in the amplitude envelope of the gamma band activity that are of the time-scale of the phase-providing frequency, they should not be filtered out. For example, if the gamma component is modulated by a 10 Hz rhythm, this modulation is reflected in two “satellite peaks” in the spectrum that are located 10 Hz above and 10 Hz below the main gamma peak. This means that the bandwidth of the filter should be at least 20 Hz to make sure that the amplitude modulations are captured. Analogously for other phase-providing frequencies, the bandwidth of the filter that isolates the gamma component should always be at least twice the phase-providing frequency. The bandwidth of the filter (the width of the rectangular window in the frequency domain) was set to 3 times the phase-providing frequency indicated on the x-axis in Figure 2-7A and set to 20 Hz in S 3 Fig. After the filtering the magnitude of the analytic gamma component provides an estimate for the instantaneous amplitude.

2.2.7.3 Mutual information

The mutual information of a stimulus (X) and a response (Y) can be calculated by calculating the discrete probability density histograms (P(X)) and calculating the Shannon entropy H:

$$H(X) = - \sum_x P(X) \log_2(P(X)) \quad (2.11)$$

$$I(X, Y) = H(X) - H(X|Y) \quad (2.12)$$

Where $I(X, Y)$ is the mutual information and $H(X|Y)$ is the conditional entropy:

$$H(X|Y) = \sum_{X,Y} P(X, Y) \log_2 \left[\frac{P(X)}{P(X, Y)} \right] \quad (2.13)$$

For a more easily interpretable measure, the mutual information was normalized by the entropy of one of the two signals to keep the value between 0 and 1 (as seen in Figure 2-5B) [111].

$$MI_{norm}(X, Y | Y) = I(X, Y)/(H(X)) \quad (2.14)$$

This normalized quantity takes the value of 0 if X and Y are independent signals, and a value of 1 if X is redundant given Y, i.e. if the values of X can be completely reconstructed if only Y is known.

The performance of the phase organized code in terms of gamma separation was assessed by calculating the mutual information between the classification of neurons based on input level (4 stimuli or non-firing, Figure 2-2B) and the classification based on the gamma burst the neuron's action potential belongs to (see Figure 2-5D). Classification was done using K-means clustering [114] on input level (where neurons were assigned their own class label manually) or firing phase (non-firing neurons were assigned a class label manually). The number of clusters for input labels was fixed at 5 (4 stimuli levels and no input at all), whereas the number of clusters for the labeling based on firing phase was determined by selecting the number of clusters for which the mean value of the silhouette coefficient was highest [115]. The normalized mutual information (eq. 14) was then calculated between these two classifications to assess phase coding performance.

2.2.7.4 Bootstrap as a measure of dispersion

To get an estimate of the accuracy of the measures for phase coding and PAC (Figure 2-5A,B and Figure 2-7B respectively), we employed a statistical bootstrap procedure [116]. The data points needed for calculating of the respective measure were re-sampled with replacement to net an equal number of data points as in the original data. For the correlation coefficient (Figure 2-5A) and the mutual information (Figure 2-5B) these data points consisted of either input strength and firing phase, or input strength and gamma cycle number respectively for each firing

neuron in each of the simulated 20 alpha cycles. For estimating the dispersion of PAC (Figure 2-7B) the relevant data were composed of 20000 time bins containing gamma power envelope magnitude and instantaneous alpha phase. From this re-sampled data set the measure of interest could be calculated again. This was done 1000 times to generate distributions of PAC, MI and correlation coefficients. From these distributions, the standard error was estimated using:

$$SE_{bs}(X) = \sqrt{\frac{\sum_{i=1}^N (X_i - \hat{X})^2}{N - 1}} \quad (2.15)$$

Where $SE_{bs}(X)$ indicates the estimated standard error of measure X (in our case, PAC, MI or correlation coefficient). \hat{X} indicates the sample mean of the distribution consisting of the 1000 calculations of measure X from the resampled data sets. $N=1000$ is equal to the number of re-sampled data sets.

2

Duty cycle

We define the *duty cycle* as the fraction of the time within an alpha oscillation that neurons are firing (Figure 2-1D). We calculated this as the time span between the first and the last action potential in every alpha cycle, normalized by the period of an alpha cycle (~100 ms). This means that the duty cycle has a value between 0 (no firing at all) and 1 (continuous firing, this could mean there is no real periodicity in the signal in the alpha band).

2.3 Results

We implemented and performed simulations of 2 seconds of neural activity of the neural network model shown in Figure 2-1A for every different level of alpha inhibition strength (between 0 and 0.2 mS, see Methods section for details). We first schematically outline the core ideas of the model and then describe the simulations. The underlying idea is that areas lower in the processing hierarchy (our model network is thought to represent neurons in V1) receive LGN input to be prioritized and transmitted to areas downstream in the visual stream. These inputs reflect different presentations (a - e) and may vary in strength as suggested by the height of the pulses (Figure 2-1B). Given the hierarchy of the visual system, early visual regions project to higher visual areas with converging connections. In addition, all the excitatory neurons are subjected to inhibitory alpha oscillations at 10 Hz. The alpha oscillations are here thought to be coordinated by the thalamus [24], [117], [118].

2.3.1 Temporal coordination by the alpha oscillations

The pyramidal neurons in the network receive excitatory stimulation reflecting the visual input from the LGN (S in Figure 2-1A). As we will discuss later, the strength of this stimulation reflects both bottom-up (e.g. contrast or saliency) and top-down effects (e.g. attention or figure-ground segmentation). The slower inhibitory 10 Hz oscillatory alpha drive serves to temporally organize the neuronal firing in the early visual areas according to the neurons' individual level of excitation. Furthermore, it serves to prevent firing of neurons responding to the weakest stimulations (d and e in Figure 2-1B). This temporal organization (illustrated schematically in Figure 2-1C) is caused by an interplay of the periodic inhibitory alpha drive and the difference in excitation amongst the pools of neurons (*a - e*) representing different visual features. In the simulations we explore how robust this coding scheme is. Finally, we explore the notion of the *duty cycle*, (see methods, illustrated in Figure 2-1D). The dashed grey line in Figure 2-1D schematically depicts the inhibition threshold below which neurons can fire. If the magnitude of the alpha inhibition is increased, this threshold is reached later in the alpha cycle. Moreover, the inhibition increases faster at the end of the alpha period, causing the neurons to stop firing, which is reflected in a shortening of the duty cycle. In the simulations we examine the effects of the magnitude of the alpha inhibition on the duty cycle and the phase code.

2.3.2 Different magnitudes of alpha oscillations

The simulations in Figure 2-3 illustrate the main features of the proposed mechanism at different levels of the inhibitory alpha drive. The raster plots illustrate action potentials generated by the excitatory neurons. In these plots, the neurons are sorted along the y-axis according to the total excitatory drive (during the two second simulation). In the lower panels the red curve depicts the inhibitory input at alpha frequency. To obtain a continuous measure of spiking activity, the binary spiking events are convolved with a Gaussian kernel ($\sigma = 2.5$ ms) and summed over neurons. This is shown for both excitatory (blue) and inhibitory neurons (gray).

The first panel (Figure 2-3A) shows the network dynamics in absence of the inhibitory drive. In this case, while neurons with similar input strengths tend to fire together, the temporal firing order of the neurons does not reflect the strength of the different input "spotlights" (Figure 2-2B). Population activity of the excitatory (blue line) and inhibitory neurons (gray line) shows weak synchrony in the gamma band as we explain in the next panel. The simulation in Figure 2-3B shows that the inhibitory drive in the alpha range (red line) orders the neuronal firing according to the level of excitation. As the inhibition from the alpha drive ramps down, the neurons with the ~ 0.055 to ~ 0.07 mS input current (red population in Figure 2-2B)

fire first. As the inhibition further decreases, the next items receiving the 0.04 to 0.055 mS current fire (the orange population in Figure 2-2B) followed by the neurons receiving the 0.025 to 0.04 mS input current (neurons green population in Figure 2-2B). Individual neurons tend to fire only once per alpha cycle due to the after-hyperpolarizing current. The neurons that are excited the least never fire, since they are prevented to do so by the alpha inhibition ramping up again at the end of the cycle. Each time when neurons with similar input strength have fired, the fast GABAergic network is activated. This serves to segment the neural representations of the visual input in time. Furthermore, the GABAergic feedback supports a winner-take-all mechanism such that when the most excitable neurons activate, it delays the activation of less excited neurons [56]. Consequently, this PING mechanism produces a gamma rhythm in the population activity as seen in the blue and grey lines in the lower panels of Figure 2-3B. These excitatory-inhibitory firing bouts are separated by ~ 20 ms; i.e. the population activity is oscillating in the gamma band at ~ 50 Hz. Since the excitatory neurons are silenced during the peak of the imposed alpha inhibition, the neuronal firing has an oscillatory component in the alpha range as well. As a result, the population activity produces gamma band activity locked to the phase of the alpha oscillations. In summary, the simulation demonstrates that, at this inhibition level, the network reliably segments the visual input into three sequential neural representations based on level of excitation. Figure 2-3C shows what happens when the inhibitory alpha drive is further increased. Due to stronger inhibition the firing of the first items is delayed. Therefore, the third item cannot fire before the alpha inhibition ramps up again. This leads to a shorter window of opportunity for the excitatory neurons: a shorter duty cycle. Note that while the gamma rhythm does temporally segment neuronal firing, it does not necessarily separate the 4 neuronal “spotlights” (Figure 2-2B and S 1 Fig), this can be seen by the distribution of neurons belonging to the “yellow” spotlight among both the first and second gamma cycle in Figure 2-3C. The mechanism purely sorts based on excitatory input strength.

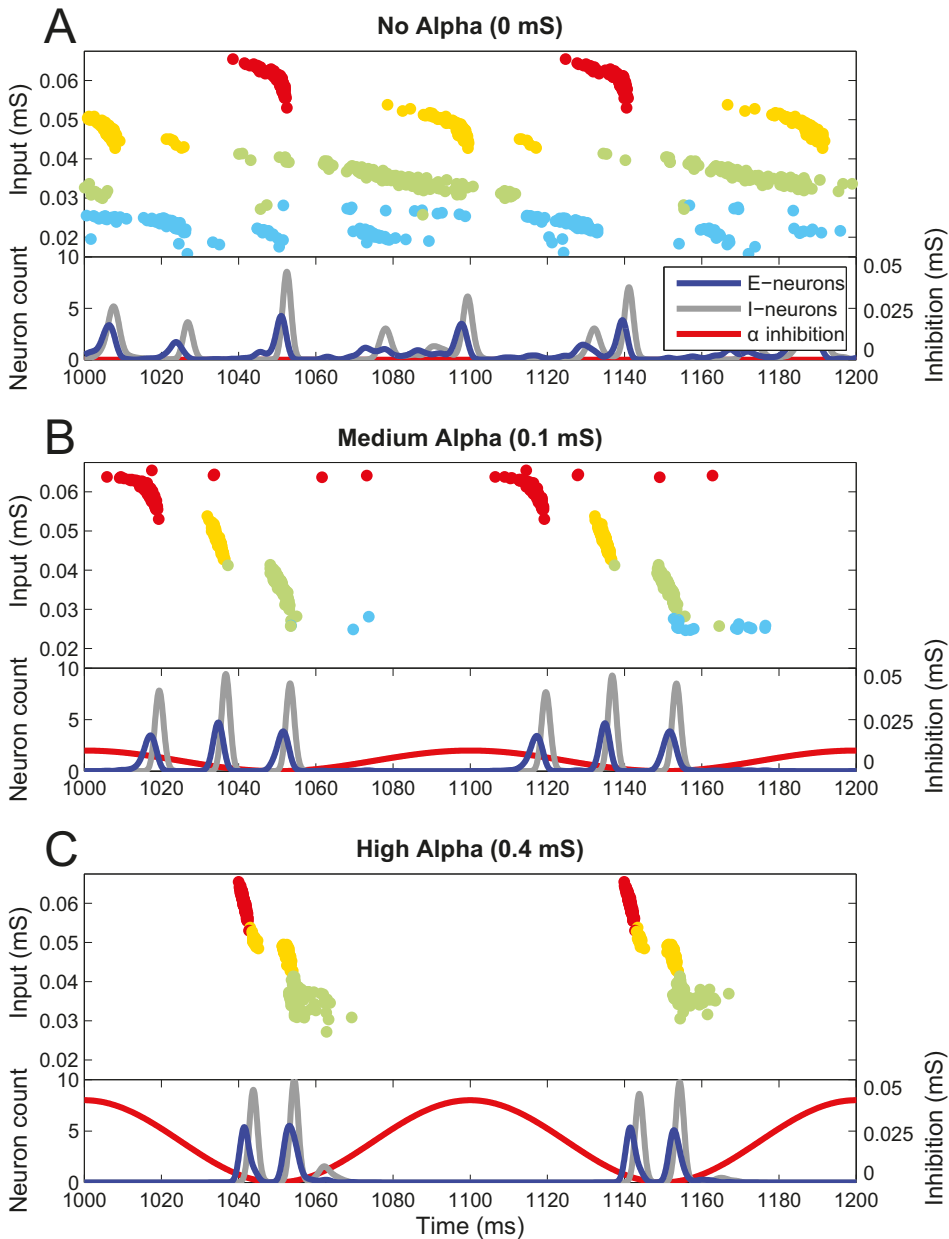


Figure 2-3. Simulations for different levels of the inhibitory alpha drive. (A-C) The figures show a raster plot of the activity of the excitatory neurons in the network. The neurons are sorted along the y-axis according to the strength of the excitatory input they receive. Secondly, they are color-coded based on which “spotlight” they belong to, see Figure 2-2B. Below each raster plot a pseudo-spiking histogram for the excitatory and inhibitory neurons is plotted (the spiking histograms are convolved with a Gaussian kernel, giving a smoother

representation of network activity), together with an overlay depicting the sinusoidal alpha inhibition projecting to the excitatory neurons similar to Figure 2-1C.

2.3.3 Duty Cycle

Figure 2-4 provides a quantification of the relationship between network dynamics and alpha inhibition strength. Figure 2-4A shows that the duty cycle decreases as the alpha inhibition increases. Next we quantified the number of gamma burst present in each alpha cycle (Figure 2-4B). The number of gamma bursts is defined as the number of peaks in the smoothed excitatory population activity (the blue trace in Figure 2-3A) in every alpha cycle. As can be seen in Figure 2-4B, the number of gamma bursts in every alpha cycle goes from three to two and eventually to one for very high alpha strengths (up to 1 mS). Besides the number of gamma bursts decreasing, the continuous decrease of the duty cycle for an alpha drive above 0.07 mS is also caused in part by an increase in the gamma frequency itself. This is visible in the spectral properties of the simulated LFP signal to be discussed below. Figure 2-4C shows that the number of neurons firing every alpha cycle decreases with increasing alpha strength. The increase of the dispersion between alpha inhibition strengths of 0.4 and 0.6 mS is explained by a subset of neurons firing only every other alpha cycle (see S 2 Fig). Taken together, these results show that a stronger inhibitory alpha drive shortens the duty cycle by suppressing firing at the expense of the neurons with the weakest input.

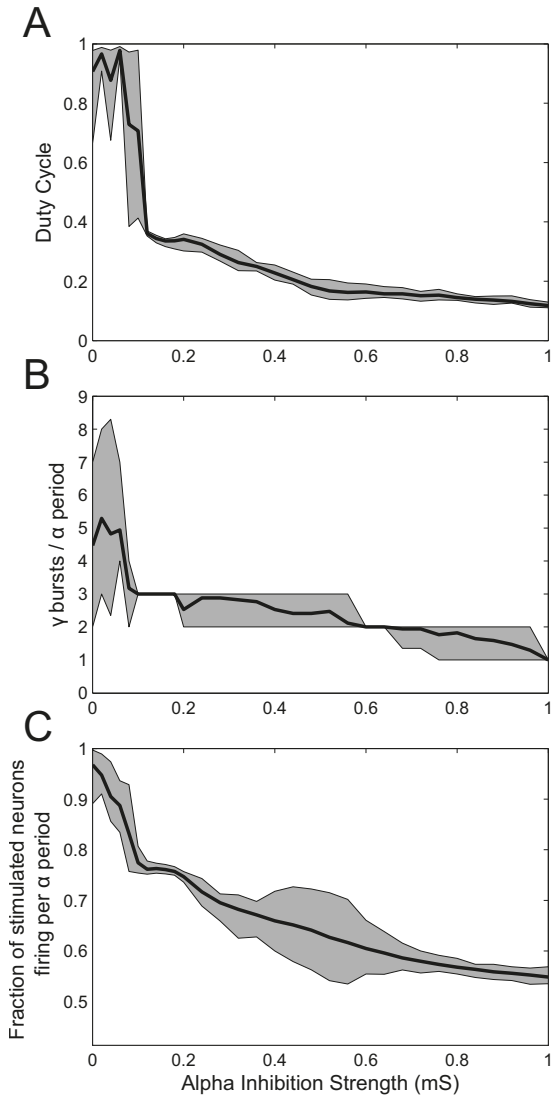


Figure 2-4. Duty cycle related properties as a function of alpha inhibition strength. (A) Duty Cycle as function of the inhibitory alpha drive. **(B)** Number of gamma bursts per alpha cycle. **(C)** Fraction of the neurons that receive stimulus input (colored circles in Fig 2B) that are spiking during every alpha cycle. The shaded areas in all 3 panels indicate the 95% confidence interval, whereas the black line indicates the mean across all alpha cycles during a 2 s interval.

2.3.4 A phase organized code

The inhibitory alpha drive sorts the action potentials in time according to the level of excitatory input [35]. In other words, the strength of the input to a pyramidal neuron is translated into the alpha phase at which it tends to fire. This effect can clearly be seen in Figure 2-3B and C: pyramidal neurons with stronger external input fire at an earlier alpha phase than neurons with a weaker input. To quantify this effect, we calculated the correlation between the input strength and the firing phase. For a reliable phase organized code, a strong correlation is required, since the phase of firing should advance with input strength. The Spearman correlation between input strength and firing phase for different levels of alpha inhibition is shown in Figure 2-5A. Because of the sinusoidal shape of the alpha drive, the decrease of the inhibition in the initial part of each alpha cycle is not linear in time. Secondly, the PING mechanism separates the action potentials into gamma bursts, rather than a continuous regular spike train. These two factors are detrimental when calculating the Pearson correlation coefficient between neuronal input and the phase of alpha in which the neuron spikes. Instead, we used Spearman's ranked correlation coefficient to quantify the monotonic (rather than a linear), relation between input level and firing phase (i.e. whether higher input leads to an earlier firing phase, this is illustrated in Figure 2-5C).

For stronger alpha oscillations, the phase organized code becomes more accurate, as can be seen by the correlation coefficient in Figure 2-5A. A caveat here is that only firing neurons are considered. Stimuli that do not trigger spikes are not considered detrimental to the phase organized code. This is reflected by the strong correlation when alpha inhibition strength is high (alpha inhibition strength above 0.7 mS). In these cases, the sinusoidal inhibition is strong enough to suppress all firing except for one gamma bursts, but the temporal ordering of the spikes within this cycle (and therefore within the alpha cycle) still reflects relative input strength.

To better assess the performance we performed a second analysis which focused on the temporal segmentation of the firing of the neurons coding for each of the four circular areas in Figure 2-2B. We compared clustering of the action potentials based on input strength to a clustering based on alpha phase (see Methods, illustrated in Figure 2-5D). To what extent the classification according to either input level or gamma cycle match each other can be quantified by the normalized mutual information between these two classifications (Figure 2-5B). A maximum performance in terms of phase organized code can be seen when the alpha inhibition strength is around 0.1mS. At this alpha strength, the network is able to segment three representations in the three different gamma cycles corresponding to three areas of different input strength (see Figure 2-2B, Figure 2-3B and Figure 2-4B), which maximizes the information content. Higher alpha inhibition strengths cause a decrease in the number of neurons that spike (see Figure 2-4C and Figure 2-3) as

well as a decrease in the match between the segmented gamma bursts and the different circular areas receiving different excitation levels in Figure 2-2B (e.g. by mixing neurons excited by the yellow area in both the first and the second gamma cycle, see Figure 2-3C).

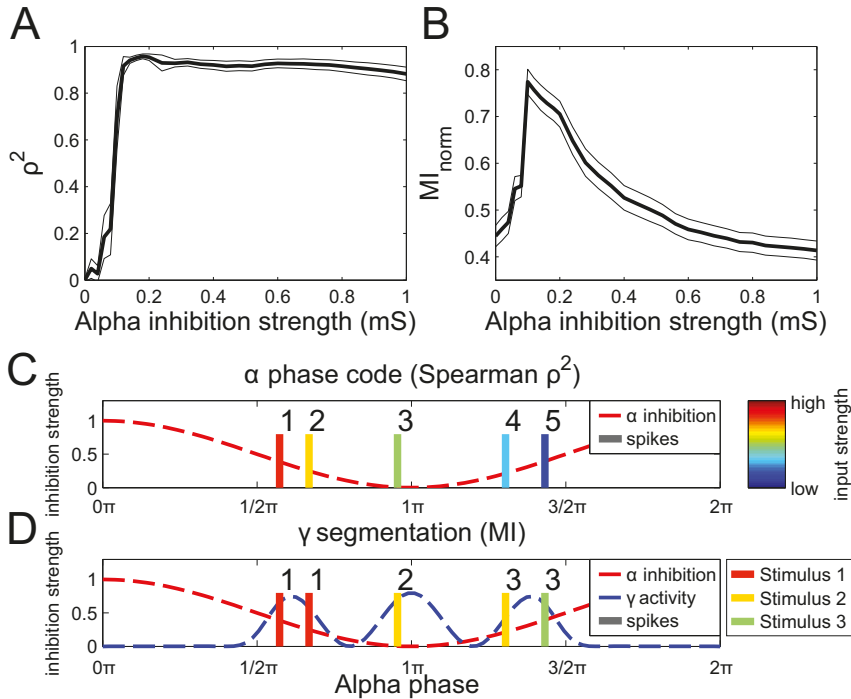


Figure 2-5. The performance in terms of the phase organized code as a function of alpha strength. (A) Phase coding quantified by calculating the square of Spearman's correlation coefficient (ρ^2) between firing phase and input level (see C). The thin black lines indicate the standard error, multiplied by a factor 10 to make them visible, as estimated by 1000-fold bootstrapping. (B) Phase coding quantified by means of mutual information between stimulus index of the neuron and index of the gamma cycle the neuron fires in (see D). As in A, the thin black curves indicate ten times the standard error as estimated by 1000-fold bootstrapping. (C) Schematic illustration of using Spearman's ρ (panel A) to assess coding performance. Color of action potentials indicate excitation level (red is high, blue is low) which is then correlated with the ranked firing phase (illustrated by the numbers 1-5). (D) Schematic illustration of how gamma segmentation performance was measured (panel B). All neurons are either classified by which gamma cycle it fires in (indicated by the numbers 1-3 above the spikes), or by the stimulus it belongs to. The stimulus classification had five different classes: four classes indicating by which of the four circular stimuli the neuron was stimulated and one class when a neuron received no excitatory stimulation at all (indicated by the color, see Fig 2B and legend to the right). The mutual information is then calculated between these two classifications.

2.3.5 Experimentally measurable quantities

From the simulated model network, we can estimate the local field potential (LFP) to make predictions that can be verified in future *in vivo* experiments. This simulated LFP takes into account all cross-membrane currents and assumes a medium with constant and homogenous permittivity (see Methods). From this simulated LFP (see S 4 Fig for some examples) some predictions can be made for quantities measurable by intracranial recordings and possibly also by electroencephalography (EEG) and magnetoencephalography (MEG) recordings.

2.3.5.1 Spectral properties

Since our network model attempts to capture phenomena in the alpha and gamma band, we have examined the spectral properties of the simulated LFP signals. The lower panel in Fig. 6 illustrates the power spectra in the alpha range as a function of alpha inhibition strength. The increase in alpha power with increasing inhibition (0 – 0.4 mS) is explained by the rhythmic silencing of neuronal firing creating a strong modulation in the population activity. Note that the total firing rate systematically decreases as the alpha inhibition increases (Figure 2-4C) in line with empirical findings [36]. As the inhibition increases even further (>0.4 mS) the alpha power decreases as an increasing number of neurons are silenced.

The power spectra for the higher frequencies as a function of alpha strength is shown in Figure 2-6 (top panel). The band-limited gamma power is visible. The alpha inhibition has a synchronizing effect on the network in the gamma band, as the gamma band components can only be seen when the alpha inhibition is above 0.1 mS (Figure 2-6, top). With weak alpha modulation (<0.1 mS) the network generates irregular gamma-band activity virtually undisturbed by the alpha inhibition (see also Figure 2-3A) and hence poorly synchronized across the entire network. This is reflected in the lack of a gamma power in Figure 2-6 (top panel) for simulations with low alpha inhibition strength. With stronger alpha inhibition (>0.1mS), the sinusoidal inhibitory drive is able to silence the network at every peak of the alpha inhibition (and in contrast letting the neurons fire in the troughs, when the inhibition is low) and the frequency and power of the gamma activity depend on the alpha inhibition strength. The gamma power eventually decreases with increasing alpha strength (>0.5 mS) caused by the fact that less neurons are firing. To understand the relationship between alpha inhibition strength and gamma frequency consider the following: when the alpha strength increases further, the descending slope of the sinusoidal inhibition becomes steeper. This causes the inhibition to drop faster over time, making it possible for the neurons in the second gamma volley to fire earlier relative to the first gamma volley. This produces an

increase in gamma frequency with the strength of the alpha drive being in the 0.1 to 0.6 mS interval (Figure 2-6, top). At around 0.2 mS the number of gamma volleys changes from three to two, causing a jump in the gamma frequency and a slight dip in the peak gamma power as it is spread out across a wider frequency band. Finally, for very high alpha strength (>0.6 mS) the two remaining gamma volleys in every alpha cycle merge together and the gamma rhythm is attenuated. Future experiments are needed to confirm the positive correlation between alpha power and gamma frequency predicted by the model.

A second gamma peak is visible in the top panel in Figure 2-6 at double the frequency of the first gamma frequency. This is a higher harmonic explained by the non-sinusoidal shape of the gamma oscillations.

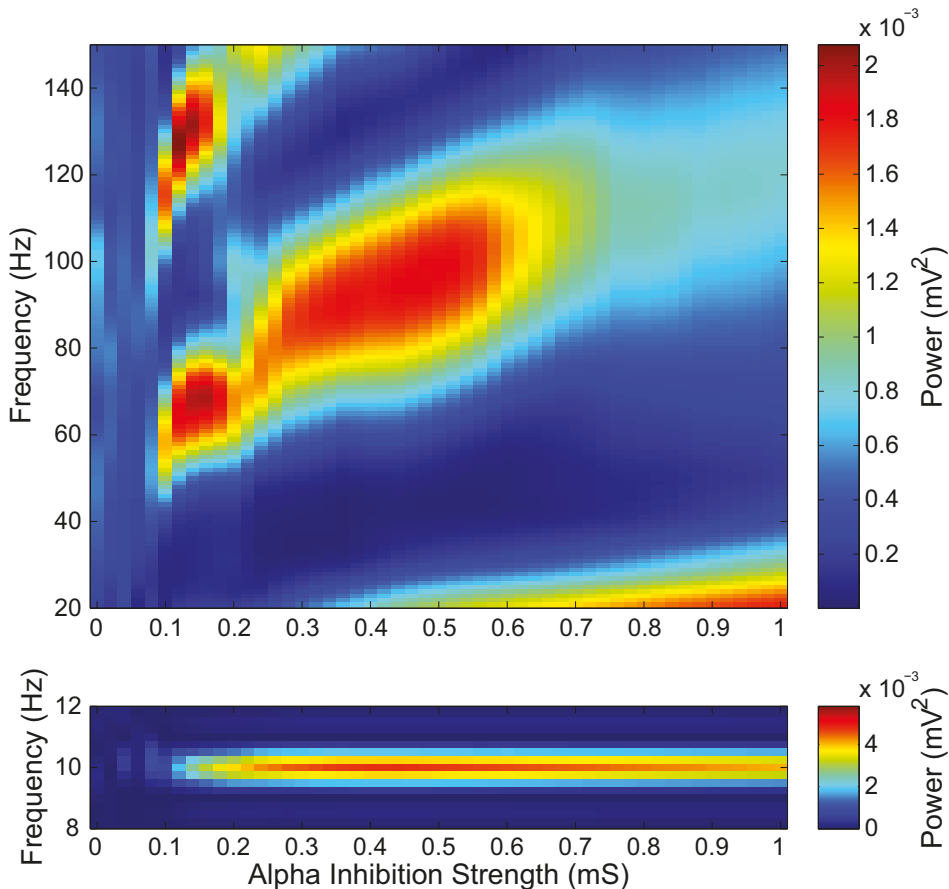


Figure 2-6. Effects of alpha inhibition strength on the spectral properties in simulated LFP. Power spectra were calculated using Welch's method and a Hamming taper, either with short windows of 100 ms to estimate gamma-band properties (**top**) or with longer windows of 1 s (**bottom**), to accurately represent the power spectral density in the alpha-band.

2.3.5.2 Phase-amplitude coupling

Phase-amplitude coupling (PAC) measures to what extent the amplitude of a high-frequency activity is modulated by the phase of a low-frequency oscillation. The PAC values calculated from the LFP signal from the simulation shown in Figure 2-3B (i.e. with an alpha inhibition strength of 0.1 mS), are presented in the comodulogram in Figure 2-7A. The gamma power envelope of around 60 Hz and the power envelope of the corresponding harmonics are locked to the 10 Hz rhythm imposed by the alpha inhibition. Some power in the gamma band also locks to the 20 Hz harmonic of the alpha rhythm, indicating that the 10 Hz periodic component in the signal is not completely sinusoidal either. This results in a higher harmonic of the ~10 Hz oscillations and should not be interpreted as a true neuronal oscillation.

Increasing alpha inhibition strength increases PAC between the alpha phase and the gamma amplitude in the simulated LFP signal (Figure 2-7B). This is mainly caused by the shortening of the duty cycle. The shorter the duty cycle, the more concentrated the gamma activity is with respect to alpha phase, resulting in a stronger PAC (see equation 10 in Methods). Similar to the power spectra (Figure 2-6, top panel) of the simulated LFP, the higher harmonics of the gamma rhythm are clearly visible when considering phase-amplitude coupling at ~120 Hz and does not reflect true neuronal oscillations at that frequency (see [119] for a discussion).

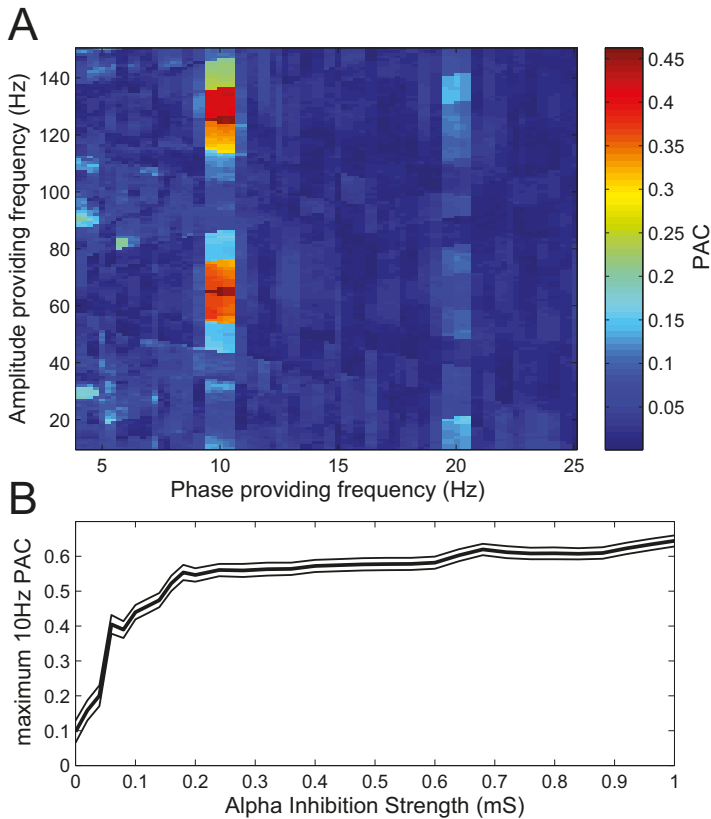


Figure 2-7. Coupling of gamma amplitude to alpha phase. (A) Comodulogram showing the PAC values calculated from the simulated LFP shown in Fig 3B (with an alpha inhibition strength of 0.1 mS). Note that gamma power of around 60 Hz and the harmonics are locked to the alpha frequency (10 Hz) and the first harmonic (20 Hz). **(B)** The height of the first gamma peak in the comodulogram (i.e. the fundamental frequency, not the higher harmonics, see A) for a phase providing frequency of 10 Hz calculated for every simulation, expressed as function of strength of the inhibitory alpha drive. The thin black lines indicate the standard error, multiplied by a factor 5 to make them visible, as estimated by 1000-fold bootstrapping.

2.4 Discussion

We have shown that an inhibitory alpha drive can help segment neural representations of a stimulus in a physiologically inspired neuronal network. The effect of alpha inhibition is two-fold: firstly, it temporally orders neuronal firing in every alpha cycle according to the neurons' level of excitation. Secondly, with increasing alpha inhibition strength it is possible to decrease the duty cycle by blocking the least excited neural representations. The activation of individual representations by the excitatory neurons is separated by bouts of GABAergic

inhibition thus producing the gamma rhythm. As a consequence, the population activity expresses itself as gamma activity phase-locked to the alpha oscillations.

2.4.1 A neuronal code organized by the phase of alpha oscillations

We have quantified the performance of the model by decoding the input strength from the firing phase of the neuron (see Figure 2-5). This produces a mechanism for prioritizing and segmenting competing visual information. In other words: early in every alpha cycle the neurons carrying the “most important” information (assumed here to be reflected by neuronal excitability) fire first, followed by slightly “less important” neurons and so on. The neurons associated with least excitability may never fire. We have previously characterized this as “to-do lists” [35]. The temporal segmentation serves to group neural firing of equal importance, or, depending on the feedback, similar features or objects. The segmentation allows down-stream regions to sequentially process individual visual features that may share the same information pathway. As such the proposed mechanism serves to alleviate the information-processing bottleneck in the visual hierarchy. It is important to note that when alpha inhibition is increased, the descending flank of the inhibition becomes steeper. This causes neurons that code for different visual features that receive similar excitation bias to fire in sequence more quickly than the PING mechanism can keep up with. This causes mixing of different visual features in the same gamma cycle (see Figure 2-3C for an example). While the neurons’ firing is still ordered in time based on excitability, this drastically decreases segmentation performance (see Figure 2-5B). This suggests that low to mid alpha levels benefit information processing, whereas high alpha signifies periods of poor information processing. The latter observation fitting with the observations of alpha oscillations in the context of functional inhibition (see section below).

The fact that neuronal firing is sorted temporally by excitability reflecting importance, combined with the fact that higher alpha power leads to shorter duty cycles is consistent with the hypothesized inhibitory role of the alpha activity. In other words: if alpha power in a brain area is high, the duty cycle is shortened and irrelevant information is suppressed. Therefore the decrease in duty cycle with an increase in alpha magnitude explains how the alpha rhythm both can serve to inhibit while at the same time coordinate neuronal firing (see also [35]). While there is some support for phase coding identified by intracranial recordings in animals [84], [120]–[122], further investigations are required to establish the prevalence of phase coding in the alpha band.

2.4.2 Phase coding in the gamma band

In our model, spike timing on a smaller timescale is also informative of the neuron's input level. The gamma phase in which a neuron fires also codes for input strength relative to the other neurons that are firing in the same gamma cycle. This results in a phase code in the gamma band, explaining why a phase code is still present in the case of high alpha inhibition strength even though the alpha cycles contains mostly just a single gamma volley (alpha inhibition strength >0.8 mS in Figure 2-4B and Figure 2-5A). This is in line with recordings in monkey visual cortex [42], [123]. Recordings in cat visual cortex have shown that temporal coding on a time-scale comparable to the period of gamma oscillations does not necessarily reflect stimulus strength [54], but instead may reflect local connectivity rather than purely a feed-forward drive. Gamma phase coding has also been reported in monkey prefrontal cortex coding for different items in short-term memory [124]. One could argue that the temporal ordering in the alpha band could act in conjunction with gamma phase coding. The phase of the alpha inhibition determines when the gamma phase code will be transmitted. Further empirical work is required to establish the functional relevance of the interplay of activity in these two frequency bands.

2.4.3 Rate versus phase coding

Hubel and Wiesel [125], [126] already showed that pyramidal cells in visual cortex can code information by sustained firing. The proposed "phase code" is different from the classical rate code. The phase code provides an order of activation of neurons coding for different visual features; however, each visual feature itself is encoded by a characteristic firing pattern. Therefore, it can co-exist alongside a classical distributed rate coding scheme. Nevertheless, one may view our proposed mechanism as incompatible with this: in our simulations the excitatory neurons lock to the alpha rhythm. This implies that individual neurons have a maximum firing or burst rate of 10 Hz. If we consider the phase code as a strict translation of input strength to firing phase this would be problematic. However, if we consider the alpha-gamma coupling as a way of prioritization, then a second – or third – spike is not a problem *per se*, in particular not if the discharge occurs in the form of bursts. In this sense phase coding and rate coding can co-exist as has been shown in rat hippocampus [89]. Secondly, it must be noted that the high firing rates, as reported in the classical experiments by Hubel and Wiesel, may occur less in natural situations. Work in the monkey visual cortex has shown that individual firing rates drop below 10 Hz when the visual stimulation consists of textures or natural images [96], [97]. This makes it easier to see how a rate and phase code could work together,

one for coding stimulus information, the other for prioritizing communication to downstream areas.

2.4.4 Wide-spread cortical synchrony in the alpha band

In our simulations the alpha oscillations synchronize the full network, since it was imposed by a global inhibitory signal. We have modeled this signal to mimic the global alpha signal thought to stem from the thalamus [23], [24], [117], [127], making it likely to represent a signal that is projected to a large part of the visual cortex. This “global” synchrony in the alpha band is consistent with experiments where a strong power peak in alpha band can be recorded over the occipital cortex in human EEG and MEG recordings [22], [25], [128]. This alpha band activity has been shown to have a functional role in attention and inhibition of processing [30], [77], [129] over large areas in the occipital cortex. This gives credence to the argument that the alpha inhibition is able to synchronize larger areas in order to arrange the temporal ordering by way of the alpha phase code.

2

2.4.5 Local cortical synchrony in the gamma band

The synchrony in the gamma band is weaker than in the alpha band. The gamma band activity as measured with EEG and MEG is typically quite weak, albeit the signal can be improved using spatial filtering techniques such as independent component analysis or explicit source modeling [130]–[132]. In our simulations gamma synchrony was also weak when no alpha was present (no strong gamma peak is visible in the power spectrum, see the top panel in Figure 2-6); however, in the context of our framework, the addition of the alpha modulation caused an increase in the gamma-band synchrony across the whole simulated network. This may suggest that gamma band activity should be synchronized to the same spatial extent as alpha oscillations. Nevertheless, gamma synchrony is thought to be more local than synchrony in the alpha band [14], [133], [134]. It is important to note that in our model simulations, the connection probability between excitatory and inhibitory cells is independent of distance (see Methods). This facilitates network-wide gamma synchrony. In reality, the spatial range of connections between excitatory and inhibitory determines the spatial scale over which synchrony is possible, since the PING mechanism depends on an excitatory-inhibitory loop [38], [39], [100]. With respect to the framework proposed here, this means that cortical areas that are not synchronous in the gamma band are spatially distant and not participating in the coding of items in the same “to-do list”. In other words, cortical

regions that project to different down-stream regions can fire at different gamma frequencies, since interference of information streams is not an issue.

2.4.6 Oscillatory input from the thalamus

A recent study in humans using MEG has shown that thalamic alpha oscillations modulate cortical gamma power [66]. However, experimental and modeling studies have pointed out that projections from lateral geniculate nucleus (LGN) to the cortex that carry oscillatory input can be both excitatory and inhibitory [127], [135]. This calls for an extension of our model in which the excitatory input is oscillatory itself, rather than constant as is the case in our simulations. Secondly, the thalamus would also ideally be suited to synchronize different neocortical regions in the alpha band, making communication through coherence possible [51]. When a downstream region is at an oscillatory inhibitory peak and the early visual region is not, this will hamper communication between the two regions. Recent work in monkey visual cortex points at the pulvinar nuclei as a possible region that coordinates the phase of alpha oscillation in neocortical regions [77].

2.4.7 The shape of the alpha oscillations

Crucial to our mechanism, the alpha inhibition provides a down-going ramp of inhibition in every cycle. This allows neurons to fire in sequence relative to their input strength. The precise frequency of this periodic inhibition is of lesser importance, as long as the period of slow inhibition is long enough to contain multiple cycles of the faster gamma rhythm.

The mechanism we propose can therefore also operate at lower frequencies. In fact, it has a lot in common with ideas on the role of that rat-hippocampal 6–10 Hz theta rhythm [136]–[138]. In non-human primates the hippocampal theta rhythm has been reported to be in the 8–11 Hz range [139]. There is a debate on which frequency range defines theta oscillations in humans, but the reported range covers from 3 to 8 Hz [140]–[142]. This opens the intriguing possibility that the same mechanistic goal can be achieved by both theta and alpha oscillations [69], although different time scales and neuronal mechanisms may be involved. An open question is then why oscillatory activity in the visual system is in the alpha band. From a teleological perspective, the frequency of the alpha oscillations in occipital cortex seems to put an upper bound on the sampling rate of visual perception [74], [143]. This would mean that an oscillation of a lower frequency would lead to lower perceptual sampling rates. This would be undesirable for visual perception. On the other hand, higher frequencies, like beta-band oscillations would not leave enough

room for multiple gamma cycles. In that sense, a frequency in the alpha band could be optimal for visual processing.

In our simulations we used a sinusoidal inhibitory drive. One could argue teleologically that a periodically linearly decreasing ramp or a “sawtooth” signal would be more convenient. Firstly, this would lead to a segmentation of the neurons organized more linearly with respect to the bias in their input; secondly it would make longer duty cycles possible while still being able to silence the network at every peak in the sawtooth. It has been demonstrated that the shape of the theta oscillations in the rat hippocampus are far from sinusoidal and approximate a sawtooth function [86], [144]. The exact shape of the inhibitory drive of the alpha oscillations in occipital cortex remains unexplored. An issue to keep in mind here, besides the direct translation of hippocampal theta activity to occipital alpha-band signals, is that despite alpha oscillations measured in the LFP or EEG appearing sinusoidal, it may very well be possible that the GABAergic *inhibitory drive* itself is sawtooth-shaped. We call for further empirical work investigating this.

2.4.8 Alpha activity as functional inhibition

Increase in alpha power as measured using extracranial techniques has been linked to functional inhibition in paradigms using visual attention [34], [145], [146]. In our model, the alpha drive has a similar role, beyond temporal ordering. When alpha inhibition strength increases, the duty cycle decreases, making it possible to ignore certain features of a stimulus, because they will no longer activate (Figure 2-4). Spatial patterns in alpha power have been shown to reflect the direction of covert attention [29], suggesting that local control of alpha inhibition strength is a possible mechanism for ignoring distracters. The model gives no indication as to how at a given retinotopic position, a high intensity distracter can be deprioritized in favor of a low intensity attended feature. This suggests that either a different mechanism implements this operation, or that our model network simulates activity on such a small spatial scale that selective visual attention coordinated by alpha activity can only be uniform across the network. In our proposed model there is a limit to what extent distracters, even when they have low input bias, can be ignored. When the alpha inhibition is very high there will always be at least one “gamma” burst firing at the trough of the inhibition. It would be easy to extend the model by adding a DC component to the inhibitory drive that increases together with the amplitude of the modulatory alpha drive [31]. The DC component would cause the firing rate of the population of excitatory cells to be more tightly (inversely) coupled to alpha power. In other words, this would mean that alpha magnitude would signal a general inhibition of local processing, even that of the locally strongest inputs, not just the

weaker inputs. Physiologically, this DC offset could be caused by more inhibitory neurons being recruited that are only weakly synchronized in the alpha band during periods of strong alpha inhibition. This would predict that the phase-amplitude coupling curve in Figure 2-7 would decrease at higher alpha inhibition strengths, since the number of neurons firing decreases. A similar effect can be seen when adding noise to the simulated LFP signal before calculating the PAC. When alpha inhibition is high, noise drowns out the low-amplitude gamma component (see the decrease of PAC in the gamma band for higher inhibition strengths in S3 Fig). Finally, in the simulations we biased the excitability of the different populations. This bias might be explained by differences in visual contrast or by top-down drives from spatial attention or figure ground segregation [35]. In future work it would be interesting to develop the implementation of these mechanisms.

2.4.9 Alpha oscillations and saccades

Recordings in monkey visual cortex have shown that after a saccadic eye movement, alpha oscillations are phase reset and increase in strength [41], [147], [148]. In the context of our proposed mechanism this would mean that the temporal ordering is most precise just after a saccadic eye movement, when alpha power is high and in the right phase. This is sensible, since this is exactly when the retina and thus visual cortex receive novel inputs that need to be prioritized. Importantly the alpha activity related to saccades also occurs when monkeys make saccades in the dark [149], suggesting that, like in our model, the alpha band activity could be the result of a modulatory signal, rather than the feedforward input from the retina via the LGN. More research is required to elucidate the role of saccades in relation to temporal coding and alpha oscillations.

2.4.10 Conclusion

We have constructed a physiological inspired model that can organize a temporal code according to the phase of alpha oscillations. The phase code serves to prioritize information by making the most excited neurons fire first in a temporal sequence and even blocking firing of the least excited neurons. The model produces gamma oscillations locked to alpha phase as measured experimentally. This mechanism could aid in interpreting complex visual scenes, by coordinating the information flow in the visual hierarchy by converting parallel input to a phase code.

Chapter 3.

A model mechanism for the generation of thalamic alpha oscillations

Adapted from:

B. Gips, O. Jensen, and J. P. J. M. van der Eerden, "A model mechanism for the generation of thalamic alpha oscillations," *In Preparation*

3

Abstract

We present a biologically plausible mechanism for the generation of alpha oscillations (7 - 13 Hz) in the visual thalamus. The computational network model relies on a mechanism of mutual inhibition via the reticulate nucleus between populations of thalamo-cortical relay cells and high-threshold bursting relay cells to generate a stable alpha rhythm. The rebound burst properties of the relay cells make it possible for three different dynamical modes to exist. In case of low feed-forward input, i.e. relating to the condition where eyes are closed, strong alpha oscillations emerge. A second mode, with medium feed-forward excitation from the retina, results in modest alpha oscillations that might serve to perform temporal framing of the visual input. A third mode of strong excitation makes the alpha rhythm disappear completely. Top-down inhibition coming from the cortex, possibly a result of visual attention, is able to move the generator back into a regime in which it produces alpha oscillations, even when feed-forward excitation is high. In this way our model of the thalamus can generate alpha activity both in agreement with the resting-state notion of alpha, as well as with active inhibition in attention tasks. Finally, we show that the network model can generate realistic stimulus evoked responses, suggesting that thalamic alpha and visual evoked responses are related and the generation of both can be performed by the same neural circuitry.

3.1 Introduction

Oscillations in the alpha band (7-13 Hz) were first recorded from the human scalp [22] and have later been recorded intracranially in both the thalamus and the cortex [23], [25], [26], [72], [75], [150], [151]. Initially the thalamus was thought of as the likely source for the alpha rhythm [150], whereas later recordings in both the thalamus and cortex of the dog demonstrated alpha sources in the cortex [23], [25], [26], [75], [151].

A simple model consisting recurrent excitation and inhibition between pyramidal cells and interneurons has been successful in modelling gamma band oscillations (>40 Hz) [38], [39], [100], [152]. The time scale of this mechanism is mainly caused by the dynamics of the excitatory and inhibitory synapses involved. A similar mechanism for the generation of slower alpha oscillations would then require slow synapses that dominate the neuronal firing dynamics, but this has so far not been found experimentally.

Recent results from recordings in the thalamus [117], [135], [153] as well simulation studies [127], [154] have shed light on a different neuronal mechanism responsible for the thalamic alpha generator. Most notably the discovery of a subset of thalamo-cortical relay (TCR) neurons that exhibit high-threshold bursting (HT) behavior in the alpha band has been important. Converging evidence from *in vivo* and *in vitro* recordings in the cat thalamus [135], [155] suggest that the TCR cells are inhibited rhythmically by local interneurons, and that the subpopulation of TCRs showing high-threshold (HT) bursts seems to be essential for this local rhythmic inhibition. These HT bursting neurons discharge coherently and phase-locked to the alpha rhythm in the LFP. As Lorincz and colleagues pointed out, this putative “temporal framing” of visual information that the thalamus passes on from the retina to the cortex, could serve as a mechanistic explanation to the suggestion that alpha oscillations supply a timing signal that organizes discrete periodic perception [35], [74], [143], [156]-[158].

A core question is how the HT bursting neurons are able to generate their alpha rhythm. The results from earlier *in vitro* work by Hughes and Crunelli [24], suggested that the HT bursting is a result of tonic depolarization. This depolarization possibly originates in the cortex. Vijayan and Kopell [127] have implemented these *in vivo* and *in vitro* findings in a model neural network. In their model the HT bursting thalamo-cortical cells (named HTC) are able to periodically generate bursts at a 10 Hz frequency, caused by a combination of a high-threshold calcium current

and a calcium-dependent after-hyperpolarization current. In essence this points to the HTC neurons being key to the thalamic “pacemaker” of the alpha rhythm. On the other hand, others have also suggested that the inhibitory neurons in the reticulate nucleus are crucial for the generation of thalamic oscillations in alpha band (7-13 Hz) [159]–[162].

In this work we further study plausible candidate circuits for the thalamic alpha generator (TAG). Our model neural network is based on the mechanism proposed by Lorincz et al. [135], and we followed the parameter choices of Vijayan and Kopell [127]. Neural input to the lateral geniculate nucleus (LGN) of the thalamus can modulate the alpha generation. In this study, top-down (e.g. indirectly from parietal regions or FEF [163]–[166] possibly via the RTN or neocortical layer 6 projections) and feed-back control from other brain areas (e.g. from visual cortex) is implicitly simulated by excitatory and inhibitory drives. We show that such signals make different modes of alpha dynamics possible. Thus our model generates alpha oscillations that may reflect either inhibition of visual input or temporal framing. This is in agreement with present theories of alpha band activity recorded over the occipital-parietal cortex in humans.

3.2 Methods

All the simulations were conducted using the Neurosim software package version 1.57 developed by Jan van der Eerden at the Donders Institute for Brain, Cognition and Behaviour. Neurosim is a software package written in FORTRAN95 that can be used to simulate neurons and biological neural networks. It solves coupled differential equations to simulate Hodgkin-Huxley type neuron models [10], or more detailed compartment models to simulate the dynamics of neurons and their interactions. Numerical simulations were computed using a variable step size Runge-Kutta method of order 8 according to the Dormand and Price algorithm [93], [167]. The relevant output variables were sampled at 10 kHz. All analyses of the simulation output were performed with Matlab (MathWorks, R2014a).

3.2.1 Neuron model

The model neurons used were single-compartment conductance based neuron models, similar to the model first proposed by Hodgkin and Huxley [10]. Four different types of neurons were used: fast-spiking interneurons (FS-I), thalamo-cortical relay neurons (TCR), high-threshold bursting relay neurons (HTC), and

inhibitory neurons found in the Reticulate nucleus of the thalamus (RTN-I). The model network is illustrated in Figure 3-1.

All neuron models feature dynamics generally following the equation for the membrane potential [168]:

$$C_m \frac{dV}{dt} = -g_{leak}(V - V_{leak}) - \sum_i I_i \quad (3.1)$$

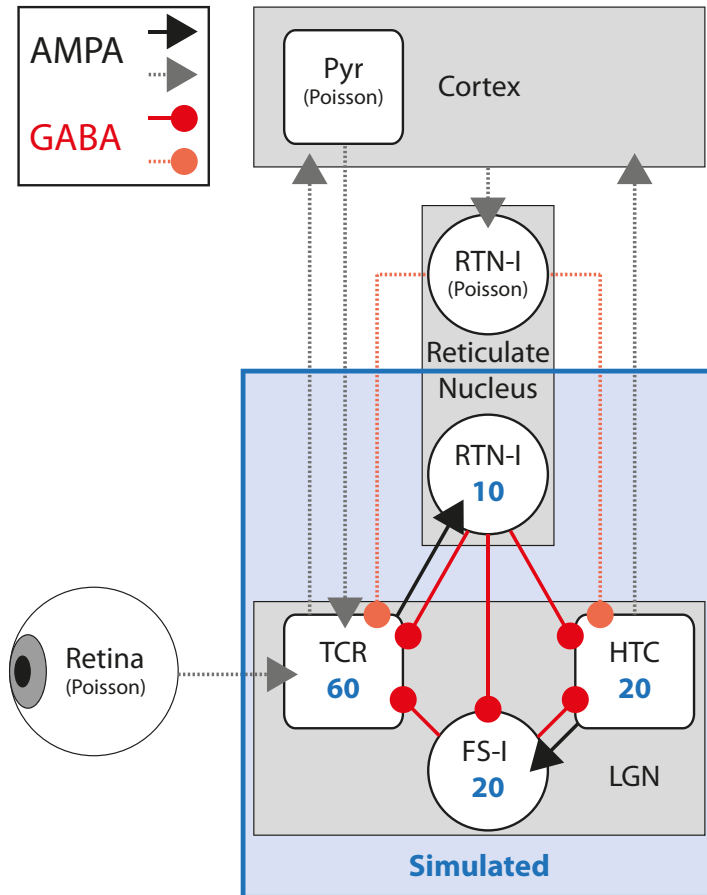
Where V is the membrane potential and C_m is the membrane's specific capacitance (equal to $1 \mu\text{F}/\text{cm}^2$). The currents I_i are voltage-dependent currents flowing through different ion channels i towards the extracellular space.

Further details on the dynamics of the different neuron types are given in Supplementary Materials.

3.2.2 Network

The model network for the thalamus is shown in Figure 3-1 and is in part based on experimental findings [24], [117], [135]. The model resembles the model proposed by Lorincz and colleagues and implemented by Vijayan and Kopell. It uses a FS-I pool (20 cells in total) as a way for the HTC and TCR cells to interact. The HTC neurons (20 cells) can produce an alpha rhythm that in turn can rhythmically inhibit the TCR neurons (60 cells) via the FS-I pool. Crucial to our model is the addition of a pool of inhibitory neurons that represents the perigeniculate nucleus (the visual part of the reticulate nucleus [135], RTN-I). The RTN-I neurons (10 in total) receive excitation from the TCR population. These inhibitory neurons project to all the cells in the LGN, most strongly to the HTC population. This causes the two excitatory populations to disynaptically inhibit each other, making for a possibly more robust oscillator. Note that the model by Vijayan and Kopell also included Reticulate Nucleus neurons, however their synaptic connections from the Reticulate nucleus to the HTC neurons were very weak (1-2 orders of magnitude weaker than other GABA-ergic synapses), and as such to our knowledge could not fulfill the feedback function present in our model (as may be gathered from the example simulations shown in Figure 1 in [127]).

The TCR neurons receive excitatory input that is thought to correspond to feed-forward signals from the retina and top-down input from cortex. They can also receive an inhibitory input arriving via the (not simulated) reticulate nucleus originating in the cortex or other areas of the thalamus [169]–[171] (see Figure 3-1). Further details on the connectivity within the network are given in Supplementary Materials.



3

Figure 3-1. Schematic representation of the model network. The blue shaded box designates the (thalamic) neurons that were explicitly simulated. The circles correspond to populations of inhibitory neurons, whereas the rounded squares correspond to populations of excitatory neurons. Red projections ending in circles correspond to inhibitory connections, black arrows correspond to excitatory connections. Dashed connections indicate implicit input from the cortex, retina and reticulate nucleus (other than the simulated RTN-I neurons). The neurons in these regions were not explicitly modelled. Instead, inputs from these regions were approximated by generating spike trains with Poisson-distributed inter-spike-intervals. Connections within populations are not shown. The number below the cell type indicates the amount of simulated neurons.

3.2.3 External drive

As visible in Figure 3-1, the thalamic network could receive excitatory input from the retina or the cortex, and an inhibitory drive from the reticulate nucleus. This

input was modelled by supplying the TCR neurons with uncorrelated input generated by 50 “Poisson neurons” (i.e. spike trains with Poisson-distributed inter-spike-intervals [11]). This external drive mimicked a pool of 50 neurons sending action potentials to the receiving neuron. The output from the 50 Poisson neurons was binarized (1 for an action potential, 0 otherwise) and subsequently convolved with the double exponential waveform simulating an excitatory or inhibitory post-synaptic currents (EPSC and IPSC respectively) in equation 3.2.

$$k_x(t) = \exp\left(-\frac{t}{\tau_2}\right) - \exp\left(-\frac{t}{\tau_1}\right), \text{ if } t > 0 \quad (3.2)$$

$$k_x(t) = 0, \text{ if } t \leq 0$$

Where $k_x(t)$ is the EPSC or IPSC kernel. For inhibitory drive, the values for τ_1 and τ_2 where equal to 2 ms and 8 ms respectively. For EPSCs these time constants where 0.5 ms and 2 ms.

The convolved spike trains where then used as a time-varying conductance term for imposed AMPA and GABA currents:

$$I_{AMPA_{imp}} = g_{AMPA_{imp}} \cdot r_{EPSC}(t) \cdot (V - V_{AMPA}) \quad (3.3)$$

$$I_{GABA_{imp}} = g_{GABA_{imp}} \cdot r_{IPSC}(t) \cdot (V - V_{GABA}) \quad (3.4)$$

Where $g_{AMPA_{imp}}(t)$ and $g_{GABA_{imp}}(t)$ correspond to synaptic strength. The generated spike trains convolved with the EPSC and IPSC kernels are denoted by $r_{EPSC}(t)$ and $r_{IPSC}(t)$ respectively. V_{AMPA} and V_{GABA} are the synaptic reversal potentials given in Table 3-2 in Supplementary Materials.

3.2.3.1 *Evoked response*

To generate the evoked response in Figure 3-6 we simulated retinal input by stimulating the network using a time-varying rate of the 50 Poisson neurons. The variation was chosen such that it represented repeated presentations of a flash stimulus. The Poisson neurons fired at a base rate of 25 spikes per second that was modulated by a time-varying function $\zeta(t)$ (see Figure 3-2). This function was generated by convolving a string of delta functions separated by inter-stimulus interval $T=600 \pm 50$ ms with a stimulus modulation kernel:

$$\zeta(t) = \text{III}_T(t) * K(t) \quad (3.5)$$

Here III_T is a Dirac comb with (variable) period T :

$$\text{III}_T(t) = \sum_{k=-\infty}^{\infty} \delta(t - kT + \eta_k) \quad (3.6)$$

The function $\delta(x)$ is the Dirac delta function (i.e. $\delta(x) = 0$ if $x \neq 0$, and $\int_{-\infty}^{\infty} \delta(x) dx = 1$), and k takes all integer values. The term η_k is sampled from a normal distribution with mean 0 ms and standard deviation of 50 ms. This makes the inter-stimulus intervals variable.

$K(t)$ is the stimulus modulation kernel:

$$K(t) = \begin{cases} 1 + \frac{M_P}{Z_P} \left(\exp\left(-\frac{t}{\tau_{1,P}}\right) - \exp\left(-\frac{t}{\tau_{2,P}}\right) \right) & \text{if } t \geq 0 \\ 1 - \frac{M_N}{Z_N} \left(\exp\left(\frac{t}{\tau_{1,N}}\right) - \exp\left(\frac{t}{\tau_{2,N}}\right) \right) & \text{if } t < 0 \end{cases} \quad (3.7)$$

The decay constants $\tau_{1,P}$ and $\tau_{2,P}$ control the length of the transient increase in firing rate just after a flash. The time constants $\tau_{1,N}$ and $\tau_{2,N}$ control the length of a short decrease in input before the start of the next stimulus (with $\tau_{1,x} > \tau_{2,x}$). The factors M_P and M_N control the magnitude of these increases and decreases in firing rate respectively. The factors Z_x with $x=P,N$ are normalization factors:

$$Z_x = \left(\frac{\tau_{2,x}}{\tau_{1,x}} \right)^{\frac{\tau_{1,x}}{\tau_{2,x} - \tau_{1,x}}} - \left(\frac{\tau_{2,x}}{\tau_{1,x}} \right)^{\frac{\tau_{2,x}}{\tau_{2,x} - \tau_{1,x}}} \quad (3.8)$$

The parameters for the stimulus modulation used in the simulations are given in Table 3-1, leading to a rate modulation ($\zeta(t)$) shown in Figure 3-2.

Table 3-1. Parameter values for stimulus modulation kernel (see equation 3.7).

$\tau_{1,P}$	$\tau_{2,P}$	$\tau_{1,N}$	$\tau_{2,N}$	M_P	M_N
100 ms	40 ms	15 ms	10 ms	0.5	0.2

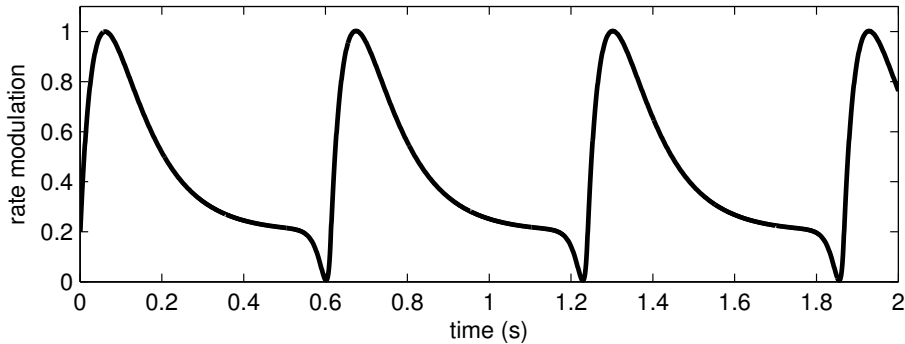


Figure 3-2. Illustration of the rate modulation function ($\zeta(t)$ in eq. 3.5). The rate modulation function is the result of convolving a series of delta functions with the stimulus modulation kernel (eq. 3.7). This rate modulation was multiplied by a base rate of 25 spikes per second to provide a time-varying rate for the 50 excitatory Poisson neurons that represent retinal input to the TCR cells. This input was used when investigating the evoked response in Figure 3-6.

3.2.3.2 *Noise input for estimation of the impulse response function*

If we approximate the TAG to be a linear time-invariant system, we can characterize its response to arbitrary stimulus input by determining its impulse response (see below). This technique was used earlier to estimate evoked responses from EEG recordings [172], [173]. To estimate the impulse response in Figure 3-7 we used a stimulus that caused a change in firing rate of the 50 Poisson neurons every 20 ms. This emulated a stimulus of which the luminance changed at a framerate of 50 Hz, similar to the stimuli used experimentally to estimate the impulse response from EEG data [172], [173]. The firing rate of the Poisson neurons in each of the 20 ms time intervals was sampled from a normal distribution with mean of 15 spikes/s and a standard deviation of 2.5 spikes/s (half-wave rectified at 0 spikes/s, i.e. no negative firing rates were possible).

3.2.4 *Analysis*

The output of the simulations (spike trains and simulated LFP signal) were analyzed using custom scripts written in MATLAB (MathWorks Inc., Natick, MA, USA).

3.2.4.1 *Estimation of power spectra*

The power spectral density (PSD) of the simulated firing rate of the TCR was estimated using Welch's method with windows of 500 ms, using 50% overlap [174]. A Hamming taper was applied to each time window.

3.2.4.2 *Time-frequency representations*

To investigate the time-varying spectral content of the evoked and impulse responses we calculated time-frequency representations (TFRs). Short-time Fourier transforms were obtained using a 400 ms sliding Hann window. Zero-padding was used to interpolate the frequency spectra to achieve the frequency resolution presented in the figures.

3.2.4.2.1 *Inter-trial coherence*

From the TFR we estimated the inter-trial coherence (ITC) in Figure 3-6F to illustrate the stability of the alpha rhythm after stimulus-induced reset across N trials (stimulus presentations). The ITC at time point t and frequency f is given by:

$$\text{ITC}(t, f) = \frac{|\sum_{j=1}^N F_j(t, f)|}{\sqrt{N \sum_{j=1}^N |F_j(t, f)|^2}} \quad (3.9)$$

Where $F_j(t, f)$ is the complex Fourier coefficient of the TFR of trial j at time point t and at frequency f .

3.2.4.3 *Estimation of the impulse response*

The estimation of the impulse response (IRF) was inspired by earlier experimental work [172], [173]. It was determined by calculating the cross-correlation of the response (firing rate) of the neurons with the 50 Hz Gaussian noise firing rate input signal and dividing this by the autocorrelation of the input signal [175]:

$$IRF = \frac{R \star S}{S \star S} \quad (3.10)$$

Where R is the demeaned spike rate of the neural subpopulation in the thalamus, and S is the input signal (i.e. the time-varying firing rate of the Poisson neurons). The operator \star denotes the cross-correlation operation.

3.3 *Results*

We constructed a model for the thalamic alpha generator (TAG, see Figure 3-1). To investigate the dynamics of the model TAG, we supplied the TCR neurons with different levels of uncorrelated inhibitory and excitatory input drive (see Methods) for a total simulation length of 2 seconds. Figure 3-3 shows example simulations of the model TAG.

Figure 3-3A shows that the TAG model is able to generate a strong alpha rhythm. Figure 3-3A shows that the TAG model was able to generate these alpha oscillations even when the TCR cells received only inhibitory drive (possibly caused by attention-related modulation of firing in the reticulate nucleus [176]). The inhibitory drive promotes the rebound-burst properties of the relay cells of the thalamus [168], [177]–[180]. The hyperpolarization caused by both the imposed IPSCs and the discharging of the FS-I and RTN-I populations caused the two populations of relay cells (TCR and HTC) to exhibit regular bursting. The mechanism is as follows: the HTC pool fires a burst of action potentials, which excites the FS-I pool. The FS-I spikes cause hyperpolarization of the TCR neurons, this causes the TCR neurons to fire a rebound burst ~60 ms later. The TCR neurons in turn excite the RTN-I neurons which prohibit the HTC neurons from bursting for about a period of an alpha cycle. As such it is the RTN-I loop together with the dynamics of the HTC pool that determines the frequency of the alpha oscillations.

When the TCR were driven by an excitatory signal reflecting a visual input (Figure 3-3B), their firing rate was increased, but they were still periodically silenced by the firing of the HTC cells, albeit in a less synchronized fashion. In this case, the periodic silencing of the TCR neurons can be seen as “temporal framing” as noted by Lorincz et al. [135], i.e. the neuronal implementation of perceptual cycles observed experimentally [157].

Finally when excitatory drive to the TCR neurons was increased even further (Figure 3-3C), the TCR neurons fully inhibited the firing of the HTC neurons via the RTN-I population. This completely abolished the alpha rhythmicity. The fact that the RTN-I neurons also project back to the TCR neurons caused a gamma rhythm to emerge [38], [39], but note that simultaneous recordings in monkey LGN and V1 have indicated that the gamma rhythm is mainly a cortical (not a thalamic) phenomenon [181].

In summary, the TAG is able to produce a stable alpha rhythm in which the HTC and TCR neurons mutually inhibit each other via the RTN and local interneurons.

Secondly this alpha rhythm can be abolished when excitatory drive to the TCR neurons is very high.

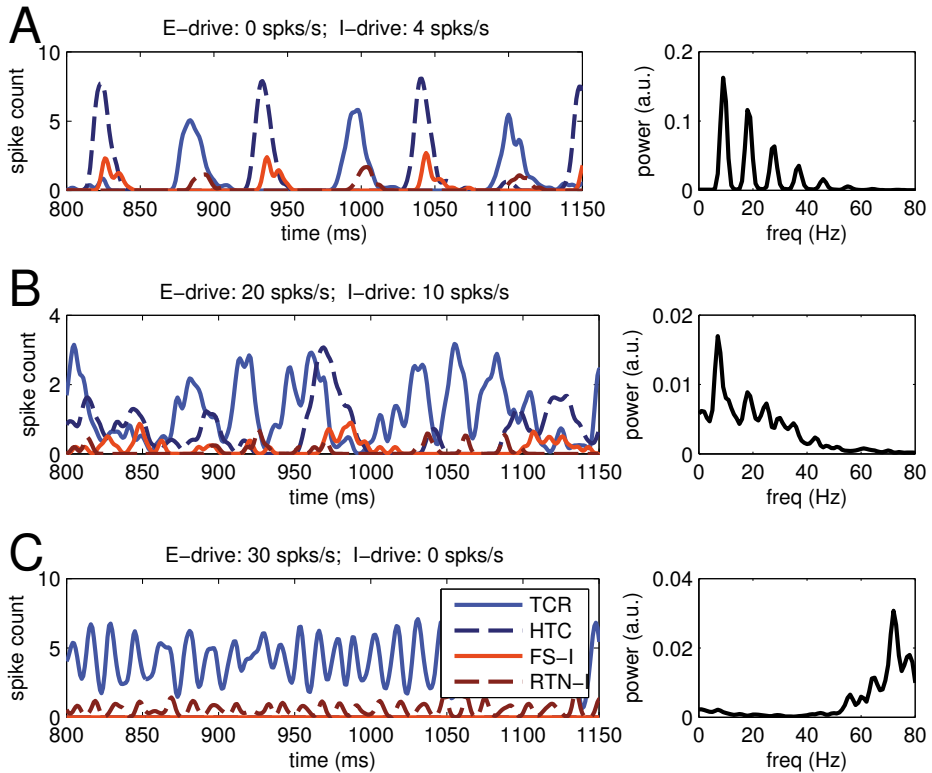


Figure 3-3. Examples of spiking behavior of the TAG, showing the three different dynamical models of the alpha generator model. **Left:** The spikes were binned with a 1 ms resolution and summed across all neurons within the population. The resulting spike rates were then smoothed by convolving with a Gaussian kernel with standard deviation of 2 ms. **Right:** The power spectrum of the simulated TCR activity (using Welch's method [174]; 500 ms windows with a hamming taper and 50 % overlap, see Methods). **(A)** Each TCR and HTC neuron is driven solely by randomly timed IPSCs coming from a pool of 50 Poisson neurons (see Methods) with a firing rate of 4 spikes per second. **(B)** Besides an inhibitory drive to both the HTC and TCR neurons of 10 spikes per second, the TCR neurons are now also driven by EPSCs (e.g. a visual input) coming from a pool of 50 Poisson neurons with a firing rate 20 spikes per second. **(C)** The TCR neurons are only driven by EPSCs coming from a pool of 50 neurons with a firing rate 30 spikes per second, whereas both pools of relay cells receive no IPSCs. This abolishes the alpha rhythm.

Figure 3-3 shows different behaviors of the TAG: the alpha rhythm can emerge from increasing the level of inhibition, from increasing the excitatory input, or can even be completely absent when excitatory input is high. To investigate this further, the behavior of the TAG model was systematically subjected to variable levels of excitation and inhibition. The results are shown in Figure 3-4. The firing rate plots (Figure 3-4A and D) show the two possible firing modes of the relay cells. When excitatory input was low (<5 spikes per second), the TCR and HTC neurons exhibited rebound bursts after every inhibitory volley from the FS-I, and RTN-I pool respectively (also see Figure 3-3A). When excitatory input is increased and the inhibitory drive is low, the TCR neurons would fire in their tonic relay firing mode [178], [182]. These dynamics make three distinct “alpha regimes” possible (Figure 3-4B,E): when input excitation is low or absent (<5 spikes per second), the network synchronizes to produce a strong ~9 Hz alpha rhythm (Figure 3-3A, “eyes closed” in Figure 3-5). When excitation is increased, the inhibitory volleys from the FS-I population are cancelled, and rebound bursts in the TCR neurons are abolished. When excitation is increased further the TCR neurons fire in relay mode [178], [182] and a new alpha rhythm (~7 Hz) emerges from the periodic silencing, rather than periodic burst firing of the TCR cells (Figure 3-3B, “eyes open” in Figure 3-5). When excitation to the TCR cells is pushed even further, the inhibitory feedback to the HTC neurons becomes strong enough to silence them, abolishing the alpha rhythm (Figure 3-3C, “No Alpha” in Figure 3-5). Figure 3-4C and F show the frequency of the generated rhythm. Note that when the firing rate of the TCR neurons is low, the alpha rhythm is not very stable (since it relies on the TCR population firing to inhibit the HTC neurons). This can cause ~20 Hz component of the signal to be stronger in power than the regular ~10 Hz alpha rhythm, as is visible in the yellow area in panel C and the corresponding area in panel F. In summary, three different dynamical mode can be observed (Figure 3-5): one characterized by the TCR neurons exhibiting rebound bursts caused by a lack of excitation, the second by relay-mode firing of the TCR cells when excitation is increased. The third mode is characterized by very strong excitation to the TCR cells, leading to complete abolishment of the alpha rhythm.

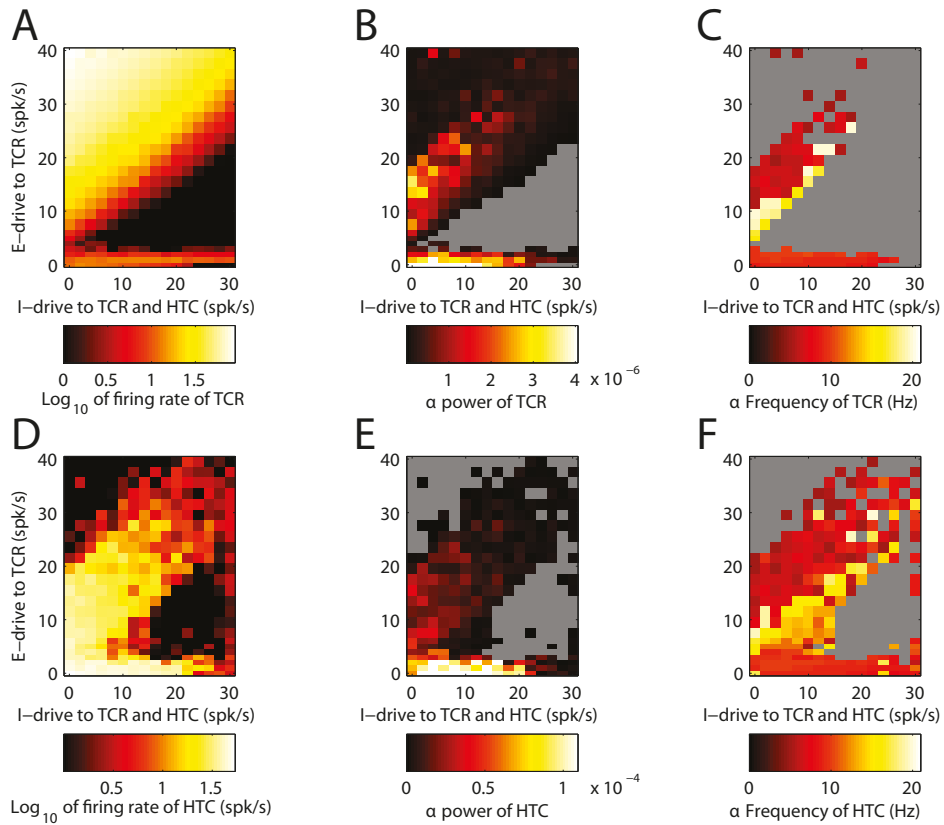


Figure 3-4. Characterization of the behavior of the model TAG, under different excitatory and inhibitory drives. The HTC neurons always receive excitatory input of 8 spikes per second to guarantee they are not silent due to a lack of drive. Grey areas were masked, since the average firing rate of the corresponding neurons (A and D) dropped below 2 spikes per second, or the alpha power (B and E) was below 1×10^{-6} . In both cases, the simulations were considered to not produce a reliable alpha rhythm. **A** The firing rate of the TCR neurons. **B** The height of the peak in the power spectral density between 5 and 20 Hz of the firing rate signal from the TCR neurons. **C** The frequency at which the peak in the power spectral density (in B) is located. **D-F** Same as A-C, but for the HTC neurons instead of the TCR neurons.

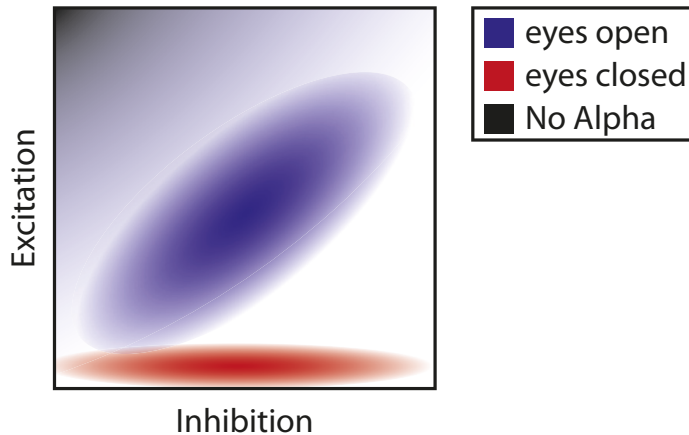


Figure 3-5. Schematic illustration indicating the Three dynamical modes visible in Figure 3-3 and Figure 3-4. When excitation is low (due to lack of retinal input), as would be the case when eyes are closed) the TCR and HTC neurons both discharge synchronized rebound bursts (red area). When excitation increases (corresponding to receiving visual input) TCR neurons operate in relay mode, but are periodically silenced by the alpha rhythm ('temporal framing'; blue area). When excitation is increased further, the alpha rhythm is abolished (black area).

Evoked responses recorded in sensory areas of the brain caused by a stimulus have power in the theta-alpha band (e.g. see [183], [184]). Since the relay cells are involved in generating the alpha rhythm, the alpha dynamics should also be reflected in evoked responses. To illustrate this, Figure 3-6A shows the average firing probabilities (akin to an ERP) aligned to the onset of 26 visual stimulus-like inputs coming from 50 Poisson neurons whose rate is modulated by the kernel shown in Figure 3-2 (see Methods). Inhibitory feedback was absent (corresponding to the dynamics operating along the left edge of the maps in Figure 3-4 and Figure 3-5). This input results in a reset of the alpha generator at $t=0$ s, indicated by the damped oscillation of around 2-3 cycles with significant phase locking across stimulus presentations 150-400 ms after stimulus onset for both the TCR and HTC neurons (Figure 3-6B). The inter-stimulus interval is 600 ± 50 ms as can be seen by the increase in firing rate of the TCR neurons that starts around $t = 0.6$ s. Note that the HTC neurons show strong firing around $t = 0$ ms. This is caused by the pre-stimulus decrease in input to the TCR cells, which interrupts the RTN-I mediated inhibition of the HTC cells, causing them to exhibit rebound bursting.

Figure 3-6C shows the average spiking probability aligned to the pre-stimulus alpha phase, rather than stimulus onset. This was done to investigate whether the phase of the alpha rhythm before stimulus onset has influence on the phase after stimulus

onset. The left panel of Figure 3-6B shows no alpha waveform after $t=0$, suggesting that the pre-stimulus phase has no systematic influence on the phase after stimulus onset, i.e. the stimulus completely resets the alpha generator. This is illustrated more quantitatively by the lack of significant phase consistency in the 150-400 ms time window across stimulus presentations in this case (Figure 3-6D).

Figure 3-6E and F show time-frequency representations of the evoked response. The activity of the HTC cells was used, as was done in [127], since the activity of these cells show the alpha component more strongly. Figure 3-6E Shows the time-resolved power locked to stimulus onset. As is also visible in Figure 3-6A, the first cycle after stimulus onset ($t = 0$ s) is longer than the average alpha cycle reflected in a dip in the alpha frequency. This single cycle of lower frequency is locked across stimulus presentations as is visible in inter-trial coherence (ITC) in Figure 3-6F. As can be seen in Figure 3-6A, this first pulse of activity ($t > 150$ ms) is followed by a return of the alpha rhythm. Finally, it loses some of its power (Figure 3-6E) and coherence across stimulus presentations (Figure 3-6F).

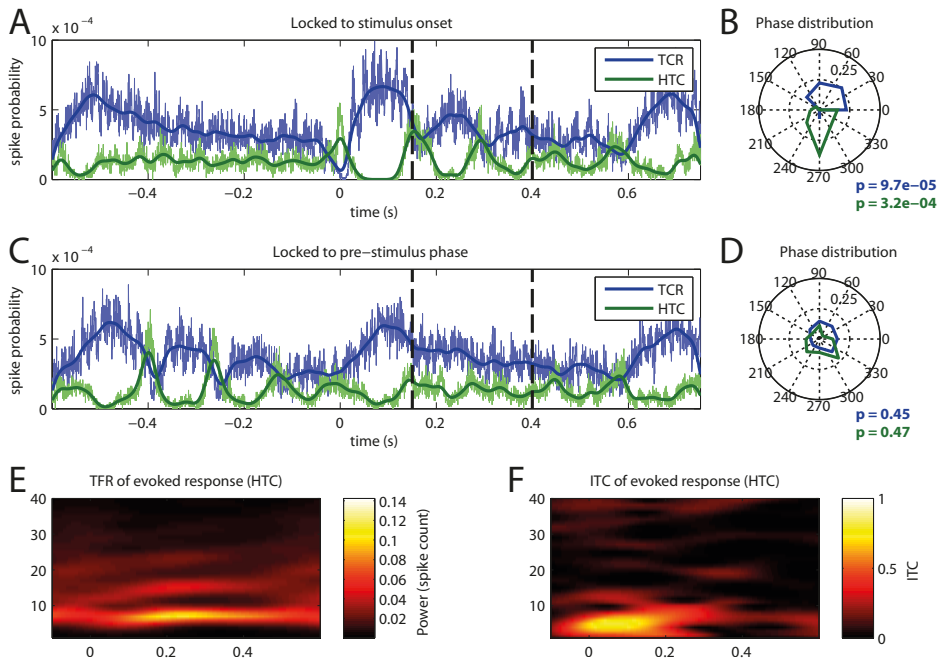


Figure 3-6. (A) response evoked by excitatory input resembling a visual stimulation. During a 16 second simulation, 26 stimuli were presented (aligned to $t = 0$ s) with an inter-stimulus interval of 600 ± 50 ms (mean \pm standard deviation). The “evoked response” shows a damped alpha oscillation ($\sim 6-8$ Hz, like the one visible in Figure 3-3B) of around 2-3 cycles. Thick darker curves show a smoothed version of the evoked response (using a Gaussian filter kernel with standard deviation of 10 ms). (B) distribution of the alpha phase for the TCR (blue) and

HTC (green) neurons between 150 ms and 400 ms after stimulus onset (see dashed vertical lines in A). Both TCR and HTC neurons show significant phase locking ($p < 0.001$, one-sample Kolmogorov–Smirnov test, uniform reference distribution) (C) Firing responses of the TCR and HTC neurons as in A, but now aligned to the pre-stimulus alpha phase. The alpha phase was estimated based on the firing rate signal of the HTC neurons between $t = -0.4$ s and $t = 0$ s. The alpha frequency was determined as the strongest component in the power spectrum between 5 and 15 Hz in this 400 ms time window. Note that the time axis is no longer relative to the stimulus onset, but rather to the alpha phase of the HTC neurons pre-stimulus. (D) distribution of the alpha phase for the TCR (blue) and HTC (green) neurons in the window from 150 ms to 400 ms after phase alignment (see dashed vertical lines in C). Neither TCR nor HTC neurons show significant phase locking ($p > 0.05$, one-sample Kolmogorov–Smirnov test, uniform reference distribution). (E) Stimulus-locked TFR of the power of the firing of the HTC neurons. (F) TFR of the Inter-trial coherence across the 26 stimuli for the firing of the HTC neurons. Note that the initial activity after stimulus onset (0 – 175 ms in panel A) is most conserved across trials and has power in the theta band (~ 5 Hz). After this, the alpha rhythm is re-established (~ 8 Hz, see also panel E), but this is less coherent across trials.

A different approach to characterizing the system is by estimating its impulse response. The system's impulse response can be estimated when subjecting it to time varying random input. This has been done before in human EEG recordings using stimuli of which the luminance changes randomly over time. Some have shown the impulse response estimated in this way to resemble an evoked response [173], while others have shown that the impulse response resembles a more sustained response reflecting the alpha rhythm [172]. We investigated our model TAG by submitting it to excitatory input to the TCR that randomly changes its strength every 20 ms (for a “frame rate” of 50 Hz), sampled from a normal distribution with mean 15 and standard deviation of 5 spikes per second (see Methods). The impulse response was then estimated by calculating the cross-correlation between the firing rates in our TAG model and the randomly varying excitatory input and dividing it by the auto-correlation of the input [175]. The results are shown in Figure 3-7. Figure 3-7A shows the estimated impulse response functions of the different neuron populations. Similar to the evoked response in Figure 3-6A, the TAG model shows a damped alpha oscillation as its impulse response function for around 2 cycles. A separate simulation where we decreased the factor of noise caused by the Poisson neurons by a factor of 10 lead to a virtually identical impulse response function (not shown). This suggests that our linear approximation is appropriate, and that the instability of the alpha oscillation in the impulse response is not the result of a non-linear interaction with noise in the input. Figure 3-7B shows the power spectra of the impulse response functions. Figure 3-7C shows the power spectrum of the firing rates of the four neuronal populations over

the full 16-second simulation. Note that both the HTC and TCR neurons show a peak in the alpha band (7-8 Hz). This indicates that even with this noisy input, alpha-band oscillations can be generated. Finally Figure 3-7D shows the TFR of the impulse responses of the HTC neurons shown in panel A.

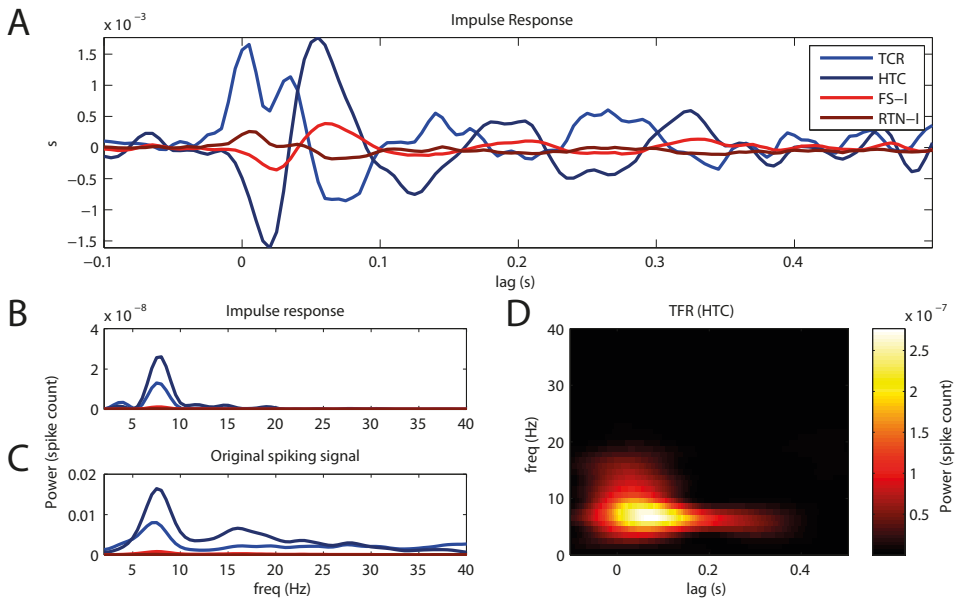


Figure 3-7. (A) Impulse response estimate of the TAG, estimated by using Gaussian noise-like input to the TCR pool. (B) Power spectra of the impulse response functions shown in panel A. (C) Power spectra of the simulation output from which the impulse response functions in panel A were extracted. Colors as in A. (D) Combined TFR of the HTC and the TCR neurons.

3.4 Discussion

3.4.1 Three dynamical modes

We have investigated a biologically plausible model network of the thalamic alpha generator. This network model was able to generate an alpha rhythm in the thalamic relay cells in three distinct regimes: strong alpha oscillations associated with the absence of input, phasic modulation of visual input, and abolished oscillations. In the two first cases the high-threshold bursting neurons (HTC) are responsible for the alpha rhythmicity in the relay cell firing by indirectly inhibiting them via the local interneurons. The difference lies in whether this indirect inhibition cause or

suppress the firing of the relay cells. Furthermore, feedback from the TCR neurons to the HTC neurons via the inhibitory RTN cells serves to strengthen the alpha rhythm.

In the regime where the relay cells received little excitatory input – as could be the case when the eyes are closed (red area in Figure 3-5) – the rhythmic inhibition could depolarize the relay cells enough to cause rebound bursting [168], [177]–[180], [185]. This caused all TCR neurons to activate in high synchrony, causing strong rhythmicity and thus high power in the alpha band. In the second regime (blue area in Figure 3-5), the network activity closely resembled the alpha rhythm described by Lorincz and colleagues [135]. The TCR neurons received enough excitation to fire continuously, but were silenced periodically by the bouts of inhibition from the local interneurons. As a result, the TCR neurons did fire at a specific phase of alpha, but instead fired throughout the alpha cycle and synchronously decreased their firing at a specific alpha phase, as measured in vivo and in vitro [135]. In the third mode, TCR neurons spike sufficiently to be able to completely suppress the HTC neurons via the RTN-mediated inhibition and alpha disappears (black area in Figure 3-5). These three regimes observed in our model simulations could be considered as a possible way of explaining the observation of strong alpha components when the eyes are closed, whilst still leaving room for functional segmentation or rhythmic modulation when visual information is processed [135], [157], [186].

3.4.2 The reticulate nucleus stabilizes the thalamic alpha rhythm

We implemented a model TAG in which TCR neurons provide negative feedback to the HTC neurons via the RTN-I neurons. Mutual inhibition between the HTC and TCR neurons stabilized the alpha rhythm by having the two subpopulations firing in anti-phase. Without the negative feedback via the RTN-I population to the HTC neurons the rhythm generation was less stable. We have performed simulations without the RTN-I (not shown) and the alpha rhythm was only stable when the HTC neurons receive a weak zero-mean input (as was done in [127]). The alpha rhythm in this network configuration could be stabilized by increasing the time constant for calcium buffering (see Supplementary Materials), e.g. to 80 ms. This would lengthen the inter-burst-interval of the HTC neurons, bringing the rhythm frequency back to the alpha frequency range. Such a time constant is significantly larger than the values between 1 ms and 5 ms used in the literature [127], [168], [187], [188]. This makes the “open” configuration without the RTN feedback less plausible.

Experimental work has pointed to the RTN as a contributor to the thalamic alpha-theta rhythms [159]–[162]. This gives credence to our model where the reticulate nucleus is able to stabilize the rhythm via inhibitory connections to the HTC populations.

3.4.3 Spike-field phase-locking

In experimental settings, alpha oscillations in the thalamus are generally investigated by recording the local field potential (e.g. [117]). Here we have instead analyzed the spike rates in the model neural network and have shown that they show rhythmicity in the alpha band. The TCR and HTC neurons fire in antiphase, this could possibly lead to the TCR and HTC rhythms cancelling each other in the LFP. However, Lorincz and colleagues showed the anti-phase spiking behavior of the TCR and HTC neuron types in the presence of a strong alpha rhythm in the LFP [135]. This indicates that the two populations do interfere destructively. One population seems to overpower the other with respect to their contribution to alpha-band power in the LFP.

Besides this, Lorincz et al. also show that TCR neurons could lock to either the peak or the trough of the ongoing alpha rhythm in the LFP. Similarly, the *in vitro* and *in vivo* recordings by Lorincz et al. show that a minority of the spikes generated by the HTC neurons occur in anti-phase to the main rhythm (e.g. see Figure 1C in [135]). This could mean that the thalamic neurons may split up into two sub groups (each containing both TCR and HTC neurons), oscillating in anti-phase. The larger of these sub groups is responsible for the alpha component in the LFP. This was also observed in some of our simulations, as can already be seen in Figure 3-3B by a subset of the HTC neurons firing in antiphase to the other HTC cells (around $t = 900$ and $t = 1040$ ms). We expect this effect to be more pronounced in simulations of larger populations, but we did not investigate this in further detail.

3.4.4 Control of alpha oscillations

To investigate how the alpha rhythm can be controlled or modulated, consider Figure 3-4 and Figure 3-5. These figures show that alpha can be strengthened or weakened by changing the balance of excitatory and inhibitory drive to the TCR cells. This means that alpha power can be changed by feed forward signals (e.g. stimulus contrast or luminance) stemming from a retinal excitatory drive. Thalamic alpha might also be controlled by top-down (e.g. due to allocation of spatial attention by FEF or parietal regions [163]–[166]) or feedback signals from the neocortex. This

drive from the cortex can either consist of direct excitation coming from layer 6 neurons, or of indirect inhibition via the reticulate nucleus [169]–[171], [189]–[191]. Note that in our current work we have not investigated the mechanisms through which the cortex is able to provide these different kinds of feedback. This important issue should be a topic of future research.

Figure 3-4B shows that alpha power in the TCR population can be changed as a function of excitatory drive. When excitation to the TCR population changes, because of change in stimulus salience, alpha power will decrease or even disappear. Cortical feedback could enhance this effect by adding some excitation on top of the retinal signal. Alternatively, it can give a net inhibitory signal, moving the dynamics to the right in the panels of Figure 3-4 and Figure 3-5. In that case alpha power would increase, despite the presence of a strong stimulus. Crandall et al. [169] have suggested that synaptic dynamics in cortical-thalamic projections may regulate whether feedback from layer 6 is dominantly excitatory or inhibitory (via the RTN).

3.4.5 Thalamo-cortical loop

While the alpha rhythm is present in thalamus, it also has neocortical sources [23], [25], [26], [150], [192] (but see [24], [72], cortical sources may still be entrained by the thalamus). In our model, the thalamic network consisting of the LGN and the reticulate nucleus is sufficient to generate the alpha rhythm. However, layer 6 of early sensory cortex has a direct feedback to the thalamus, both to the relay cells and to the reticulate nucleus [169]–[171], [189]–[191], [193], [194]. This leaves room for the neocortex to modulate the feedback to the HTC neurons via the reticulate nucleus as mentioned above, or the cortex can even be part of the feedback loop itself, i.e. the feedback could partially go from the TCR cells through layer 6 before reaching the inhibitory cells in the reticulate nucleus. In this way the generation of the alpha rhythm might depend on bidirectional thalamo-cortical interactions [181].

3.4.6 Alpha and evoked responses

Alpha oscillations have often been discussed in relation to stimulus-locked cortical evoked responses. Sometimes evoked potentials seem to be the result of the superposition of oscillations across trials that are (partially) phase-reset by the stimulus [183], [195], [196]. In other cases, alpha oscillations and evoked responses seem to be independent [197]. The evoked response in Figure 3-6A applies to the former case. The transient increase of excitation to the TCR neurons can “reset” the alpha oscillation in the sense that most of the TCR neurons tend to fire in synchrony

directly after stimulus onset, independent of the phase of the ongoing alpha (Figure 3-6C). In the current work we have not investigated the effect of the strength of the stimulus pulse (Figure 3-2). Differences in stimulus strength may account for different degrees of phase resetting.

We estimated the impulse response function in Figure 3-7 to consider the “evoked response” in a more systematic way. I.e. one which is less dependent on the precise parametrization of the simulated retinal input to the LGN related to the stimulus. The impulse response is similar to the evoked response in Figure 3-6A: it also dies out after two alpha cycles. This analysis was based on work by VanRullen and Macdonald [172], who in turn were inspired by work by Lalor et al. [173]. Lalor and colleagues introduced the method to standardize the visual evoked response. VanRullen and Macdonald used it with an attention task to extract an “echo”, resembling an alpha oscillation (lasting up to 1 second).

Assuming oscillations in thalamus and striate cortex are highly related (as discussed above), we can compare our model to the experimental cortical EEG results from [172], [173]. Our model was able to reproduce results similar to those from Lalor and colleagues, but not the extended “echo” reported by VanRullen and Macdonald and reproduced by J.D. Herring et al. (private communication). We speculate that attentional modulation and (rhythmic) feed-back from the cortex could stabilize the alpha component in the impulse response.

We have demonstrated that a model of thalamic alpha generator can reproduce results from human and animal electrophysiological experiments. It can generate responses similar to those evoked by visual stimuli, as well as a stable alpha rhythm that can both reflect inhibition and temporal framing. The alpha rhythm can be flexibly modulated in strength. Future work should focus on the role of cortical feedback and top-down modulation, i.e. how the cortex is able to influence the thalamic alpha, and on the relation between cortical and thalamic alpha oscillations.

3.5 Supplementary Materials

3.5.1 Neuron model

The currents flowing through different ion channels are generally described as:

$$I_i = f_i(m_i, n_i) \cdot g_i \cdot (V - V_i) \quad (3.11)$$

Where V_i is the reversal potential for current I_i . Reversal potentials for the different currents as well as the variable factors $f_i(m_i, n_i)$ are given in Table 3-2.

For most currents the variable factor of the conductance is of the form:

$$f_i(m_i, n_i) = m_i^M n_i^N \quad (3.12)$$

The activation and inactivation variables (m and n in equation 3.12) follow first order dynamics. For sodium currents (I_{Na}), potassium currents (I_K), AMPA-mediated excitatory (I_{AMPA}) and GABA-mediated inhibitory synaptic currents (I_{GABA}) we use the form:

$$\frac{dx}{dt} = \alpha_x(V)(1 - x) - \beta_x(V)x \quad (3.13)$$

Whereas for the slowly non-inactivating potassium current (I_{KM}), the low-threshold Calcium current ($I_{Ca(LT)}$), the high-threshold calcium current ($I_{Ca(HT)}$), and the hyperpolarization-activated cation current (I_h) we employ:

$$\frac{dx}{dt} = (x_\infty(V) - x)/\tau_x(V) \quad (3.14)$$

Where $x = m_i, n_i$ corresponds to the different activation and inactivation variables. The rate functions $\alpha_x(V)$ and $\beta_x(V)$, or $x_\infty(V)$ and $\tau_x(V)$ are specific for channels and the same for all neurons (if applicable), they are given in Table 3-3.

The parameters that differ between the two neuron models, i.e. the maximum conductances g_i in equation 2, and the parameters for the rate functions (potential shift V_T and time constant τ_{max}) are given in Table 3-4.

3.5.1.1 FS-I neurons

The fast-spiking inhibitory neurons contain five different currents:

The sodium (I_{Na}) and potassium (I_K) currents mainly responsible for the generation of action potentials, a slowly non-inactivating potassium current (I_{KM}), and two different synaptic currents: the excitatory (I_{AMPA}) and inhibitory (I_{GABA}) synaptic currents.

3.5.1.2 *TCR neurons*

The model for the thalamo-cortical relay neurons is based on the model described in the work by Vijayan and Kopell [127], which is developed from work by Destexhe et al. [168].

Like the FS-I neurons, the TCR neurons contain the sodium, potassium, and the synaptic currents. Besides these four, the TCR neurons receive three extra currents. The first is an extra potassium leak current (in addition to the general leak current in equation 3.1). This current is passive:

$$I_{K_L} = -g_{K_L}(V - V_{K_L}) \quad (3.15)$$

The other two have activation and inactivation variables governed by equation 3.14: the low-threshold calcium current ($I_{Ca(LT)}$) and the hyperpolarization-activated cation current (I_h).

3.5.1.3 *HTC neurons*

A subset (~25-30%) of the neurons that relay information from the thalamus to the cortex have different dynamics and appear to be crucial to the generation of the alpha rhythm [24], [117], [135]. The model for these high-threshold bursting thalamo-cortical neurons (HTC) is also based on the models described in the work by Vijayan and Kopell [127] and Destexhe et al. [168]. They contain all of the currents of the TCR-model (although with slight changes in the parameters, see Table 3-4). On top of these, two more currents are added: a high-threshold calcium current ($I_{Ca(HT)}$), and a calcium-activated potassium current (I_{AHP}). Unlike most other currents, I_{AHP} does not depend on the membrane potential, but instead is a function of the local calcium concentration inside the cell.

3.5.1.4 *RTN neurons*

The model for the neurons in the reticulate nucleus is based on the model described in the work by Vijayan and Kopell [127]. The reticulate cells are bursting inhibitory neurons and their model is similar to TCR neurons, but the conductance of the potassium leak current (g_{K_L} in eq. 3.15), as well as low-threshold calcium current ($I_{Ca(LT)}$) are modified (see Table 3-3 and Table 3-4).

3.5.1.5 *Calcium dynamics*

The calcium concentration in the TCR, HTC and RTN neurons evolves according to:

$$\frac{d[Ca]}{dt} = \frac{[Ca]_{\infty} - [Ca]}{\tau_{[Ca]}} - u \cdot (I_{Ca(HT)} + I_{Ca(LT)}) \quad (3.16)$$

Where $[Ca]_{\infty} = 0.24 \text{ nM}$ is the equilibrium calcium concentration, and $u = 0.27126 \times 10^{-6} \text{ nmol/nC/cm}$ takes into account the channel density. In the previous work by Vijayan and Kopell [127], the model by Destexhe et al. [168] was used and the time constant for the calcium dynamics ($\tau_{[Ca]}$) was set to 5 ms (see their supplementary materials), others have reported values of the same order of magnitude (1 and 3.3 ms [187], [188]).

The reversal potentials for the calcium currents ($I_{Ca(LT)}$ and $I_{Ca(HT)}$) also depend on the local calcium concentration according to the Nernst equation:

$$V_{Ca} = \frac{RT}{zF} \ln \left(\frac{[Ca]_{out}}{[Ca]} \right) \quad (3.17)$$

Where $[Ca]_{out} = 1500 \text{ nM}$ is the calcium concentration in the extracellular space and $RT/zF = 13.37 \text{ mV}$ at $T = 37 \text{ }^{\circ}\text{C}$.

Table 3-2. Reversal potentials and variable gating factors for the different transmembrane currents (equations 3.11 and 3.12).

	V_i (mV)	$f(m, n)$
leak	-70	1
Leak (RTN)	-73	1
KL	-100	1
Na	50	m^3n^2
K	-90	n^4
K_M	-90	n
AHP	-100	m^2
h	-40	n
Ca(LT)	n/a	m^2n
Ca(HT)	n/a	m^2n
AMPA	0	m
GABA	-80	m

Table 3-3. Activation and inactivation dynamics of transmembrane currents.

n_{Na}	$\alpha = 0.128 \exp\left[-\frac{V + 44.5}{18}\right]$	$\beta = \frac{4}{\left(1 + \exp\left[-\frac{V + 21.5}{5}\right]\right)}$
m_{Na}	$\alpha = \frac{0.32(V - (13 + V_T))}{1 - \exp\left[-\frac{V - (13 + V_T)}{4}\right]}$	$\beta = -0.28 \frac{V + 21.5}{1 - \exp\left[\frac{V + 21.5}{5}\right]}$
n_K	$\alpha = \frac{0.032(V - (15 + V_T))}{1 - \exp\left[-\frac{V - (15 + V_T)}{5}\right]}$	$\beta = 0.5 \exp\left[-\frac{V + 0.515}{40}\right]$
m_{KM}	$x_\infty = 1/(1 + \exp\left[-\frac{V + 35}{10}\right])$	$\tau_x = \frac{\tau_{max}}{3.3 \exp[0.05(V + 35)] + \exp[-0.05(V + 35)]}$
m_{AHP}	$x_\infty = \frac{48[Ca]^2}{48[Ca]^2 + 0.09}$	$\tau_x = \frac{1}{48[Ca]^2 + 0.09}$
n_h	$x_\infty = 1/(1 + \exp\left[\frac{V + 75}{5.5}\right])$	$\tau_x = 20 + \frac{1000}{\exp\left(\frac{V + 71.5}{14.2}\right) + \exp\left(-\frac{V + 89}{11.6}\right)}$
$m_{Ca(LT)}$	$x_\infty = \frac{1}{1 + \exp\left(-\frac{V + 59}{6.2}\right)}$	$\tau_x = N/A$ (instantaneous)
$n_{Ca(LT)}$	$x_\infty = \frac{1}{1 + \exp\left(\frac{V + 83}{4}\right)}$	$\tau_x = \frac{30.8 + 211.4 + \frac{\exp\left(\left(V + \frac{115.2}{5}\right)\right)}{1 + \exp\left(\frac{V + 86}{3.2}\right)}}{3.737}$
$m_{Ca(LT)}$ (RTN)	$x_\infty = \frac{1}{1 + \exp\left(-\frac{V + 53}{7.4}\right)}$	$\tau_x = 0.999 + \frac{0.333}{\exp\left(\frac{V + 27}{10}\right) + \exp\left(-\frac{V + 102}{15}\right)}$
$n_{Ca(LT)}$ (RTN)	$x_\infty = \frac{1}{1 + \exp\left(\frac{V + 80}{5}\right)}$	$\tau_x = 6 + \frac{0.333}{\exp\left(\frac{V + 48}{4}\right) + \exp\left(-\frac{V + 407}{50}\right)}$
$m_{Ca(HT)}$	$x_\infty = \frac{1}{1 + \exp\left(-\frac{V + 40.1}{3.5}\right)}$	$\tau_x = N/A$ (instantaneous)
$n_{Ca(HT)}$	$x_\infty = \frac{1}{1 + \exp\left(\frac{V + 62.2}{5.5}\right)}$	$\tau_x = 0.1483 \exp(-0.09398 V) + 5.284 \exp(0.008855 V)$
m_{AMPA}	$\alpha = \frac{40}{1 + \exp\left(-\frac{V}{2}\right)}$	$\beta = \frac{1}{2.4}$
m_{GABA}	$\alpha = \frac{5.69}{1 + \exp\left(-\frac{V}{2}\right)}$	$\beta = \frac{1}{1.8}$

Table 3-4. Neuron-specific parameters

	FS-I	TCR	HTC	RTN
g_{leak} (mS/cm ²)	0.015	0.01	0.01	0.05
g_{Na} (mS/cm ²)	46	90	90	100
g_K (mS/cm ²)	5.1	10	10	10
g_{K_L} (mS/cm ²)	-	0.0028	0.0069	0.08
V_T (mV)	-61.84	-25	-25	-55
g_{K_M} (mS/cm ²)	0.07	-	-	-
τ_{max} (ms)	824.5	-	-	-
g_h (mS/cm ²)	-	0.1	0.36	-
$g_{Ca(LT)}$ (mS/cm ²)	-	2	2	2.3
$g_{Ca(HT)}$ (mS/cm ²)	-	-	4	-
g_{AHP} (mS/cm ²)	-	-	15	-

3.5.2 Network Connectivity

3.5.2.1 Synaptic connections

The neurons influence each other via synaptic currents. The synaptic currents can be either excitatory AMPA-type, or inhibitory GABA-type synapses. The synaptic current is calculated using:

$$I_s = g_s q_s (V - V_s) \quad (3.18)$$

Where V_s is the reversal potential of the synapse (either V_{AMPA} or V_{GABA} , see Table 3-2), and g_s the maximum conductance of the synapse (see below). The dynamics of

the synapse (q_s) are based on [95] (AMPA) and [127] (GABA) and are given by the equation:

$$\frac{dq_s}{dt} = A_{syn}(V_{pre}) * (1 - q_s) - \frac{q_s}{\tau_s^-} \quad (3.19)$$

Where τ_s^- is the synapse-specific decay time constant ($\tau_{AMPA}^- = 2.4$ ms; $\tau_{GABA}^- = 6.25$ ms). The factor $A_s(V_{pre})$ is a function of the membrane potential of the presynaptic neuron (V_{pre}):

$$A_s(V_{pre}) = \frac{\frac{1}{\tau_s^+} - \frac{1}{\tau_s^-}}{1 + \exp\left(-\frac{V_{pre}}{2}\right)} \quad (3.20)$$

The rise time constant (τ_s^+) is once again different for both synapse types ($\tau_{AMPA}^+ = 0.025$ ms; $\tau_{GABA}^+ = 0.225$ ms).

3.5.2.2 *Generating connections*

The connectivity between neurons was constructed using the parameters in Table 3-5. For each pair of populations (A and B) the amount of connections going from each neuron in population A to each neuron in population B were randomly sampled from a uniform distribution. The strength of the connections (g_{syn}) were in turn sampled from a normal distribution with given mean (\bar{g}) and standard deviation (σ). For example: every neuron in the RTN-I population receives input from 10 randomly chosen TCR neurons. The strength of these excitatory synapses is on average equal to 0.3 mS/cm², the variance (σ^2) in the connection strength among synapses of this type is 0.0025 mS²/cm⁴.

Table 3-5. Connectivity within the thalamic alpha generator.

populations	Type	# of conn.	\bar{g} (mS/cm ²)	σ (mS/cm ²)
TCR → RTN-I	AMPA	10	0.3	0.05
HTC → FS-I	AMPA	5	0.5	0.05
HTC → HTC	AMPA	2	0.2	0.02
RTN-I → FS-I	GABA	3	0.3	0.01
RTN-I → RTN-I	GABA	3	0.3	0.01
RTN-I → TCR	GABA	3	0.15	0.01
RTN-I → HTC	GABA	8	0.4	0.01
FS-I → TCR	GABA	3	0.1	0.01
FS-I → HTC	GABA	3	0.1	0.01
FS-I → FS-I	GABA	3	0.3	0.01

3.5.2.3 *Gap junctions*

The HTC neurons are interconnected with gap junctions [127], [135]. The gap junctions are responsible for a second current (I_{GJ}) through which HTC neurons can interact:

$$I_{GJ} = g_{GJ}(V - V_{pre}) \quad (3.21)$$

Where V_{pre} corresponds to the membrane potential of the “presynaptic” neuron. Every HTC neuron is connected with 3 random other HTC neurons through gap junctions. The strength of these gap junctions (g_{GJ}) is sampled from a normal distribution with a mean of 0.004 mS/cm² and with a variance of 0.001 mS²/cm⁴, similar to the gap junction strength of 0.003– 0.005 mS/cm² reported in [127].

Chapter 4.

A model of microsaccade-rhythmic modulation synchronization and coding in early visual cortex

Adapted from:

E. Lowet, B. Gips, M. J. Roberts, P. De Weerd, O. Jensen, and J. P. J. M. van der Eerden, "Microsaccade-rhythmic 3-4Hz modulation of synchronization and coding in early visual cortex," *In Preparation*

Abstract

The visual environment is actively explored through saccadic eye movements. Saccades strongly modulate not only neural spike rates, but also temporal correlations (synchrony) among neurons. Neural synchrony supports visual coding and enhances information transfer between visual areas. The changes of synchronization induced by saccades and their implication for visual coding are not well understood. Here, we show that two distinct synchrony regimes observed in early visual cortex V1 and V2 are reproduced by computational modeling of microsaccade-dependent activity. In the period shortly after the microsaccade (0 - 100 ms, to which we refer as transient), synchrony is high across the network due to a common reset, allowing for robust and fast latency coding. In the subsequent period (100 - 300 ms, to which we refer as the sustained period) the network exhibited narrow-band gamma-range synchrony, reflecting mutual synaptic interactions as well as stimulus parameters. We show that the microsaccade modulation of V1 synchrony influenced the neuronal activity of V2 receptive fields. We derive experimental predictions that can be tested using current methodology. The microsaccade-rhythmic alternation between initial fast coding relying on transient synchrony and subsequent contextual coding relying on sustained local gamma synchrony provides a basic repeating sensory processing pattern that might operate in other sensory rhythmic sampling processes as well.

4.1 Introduction

Perception is an active process [198]–[200], in which animals explore their environment through specific movements of their sensory organs. For most animals relying on visual perception, particularly for primates, large and small saccadic eye movements play a critical role in visual exploration [201]–[203]. The role of saccades in primate perception and cognition (e.g. visual attention) has been intensively studied over the last decades [202], [204]. Even during fixation, gaze direction is not stable, but the eyes continuously exhibit small saccadic movements ($< 1\text{deg}$). These small eye movements appear to be mainly controlled by the same neural circuitry as larger saccades [203]. These small saccades, termed microsaccades, have recently been intensively studied [205]. Strikingly, research has shown that they have a marked impact on neural activity over the whole visual subcortical and cortical circuitry [202], [206], [207]. They modulate neural spike rates [204], [208], [209], spike bursting [210] and neural synchrony [147], [206], [211], [212]. Microsaccades may be important to refresh the visual image [205], for optimal local sampling during natural viewing [213] and for visual attentional selection [214]. They have also been suggested to counteract fading/adaptation [215], but recent work indicates that this is not a function unique to microsaccades [205], [216].

Microsaccades regularly perturb neural processing, prohibiting visual neurons to remain in a stationary regime. The use of trial-averaging to improve signal-to-noise ratio has for a long time obscured their role in the highly non-stationary neural processing [217]. Recent studies using single-trial analysis have shown that neural activity exhibits strong temporal variation locked to low-frequency rhythms [41], [58], [61], [67], [68], [147], [202], [218]. Low-frequency rhythms (delta and theta frequencies, 0.5-8Hz) have been shown to play a role in various sensory areas as well as in other subcortical and cortical areas. They strongly modulate neural spike rates and higher-frequency neural rhythms, in particular gamma rhythms (25-80 Hz) [58], [64], [65], [68], [219]. In the primate visual cortex, low-frequency rhythmic activity in the delta range correlates with the (micro)saccade rhythm [41], [147], [211]. The microsaccade-linked neural rhythmic patterns are in agreement with behavioral studies showing rhythmic modulation of perceptual and cognitive performance [71], [220]–[222].

The implications of the microsaccade-induced rhythms for neural coding and information transfer in visual cortex are not well understood. Studies have shown that microsaccades can enhance synchronization-based neural coding [148], [223], in particular during microsaccade-induced transients. The ‘reset’ of neural activity

accompanying these transients [147], [224] may enable latency coding [225] for fast and efficient information transfer of new visual input. Indeed, it has been shown that the first spike after a saccade is highly informative of the stimulus [226]. However, neural synchronization occurs not only at the transient shortly after the microsaccade, but also throughout the microsaccade interval [41], [147], [224], [227].

4.1.1.1 *General view on temporal coordination of microsaccade-shaped cortical activity*

We can understand the differences in the transient activity shortly after the microsaccade and the “sustained” period following it in the microsaccade interval using general principles of synchronization theory [228]–[230].

We hypothesize that the phase-coordination of cortical activity during the transient and the sustained period rely on two distinct mechanisms. Phase-coordination in the transient period results from an external common resetting impulse (Figure 4-1A). Conversely, in the sustained period phase-coordination is achieved through mutual synchronization (Figure 4-1B).

A resetting impulse can either phase shift an ongoing oscillation or start the generation mechanism in the absence of an ongoing oscillation. Transient neural activation that travels from the retina along the visual hierarchy (feedforward sweep, [231]), as observed after stimulus onsets or (micro)saccades [149], can provide such global and external resetting impulses for a visual cortical area like V1. For microsaccades, a top-down corollary discharge originating from fronto-parietal regions as well as subcortical regions, might further shape the transient-related resetting (including pre-saccadic inhibition, [207]). Importantly, the external resetting impulses are independent of connectivity of V1 neurons (Figure 4-1C). Furthermore, they act at a fast time-scale and large spatial-scale. However, the phase coordination is not sustainable and fades quickly after the end of the resetting impulse.

It is important to distinguish between the observed and the intrinsic frequency of an oscillator, when investigating phase-coordination through mutual synchronization. The intrinsic frequency is the frequency of the oscillator receiving input, if it were completely decoupled from all other oscillators. However, sufficiently coupled oscillators mutually adjust their phases (by phase delay/advance) over time such as to converge on a common frequency [230]. This will lead to an observed frequency differing from the intrinsic frequency. There are two important variables that regulate the synchronization process. The first factor

is the interaction (coupling) strength. The interaction strength defines how strongly the phase of an oscillator is shifted (advanced or delayed) by another oscillator. In neural terms, interaction strength is mainly defined by anatomical connection strength between two oscillating (sub)networks and by the amplitude of an oscillation [232]. The second factor is detuning, defined as the difference in intrinsic frequency of the two oscillators. The larger the detuning, the stronger the coupling needs to be for the oscillators to converge to a common frequency. The most common in-vivo modulator of detuning is the variability of the network input. For gamma-band activity in V1, it has been shown that the excitatory input drive, determined largely by visual contrast, strongly modulates the intrinsic frequency in a retinotopic manner [40], [42], [44], [45]. The regulation of synchronization by interaction strength and detuning is best visualized by mapping the synchronization values in the 2D space spanned by these two parameters [228]–[230]. This mapping yields a well-defined region of synchronization with an inverted triangular shape, the so-called Arnold tongue [233] (Figure 4-1D).

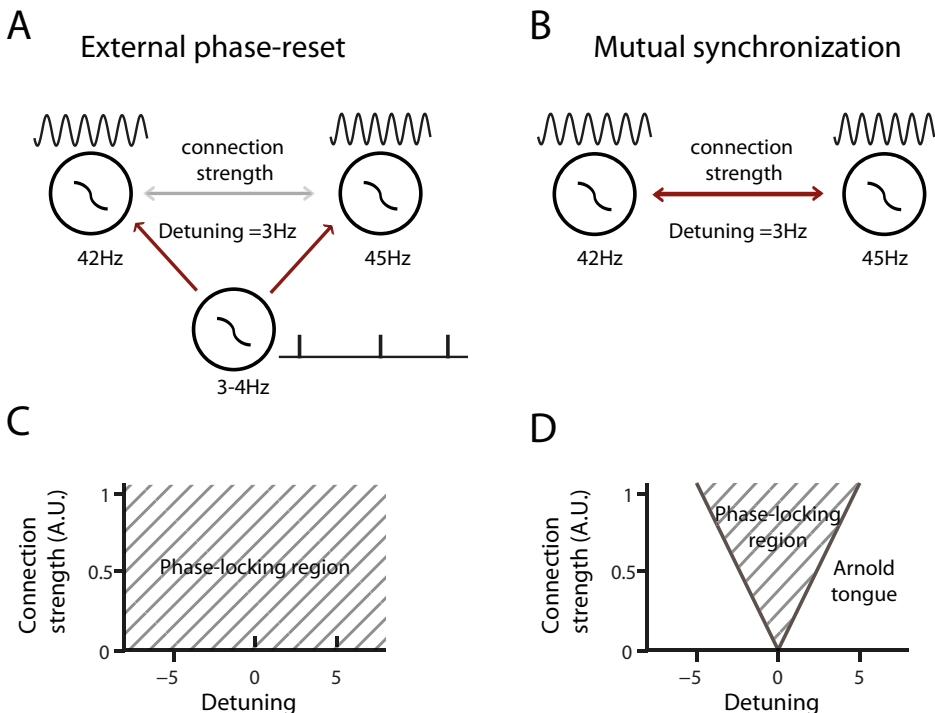


Figure 4-1. The two different ways of achieving synchrony explained schematically. (A) Synchrony is achieved through (periodic) resetting by an outside source. (B) Synchrony arises through mutual interactions. (C) When synchrony is determined by an outside resetting pulse, connection strength and detuning no longer influence synchrony, therefore

the Arnold Tongue is not visible in this case. **(D)** When synchrony is caused by mutual interactions, the connection strength has to be high enough to overcome any differences in intrinsic frequency (detuning). This results in a triangular region of synchrony also known as the *Arnold Tongue* shown here.

In the current work, we investigate how synchronization and coding properties could differ between the transient activity directly following a micro-saccade and the later ‘sustained’ activity. We used computational modeling of spatial excitatory-inhibitory spiking networks receiving microsaccade-modulated input. First, we constrained the network model using previously reported spectral dynamics of monkey V1 LFP [41]. We then show that synchronization properties differed fundamentally between the transient and the sustained period. During the transient, synchrony at various frequency-bands was high across the network, for all stimulus input patterns, allowing robust latency coding. During the sustained period, synchronization in the gamma-range was spatially local and shaped by both the underlying connectivity and the stimulus input properties. In a neural network mimicking (anisotropic) horizontal connections among V1 neurons found in tree shrew [106], we showed that the adaptive synchronization in the sustained period in our model network had implications for information transfer to a second downstream network and therefore the receptive fields (RF) of the second network. We found that the sustained synchronization in the microsaccade interval enabled coding of stimulus orientation in the down-stream network. It also allowed flexible shaping of the down-stream RFs to adapt to local stimulus contrast. Our analyses suggest that the synchronization-dependent shaping of RF properties may be important for early local visual feature grouping and segmentation processes. Taken together, we conclude that the early highly synchronized transient activity following a microsaccade permits rapid initial coding, whereas the following sustained activity with local synchrony allows context-dependent coding of the visual input. The two step microsaccade-linked processing can likely be generalized to large saccades [204] and possibly to other rhythmic sensory sampling processes as well, such as sniffing [199], [234] and whisker movement [198], [235], [236].

4.2 Methods

4.2.1 Neuron model

The model neurons used were two-dimensional simple models first introduced by Izhikevich [9], extended with exponentially decaying synapses. The dynamics of neuron i are given by equations 4.1-4.4.

$$\dot{V}_i = 0.04V_i^2 + 5V_i + 140 - u_i + I_i(t) \quad (4.1)$$

$$\dot{u}_i = a(bV_i - u) \quad (4.2)$$

$$\dot{s}_i = -s_i/\tau_i \quad (4.3)$$

$$\text{if } V_i \geq 30 \text{ mV, then } \begin{cases} V_i \leftarrow c \\ u_i \leftarrow u_i + d \\ s_i \leftarrow 1 \end{cases} \quad (4.4)$$

V_i represents the neurons membrane potential, whereas u_i represents a membrane recovery variable. The membrane potential is reset to the value of c (and thus an action potential is said to be generated) when it reaches a threshold value (30 mV). Parameters a , b , c and d are taken from previously published work [9] for the two different types of neurons used: regular spiking excitatory neurons (RS) and fast spiking inhibitory neurons (FS), see Table 6. The dynamics of the presynaptic gate are denoted by s_i . The total input to neuron i (I_i) consists of the sum of the synaptic inputs, together with any imposed input currents and their noise:

$$I_i(t) = \sum_j s_j g_{i,j} (V_{\text{rev},j} - V_i) + I_i^{\text{imp}}(t) + \eta(t) \quad (4.5)$$

Where V_{rev} is the reversal potential of the synaptic connection and the conductance-like factor g_{ij} is the synaptic connection strength between neuron j and i . Both the time constants τ_i and the reversal potentials $V_{\text{rev},i}$ depend on the type of synapse (AMPA or GABA) and therefore depend on the type of the presynaptic neuron (see Table 6).

Table 6. Parameters for the regular spiking excitatory neurons (RS) and fast spiking inhibitory neurons (FS).

	RS	FS
a	0.02	0.1
b	0.2	0.2
c	-65	-65
d	8	2
τ	10 ms	5 ms
V_{rev}	50 mV	-90 mV

The dynamical equations (4.1-4.4) were numerically integrated using the Runge-Kutta method [111] with a time-step of 0.5 ms.

The noise $\eta(t)$ on the imposed input current (see equation 4.5) was sampled in each simulated time-step from a normal distributions with standard deviation equal to the square root of the strength of the imposed input current divided by a signal-to-noise factor (snr), which is simulation-specific:

$$\eta(t) \sim N(0, \sqrt{\frac{I_i^{imp}(t)}{snr}}) \quad (4.6)$$

4.2.1.1 *Imposed input currents*

The network of neurons receives an imposed input current, representing synaptic input from the thalamic lateral geniculate nucleus (LGN). The input current consisted of two factors:

$$I_i^{imp}(t) = J_i \cdot \zeta(t) \quad (4.7)$$

Where J_i is neuron-dependent and it corresponds to the current representing the stimulus input pattern in a retinotopic sense. The time-dependent term $\zeta(t)$ is the microsaccade modulation function, which was generated by convolving a string of delta functions separated by inter-saccadic interval $T=400$ ms with a microsaccade modulation kernel:

$$\zeta(t) = \text{III}_T(t) * K(t) \quad (4.8)$$

Here III_T denotes the Dirac comb function with period T :

$$\text{III}_T(t) = \sum_{k=-\infty}^{\infty} \delta(t - kT) \quad (4.9)$$

The function $\delta(x)$ is the Dirac delta function (i.e. $\delta(x) = 0$ for $x \neq 0$ but $\int \delta(x)dx = 1$ for interation intervals containing $x = 0$), and k takes all integer values.

$K(t)$ is the microsaccade modulation kernel:

$$K(t') = \begin{cases} 1 + \frac{M_P}{Z_P} * \left(\exp\left(-\frac{t'}{\tau_{1,P}}\right) - \exp\left(-\frac{t'}{\tau_{2,P}}\right) \right) & \text{if } t \geq 0 \\ 1 - \frac{M_N}{Z_N} * \left(\exp\left(\frac{t'}{\tau_{1,N}}\right) - \exp\left(\frac{t'}{\tau_{2,N}}\right) \right) & \text{if } t < 0 \end{cases} \quad (4.10)$$

The decay constants $\tau_{1,P}$ and $\tau_{2,P}$ control the length of the transient and $\tau_{1,N}$ and $\tau_{2,N}$ control the length of the pre-saccadic inhibition (with $\tau_{1,x} > \tau_{2,x}$). The factors M_P

and M_N control the strength of the transient and the pre-saccadic inhibition respectively. The normalization factor Z_x with $x = P, N$ is:

$$Z_x = \left(\frac{\tau_{2,x}}{\tau_{1,x}} \right)^{\frac{\tau_{1,x}}{\tau_{2,x} - \tau_{1,x}}} - \left(\frac{\tau_{2,x}}{\tau_{1,x}} \right)^{\frac{\tau_{2,x}}{\tau_{2,x} - \tau_{1,x}}} \quad (4.11)$$

The microsaccade modulation parameters are given in Table 3-1.

Table 7. Parameter values for the microsaccade modulation kernel (see equation 4.10).

$\tau_{1,P}$	$\tau_{2,P}$	$\tau_{1,N}$	$\tau_{2,N}$	M_P	M_N
100 ms	40 ms	15 ms	10 ms	0.5	0.2

Convolving the kernel with these parameter values, leads to the microsaccade modulation function $\zeta(t)$ illustrated in Figure 4-2A.

For Figure 4-4A the mean input was an oriented bar-shaped input pattern to illustrate its influence on the spatial distribution of gamma synchronization. The shape was constructed from a 2-D thresholded sinusoidal function with added noise:

$$J(x, y) = \Theta \left[\cos \left((1 + a)\pi \left(\frac{x}{L} - \frac{1}{2} \right) \right) \cos \left((1 + b)\pi \left(\frac{y}{L} - \frac{1}{2} \right) \right) - 0.5 \right] \quad (4.12)$$

$$* 0.5 * \left(\cos \left(4\pi \frac{ax + by}{L} - \frac{1}{2} \right) + 1 \right)$$

Where $\Theta[x]$ is the Heaviside step function (i.e. $\Theta(x \geq 0) = 1$ and $\Theta(x < 0) = 0$). L is the size of the neuronal grid (in this case, $L=40$). The factors a and b determine whether the stimulus is oriented horizontally or vertically. For the stimulus in the top row of Figure 4-4A, $a=1$ and $b=0$. For the bottom row $a=0$ and $b=1$.

For Figure 4-6 and Figure 4-7, we chose patches of natural stimuli from the Berkeley segmentation dataset (BSDS500, [237]). The luminance of every pixel of a 40 x 40 patch determined the mean input strength of the corresponding neuron (J_i in equation 4.7). The luminance values were first normalized to be between 0 and 1. After this, the input to the E neurons was multiplied by a factor 7, whereas the input to the I neurons scaled by 3.5

4.2.1.2 Neural connectivity

The probability of neurons to be synaptically connected depends on their Euclidean distance D . Note that we employed periodic boundary conditions when calculating D (i.e. a neuron on the left edge of the grid is a neighbor of both the neuron to the right of it as well as the neuron on the right edge of the grid). All connection patterns were generated using Gaussian distributions.

$$P(D) = \frac{1}{Z} \exp\left(-\frac{D^2}{2\sigma_S^2}\right) \quad (4.13)$$

Here σ_S determines the reach of the neuronal connections, this value changed between simulations (see below). Z is a normalization factor. The probability of a neuron to connect to itself is set to 0.

Every neuron receives a fixed total number of inputs, N_S , all of which have the same strength g_S . The parameters N_S , g_S and σ_S were specific to sender-receiver pair cell type (e.g. N_S was different for $S = \text{"E to I"}$ connections compared to $S = \text{"E to E"}$ connections. As was g_S).

The Gaussian connection probability distribution was then sampled N_S times to generate the synaptic connections. During this sampling process, a neuron pair could be sampled more than once, linearly increasing the connection strength between that neuron sender-receiver pair.

In general, excitatory connections had a longer reach than inhibitory connections. For the network used for Figure 4-2 and Figure 4-3 the reach of the excitatory connections (σ_S) was set to 20, whereas inhibitory connections were more local and σ_S was set to 1.

In the case of the anisotropic network in Figure 4-4 and Figure 4-5, connectivity within V1 was the same as in the network used for Figure 4-3, with exception of the EE-connections. For Figure 4-4B (for illustration) only EE-connections emerging from the middle of the network was kept and the strength scaled by factor 3. The EE connection pattern was then spatially restricted having an oriented bar-like shape, similar to the input pattern in Figure 4-4A. For Figure 4-5 all connections in the x-direction were scaled with a factor of 3 before generating the connections profile, leading to the elliptical profiles seen in Figure 4-5B (this was done for both the excitatory and inhibitory connections, the latter are not shown in Figure 4-5B). The connection probabilities within V2 were all set to be uniform (similar to using very large values for σ_S in equation 4.13). Feedforward connections between V1 and V2 were only excitatory and were also uniform. Networks used in Figure 4-6 and Figure 4-7 had same connection properties as the network in Figure 4-3.

4.2.2 Local Field Potential

A local field potential (LFP) signal was approximated by the summation of membrane potentials of nearby excitatory cells. The contribution of a neuron to the LFP signal recorded at a virtual electrode decreased with its Euclidean distance D to that virtual electrode according to a Gaussian kernel:

$$K_{LFP}(D) = \exp\left(-\frac{D^2}{2\sigma_{LFP}^2}\right) \quad (4.14)$$

Here σ_{LFP} determines the spatial spread of the LFP and was set to 1 neuron distance on the square grid.

4.2.2.1 LFP electrode grid

In the simulations a 40×40 square grid of excitatory neurons was covered by a 10×10 grid of virtual electrodes of the same size (i.e. with a distance between electrodes equal to 4 times the distance between excitatory cells).

4.2.3 Spike-triggered averaging (STA)

To estimate the effective (functional) connectivity from V1 neurons to V2 neurons we used a spike-triggered averaging (STA) approach. We used the V2 spike as trigger to define time windows over which preceding V1 spike activity is averaged. In this way, we computed the V1 spike probability occurring just before a V2 spike. For a given V2 neuron, we computed the above defined STA only for those V1 neurons that are presynaptic to the V2 neuron.

$$STA(\tau) = \frac{1}{N_2} \sum_{t=1}^T v_1(t-\tau)v_2(t) \quad (4.15)$$

Here $v_2(t)$ is the number of V2 neurons spiking at the trigger time t , for each of these V2 neurons $v_1(t-\tau)$ is the number of presynaptic V1 neurons spiking at time $t-\tau$ and N_2 is the total number of V2 spikes. To get one STA value we averaged $STA(\tau)$ over $\tau = -8$ ms to $\tau = -2$ ms. Finally, we subtracted a shuffled STA to correct for spurious variation due to spike rate differences. For shuffling we applied the same analysis as above, but chose a random set of time points as triggers.

4.2.4 Mutual Information

We used a mutual information metric (MI) to estimate the mutual dependence between the transfer entropy and properties of the sending neurons such as firing rate, firing phase and phase locking with its neighbors. The mutual information of two signals (X and Y) can be calculated by the discrete probability density histograms (P) and calculating the Shannon entropy (H):

$$H(X) = - \sum_{x \in X} P(x) \log_2(P(x)) \quad (4.16)$$

Here x runs over all instants of the signal X . The mutual information $I(X, Y)$ is defined as

$$I(X, Y) = H(X) - H(X|Y) \quad (4.17)$$

where $H(X|Y)$ is the conditional entropy:

$$H(X|Y) = \sum_{x \in X, y \in Y} P(x, y) \log_2 \left[\frac{P(x)}{P(x, y)} \right] \quad (4.18)$$

4.2.5 Spectral analysis

4.2.5.1 Time-frequency representation

Time-resolved spectral information of the simulated time-series was obtained from time-frequency representations (TFRs). They were calculated by estimating spectral power of the simulated LFP signals. Short-time Fourier transforms were obtained using a 150 ms sliding Hann window. Zero-padding was used to interpolate the frequency spectra to achieve the frequency resolution presented in the figures.

4.2.5.2 Instantaneous gamma phase estimate

In the sustained period of an inter saccade interval, the neuronal network dynamics is dominated by gamma activity. Therefore, the instantaneous gamma phase of a measured signal can be estimated from a Hilbert transform after band-pass filtering the signal between 25 and 50 Hz (4th order Butterworth IIR filter).

4.2.5.3 Phase locking value and mean phase

For quantifying consistent synchrony across sites we employed the phase locking value (PLV) [238]. The PLV measures the consistency of the phase difference between two LFP signals across saccades using:

$$PLV_{x,y} = \left| \sum_{n=1}^N \exp(i(\phi_{n,y} - \phi_{n,x})) \right| \quad (4.19)$$

Where N is total number of saccades and $i = \sqrt{-1}$. The phase of LFP signal x in saccade n is denoted by $\phi_{n,x}$. For the PLVs in Figure 4-3F, for each frequency the instantaneous phase was estimated using a Fourier transform. In all other figures the instantaneous gamma phase estimate was estimated as explained above. PLVs take values between 0 (no phase locking) and 1 (perfect phase synchrony between

sites across saccades). Note that the phase signals $\phi_{n,x}$ can be a function of time to result in time-resolved PLVs.

The mean phase difference ($\bar{\theta}$) between the sites can be calculated by taking the argument, rather than the modulus:

$$\bar{\theta}_{i,j} = \arg \left(\sum_{n=1}^N \exp(i(\phi_{n,j} - \phi_{n,i})) \right) \quad (4.20)$$

4.2.6 Quantifying orientation sensitivity

We used the orientation selectivity index (OSI) defined as the mean vector length [239] in the complex plane to quantify orientation sensitivity in Figure 4-5G. It is defined as:

$$OSI = \frac{1}{\sum_k r_k} \left| \sum_k r_k \exp(i2\theta_k) \right| \quad (4.21)$$

Where r_k is the activity in response to stimulus k (e.g. the sum of action potentials in V2 in a time window). Stimulus k has orientation of θ_k radians.

4.2.7 Short summary of the monkey data

A detailed description of the microsaccade-linked spectral gamma dynamics in monkey V1 and V2 during visual stimulation can be found in [41]. Here, we use the recorded V1 data [240] for illustrative purposes only and we show that V1 spectral data is well captured by the modeled network dynamics. For Figure 4-2B we used recorded V1 LFP data of one representative session. Data were acquired using U-probes (Plexon Inc.) consisting of 16 contacts (150 μ m inter-contact spacing). The task of the monkey was to fixate a dot on the screen while a whole-field grating was shown for 2 seconds. Monkey fixation behavior was monitored using a low-resolution eye tracker directed at one eye (Arrington, 60 Hz). In addition, we used a higher resolution eye tracking system (Thomas Recording, 240 Hz) to measure microsaccades in the other eye (optimized for microsaccade detection in terms of temporal and spatial resolution). For a complete description of the experiments, see [240]

4.3 Results

4.3.1 Modeling of microsaccade-induced V1 neural oscillatory dynamics

It has been shown that microsaccades have substantial impact on neural activity in subcortical visual areas such as the LGN [207], [210] and visual cortex [202]. Microsaccades lead to modulation of the spike rate [208], [209], changes in synchrony [147] and spike firing patterns [210].

We constructed a model network (Figure 4-2A) to study the effects of microsaccades. At the core of our model is an excitatory-inhibitory neural network mimicking V1 (see Methods). The connections between the excitatory and inhibitory cells make it possible for the network to produce Pyramidal-InterNeuron Gamma (PING) rhythms [39], [152]. V1 receives input from LGN relay neurons, here represented by a direct current input. For the saccadic modulation of the spike rate of the LGN relay neurons we follow the experimental results of [204], [207], using a double exponential kernel (see Methods and Figure 4-2A). Note that it is not completely clear whether the modulations in the LGN firing rate are due to image shifts on the retina, corollary discharges, or both [206]. Our model does not attempt to distinguish between these two possible contributing factors.

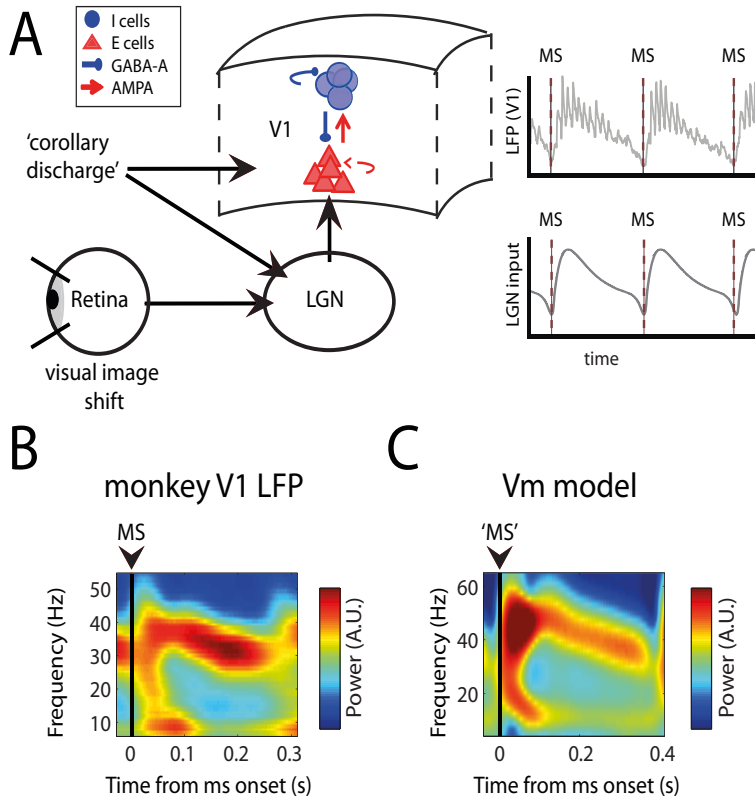


Figure 4-2. Modeling microsaccade V1 neural dynamics. **(A)** Conceptual overview over the model. A (small) region in V1 was modeled as a PING network of spiking excitatory (E cells, Regular Spiking) and inhibitory neurons (I cells, Fast-Spiking). They were connected through AMPA and GABA-A type synapses (see Methods and Figure 4-3A for details). We imposed on this network currents mimicking microsaccade (MS) modulated input from LGN and/or corollary discharges to V1 (see Methods) We used the spikes and approximate local field potentials in the PING network (Vm) for subsequent analysis. **(B)** A representative experimental microsaccade-triggered time-frequency representation (TFR) of V1 LFP power. Microsaccades occurred at $t = 0$ s. Note the broad band activity just after the saccade onset (0-100 ms) followed by a narrow band gamma signal (100 ms onwards). **(C)** A microsaccade-triggered TFR of the simulated LFP. Conventions as in B. The model visual cortex (Vm) is able to produce both a broad band signal directly following the saccade onset (transient) as well as the narrow band gamma response afterwards (sustained).

Figure 4-2B shows a representative microsaccade-onset-triggered time-frequency representation (TFR) of power of the local field potential recorded in monkey V1 [41], [147]. We observed a power increase in the alpha/beta frequency range (~10-20Hz) shortly after the microsaccade, as well as a strong, long-lasting gamma-band (25-50Hz) increase. It has been shown that the spectral changes are linked to the

microsaccade evoked response [41], [147] and are associated with spectral phase reset in the alpha/beta frequency range [147]. The spectral response resembles the transient responses after stimulus onset described by [241]. Since the image shift on the retina induced by the saccade physically resembles a stimulus onset, it is likely that this is mainly responsible for this transient response. However, corollary discharge and ongoing rhythmic activity further shape the transient response.

Around 100ms after the microsaccade, more narrow-band gamma power with a lower frequency can be observed that remains until the next microsaccade. Alpha/Beta power is reduced during this period. This period resembles the spectral profile described for the 'sustained' response after stimulus onset [241]. Strictly speaking, the observed dynamics of gamma rhythms cannot be termed 'sustained' or 'stable', since gamma synchrony is short, and the frequency decreases over time. However, to contrast with the strong transient dynamics in the early period after the microsaccade, we keep the name 'sustained' for simplicity.

In Figure 4-2C we show the TFR of power calculated for the network simulations (for details on the network, see Figure 4-3) triggered to the microsaccade. The network spectral dynamics were strikingly similar to the observed V1 spectral dynamics with early transient alpha/beta and later more sustained gamma power. The individual spike rate of the excitatory neurons was in the alpha-beta range. Despite spiking being irregular, microsaccades led to a short strong alignment of many excitatory neurons, which in turn led to power in the lower frequency bands (<20 Hz). The gamma oscillations, emerging from excitatory-inhibitory interactions, also exhibited a behavior similar to the V1 experimental data, including decreasing frequency over time. It has been shown that the dominating gamma frequency is dependent on input-strength [39], [40], [43]–[46]. Hence, the observed pattern of a gamma frequency that decreases over time can be attributed to the exponential decay in microsaccade spike rate modulation function (Figure 4-2A). In addition, adaptation properties of pyramidal cells could also play a role [202], [205], but we did not explicitly investigate this question further.

Overall, the network simulations yielded an excellent replication of the spectral dynamics observed in monkey V1 in response to saccades.

4.3.2 The transient and sustained period after a microsaccade have different synchronization properties

The main goal of this study is to investigate the information processing properties during the 'transient' and 'sustained' period after a microsaccade. To illustrate the differences between transient and sustained activity we used further simulations of the Vm model used to generate Figure 4-2C. The structure of the network is shown in Figure 4-3A. The network consisted of a 40×40 grid of excitatory RS cells on which a 20×20 grid of inhibitory FS cells was overlaid. The connectivity within the network decreased with distance according to Gaussian connection probabilities. Periodic boundary conditions were applied to decrease finite-size effects (see methods). A 10×10 grid of virtual electrodes was placed over the grid that averages the local membrane potentials according to a Gaussian kernel (see methods) to estimate a local field potential (LFP).

In Figure 4-3 we illustrate that gamma synchrony in the sustained period depends on distance within the network. The retinotopic input to the RS cells before applying microsaccade modulation is depicted in Figure 4-3B. This pattern was kept constant across simulated saccades. The phase-locking value (PLV, see methods) across the 50 simulated saccades was calculated for all pairs of LFP electrodes. The average PLVs for all neighboring electrodes are shown in Figure 4-3C, whereas the average PLVs for all pairs of neurons at maximal distance (keeping in mind the periodic boundary conditions of the network, see Figure 4-3A) are shown in Figure 4-3D. A striking difference between panels C and D is the lack of gamma-band (25-40 Hz) synchrony between distant electrodes in Figure 4-3D during the sustained period. This effect of distance is absent in the transient part of the response.

To further analyze this difference, we plotted the PLVs for the gamma at 30 ms and at 300 ms post-saccade as a function of electrode distance in Figure 4-3E (see the two white crosses surrounded by grey and black circles respectively in panels C,D, and F). Note that the PLVs in the sustained period (300 ms) show a dependence on distance, whereas this is not the case for the PLVs during the transient (30 ms). The distance dependence of the PLV is further illustrated in Figure 4-3F. Panel F shows that only the gamma band activity in the sustained period shows a significant linear correlation with cortical distance. Both connectivity strength and stimulus correlation drop with distance, therefore both possibly contribute to this effect. In summary, gamma synchrony is higher between nearby neurons than between distant neuron pairs, but only during the sustained phase.

A model of microsaccade-rhythmic modulation synchronization and coding in early visual cortex

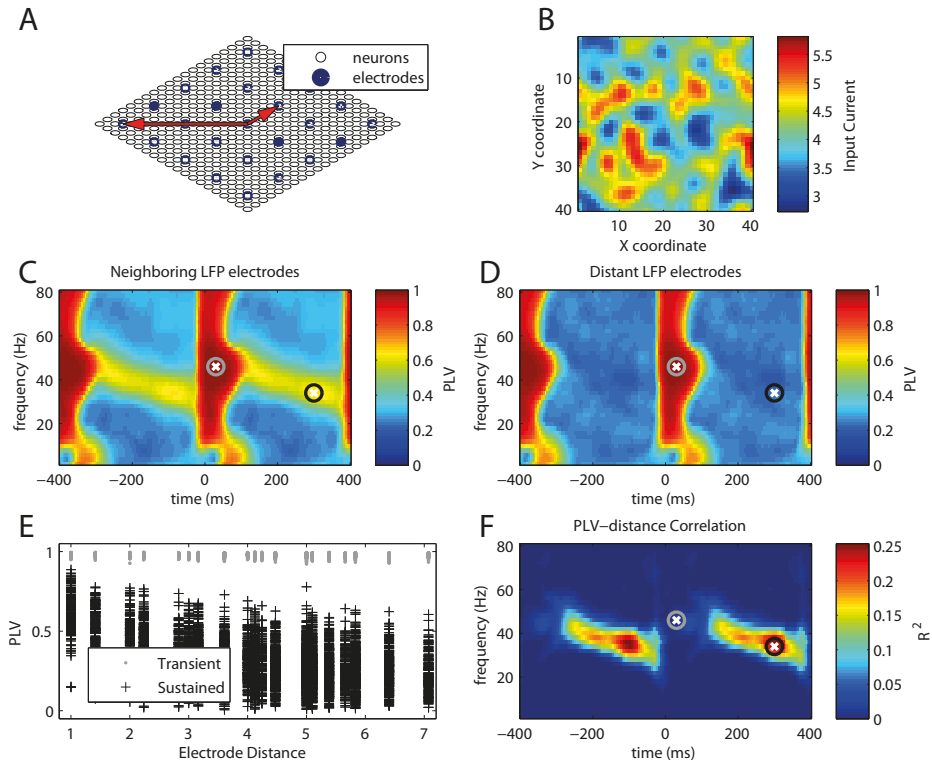


Figure 4-3. Synchrony across the network depends on connection strength more strongly during sustained gamma band activity than during microsaccade-induced transients. Synchrony was measured by phase-locking value (PLV). (A) A scaled-down schematic representation of the model network. Inhibitory neurons are omitted for clarity. The full network consists of excitatory neurons placed on a square 40×40 grid together with a square grid of the same diameter containing 20×20 inhibitory neurons (not depicted). LFP electrodes are placed on a 10×10 grid spread equally across the 40×40 neuronal grid. The boundaries of the grid are periodic, i.e. the neurons are placed atop a toroidal surface. The two red arrows indicate two electrode pairs: a neighbor pair, at minimal distance, and a pair at maximal distance. (B) Network was driven by input consisting of retinotopically smoothed Gaussian white noise. This input current was modulated over time by multiplying it by the microsaccade modulation kernel (see Figure 4-2A, below right) for a total of 50 microsaccades. The SNR factor of the temporal Gaussian noise was equal to 1 (see methods). (C) Mean synchrony strength expressed as PLV across microsaccades between neighboring LFP electrodes (see smallest of the red arrows in A). Encircled white crosses indicate the time-frequency points that are chosen as representative for “transient activity” (grey circle) and for “sustained activity” (black circle) in E. (D) Same as C, but now between LFP electrodes with maximal distance to each other (see longest of the red arrows in A). Note the lack of synchrony in the gamma band during the sustained period ($t = 150\text{-}350$ ms) (E) A scatter plot showing the PLVs for transient and sustained gamma rhythms (see encircled crosses in C, D

and F) as a function of distance between electrodes. (F) The correlation coefficients between electrode distance and PLV (see E) for a broad range of frequencies and all inter-saccade time points. Only the synchrony in the narrow-band gamma activity (25-50 Hz) during the sustained period depends on the electrode distance. This correlation can be seen in the black plusses (sustained) in panel E, but not in the grey dots (transient).

4.3.3 Coordinated network synchronization only in the sustained period

To formally test whether there are two phase-coordination mechanisms in play, we investigated whether the Arnold tongue [233] could be retrieved from the early (transient) and late (sustained) period after the microsaccade. To manipulate interaction strength and detuning in our neural network simulations, we manipulated the synaptic connectivity strength and the input drive difference respectively [42].

As an illustration, we first manipulated the detuning parameter by giving the Vm network with isotropic local connectivity (see Figure 4-3A) two different spatial input driving patterns. In Figure 4-4A, a smoothed bar-shaped stimulus was shown (left). To illustrate the effects on the gamma-band phase-coordination in the transient and sustained period, we computed the spatial distribution of phase-locking values (PLV, [238]) referenced to the neuron in the center of the 2D network. The PLVs in the transient period were uniformly high (Figure 4-4A, middle). This is caused by the steep rise of microsaccade-modulated input (Figure 4-2A) that is similar for all neurons in the network. During the sustained period, the distribution of PLVs was more local and reflected the orientation of the bar stimulus (Figure 4-4A, right). For an illustration of the effect of connectivity on the PLV, we performed another simulation in which we used horizontal or vertical anisotropy in the connection probability of the Vm network (Figure 4-4B, left), but left the input uniform across the network. The PLV distribution in the transient period was again high and uniform (Figure 4-4B, middle), whereas it was local in the sustained period, but this time dictated by the connectivity structure (Figure 4-4B right). Taken together, these two simulations explain why an Arnold tongue, a central synchronization characteristic, can be observed only in the sustained period.

We directly tested the existence of the Arnold tongue, and thus the importance of neuronal coupling with a third simulation. We spatially varied the input strength in a network with isotropically connected neurons as shown previously (Figure 4-3A,B). In this simulation we placed a LFP electrode on every neuron and mapped all the PLV values between network locations during the transient as well as

sustained period as a function of the neurons' connection strength and input difference. We indeed only observed the Arnold tongue from PLV estimates selected from the sustained period (Figure 4-4C). We also mapped the phase difference between network location in the parameter space of connectivity strength and input difference (Figure 4-4D). Also here we observed differences between the transient and sustained period after a microsaccade. In both periods, we observed that phase-difference coded for the input-difference. The phase-difference depended more strongly on input difference in the sustained period than in the transient period. In addition, in the sustained period the phase difference depends on connectivity strength. This is expected from synchronization theory [228]–[230] and has been recently observed for the V1 gamma-band [123], [212].

Taken together, Figure 4 strongly supports the fact that synchronization in the transient period is driven by phase resetting of microsaccades, whereas in the sustained period neural connectivity plays a prominent role. We conclude that the theory of coupled oscillators provides a powerful framework to investigate and distinguish these two synchronization regimes.

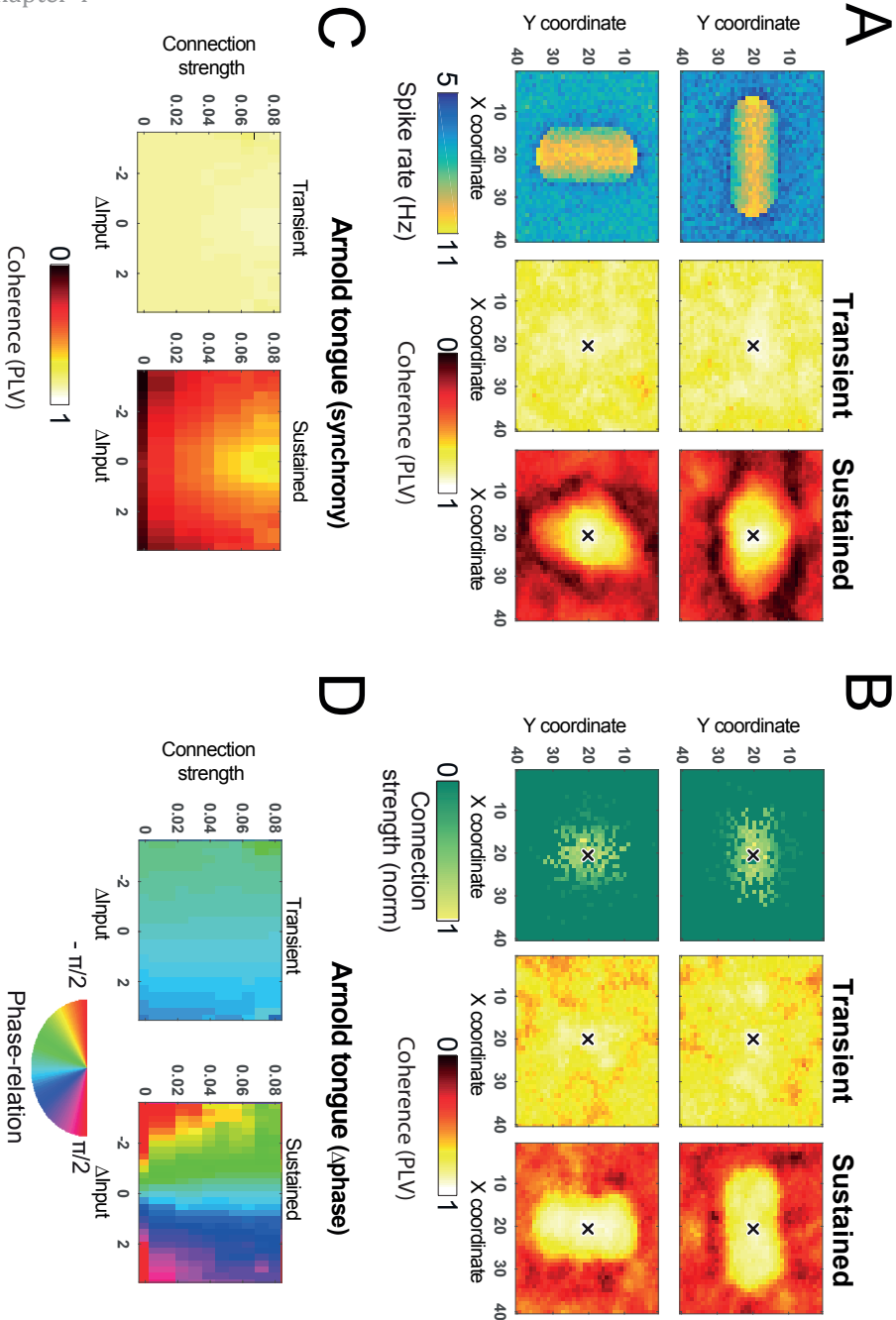


Figure 4-4. Microsaccade-dependent spatio-temporal organization of network activity. Network was a lattice with excitatory-inhibitory neurons locally connected with periodic boundary conditions (similar to Figure 4-2A) (A) Oriented stimulus, isotropic connectivity. Left: Firing rates of E-neurons of a network that was driven by a horizontal (top) or vertical (bottom) bar-shaped stimulus. Network synchronization (PLV with the center neuron, denoted by a black cross, as reference) is shown in the transient (middle) and in the sustained

period (right) with 50-ms time windows. Middle: In the transient period, PLV with the center neuron was high over the whole network, due to the micro-saccade-induced reset. Right: In contrast, in the sustained period, the PLV was high only close to the reference neuron in the network center and the PLV profile was shaped by the orientation of the bar-shaped stimulus. **(B)** Isotropic stimulus, anisotropic connectivity. Left: the center neuron (indicated by a black cross) was preferentially connected to neurons left and right from it (top), or to neurons below and above it (bottom). Middle: In the transient period throughout the network the PLV with the center neuron (indicated by a black cross) was high. Right: During the sustained period PLV was only high close to the reference neuron and the shape of the PLV profile reflected the preferred connectivity orientation. **(C-D)** Arnold tongue: synchronization in the parameter space of connectivity strength and neuron input difference. The simulation used for this analysis contained a network with isotropically connected neurons (as in Figure 4-3 and panel A) with locally varying input strength (as in Figure 4-3B) **(C)** In the transient period, PLV was high for any combination of connectivity strength and input difference (left), whereas in the sustained period PLV was dependent on both input difference and connectivity (right). The synchronization region had a triangular shape known as Arnold tongue. **(D)** The same as C, but for mean phase difference.

4.3.4 Functional implications of the two temporal-coordination mechanisms for inter-areal processing and communication

Figure 4-4 showed that local connections can change the synchrony during the sustained period of the inter-saccade interval. To illustrate possible consequences of changes in synchrony for information processing, we conducted additional simulations with a network consisting of two visual model (sub-)networks (V1 and V2, Figure 4-5A). The first sub-network (V1) is a 40×40 PING network similar to the one shown in Figure 4-3A. V1 receives direct input modulated by the microsaccade kernel (Figure 4-2A) consisting of a sinusoidal grating (Figure 4-5A, right). Similar to Figure 4-4B, left, we gave structure to the local connectivity in V1, sampling the connections from anisotropic Gaussian distributions. The resulting elliptical connectivity profiles (Figure 4-5A,B) made our model V1 sensitive to the orientation of an input pattern. This anisotropic connection pattern resembles the experimental finding of anisotropy in the long horizontal connections in the tree shrew striate cortex [106]. This connection pattern might facilitate processing of (the curvature of) line segments. The purpose of the model is not to capture the emergence of orientation tuning occurring in single cells at columnar level in V1. Instead, the model captures the effect of anisotropic ('oriented') spatial distribution

of horizontal connections and their impact on spatial coordination of V1 output and receiving neurons in V2.

The second sub-network (V2) represents one column in visual cortex (higher in the visual hierarchy than V1) and consists of a collection of 100 excitatory and 25 inhibitory neurons that receive input from all V1 neurons and were interconnected uniformly (see Methods). Besides the feed-forward drive from V1, V2 also receives a uniform background drive to increase the neurons' excitability.

Figure 4-5C and D show the TFR of the power in V1 and V2 respectively. Both V1 and V2 generated the characteristic transient with high firing rate after the onset of the simulated saccade, followed by a sustained gamma response with lower firing rate (see Figure 4-5E for differences in firing rates between the transient and sustained phases).

Figure 4-5F and G illustrate the main point: a consequence of the different gamma synchronization dynamics in the sustained period compared to the transient. The V1 sub-network was presented with gratings of 16 different orientations (one of these shown in Figure 4-5A, right). Figure 4-5F shows that the average spike rate of V1 was independent of stimulus orientation during the whole inter-saccadic interval (resulting in a similar number of spikes sent to V2 for every orientation). The same holds for the transient period in V2. In the sustained period however, the anisotropic connectivity causes different synchrony in V1, which in turn alters the input to V2 (not in the number of spikes, but the timing thereof). This causes the grating that is "parallel" to the connectivity (i.e. vertically oriented, similar to the connection patterns in panel B) to produce a stronger response in V2. This effect is quantified in Figure 4-5G by calculating the mean vector length (see Methods). In summary, the differences in gamma synchrony resulting from the (anisotropic) connection pattern in V1 make it possible for V2 to detect oriented spatial arrangements of stimuli during the sustained period, but this is not possible during the transient. Note that the transient activity in V1 still reflects the individual neuron input, and therefore allows some sort of rate or latency code (see also the left panel of Figure 4-4D). However, due to the uniform connectivity from V1 to V2, the V2 network is not sensitive to such details. Furthermore, the sensitivity to spatial orientation of stimuli coded on a spatial scale spanning several columns requires a genuine contribution of horizontal connections that complements local orientation computation in early visual cortex that is largely inherited from LGN. We use this simulation as a demonstration of the general concept of horizontal connectivity having a potentially significant effect during the sustained period.

A model of microsaccade-rhythmic modulation synchronization and coding in early visual cortex

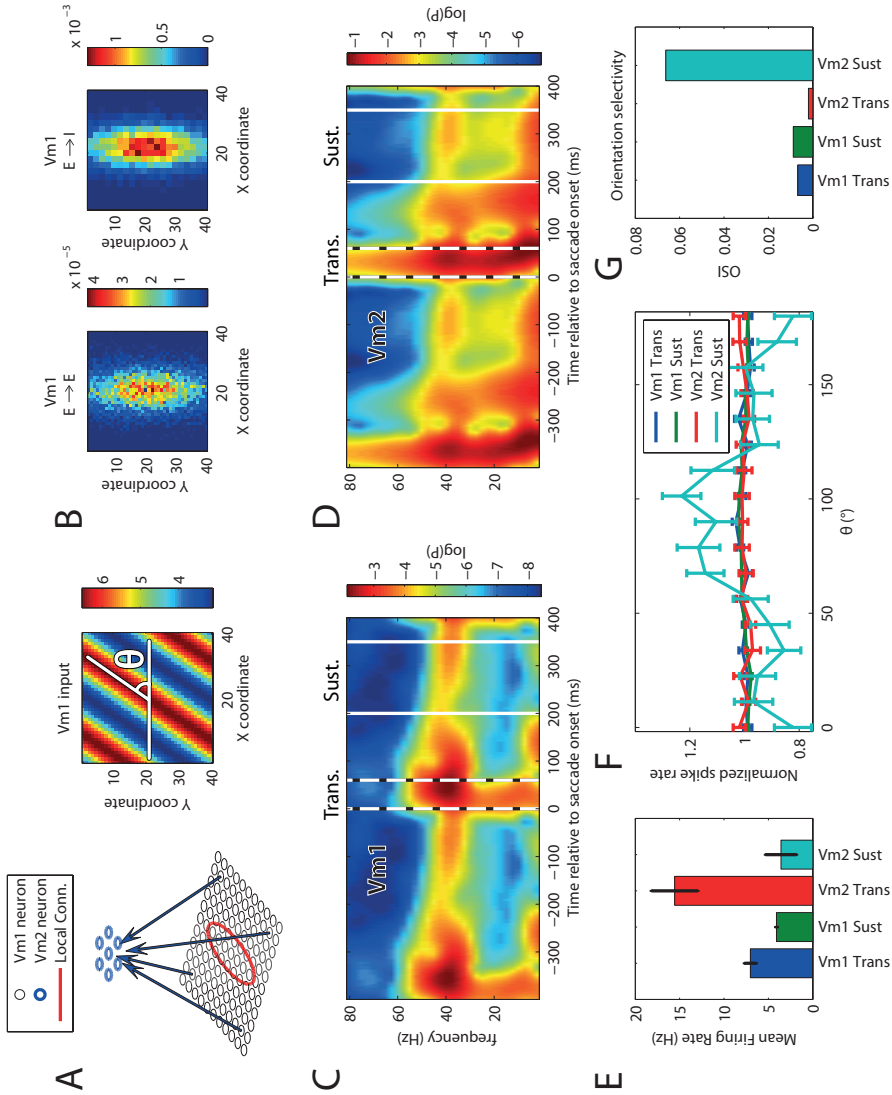


Figure 4-5. Set up of a V1-V2 model network with anisotropic connection patterns. **(A)** Left: Schematic representation of the network with its two sub-networks. Neurons in the first sub-network (V1; 40 × 40 E-neurons, 20 × 20 I-neurons) receive direct input and project to the second sub-network (V2; 100 E-neurons, 25 I-neurons) and to themselves. Neurons in V2 only project locally, i.e. there is no feedback to V1. The local connections in V1 are sampled from anisotropic Gaussians, illustrated by the red oval (see B). The feed-forward connections (from V1 to V2) and local connections in V2 are sampled from a uniform distribution. Right: an example of the direct input to V1. V1 received one of 16 differently oriented gratings. The orientation (θ) of the grating is illustrated by the white overlay. **(B)** The connections from the center excitatory neuron in V1. Left: connections to other excitatory neurons within V1. Right: connections to inhibitory neurons within V1. **(C,D)** Time-frequency representation of the

mean LFP power, locked to saccade onset. Average across the electrodes in V1 (C) or for the single electrode in V2 (D). The vertical lines indicate the borders of the transient (0 – 70 ms, dashed) and the sustained period (200 – 350 ms, solid white) that were used for analysis in E-G. (E) The mean firing rates for the two response periods in V1 and V2. Error bars denote standard deviation across the 50 microsaccades. (F) The modulation of spike rate (normalized by the orientation average) as a function of stimulus orientation during the transient and sustained periods in V1 and V2. Error bars denote standard error of the mean across the 50 microsaccades. (G) Orientation sensitivity in E quantified by calculating the orientation selectivity index (OSI, see methods).

We next turn to the effect of synchrony in the sustained phase on the information transfer between areas in the case of natural images. We ran V1-V2 network simulations employing isotropic connectivity within V1 and a convergent isotropic Gaussian connectivity between the two sub-networks (Figure 4-6A, top, and methods). The input to the V1 sub-network represented parts of a natural image (Figure 4-6A, bottom). Synchrony was once again uniform across our model V1 during the transient, but decayed over distance in the sustained phase (Figure 4-6B). To quantify the information transfer from V1 to V2 we calculated the average activity in excitatory V1 neurons just before an excitatory spike in V2, i.e. a spike triggered average (STA, see methods). Figure 4-6C and E show the resulting V1→V2 STA maps calculated for V2 spiking in the transient (left) and sustained periods (right). The STA maps should be understood as the effective (functional) receptive field (RF) of V2. Figure 4-6D and G illustrate why the effective RF of a V2 neuron can differ markedly from its anatomically-defined RF, which was isotropic Gaussian in these simulations (i.e. the connection pattern from V1 to V2).

Our simulations show that in the transient phase the STA strongly reflected the intrinsic V1 spike rates (set by the luminance values of the natural image pixels). This lead to highly biased effective RFs towards image regions of high input. In contrast, the right panel in Figure 4-6C indicates that during the sustained period, the produced STA maps were strongly biased by the gamma synchronization (Figure 4-6B). V1 neurons with similar spike rates (low detuning) were more likely to synchronize and were hence more effective in driving V2 neurons. Therefore, during the sustained period the spatial input similarity (homogeneity) within a natural image patch is a central component in shaping the effective RFs in V2. In Figure 6E-G we show an example where the region of high input strength coincides with high input homogeneity resulting in similar transient and sustained STA maps.

In summary, the neurons in V2 are mostly influenced by V1 neurons near the center of the feed-forward receptive field to these neurons (defined by their synaptic connectivity profile see Figure 4-6D,G). This influence is biased by local stimulus strength during the transient and by spatially homogenous input during the

sustained period. Note that in some cases neurons with a lower intrinsic firing rate have a stronger effect on the downstream population than those with a higher intrinsic firing rate. This occurs for image regions with low, nearly uniform intensity and consequently high neural synchrony (e.g. see the STA map in Figure 4-6C extending over the dark region, rather than the high-intensity light region). Thus, in the sustained period the interplay between stimulus and connection pattern causes a pattern of gamma synchrony that strongly influences the communication to the down-stream areas. Together this could cause the receptive field of down-stream neurons to change when going from the transient to the sustained period.

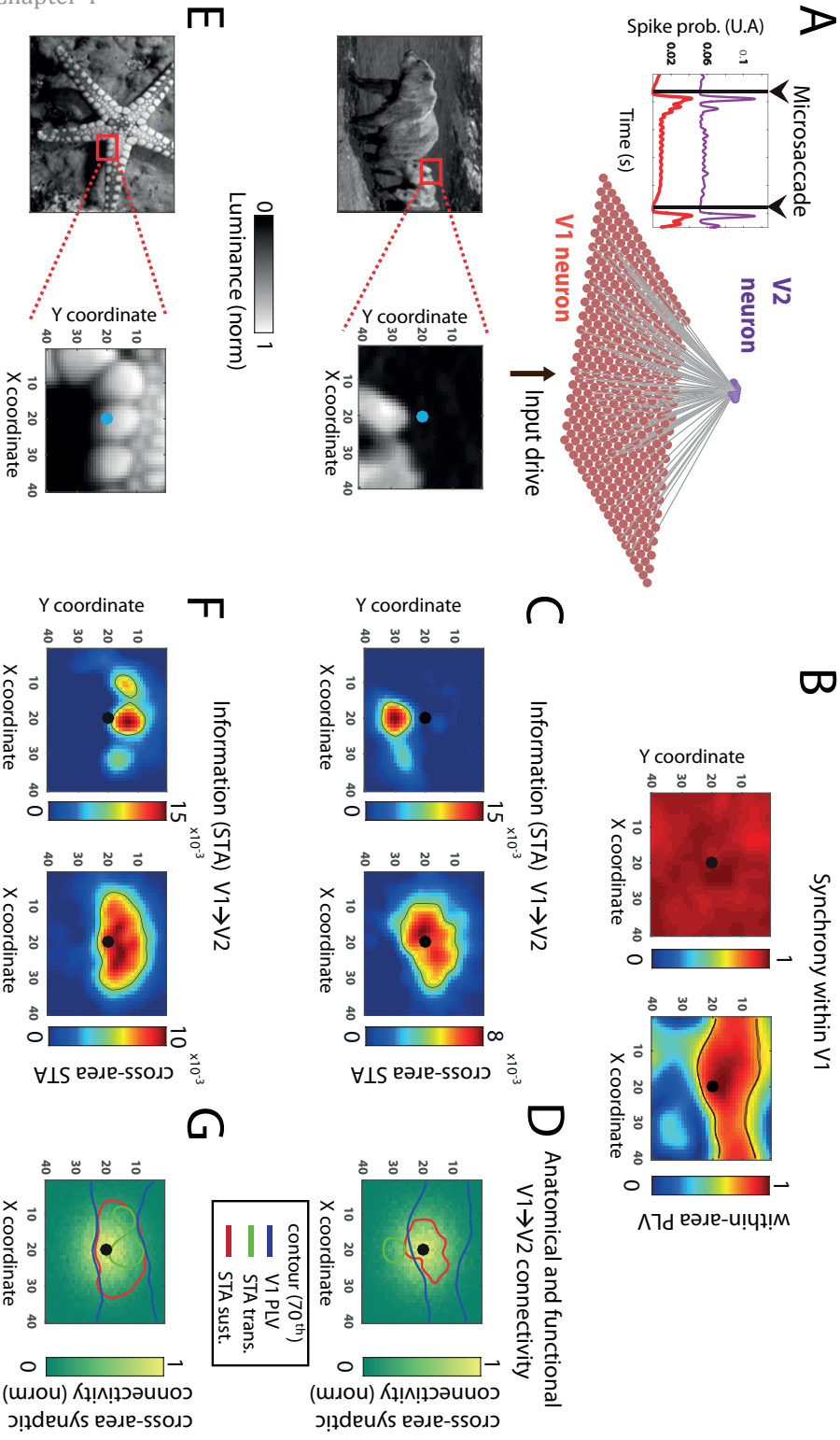


Figure 4-6. Microsaccade-dependent synchronization shapes information transfer to down-stream neurons. **(A)** Excitatory-inhibitory visual model network, receiving microsaccade modulated spatially-structured input derived from natural image luminance (bottom). The V1 network was unidirectionally connected to a down-stream V2 neuron. **(B)** The synchronization profile (measured by PLV) of the center V1 neuron to all other neurons in V1 is shown for the input in A. During the transient period, synchrony is high across the V1 network, whereas synchrony is local and anisotropic in the sustained period. Synchrony is high for neurons receiving similar input. **(C)** Information transfer of V1 neurons to V2 (quantified as $STA(V1 \rightarrow V2)$, see methods). (left), In the transient period, STA is high for neurons with strong input (and therefore high firing rate). (right) In contrast, in the sustained period the STA map shows high values for neurons with similar input. **(D)** Contour lines of PLV in V1 during the sustained period (see B) as well as for the STA from V1 to V2 (see C) overlaid on of the anatomical connectivity. The STA maps (green and red contour lines) do not strictly follow the synaptic connectivity profile (heat map). During the transient they are biased towards higher input. In the sustained period they are biased towards higher synchrony (PLV, blue contours). **(E)** The same simulation as in panel A, but now using a different stimulus image, where the center neuron in V1 is situated over a bright patch. **(F)** Similar to C, but for the simulation using the stimulus in E. This second stimulus leads to STA maps that are similar in both the transient (left) and sustained (right) periods. **(G)** Similar to D, but using the stimulus in E. With this stimulus, the STA maps show large amount of overlap in both the transient and sustained periods. This is caused by the fact that the neurons synchronizing to the center neuron are also the neurons with high input.

In the previous sections we have shown that in principle stimulus information could be coded through spike rate (Figure 4-6), synchrony (Figure 4-6) or phase (Figure 4-4D). Figure 4-7A-C visualizes these three coding schemes. The potential efficacy, estimated by mutual information (MI), of these schemes in the transient and sustained period is shown in Figure 4-7D-G. The STA between the excitatory spikes in V1 and the excitatory spikes in V2 was calculated for the transient (D,E) and sustained periods (F,G), similar to Figure 4-6C,F. This analysis revealed that our model network suggests different optimal mechanisms for information transfer for the transient and the sustained periods. In the transient phase, the firing rate is high and predictive of the STA. Besides this, the phase of firing also predicts the STA-estimate, corresponding to a latency code (Figure 4-7E, also see Figure 4-4D). In the sustained period, firing rates are lower and seem therefore less important for information transmission. By contrast, synchronous firing, is more relevant as indicated by the high MI between PLV and STA (Figure 4-7G). The right panels in Figure 4-7D and Figure 4-7F show that the phase distribution is broader and that there is an optimal phase (between -2 and -0.5 radians) in which STA is maximized. In summary, the transient and sustained modes of activity differ in the accuracy with which information could be transmitted. The transient is characterized by a rate and

latency code. In the sustained period, individual firing rate is less accurate, instead, efficient communication is best built on gamma synchrony and phase differences.

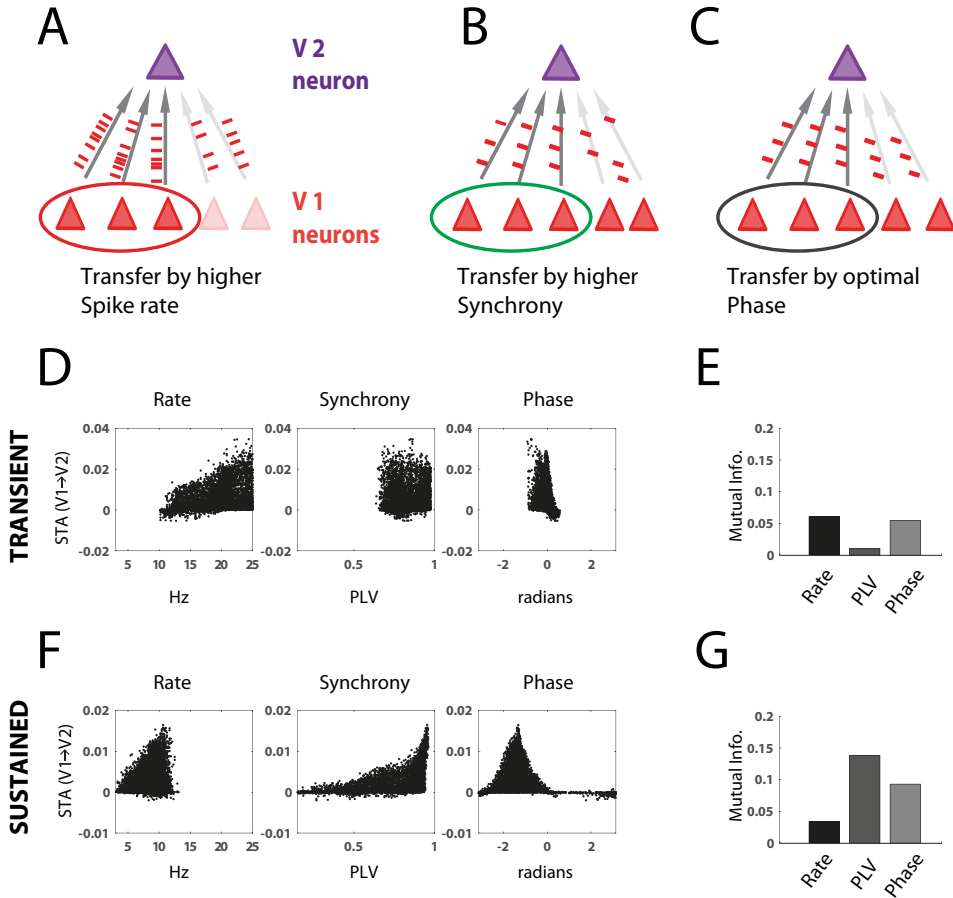


Figure 4-7. Information transmission (quantified by the STA, see methods) from V1 neurons to V2 neurons. **(A-C)** Schematic illustration of factors that could modulate the influence of a particular V1 neuron on a V2 neuron. We compare the information transfer in the transient and sustained period if the activation of V2 is mostly determined by higher spike rates **(A)**, local synchronization **(B)** or optimal phase differences **(C)** in V1. **(D)** Scatter plots from simulations using 100 different natural images. STA is plotted as a function of: (left) spike rate, (middle) synchrony, (right) gamma phase difference. Note: since the transient is relatively short, “phase” is equivalent to spike latency relative to the saccade onset. **(E)** We used (normalized) mutual information to quantify how much of the variance in STA between V1 and V2 neuron is explained by the V1 neuron’s spike rate, synchrony and phase. In the transient period the transfer entropy was best explained by spike rate and phase. **(F)** Similar to D, but for the sustained period instead of the transient. **(G)**. Similar to E, but the sustained period was analyzed instead of the transient. Here the STA is mainly explained by synchrony

and phase. This shows that synchrony-dependent organization in the sustained period has strong effects on feedforward information transmission.

4.4 Discussion

4.4.1 Summary

In this study, we investigated the impact of microsaccades on neural network synchronization and the implication for information transfer using a computational model that was constrained by data from recordings in monkey visual cortex. The network simulations showed oscillatory dynamics locked to microsaccades, closely replicating those recorded in monkey V1 (Figure 4-2) [41], [147]. Our network simulations suggested to distinguish transient (0-100 ms) and sustained (100ms onwards) post-saccade periods, which are characterized by different modes of activity. In the transient period, neural synchrony is high across large cortical areas, allowing for feed-forward processing of the stimulus based on both firing order (latency code) as well as rate (Figure 4-4, Figure 4-7). In contrast, oscillatory synchronization in the later sustained period is more local and, besides sensitive to the stimulus, is also modulated by local (recurrent) connection patterns (Figure 4-4). This influence of local connectivity is mostly reflected in synchrony and relative firing phase (Figure 4-5, Figure 4-7). This suggests that the transient activity reflects fast initial feed-forward processing of (raw) visual information from the retina and LGN, whereas the sustained activity reflects context-dependent local computation and possibly the processing of finer visual detail.

4.4.2 *Gamma synchronization is nested within a microsaccade rhythm*

In line with experimental observations in monkey V1 [41], [147], [227], we observed that the continuous occurrence (every 200-500ms) of saccades and microsaccades during normal awake visual processing prohibit the network dynamics from being stable beyond saccades. Instead, they are continuously perturbed even during fixation behavior. This explains why gamma synchronization has been reported as being transient or “bursty” in the visual cortex [242], [243], similar to in prefrontal cortex [244] and hippocampus [85]. Approximately

stationary oscillations occur only for a short time within the inter-saccade intervals (~150-400ms after the saccade onset).

The short-lived nature of gamma synchronization has important implications for how it might operate and how it should be analyzed [217]. For example, studies testing the role of gamma in vision and higher cognition should account for the short-lived nature of gamma and separate it from transient dynamics that likely also have power in the gamma-band. As we have shown here in the case of microsaccades, these transients can occur continuously in awake animals and can be generated endogenously without the need for an external trigger (such as stimulus onset).

4.4.3 Transient broadband synchrony and narrow-band gamma synchrony rely on different coordination mechanisms

Neural synchrony has often been divided into evoked transient synchrony and induced narrow-band synchrony [245]. The former is precisely locked to an event (e.g. stimulus onset), associated with broadband synchrony and persists only shortly in time after the event, whereas the latter occurs with some time delay after an event, and is not phase-locked to it [246]. This induced activity is often associated with more narrow-band synchrony (clear bands in the Fourier spectrum) and persists for longer time (e.g. till the next saccade/microsaccade) [241], [247].

Transient broadband synchrony has been widely observed after stimulus onsets [241], after saccades [149] as well as after microsaccades [147], [211].

A critical feature of transient synchrony is that the event that triggers it affects many neurons in a cortical area (causing a 'common reset'). In the case of microsaccades, their occurrence will affect many neurons in V1 at the same time, independent of how they are synaptically connected with each other. This leads to high and widespread synchrony over a cortical area that are locked to stimulus or microsaccade onset [147], [149], [183], [248], [249]

Because transient synchrony emerges through a common reset impulse coming from outside the network, it often is a well-defined phenomenon with easy experimental access (e.g. stimulus onset, or saccadic eye movement). It is also robust in the sense that its presence does not depend critically on particular stimulus parameters. For example, stimulus-onset transient synchrony (called the visual evoked potential, VEP) can be observed reliably across different stimulus conditions and natural images [250]. However, details of the transient response can depend on stimulus properties. The best documented parameter is its latency [251]–[253]. This

reliable effect on latency of sensory variables during transient response has been suggested to be essential for rapid initial visual processing [148], [223], [225], [254].

Transient synchrony decays quickly after stimulus or (micro)saccade onset and is gradually replaced (in many cases) by narrow-band rhythmic synchrony. Here we will focus on gamma-band synchrony that is prevalent in cortical V1. It has been shown that narrow-band gamma emerges locally within a cortical patch [37], [100], [255] and depends critically on neural interactions (particularly on interneurons [38], [39]). This is further supported by observations that V1 gamma synchrony is confined by the spread of horizontal connectivity [45], [256]–[258]. In addition, gamma synchrony is highly dependent on stimulus input parameters and their spatial patterns [40], [42], [45], [257]. This explains the highly variable characteristics of gamma synchrony (including the absence thereof) reported in natural viewing conditions [227], [259].

In contrast to the transient synchrony that relies on a common reset mechanism, the following sustained gamma synchrony is achieved through mutual phase adjustments of neural groups relying on mutual intracortical connections. Theoretically, the gamma synchronization process can be captured by the theory of weakly coupled oscillators [228], [260]–[263]. Recent evidence supports that narrow-band gamma rhythms operate according to these principles (Akam et al., 2012; Lowet et al., 2016b). The neural network simulations in this study are in line with this theory as well.

All of this has important implications for the role of gamma synchrony in visual coding. First, gamma synchrony depends strongly on intracortical connectivity and hence can filter and transfer information that is implicitly encoded in connectivity patterns (for example orientation-tuned horizontal connectivity, Figure 4-5). Second, gamma synchrony strongly depends on (spatial) properties of the sensory input (e.g. contrast difference) and hence synchrony (or absence thereof) can directly code for important patterns occurring in the sensory world [50].

Hence, the highly variable nature of gamma synchrony, enables gamma rhythms to be informative of stimulus details [264] and provides it with unique properties not shared by transient synchrony.

4.4.4 Cross-area neural communication is shaped differently by the two microsaccade-linked synchrony regimes

An important issue for the relevance of gamma rhythmic spike activity for brain processes [100], [255] is whether receiver neurons are able to sense synchronous and fast rhythmic input.

Several properties of brain networks indicate that gamma rhythmicity will affect neuronal spiking behavior. Neurons in the brain are heavily interconnected [265], [266] and a single synaptic potential will rarely generate a spike and hence coincidence of multiple synaptic potentials is required [13]. This fits with observations that precise spike timing can reflect a neural code [84], [267]–[269] and is critical for plasticity [270]–[272].

These properties support the notion that neural synchrony strongly impacts cross-areal communication. Direct experimental evidence for this impact has been provided for connections between LGN and V1 [273] and between V1 and V2 [274]. In line with this, our network simulations show (Figure 4-5, Figure 4-7) that synchrony in the sending population can be beneficial, if not necessary, for efficient interareal communication.

We found that during the transient period, cross-areal information transfer was modulated mainly by spike latency (phase) and firing rate, whereas during the later sustained period, cross-areal information transfer was further shaped by gamma synchronization in the sending region.

Related to this is the concept of a neuron's receptive field (RF). Figure 4-6 shows that in the sustained period the RF of our model V2 (defined here as the neurons in V1 that strongly influence V2) is different from the RF in the transient period. The RF in our model V2 during the sustained period depends on stimulus properties as well as local connectivity. These findings are in agreement with experimental evidence for stimulus-dependent RFs [275], [276]. This calls for a dynamic view of RFs in which the sensitivity to the visual field is importantly shaped by synchrony of up-stream neurons.

Note that our model does not include cross-area feed-back connections or top-down signals. Experiments in monkey V1 in the context of figure-ground segregation [277] suggest that feedback signals from other cortical or subcortical areas arrive >100 ms after stimulus onset. The cross-area feedback signals related to the new image on the retina after a saccadic eye movement will likely follow a similar timescale. This would mean that cross-area feed-back signals will add to the influence of the horizontal connections during the sustained period and can have an additional influence on the RF.

4.4.5 Model caveats

We feel it is important to note some limitations of our model. First, parameters such as input strength, neural noise, connectivity strength are not explicitly constrained by experimental data. This means that predictions are of a qualitative nature. Our model of visual cortex lacks synaptic interactions with long time-scales, such as GABA-B and NMDA synapses or synaptic plasticity. How exactly these slower channel dynamics interact with the microsaccade-dependent activity studied here, needs further investigation.

It is not well understood whether the observed changes in neural activity locked to a saccade are due to the rapid visual input change on the retina or due to a corollary discharge (efference copy, [206], [208], [278], [279]). Our model makes no attempt to disentangle these two possibilities. Similarly, we are unaware of the cause of the gradual decrease of the gamma frequency over time during the sustained period (here modelled as a decrease in input drive, see Figure 4-2). It is possible that these dynamics are the result of an accumulation of adaptation effects in the retina, LGN and the cortex itself [280], [281].

Finally, the predictions from our model are not specific with regard to cortical layers. Others have suggested that feed-forward, feed-back and horizontal connections mainly project to different layers [277], [282], [283]. This could mean that the transient and sustained activity modes are separated in space (cortical depth) as well as time.

In Figure 4-5, our model is able to display some sort of orientation preference that is not entirely congruent with established models for the emergence of orientation selectivity [104], [284]. Our model V1 units were insensitive for orientation, selectivity only emerges in V2 as a consequence of connectivity within V1. In reality, neurons in V1 [126], LGN [284], [285] and even in the retina [286] have been shown to exhibit orientation selectivity. Therefore the results in Figure 4-5 should not be interpreted as a good model for orientation selectivity in striate cortex, but rather an example of how horizontal connections and synchrony can influence network processing in the sustained period. Note, however, that orientation selective cells have been shown to preferentially project along one axis in retinotopic coordinates not unlike the connection pattern in Figure 4-5A [106]. Effects like those in Figure 4-5 can conceivably contribute to emergence of orientation selectivity along the visual pathway [284]. Our model results predict that this effect may change orientation tuning down-stream of area V1 in the sustained period compared to the transient.

4.4.6 Beyond striate cortex

Our model is based on processing in early visual cortex. One may ask whether a similar mechanism of rhythmic switching between a transient and sustained mode of neural activity may exist in other areas in cortex. It is possible that other early sensory areas may exhibit similar dynamics, especially in the context of Active Sensing [200]. One example is sniffing behavior when considering olfaction. Sniffing is a rhythmic (3-7 Hz) activity responsible for active sampling of olfactory information. This sniffing rhythm is reflected in neural responses [199], [234]. Similarly, rhythmic whisker movement has been shown to actively sample somatosensory information in a rhythmic manner [198], [236]. Like the microsaccades in our model, these sampling actions (i.e. sniffing or whisking) will cause transient activity in the relevant sensory cortex. In the interval between the sampling actions there would be time for the neural activity to show the sustained dynamics, similar the sustained activity during the inter-saccade interval in early visual cortex.

A trigger for rhythmic switching between sustained and transient modes could also be provided by endogenous slow oscillations in the delta-theta range (1-10 Hz, [21]). This could enable rhythmic switching in cortical and sub-cortical areas that lack a direct rhythmic input resulting from active sampling (i.e. non-sensory areas). The phase of these slow rhythms has been shown to modulate neural activity [85], [287], possibly related to an attentional rhythm [157], [220], [221], [235].

Taken together, our work outlines a fundamental rhythmic switching mechanism of feedforward and local processing during active sensory processing that might well generalize to other sensory modalities and animal groups.

Chapter 5.

Discovering recurring patterns in electrophysiological recordings

Adapted from:

B. Gips, A. Bahramisharif, E. Lowet, M. J. Roberts, P. de Weerd, O. Jensen, and J. van der Eerden, “Discovering recurring patterns in electrophysiological recordings,” *J. Neurosci. Methods*, vol. 275, pp. 66–79, Jan. 2017.

Abstract

Fourier-based techniques are used abundantly in the analysis of electrophysiological data. However, these techniques are of limited value when the signal of interest is non-sinusoidal or non-periodic.

We present sliding window matching (SWM): a new data-driven method for discovering recurring temporal patterns in electrophysiological data. SWM is effective in detecting recurring but unknown patterns even when they appear non-periodically.

To demonstrate this, we used SWM on oscillations in local field potential (LFP) recordings from the rat hippocampus and monkey V1. The application of SWM yielded two interesting findings. We could show that rat hippocampal theta and monkey V1 gamma oscillations were both skewed (i.e. asymmetric in time), rather than being sinusoidal. Furthermore, gamma oscillations in monkey V1 were skewed differently in the superficial compared to the deeper cortical layers. Second, we used SWM to analyze responses evoked by stimuli or microsaccades even when the onset timing of stimulus or microsaccades was unknown.

We first validated the method on simulated datasets, and we checked that for recordings with a sufficiently low noise level the SWM results were consistent with results from the widely used phase alignment (PA) method.

We conclude that the proposed method has wide applicability in the exploration of noisy time series data where the onset times of particular events are unknown by the experimenter such as in resting state and sleep recordings.

5.1 Introduction

Neural oscillations are an intrinsic property of a working brain. Their amplitude reflects whether the activity of neurons in a particular brain region synchronizes or desynchronizes, whereas their phase might provide information on the communication between brain regions [51], [52], [128]. Fourier-based approaches are commonly used to extract phase and amplitude information of neurophysiological data. However, there are no *a priori* reasons for neuronal oscillations to be sinusoidal. In such cases higher harmonics of the base frequency are required to fully describe the repetitive pattern. Therefore, Fourier-based descriptions of data in terms of power and phase in a relatively narrow frequency band may not adequately characterize the data. The importance of non-sinusoidal waveforms is discussed in many other works. It has been suggested for example that the peaks and troughs of oscillations have different functions [34]–[36]. This was supported by Mazaheri and Jensen [288], who found that the peaks are more strongly modulated than the troughs in human occipital alpha oscillations (~ 10 Hz). Moreover, Belluscio and colleagues [86], investigated the shape of rat hippocampal theta oscillations (~ 8 Hz). They showed that hippocampal theta oscillations are sawtooth-like rather than sinusoidal waveforms. This sawtooth-like shape may point to a global signal temporally ordering neuronal firing along the long down-going flank [35], [69], [158]. As the amplitude of the rat hippocampal theta oscillations is very high relative to the background noise, the skewness of the sawtooth shape could be demonstrated after applying a simple band-pass filter (1–80 Hz) and detecting local maxima and minima. This might not be an option when the signal-to-noise ratio is low, as is the case for example in the non-invasive MEG or EEG recordings. It would be useful to have a method that identifies recurring patterns (i.e. motifs) even if they are non-sinusoidal, and for a broad range of signal-to-noise ratios. Here, we propose a sensitive and broadly applicable method for discovering recurring patterns in time series data which we call sliding window matching (SWM).

Methods often used to deal with non-stationary signals are time-frequency analyses such as short time Fourier transforms or some sort of wavelet transform [289]–[291]. These methods, however, generally still work within the Fourier framework of sinusoidal basis functions, so they tend to share some of the disadvantages mentioned above.

Other methods have been proposed such as empirical mode decomposition [292]–[294] or those based on single spectrum analysis [295]–[299]. These methods attempt to decompose the signals without using sine and cosine basis functions. They tend to assume that the components are periodic, albeit that the frequency does not have to be fully constant over time. Brain signals, however, may often not be periodic, but instead appear and disappear on unpredictable intervals. Another popular method is Matching Pursuit [300]. This method finds components in the data based on an over complete dictionary of basis functions. Matching pursuit does not require periodicity. Instead, the difficulty with matching pursuit lies in the choice of basis functions in the dictionary. Most common matching pursuit application use dictionaries with windowed sine waves, bringing with them some of the same problems as normal Fourier analysis mentioned above.

In this paper we will show that SWM is well-suited for detecting repeated and non-sinusoidal components in recorded signals. These components can be periodic, such as neural oscillations, or non-periodic such as evoked potentials. We will demonstrate its capabilities by characterizing (periodic) oscillatory LFP recordings in rat hippocampus and monkey V1 and we will compare it to a more commonly used short-time Fourier transform method that uses wavelet convolution. Secondly we will show that SWM can detect saccade and stimulus evoked potentials in monkey V1. In summary we show that SWM is effective in discovering not only motifs with known shape that occur at a given time relative to a known trigger event (or periodically) but also in discovering motifs with unknown shape and occurring at unpredictable moments in the time series.

5.2 Methods

We present a new algorithm that finds repeating patterns in a dataset that we call *motifs* (see Figure 5-1 for an illustration). All analyses were performed using MATLAB (MathWorks).

5.2.1 Sliding window matching

The SWM algorithm positions windows over the data in such a way that the contents in all windows are maximally similar. It does this by sliding the windows separately across the data using a Monte-Carlo approach until their contents are maximally similar (Figure 5-1, also see Algorithm 1). In doing this, the algorithm will find patterns (motifs) that are repeated in the data. It is important to note that the motif

locations do not have to be periodic. I.e. the temporal spacing between the motifs in the data can be variable.

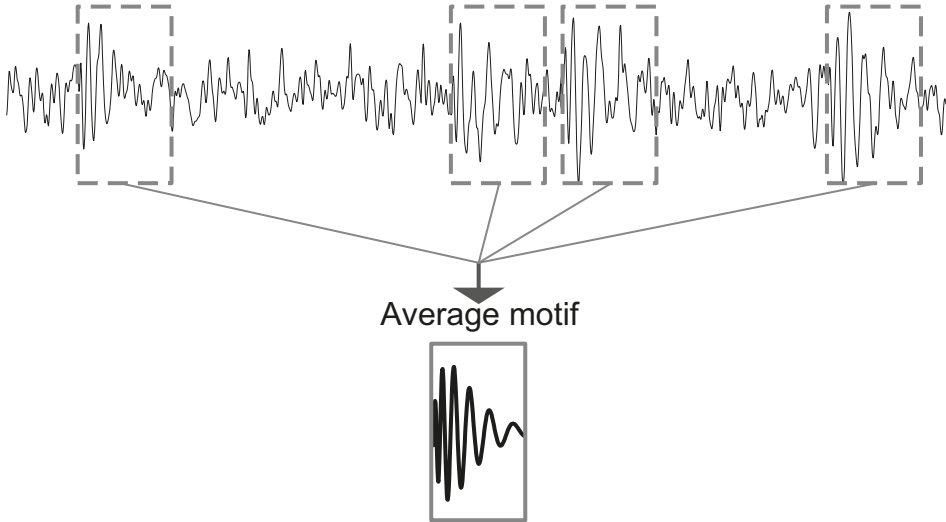


Figure 5-1. Conceptual illustration of the SWM algorithm and the concept of motifs. SWM tries to find recurring patterns (i.e. motifs) in the data (top trace) by sliding windows (dashed grey rectangles overlaid on the data trace) across the time dimension. The windows are moved randomly and the contents of the windows are compared to the mean across all the windows (average motif, bottom). When the SWM algorithm has converged, all windows contain a pattern that looks maximally like the average pattern of all windows. In this way, the motif and its occurrences in the data have effectively been detected.

5.2.1.1 *The cost function*

The SWM algorithm works by minimizing a cost function (eq. 5.1) evaluating the similarity of all windows. When the minimum is found, a motif, i.e. the average signal in the windows, has been identified. N is the number of windows and L is the window length:

$$J = \frac{1}{2(N-1)} \sum_{i,j=1}^N d_{i,j}^2 \quad (5.1)$$

$$d_{i,j}^2 = \frac{1}{L} (\mathbf{z}_i - \mathbf{z}_j)^T \cdot (\mathbf{z}_i - \mathbf{z}_j) \quad (5.2)$$

$$\mathbf{z} = \frac{\mathbf{x} - \mu_x}{\sigma_x} \quad (5.3)$$

In equation 1, i and j are window indices and the sum is over all pairs of windows. The superscript T in equation 2 indicates the transpose of the difference vector $\mathbf{z}_i - \mathbf{z}_j$. The more similar the windows are, the lower the variance across them and therefore the lower the cost J . The z-scoring (eq. 5.3) is done for every window individually to counter signal drift and amplitude fluctuations. Additionally, it ensures that the algorithm does not converge to periods of low-amplitude signals dominated by noise. Without this normalization, cost will be lowest in the windows only containing background noise, i.e. without any additional variance caused by any motif which has greater amplitude than the background noise. The value J measures the correlation among the signals in the windows, i.e. the higher the correlation coefficients between all windows, the lower the cost (see Supplemental material).

5.2.1.2 *Minimizing the cost function*

Our algorithm uses a Markov Chain Monte Carlo (MCMC) sampling technique [301], [302] to minimize J (see Algorithm 1). MCMC sampling techniques are often used to estimate probability density functions [303]. It is important to note that we use MCMC sampling strictly for finding the global minimum of the cost function J and as such we do not use it in the context of Bayesian statistical models [304]. In most iteration steps a single window is moved to a random new position and the move is accepted if it decreases the cost J . If the cost increases with the new position, it is accepted only with a certain probability. This acceptance probability decreases with the change in cost (Algorithm 1, line 8: $p_{\text{accept}} = \exp(-\Delta J/T)$) where T denotes the ‘temperature’ factor. If T is high, window shifts that increase the cost (i.e. away from the nearest minimum) are more likely to be accepted. In some iterations the algorithm moves all windows at once in the same direction with the same step size (lines 17-25 in Algorithm 2 in Appendix A). The cost associated with the new window positions is evaluated and the move is again accepted with a probability based on the change in cost function. This makes it possible for the algorithm to jump to a different minimum with a low cost that is hard to reach by way of the other MCMC steps consisting of a change of a single window position.

To avoid that the minimization algorithm gets stuck in local minima, we used a Parallel Tempering [305] strategy to find the global minimum of the cost function J (see Algorithm 2 in Appendix A). This algorithm effectively minimizes at several temperatures in parallel. Therefore the method is computationally more demanding than straightforward isothermal minimization or simulated annealing [306]**. Using

** Note that unlike in simulated annealing, the temperatures in parallel tempering remain fixed. They are not decreased across iterations.

information of these different temperatures, the algorithm can escape from local minima. The efficiency of the method to find the global minimum implies that the final solution is independent of the initial window locations.

```

Initialization:
1  Define window length ( $L$ ) and minimal window spacing ( $G$ ).
2  Initialize window positions  $X_1, X_2, \dots, X_N$ .
   These window positions are separated by twice the
   minimal window spacing, i.e.  $X_n - X_{n-1} = 2G$ . So the
   total number of windows ( $N$ ) depends on the length of
   the data time series,  $L$  and  $G$ .
   Alternatively, for investigating evoked responses, a
   number of windows per trial can be given instead.
3  Calculate initial cost  $J_0$  (eq. 5.1) ;

4  while  $i < \text{maxIterations}$  do
5      Pick a random window position  $X_n$ 
6      Find a new allowed position  $X_n'$  for the window by
       moving it randomly along the time axis. (allowed
       positions: at least  $G$  separated from the preceding
       and following window);
7      Calculate the cost using  $X_n'$ ,  $J'$ , and with this
       the change in cost function  $\Delta J = J' - J_{i-1}$ 
8      Calculate acceptance probability  $p_{\text{accept}} = \exp(-\Delta J/T)$ 
9      if  $\text{rand}(0,1) < p_{\text{accept}}$  then
10         Accept change:
11          $J_i \leftarrow J'$ 
12          $X_n \leftarrow X_n'$ 
13     else
14         Do not accept change:
15          $J_i \leftarrow J_{i-1}$ 
16     end
17      $i \leftarrow i+1$ 
18 end

```

Algorithm 1. General algorithm for finding recurring shapes, i.e. motifs, in electrophysiological data using a MCMC technique.

5.2.1.3 Parameters and output

The output of the algorithm is the window position vector \mathbf{X}_q . When the algorithm converges, the output vector \mathbf{X}_q and the motif found may still depend on number of windows N , window length L and minimal window spacing G (see Figure 5-2A). For example, when the data contains multiple oscillatory components of different frequencies, L of 100-150 ms may find the alpha-band oscillations (8-12 Hz) if present, whereas longer L will lead to waveforms in the theta (4-8 Hz) or delta (1.5-4 Hz) range. When studying high-frequency phenomena in electrophysiological data such as the shape of gamma oscillations (see Figure 5-7), it is recommended to use high-pass filtering below the frequency of interest before applying SWM, to make sure that the algorithm will not converge to a low-frequency motif with large signal-to-noise ratio.

Evoked responses in electrophysiological recordings generally have a higher signal-to-noise ratio than neural oscillations and are expected to have low variability across occurrences. Therefore, SWM tends to converge to evoked responses if their timescale is similar to L , and the number of windows (N , the length of vector \mathbf{X}_q) is roughly equal to or lower than the number of evoked responses in the data. It should be realized that the motif may be placed at an arbitrary position within the window, especially when L is not exactly equal to the length of the evoked response (Figure 5-2B). The guard parameter G is the minimal distance between two window positions. If a new window location is less than G removed from a neighboring window (Figure 5-2A), the move is not accepted. This ensures that the algorithm will not stack all windows on the same piece of data, which would lead to a zero cost. G is generally best chosen to be of similar size to the motif one is trying to find, i.e. large enough that the windows will not have too much overlap, but small enough that they have enough space to be positioned over the data.

It is important to note that the precise values for N , L and G are not crucial for the motif (shape) as long they are chosen in the order of magnitude as discussed above (i.e. estimated number of occurrences for N and estimated length of the motif of interest for L and G)

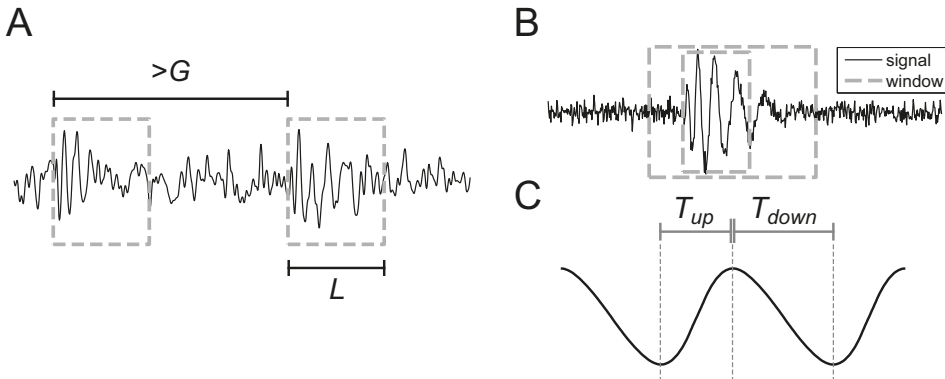


Figure 5-2. (A) L is the length of the windows, whereas G determines the minimal distance between two successive windows. In the case of having multiple components in the data, the choice of L affects the results. Since having noise in the data increases the cost (eq. 5.1-5.3), SWM will converge to a motif that has high signal to noise ratio across the entire window and length of at least L . (B) Setting the window length to different values can cause the main motif features to be positioned differently within the window. The smaller window may tightly hug the motif, but the larger window may contain the motif in different positions within it. (C) T_{up} and T_{down} are the temporal duration of the up-going and down-going flank used to calculate the skewness index (eq. 5.4). In the case of a perfect sawtooth waveform, either T_{up} or T_{down} approaches the limit of 0.

5.2.2 Analysis of the motifs

5.2.2.1 Skewness Index

We define the skewness index (SI) in equation 4 (see Figure 5-2C), where T_{up} is the time from trough to peak and T_{down} is the time from peak to trough.

$$SI = \frac{T_{up} - T_{down}}{T_{up} + T_{down}} \quad (5.4)$$

The SI of a temporally symmetrical waveform (e.g. a sinusoid) is zero, whereas the SI of a sawtooth fully skewed to the left or the right approaches the limits of -1 and 1 respectively.

5.2.2.2 Statistics

Since individual time-windows are too noisy for a reliable estimation of T_{up} and T_{down} , we used a bootstrap approach [116] to assess the accuracy of the measured skewness index (SI). Estimation of mean SI and standard error was done by generating new average motifs by sampling with replacement N windows from the N windows found by either the SWM or the PA algorithm. This was done 1000-fold to yield a probability distribution for the SI . Values for T_{up} and T_{down} are discrete due

to the fixed sampling rate of the original signal; this therefore leads to discrete values of the SI. However, bootstrapping techniques require a continuous measure. To overcome this, the motifs are interpolated using cubic spline interpolation to a sampling rate of 100 kHz, giving smooth probability distributions of the SI. Standard errors of the mean SI are calculated from these probability distributions.

5.2.3 Validation

In order to validate our SWM method and to illustrate its potential, we compared its results with those of the established phase alignment (PA) method [307]. With both methods we identified motifs in synthesized data as well as in empirical data from rat hippocampus and monkey V1.

5.2.3.1 Phase-alignment method

With PA we mean a method of cutting out and aligning short sections of a signal according to instantaneous phase in a predefined narrow frequency band.

We performed a complex Gabor wavelet (eq. 5.5) convolution [308] to calculate a time-resolved estimate of the phase and amplitude at the frequency of interest (f_0).

$$w(\tau) = \frac{1}{\sqrt{2\pi\sigma^2}} \exp\left(-\frac{\tau^2}{2\sigma^2}\right) \exp(-i2\pi f_0 \tau) \quad (5.5)$$

5.2.3.2

In the current work we applied a wavelet with bandwidth of $1/(2\pi\sigma) = 2$ Hz. Similar to the SWM algorithm, windows with a length of about $1/f_0$ can be defined, centered at the same instantaneous phase in the frequency band centered at f_0 . From the set of aligned windows, the ones with high instantaneous amplitude can be selected to extract the motifs with putatively highest signal-to-noise ratio. For our purpose of validating SWM based on PA, we extracted the windows centered on the peak of the oscillation waveform (phase = 0). Also we extracted the same number of windows in the PA and in the SWM analyses of each data set.

5.2.3.3 Simulated data

Two hundred time series (i.e. trials) of 1 s and a sampling rate of 1 kHz were generated containing pink (1/f) noise together with a 10 Hz periodic sawtooth signal (Figure 5-3A) that acted as the motif of interest. The signal to noise ratio (SNR) of the simulated data shown in Figure 5-3 and Figure 5-4 was calculated as the ratio between the time-domain variances of the isolated noise and the sawtooth signal.

The pink noise was generated by applying an inverse Fourier transform to a spectrum with amplitudes equal to $1/f$. In order for the amplitude to not diverge at low frequencies, the pink spectrum is cut off below 1 Hz. The amplitudes in the spectrum were then multiplied by a signal-to-noise factor to make the noise stronger or weaker relative to the sawtooth signal (see Figure 5-3B). The phase for every Fourier coefficient was randomly assigned a value between $-\pi$ and $+\pi$. In this manner the artificial signal had characteristics similar to experimental recordings: most notably the $1/f^2$ shape of the power spectral densities found in the human extracranial scalp recordings [309]–[311] and animal intracortical recordings [312], [313].

5.2.3.4 *Rat hippocampus*

The recordings used in this study were previously included in two other studies, and data collection methods were described in detail previously [314], [315]. In brief: electrodes were implanted in the hippocampal area CA1 and the hippocampal fissure of three male Long-Evans rats to record the local field potential (LFP). The LFP recordings were made while the rats were freely moving around in their individual cages (~ 40 cm \times 40 cm \times 40 cm) built from clear acrylic and containing enrichment materials (e.g., plastic balls, cardboard tubes, and wooden blocks). Rats were allowed to recover from surgery for at least 1 week prior to data collection. During the data collection period, rats were placed on a food deprivation regime that maintained them at $\sim 90\%$ of their free-feeding body weight. All experiments were conducted according to the United States National Institutes of Health Guide for the Care and Use of Laboratory Animals under a protocol approved by the University of Texas at Austin Institutional Animal Care and Use Committee. The data was acquired with a sampling rate of 2000 Hz. Around 10 minutes of continuous data were analyzed from each rat.

5.2.3.5 *Monkey V1*

The exact dataset has not been published before, but was recorded in a setup similar to the one used in previous work by Roberts et al. [40]. In short: in the experimental setup, a monkey sat in a dark room with its eyes directed towards a computer screen. After one second of fixating on a central dot on a grey screen, a square-wave grating of variable orientation appeared in the para-foveal vision of the monkey. The monkey had to detect a change in the color of the fixation spot and report it by making a saccadic eye movement to a target. The onset of the color change was variable and the final saccade was not included in the data that are analyzed in the present work. During this experiment the local field potential in the primary visual

cortex of the monkey was recorded at different depths (16 contact points with 150 μm spacing). The data was recorded with a sampling rate of 1000 Hz. Eye position was recorded using an infrared camera system (Thomas Recording) with 240 Hz sampling. In total, 402 trials were recorded. All procedures were in accordance with the European Communities Council Directive 1986 (86/609/EEC) and in EU directive 2010/63 EU as well as approved by the local ethics committee (Radboud University Dier Experimenten Commissie). Following initial training, the monkey was implanted with a titanium head holder (Crist Instrument) and a recording chamber (Crist Instrument) above V1/V2 under general anesthesia and sterile conditions. In a second surgery, after further training, a craniotomy was made above V1/V2.

5.3 Results

5.3.1 Characteristics of neuronal oscillations

SWM can be applied to identify the wave-shape of non-sinusoidal oscillations. We used SWM first on synthetic data and compared it to the phase alignment (PA) method. After this, the SWM algorithm was applied to experimental rat and monkey recordings to assess the skewness of rat hippocampal theta waves and monkey visual induced gamma.

5.3.1.1 *Detecting the shape of oscillatory signals in simulated data*

Simulated data with a periodic sawtooth function embedded in $1/f$ noise was constructed (Figure 5-3A and B, different SNR values are coded by color. Blue: no noise; purple: 0.1; red: 1.0, see section 5.2.3.3). Figure 5-3C shows the average signal as found by PA using a complex Gabor wavelet centered on $f_0 = 10$ Hz with a bandwidth of $1/(2\pi\sigma) = 2$ Hz (eq. 5.5). Figure 5-3D shows the motif found by SWM using a window length of $L = 200$ ms. Both the PA and SWM approach identified the periodic sawtooth shape without noise (Figure 5-3C, D; blue trace), with PA even returning the exact sawtooth when $\text{SNR} \rightarrow \infty$. In PA a stronger bias towards sinusoidal motifs was found: the motifs found at lower SNR values (red and purple traces in Figure 5-3C-D) by using PA (Figure 5-3C) are much more sinusoidal than those found by SWM (Figure 5-3D). Quantitatively this is shown in Figure 5-4. We varied the SNR and applied both PA and SWM to find the sawtooth motif and determine its skewness (see section 5.2.3 and Figure 5-2C). The addition of noise decreased the measured skewness index of the mean sawtooth shape in all cases.

Note however that SWM yielded skewness estimates close to the noiseless value for SNRs as low as 0.2, whereas PA still gave a ~25% reduction at SNR = 1.

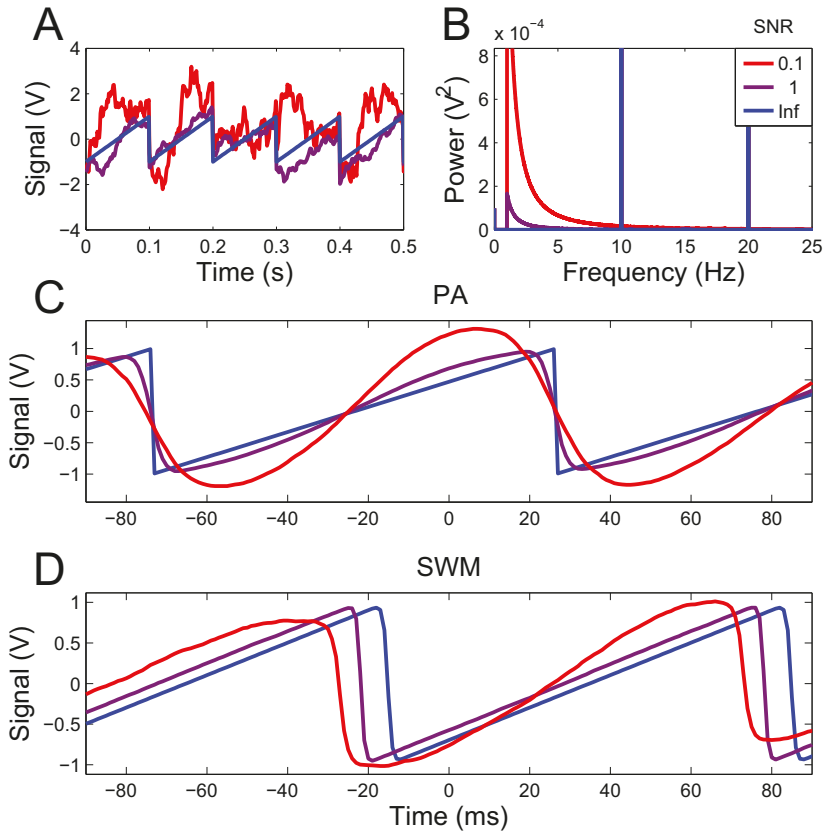


Figure 5-3. Results of applying phase alignment and the SWM algorithm to simulated data. (A) Examples of three constructed signals: a regular 10 Hz sawtooth without (blue) and two with $1/f$ noise (purple and red). (B) Power spectral densities of the four signals. All three spectra have the same narrow peaks at 10 Hz and the first higher harmonic at 20 Hz. (C, D) The resulting motifs found by PA (C) and the SMW algorithm (D), traces indicate different signal to noise ratio levels as in B.

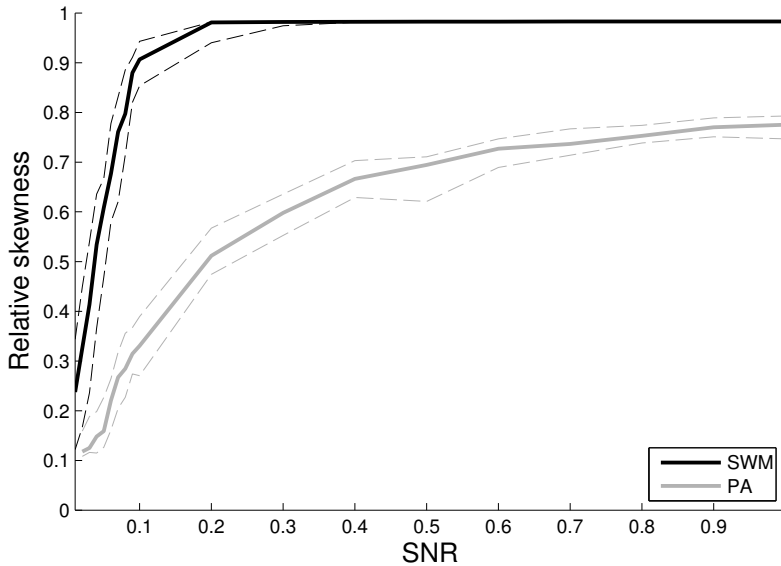


Figure 5-4. Comparison of the skewness indices found by using the SWM and PA methods for extracting the mean waveform for simulated data with different signal-to-noise ratio (SNR). The skewness indices were normalized to the skewness index of 0.98 of the noiseless signal. The grey and black lines show the median of 20 simulations for every SNR level using PA and SWM respectively to estimate skewness. Dashed lines show the corresponding 0.25 and 0.75 quartiles. The SWM method is superior to PA in estimating the skewness of the signal with lower SNR. Already at a SNR of 0.2 the method found a skewness index close to the noiseless case.

5.3.1.2 *Rat hippocampal theta*

We applied SWM to LFP recordings from the rat hippocampal region CA1 and hippocampal fissure while the rats were freely moving around in their individual cages using SWM (Figure 5-5A) and PA method (Figure 5-5B). Before applying SWM, the data were high-pass filtered at 5 Hz using a 4th order Butterworth IIR filter. The window length L was then set to 200 ms to capture ~ 1.5 theta cycles. The minimal window spacing G was set to 100 ms (i.e. having a maximal overlap of 100 ms) such that two subsequent windows could capture subsequent theta waveforms. Since the theta oscillations are quite prominent in LFP recordings in the hippocampal regions, we set the number of windows N in such a way to achieve $\sim 75\%$ data covered by the windows. Figure 5-5A and B show that a triangular-shaped periodic theta waveform can be found in both area CA1 and the hippocampal fissure. Figure 5-5C shows the corresponding skewness indices. This is in line with what Belluscio and colleagues [86] have demonstrated. They measured mean skewness indices of -0.3 and -0.15 in CA1 when the animals were running in a linear maze or in REM sleep

respectively (Belluscio and colleagues used a different measure called the asymmetry index in their work, defined as the logarithm of the ratio between T_{up} and T_{down} , here we have converted their reported values to our SI definition for easy comparison). The right panel in Figure 5-5A illustrates that SWM does not explicitly control the position of the motif within the window. Hence, although the motif found in area CA1 in Rat 2 is in antiphase with the motifs found in CA1 in the other two rats, this does not reflect meaningful differences (see Figure 5-2C). Figure 5-5C indicates that both SWM and PA are sufficiently sensitive for estimating the skewness in the rat hippocampal theta. This was to be expected in view of the very high SNR for the theta waveforms (cf Figure 5-4).

The right panels in A and B show that SWM identifies a gamma component, locked to the theta wave form, which is missed by PA. The existence of such a component could indicate either phase-amplitude coupling or phase-phase coupling. The latter is in agreement with the findings by Belluscio and colleagues [86] (but see [316]). Observations like ours, may be used in future work to counter recent valid criticism on measures of cross-frequency interactions [119], some attributing apparent cross-frequency interactions to non-sinusoidal wave shapes [317]. Motifs like the one found in CA1 (Figure 5-5A) using SWM suggest a true cross-frequency coupling between theta and gamma.^{††}

^{††} Note that we merely illustrate the possible use of SWM in this debate; further quantitative analysis is required to confirm findings like these.

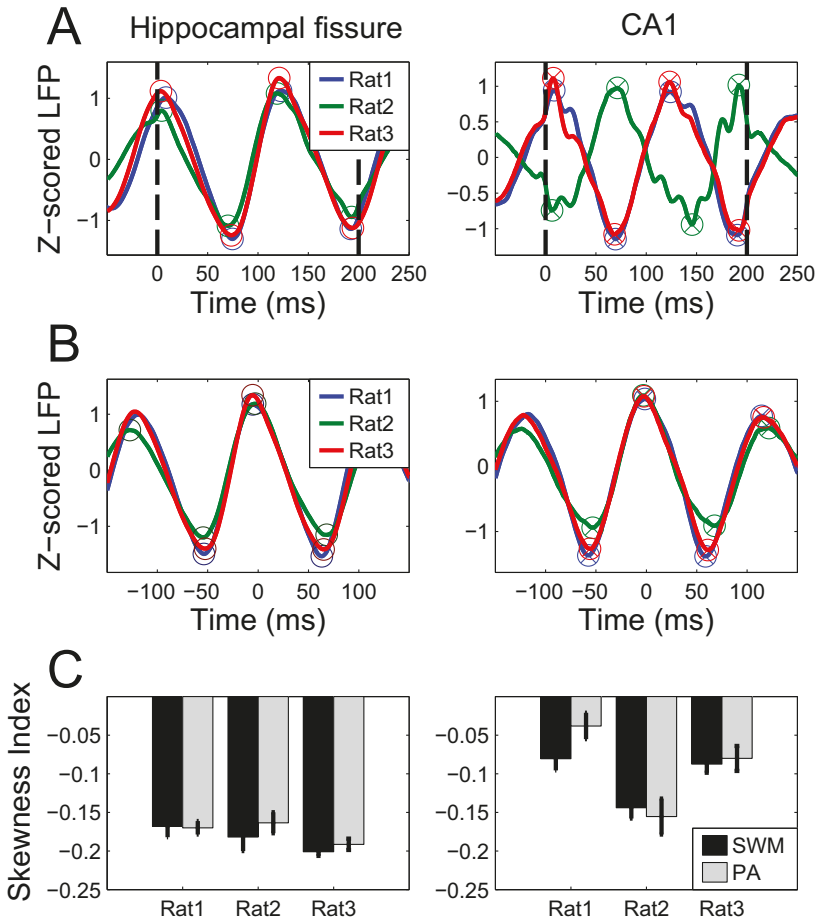


Figure 5-5. (A) Found theta shapes in rat LFP recordings in hippocampal fissure (left) and area CA1 (right) in 3 different rats. Vertical black dashed lines are the borders of the windows found by the SWM algorithm. The open circles denote the average position of the detected peaks and troughs for estimating T_{up} and T_{down} for calculating skewness using equation 4. (B) Same as A, but using PA rather than SWM. (C) Skewness of the waveforms in A and B. Black bars denote standard error of the mean as estimated by the bootstrap procedure (see section 5.2.2.2). Black bars indicate results from SWM (see A), grey bars correspond to the waveforms found using PA (see B).

5.3.1.3 *Monkey V1 gamma*

We applied the SWM algorithm to laminar LFP recordings from monkey V1 (see section 5.2.3.5) during presentation of a square-wave grating presented peripherally. Figure 5-6 shows the time-frequency representation of power around stimulus onset. A broadband evoked response can be seen, followed by an increase

in gamma power as highlighted by the dashed white rectangle. The first 200 ms after stimulus onset were omitted from the analysis to avoid the evoked response and therefore focus on the induced gamma oscillations.

It has been proposed that two spatially distinct generators of gamma oscillations are active in V1 [318], correlation coefficients were calculated for the data filtered between 35 and 55 Hz for the pairs of the 16 contact points on the laminar probe. Figure 5-7A shows these correlation coefficients, together with the border of pia and cortex and the border between granular and infragranular layers (see Figure S 1), labeled L1 and L4 respectively. The figure clearly shows two clusters of correlated gamma activity, one in the superficial layers (L1-L4) and one in the infragranular layers.

The SWM algorithm was applied to the post-stimulus data to detect the shape of these gamma oscillations for the 16 contact points on the electrode shank separately. The data was high-pass filtered at 25 Hz to remove signals in the 5 - 25 Hz band evoked by micro-saccades [41], [148] (Figure 5-6 and Figure 5-9). Otherwise the SWM algorithm would converge to these evoked responses. After the motifs were identified by SWM, they were extracted from the raw, unfiltered data, to restore any possible low-frequency components present in the motifs. The skewness index was calculated for these 16 motifs and is shown in Figure 5-7B. These skewness indices are different for the gamma motifs found above the granular layer, compared to those present below it. The superficial motif derived from the signals from all L1-L4 contact points and the deep layer motif, derived from the contact points below L4 are shown in Figure 5-7C. The superficial skewness was significantly different from the deep layer skewness (0.2033 ± 0.0034 vs -0.0596 ± 0.0044 . Mean \pm standard error; two-sample t-test ($t(104562) = -46.7$, $p < 0.001$). This result could be replicated using PA instead of SWM (Figure S 2B-D), but the skewness was less pronounced and not significantly different from zero in all contact points. This difference between PA and SWM can be understood by the lower sensitivity of PA, as discussed in section 5.3.1.1. In summary, SWM was able to detect a significant skewness in the induced gamma responses; moreover, the skewness was different for the superficial and deep gamma components.

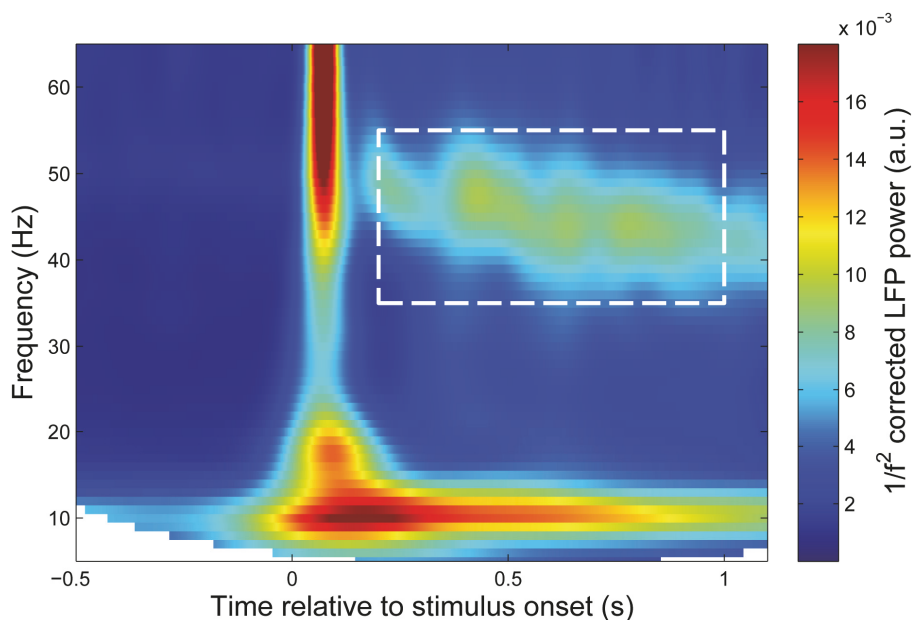


Figure 5-6. Time-frequency representations of monkey V1 LFP recordings. The power spectra are corrected by multiplying with f^2 to make both the alpha (10 Hz) and gamma band activity visible in the same figure. The dashed rectangle emphasizes the band-limited gamma component present in the post-stimulus period in the recordings.

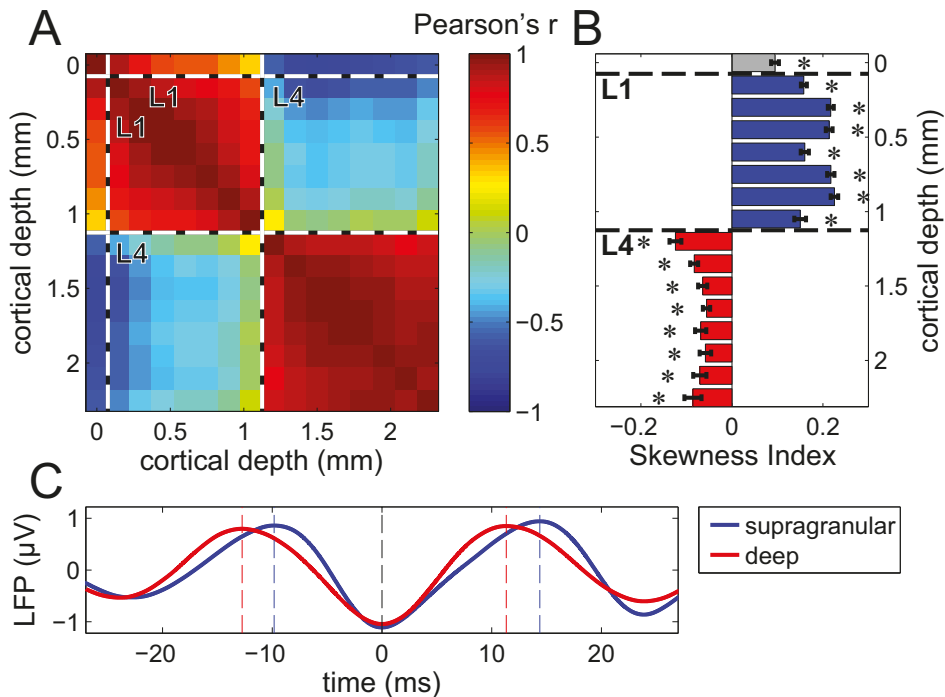


Figure 5-7. Properties of stimulus induced gamma-band activity in LFP recordings in monkey V1. **(A)** Pearson's correlation coefficient of gamma-band filtered data (35-55 Hz), corresponding to the induced activity in the dashed box in Figure 5-6). The supragranular contact points show a coherent gamma-band signal that was distinct from the signal measured by the deep contact points. Dashed lines labeled L1 and L4 indicate detected border (see Figure S 1) of dura/L1 and L4/L5 respectively. **(B)** Mean skewness of detected gamma waveforms at each contact point. Error bars denote standard error of the mean estimated by a 1000-fold bootstrap method (see section 5.2.2.2), Asterisks indicate significant differences from zero ($|t(6898)| > 3.1$, $p < 0.001$, single-sample t-test). Blue denotes electrode contact points in the cortex situated above the L4-L5 boundary, red denotes contact points below this boundary. **(C)** The averaged gamma motifs found in the supragranular electrodes (blue in panel B) aligned to the central trough with the average motif found in the signal recorded deeper in the cortex (red in panel B). The supragranular gamma was significantly more positively skewed ($P < 0.001$, estimated with a 1000-fold bootstrap. See section 5.2.2.2) than the deep gamma with respective SI of 0.2033 ± 0.0034 versus -0.0596 ± 0.0044 (mean \pm standard error).

5.3.2 Detecting stimulus evoked potentials

Evoked responses are patterns which consistently occur locked to an event. We demonstrate how SWM is beneficial when detecting evoked potentials by finding

stimulus- and saccade-evoked potentials using data from monkey V1 recordings. By having access to the actual event times of the evoked responses (i.e. the stimulus or saccade onset times) we can evaluate SWM's performance. In general, there is inherent ambiguity as to the exact locking of evoked potentials in V1. There could, for instance, be locking to the onset or the offset of the event, or there may be no consistent and precise locking. Since SWM is data-driven, we demonstrate that it can work around this ambiguity.

We applied SWM to the laminar LFP recordings in monkey V1 (see section 5.2.3.5). The onset of the stimulus evoked a typical response in the local field potential of the monkey's V1. To demonstrate the (temporal) accuracy of the SWM algorithm, we used it to analyze these evoked responses. We cut out 1 second of data in each of the 402 trials centered on the stimulus onset. We then performed SWM using 1 window per trial and a window length $L = 300$ ms. The dataset contained recordings at 16 different cortical depths, therefore, the windows were 2-dimensional arrays (16 cortical depths by 300 time points). The cost function was calculated across all cortical depths at once. This resulted in a 2-dimensional motif as shown in Figure 5-8B. The evoked response after aligning the data at the stimulus onset (captured by a photodiode attached to the screen) is shown in Figure 5-8A. In Figure 5-8C the difference between the evoked response and the motif found by SWM is shown. Only slight differences (compare scaling between C and A/B) could be discerned between the two responses. This can also be seen in Figure 5-8D where the window positions yielded by SWM have a distribution that is only around 4 ms wide (full width at half maximum). Note that in Figure 5-8B the motif found by SWM is aligned to the evoked response in A by shifting it temporally (i.e. time point $t=0$ on the x-axis in Figure 5-8B is not found by SWM, but by comparison to Figure 5-8A).

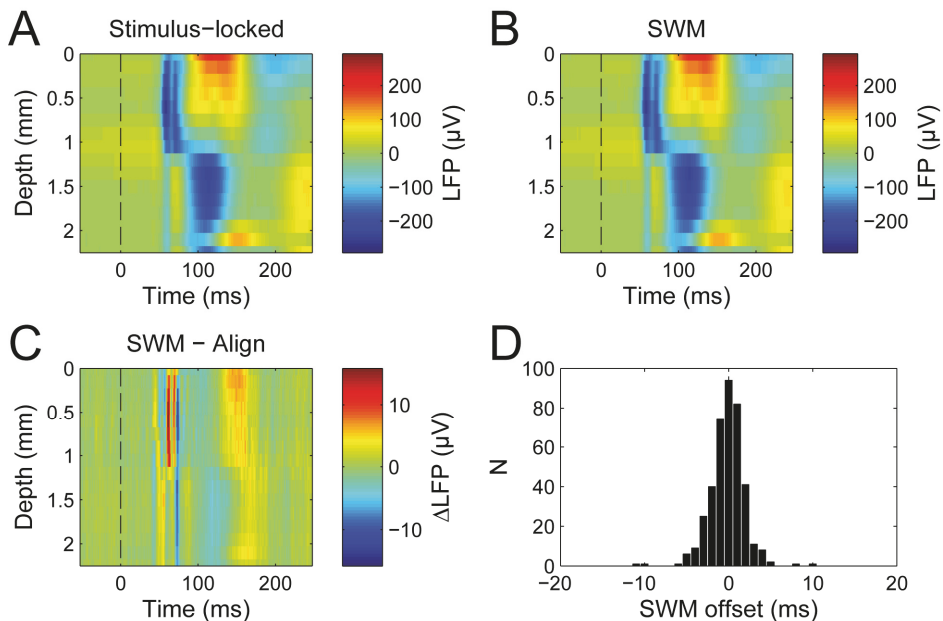


Figure 5-8. Detecting the stimulus evoked response using SWM. (A) The average response evoked by the stimulus in the LFP across the different layers of V1. The trials were aligned to the stimulus onset before averaging. The dashed vertical line indicates the stimulus onset. (B) The motif (average window contents) as found by SWM. Note that it is virtually identical to the evoked response shown in A. The vertical dashed line indicates the mean location of the stimulus onset. (C) The difference between the LFPs in B and A. (D) Histogram showing the temporal location of the windows relative to the stimulus onset (at 0 ms). This discrepancy is caused by a combination of variance in the evoked response shapes across trials and a possible jitter across trials between stimulus onset and evoked response.

5.3.3 Detecting microsaccades

When an experimental paradigm demands a monkey to fixate, the monkey is able to keep its eyes relatively still, but will still make small eye movements around the fixation spot called microsaccades [205]. Microsaccades also evoke a response in V1 [147], [148].

In the dataset used, eye movements were recorded allowing us to extract the responses in the LFP related to microsaccades; in this case eye movements in the order of 0.1 to 0.8 degrees occurring at 3-4 Hz. The temporal locations of microsaccade onsets were determined by thresholding the eye velocity signal [214], using a velocity threshold of 5 times the standard deviation and a minimum saccade duration of 10 ms. We tested the quality of SWM by determining the microsaccade

moments by applying SWM to the LFP data, without using the eye tracker recordings. SWM was applied to data recorded at least 200 ms after stimulus onset. The trial lengths were variable; the mean trial length was ~1100 ms. The window length was $L = 150$ ms (to match the size of the saccade triggered response, see Figure 5-9A) using on average 2 windows per trial. This probably underestimates the number of microsaccades present in the dataset. This was done to avoid windows not containing a saccade evoked response (e.g. when a trial contains 2 saccades, but 3 windows per trial are used, one window will by necessity contain noise, rather than the saccade related response). The average eye tracker-based saccade locked response and the SWM motif are shown in Figure 5-9A-B with the corresponding mean eye speed shown in C and D. The peak in Figure 5-9C and D, indicates that most SWM windows are correlated with microsaccades. However, the peak in the eye velocity profile found by SWM was lower and wider than the peak in Figure 5-9C. This can be caused by jitter between the onset of eye movement and the start of the evoked response. The jitter between microsaccades and SWM windows was clearly larger than between stimulus onset evoked potentials and SWM shown in Figure 5-8D. This can be partly explained by the low sampling rate of the eye tracking (240 Hz) compared to 1000 Hz of the LFP, see section 5.2.3.5. A second cause was that SWM converged to a configuration where not all window positions corresponded to a microsaccade. Since in the present case we had sufficient eye movement information, these two effects could be disentangled. Based on eye velocity we conclude that 443 out of 615 converged windows contained an actual saccade; the others contained an unexplained similarly-looking alpha waveform, see Figure S3.

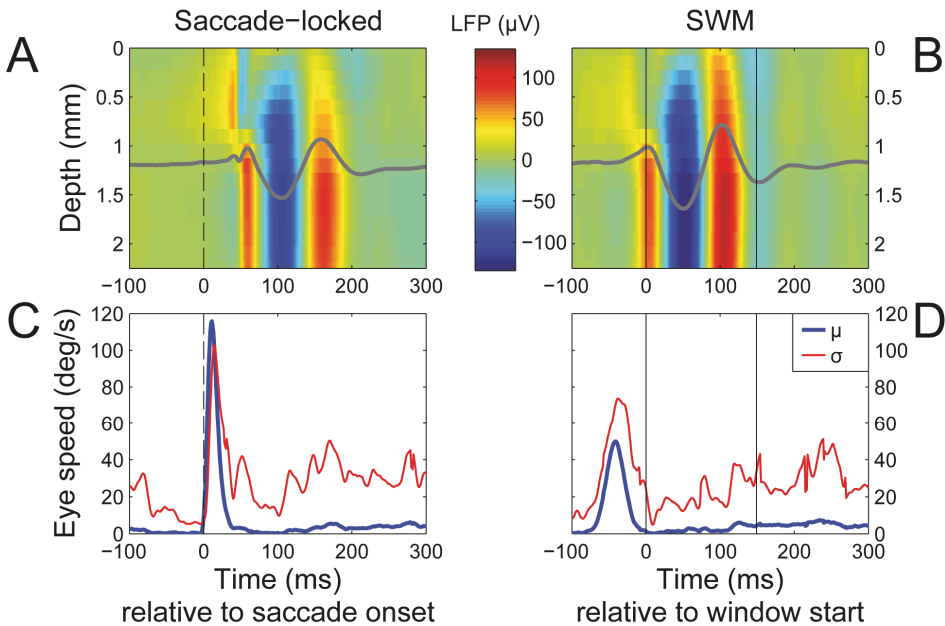


Figure 5-9. Detecting the microsaccade evoked response using SWM. **(A)** The average response evoked by the microsaccade in the LFP across the different layers of V1. The trials were averaged aligned to the saccade onset. The dashed vertical line indicates the saccade onset. The overlaid dark trace shows the mean LFP across all 16 contact points. **(B)** The motif (average window content) as found by SWM using 150 ms window length (L). The vertical black lines indicate the start and end of the window respectively. The time axis is relative to window start. Dark trace shows mean across the 16 contact points as in A. **(C)** The eye velocity averaged across the all the data segments locked to the onset of detected saccades (blue curve) and the standard deviation of the eye velocity across all detected saccades (red curve). Note that by definition this shows the average velocity profile of all microsaccades that were detected. **(D)** Mean eye velocity (blue) and corresponding standard deviation (red) as in C, but now locked to the windows found by SWM. As in B, time axis is relative to window start and black vertical lines indicate start and end of the 150 ms windows.

5.4 Discussion

In this paper we have proposed a new method, called *sliding window matching* (SWM), for detecting and analyzing recurring patterns (motifs) in electrophysiological datasets. We demonstrated that we could find and characterize waveforms of sustained neuronal oscillations as well as those evoked by a stimulus without prior knowledge of the timing of occurrence of these motifs.

5.4.1 Application to oscillatory signals

SWM can be used to extract the shape of cortical oscillations when signal to noise ratio is low (Figure 5-4). We validated this in simulated data, showing that Fourier based approaches are biased towards finding sinusoidal motifs, whereas SWM correctly identifies more general waveforms. The SWM method was able to replicate the skewed waveforms in rat hippocampal theta as shown by Belluscio and colleagues [86]. When applied to laminar recordings in monkey V1, the gamma motif induced by a grating stimulus could be detected and, interestingly, gamma oscillations were also skewed. A possible cause of this skewness is a difference in neuronal synchrony during the up-going versus the down-going flank of the gamma activity. Gamma activity involves an interplay between excitatory and inhibitory neuronal populations [38], [39], [100]. If one population fires more synchronously (i.e. more concentrated in time) than the other, then the corresponding flank (T_{up} or T_{down}) may last for a shorter time.

Furthermore, analysis of monkey V1 data replicated the finding of separate gamma oscillations in the deep and superficial layers [318]; this was accompanied by the significant difference in skewness between deep and superficial gamma waveforms ($p < 0.001$). In principle this difference could result from a change in the polarity of the signal. Considering that the absolute correlation coefficient of the gamma-band activity between the clusters was lower than within (as is the gamma-band coherence, which should be of equal magnitude between and within the clusters if the superficial and deep gamma signals merely differed in their polarity, see Figure S 2A), it is unlikely that the two gamma oscillations are generated by the same source, with only the polarity flipped. Hence, it is more likely that the recorded activity originated from two distinct gamma sources having some partial synchrony (note the non-zero correlation/coherence between the superficial and deep gamma activity). One of these sources could be observed in the superficial layers of V1, the other in the deeper layers. To further investigate these two sources, the method proposed in the present paper, could be combined with a CSD analysis [151], [319]–[321] of high-density laminar probe data to yield more definitive results.

5.4.2 Application to evoked responses

By applying SWM to LFP recordings from V1 in a macaque monkey, we demonstrated how SWM could determine the moment at which the response evoked by a visual stimulus occurred (Figure 5-8). The delay between stimulus onset and evoked response could conceivably be jittered on a trial-by-trial basis, possibly caused by variable hysteresis effects and delays in the neural network. In such cases, SWM could identify this jitter (but note that variance in the evoked

response shape across trials, especially changes in temporal length of the evoked response, can also cause this perceived jitter in the output of SWM).

To illustrate the power of SWM, we applied SWM to locate micro-saccade evoked potentials where the locking of the evoked potential to the event is ambiguous (Figure 5-9). Compared to stimulus evoked responses, the detection of responses evoked by microsaccades is more difficult. The following points could play a role: 1) The responses evoked by the microsaccades were less similar across trials, compared to the stimulus evoked responses. This could be due to differences in microsaccade amplitudes and directions as well as effects from the activity preceding a microsaccade 2) The saccade evoked responses were smaller in amplitude than those evoked by the grating stimuli, leading to a reduced signal-to-noise ratio. 3) The time span between saccade onset and saccade evoked response was more variable than that between stimulus onset and stimulus evoked response. With the available eye tracking equipment, any physiological variability will be enhanced by the discrepancy between the sampling rate of the LFP recording (1 kHz) and that of the eye tracking equipment (240 Hz). 4) Other components (e.g. alpha-band neuronal oscillations) in the signal had a shape that is similar to the saccade evoked response. This would cause some of the SWM windows to converge to parts of the data containing high amplitude alpha oscillations (172 out of 615 windows did not contain an actual saccade; instead they contained a similarly-looking alpha waveform, see Figure S3). The fact that it seems quite difficult to disentangle the two based on shape alone, raises the question to what extent alpha oscillations and (micro-) saccades are related. To answer this question further research is needed.

5.4.3 Comparison to other techniques and recommendations

SWM is not the only analysis method that uses sliding windows. Several techniques using some form of template matching [322] have been used by others in electrophysiological signal analysis [82] and artifact rejection [323]. However, it differs from these techniques in the sense that SWM does not require an *a priori* template (the motif), but discovers it from the data. In that sense it is similar to the Woody filter [324]. The Woody filter, however, requires a priori knowledge of the approximate temporal locations of the motifs, whereas SWM will automatically detect these. If one just wants to increase the SNR in evoked potentials locked to an external event, it is recommended to use something similar to a Woody filter or other automated denoising techniques (e.g. [325]). Since both the approximate

location and shape of the motifs are already known, these methods will be much more time-efficient.

In the context of the analysis of non-sinusoidal, non-stationary signals, there exists a broad literature based on *empirical mode decomposition* (EMD) [292]–[294]. EMD is able to separate the original signal into intrinsic mode functions. After obtaining these intrinsic mode functions, a Hilbert transform can be performed to derive an analytic representation of these modes to estimate the instantaneous phase. From then on, the motifs can be extracted by aligning parts of the data with the same phase similar to the phase alignment method mentioned in section 5.2.3.1. These empirical modes are free to change their frequency content over time, which provides greater flexibility and it requires less a priori knowledge (such as the central frequency and the bandwidth of the filter used in the PA method). On the other hand, this means that the correct mode needs to be selected from all intrinsic mode functions that have been extracted. Besides this, EMD is likely to lead to multiple modes containing similar spectral content, just at different moments in time. This means that the motifs of interest may be split across multiple modes. As a control, we applied this hybrid EMD-PA method to the signal with an SNR of 0.5 from Figure 5-4. We selected the mode that most looked like a band-limited 10 Hz signal by hand, and found that it underperformed compared to regular PA with a detected SI of 0.49 ± 0.08 .

Finally, EMD is designed to find oscillatory modes, not repeating patterns. This fact makes it more difficult for EMD-based techniques to deal with irregularly popping up motifs that SWM is designed to detect. This makes EMD suited to extracting the periodic theta and gamma waves in rat hippocampus and monkey V1 in sections 5.3.1.2 and 5.3.1.3, but not suited for finding evoked responses such as in sections 5.3.2 and 5.3.3.

SWM relies on a parallel tempering MCMC sampling technique. This is an optimization method that is powerful in avoiding convergence to local minima and finding the global minimum. It is computationally more demanding than techniques that do not explicitly try to minimize a certain cost function, such as phase alignment or EMD. This effect is worse for larger datasets, since, unlike PA, convergence time for SWM does not scale linearly with sample size. The size of the energy landscape that SWM needs to sample to find the minimum in the cost function increases roughly exponentially with the size of the dataset. For reference, detecting the stimulus evoked responses in the 402 trials each consisting of 16 electrodes having recorded 1000 data points required on the order of hours on a modern machine, whereas a method similar to PA (as used in Figure 5-3 and Figure 5-4) would only last around 10 seconds. Compared to SWM, PA can be a much faster technique that yields a unique solution. However, the motifs need to have a high signal to noise

ratio in a narrow frequency band. Secondly, because of the focus on a narrow frequency band, PA will return a mixture of motifs if the data contains two or more different motifs with overlap in the spectral content. In its present form, in this case, SWM will converge to the dominant motif, i.e. the motif with the lowest variability and highest SNR. This may partly explain the sharp transition of the gamma skewness from positive to negative when going from electrode contact point 8 to 9 in Figure 5-7B. In such a case, the algorithm could be extended to include clustering. Instead of comparing the contents of a window to all others to calculate the cost, the window is only compared to the other windows in the same cluster. Secondly, instead of only attempting to slide a window, the algorithm should also attempt to move a window to a different cluster and then estimate the change in cost function to calculate the acceptance probability. This could yield other, less dominant motifs in the other clusters.

When investigating oscillatory waveforms, it is arbitrary to which “phase” of the oscillation SWM converges. This is visible in Figure 5-5B: the motif found in area CA1 in Rat 2 is in antiphase with the motifs found in CA1 in the other two rats. In contrast, when using PA, the phase of the extracted motif is, by definition, controlled. In principle this is not a crucial deficiency of the algorithm and is mainly important for visualization purposes.

Despite the fact that SWM is data driven, it may generally help to use some a priori knowledge about the motifs one wants to detect as well as the noise it is embedded in. During a preprocessing step, irrelevant components of the data will sometimes have to be removed, lest SWM converges to these irrelevant components rather than the motif of interest. For example, to detect the gamma motif in monkey V1 (Figure 5-7), it was helpful to filter out high-amplitude, low-frequency components that were not of interest. Especially in electrophysiological data where a $1/f$ amplitude spectrum is often reported [312], [313] this will be necessary, since the low-frequency noise will always have a relatively high amplitude. Note that if the window length is small relative to the period of a low-frequency oscillation, this high-pass filtering with this frequency threshold resembles linear detrending the data in each window. One could consider changing the cost function to explicitly incorporate linear detrending, making less preprocessing necessary. The same holds for parameters such as the approximate length of the motif; the parameter of window length L can determine to a large extent to which component the algorithm converges, so an approximate length of the motif of interest should be known a priori. Parameters that determine the rate of convergence of the Parallel Tempering technique (i.e. k and T , see Algorithm 2 in Appendix A) also need to be set when applying SWM. Good values for these parameters depend on the dataset. It is therefore recommended to perform a few test runs with different ranges of

temperature factors (T , generally a set of logarithmically spaced temperatures) and switching probabilities (k) and investigate the trajectories of the cost function, to make sure that: 1) states are switched often enough between different temperatures. This can be achieved by increasing the number of parallel temperatures or decreasing the factor k . 2) The highest and lowest temperatures should both stay on a fairly constant cost value at the end of the run (indicating the maximum and the minimum cost value, respectively). See Figure S 4 for an illustration.

If nothing is known about the motifs a priori, i.e. when SWM is used in a pure exploratory sense, one may want to establish to what extent the motif found is meaningful. Note that when SWM is used on pure noise, the algorithm will also converge by finding pieces of noise that look most alike, but this found “motif” should be considered as meaningless.

A first indication of how meaningful the results are, is the final cost of the converged solution. If normalized by the number of windows (N in equation 1), this should be a value between 0 and 1. The closer to 0, the higher the signal to noise ratio in the found motif. A low cost value would be unlikely in the case of fitting noise. However, since this is a measure of SNR, the minimal cost will also be higher (closer to 1) if the motif is weaker with respect to the noise in the signal, so solely relying on the cost is insufficient to tell meaningful from meaningless results. The most straightforward way of establishing “meaning” for the found motif would be to correlate the motifs with something to which the SWM algorithm is blind (e.g. a behavioral measure such as eye movement, or data from other sensors recorded at the same time, but not used for SWM). If this is not possible, one would like to compare the correlation among the found motif windows to the autocorrelation of the noise in the signal. A possible way to do this is illustrated in Figure S 5. In short, the found windows are cross-correlated with the data individually (using Pearson’s correlation coefficient to remove variations in amplitude). After this cross-correlation operation, the highest peaks in the cross-correlograms of Pearson correlation coefficients are extracted. These peak values are then averaged, resulting in a distribution of averaged correlation coefficients (one for each found window). This distribution is then compared to a reference distribution where randomly positioned windows (i.e. most likely not containing a motif) were used to cross-correlate instead of those found by SWM. If the SWM algorithm converged to legitimate motifs, the former distribution should contain higher values compared to the latter. If SWM was used to “fit noise” as in the example given above, both distributions should be equivalent, since both the randomly selected windows and the windows found by SWM should contain noise that is statistically the same with respect to the rest of the data. The two distributions can be compared using a one-sided Mann–Whitney U test to

establish statistical significance (see Figure S 5 for a few examples of applying this statistical test). Note that this test would result in a false negative in the specific case of a perfectly periodic “motif” with constant (or absent) noise. In this case any randomly placed window will contain equal amounts of motif and noise, and therefore the two distributions will be equal. This tendency can be seen in the case of the theta rhythm in the rat (Figure S 5A) where the reference distribution shows considerable overlap with the test distribution caused by the high periodicity and ubiquity of the theta rhythm.

The strategy mentioned similar to the one above for determining the usefulness of the found motif can be used to evaluate whether a correct number of windows was used (N in equation 1). One could look at the Pearson correlation of each individual found window with the found mean motif. If this distribution contains many low outliers, or even correlations below 0, this means that the chosen value for N was too large, since windows were positioned over data that does not match the motif. If, however, N was chosen sufficiently small, the motif shape will be correctly determined without mixing in of noise. After SWM has converged, peaks in the cross-correlogram of the motif found with the rest of the data can be used to find the other occurrences of the motif that could not be identified because N was too small. If the number of high peaks in the correlogram is much larger than N , it may be wise to restart the SWM algorithm with a higher value of N , closer to the number of peaks found in the correlogram.

5.4.4 Possible applications in neuroscience

The different gamma motifs in monkey V1 in different laminae add some interesting insight regarding the cortical source and the mechanism behind gamma oscillations. In addition, the findings described open the possibility that SWM could contribute to functional dissociations among cortical layers. In the present work, analysis has been limited to LFP measurements, but it may be interesting to detect action potentials locked to the extracted waveforms. For example, in the gamma range, if pyramidal cells and interneurons lock their spiking to different flanks of the gamma cycle, this may be informative with regard to the mechanisms generating the gamma rhythm. As has been proposed before [38], [39], the gamma rhythm can be dictated either by the population of interneurons alone, or by an interplay between both the pyramidal cells and the interneurons.

In the present study, we demonstrated the reliability of SWM in cases in which the triggering information (stimulus onsets and microsaccades) is available, or in which the effects on the recorded activity is relatively well-known. However, SWM can be useful in discovering fully unknown waveform signatures in cases where also the

triggering information is unknown. This can be the case when studying events in electrophysiological signals during sleep (e.g. sleep spindles [326] and sharp wave-ripple complexes [327]), or identification of interictal discharges in epilepsy patients [328], or even when studying higher cognitive processes, such as decision making. Secondly, SWM is not bound to electrophysiological data and besides LFP, MEG and EEG recordings, SWM can be used on any other dataset that is expected to contain recurring patterns (such as resting-state fMRI [329]). Secondly, SWM may be employed for artifact detection. When artifacts in the recorded signal have a consistent shape, such as eye-blinks in EEG and MEG recordings, SWM can be employed to find them such that they can be discarded or regressed out.

5.5 Conclusion

We introduced SWM as a data-driven approach for detecting recurring patterns in (neurophysiological) data. Using simulated and empirical data, we have shown that SWM can reliably detect the shape of oscillatory waveforms and evoked responses. The application of SWM to neurophysiological data opens up new possibilities in understanding how brain signals are generated.

5.6 Acknowledgements

We are extremely grateful to Laura Lee Colgin at the University of Texas at Austin for providing us with the data from rat hippocampal recordings used in this work. The current work was supported by the Organization for Scientific Research (NWO) through the ALW Open Competition Grant (822-02-011).

5.7 Appendices

5.7.1.1 Appendix A. Parallel tempering SWM algorithm

Initialization:

- 1 Define window length (L) and minimal window spacing (G).
- 2 Define Q different temperatures T_1, T_2, \dots, T_Q with T_q decreasing from T_1 to T_Q .
- 3 Initialize window starting positions $\mathbf{x}_q = [X_1, X_2, \dots, X_N]$ for every temperature T_q as in Algorithm 1.
- 4 Calculate initial cost $J_{q,0}$ (eq. 5.1) for every parallel temperature;

```

5  while  $i_{out} < \text{maxIterations}$  do
6      for  $i = 1:\text{maxSubIterations}$ 
7          Perform while-loop in algorithm 1 (lines 4-
            18) for every parallel temperature
            separately
8      end
9      Pick a pair of neighboring temperatures at random:
             $T_q$  and  $T_{q+1}$ .
10      $p_{\text{swap}} = \exp(k * (J_q - J_{q+1}) / (T_q - T_{q+1}))$ 
11     if  $\text{rand}(0,1) < p_{\text{swap}}$ 
12         Swap states between parallel temperatures:
13          $\mathbf{X}' = \mathbf{X}_q$ 
14          $\mathbf{X}_q \leftarrow \mathbf{X}_{q+1}$ 
15          $\mathbf{X}_{q+1} \leftarrow \mathbf{X}'$ 
16     end
17     for  $q = 1:Q$ 
18         Move all positions in  $\mathbf{X}_q$  randomly by the same
            amount/step
            (instead of only a single window as in (line
            5-6 in Algorithm 1):  $\mathbf{X}' = \mathbf{X}_q + \text{step}$ 
19         Calculate the new cost  $J'$  using  $\mathbf{X}'$  and with
            this the change in cost function  $\Delta J = J_{q,i-1} - J'$ ;
20         Calculate acceptance probability  $p_{\text{accept}} = \exp(\Delta J/T)$ 
21         if  $\text{rand}(0,1) < p_{\text{accept}}$  then
22              $J_{q,i} \leftarrow J'$ 
23              $\mathbf{X}_q \leftarrow \mathbf{X}'$ 
24         end
25     end
26      $i_{out} \leftarrow i_{out} + 1$ 
27 end

```

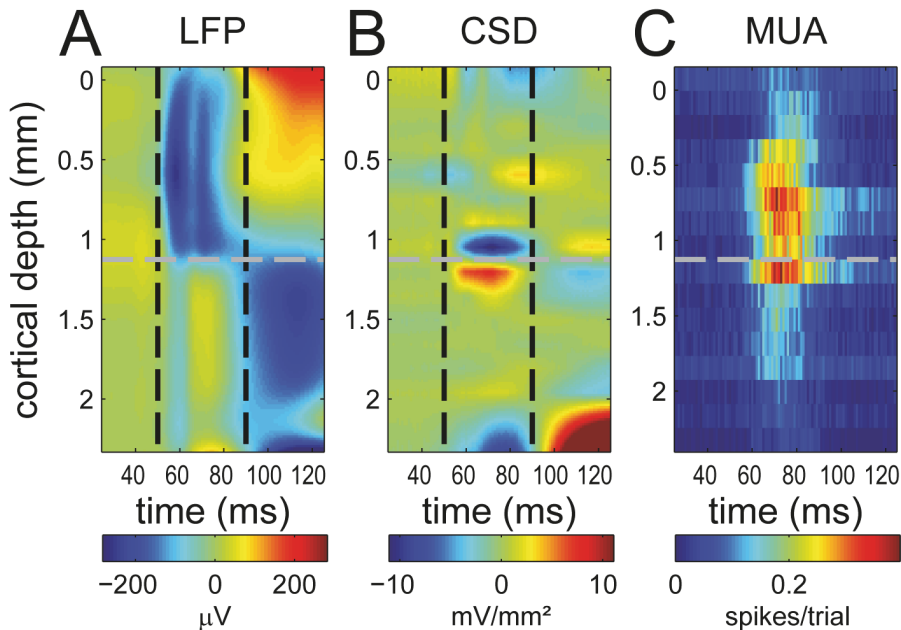
Algorithm 2. Combining **Algorithm 1** with Parallel Tempering to better find the global minimum of cost function J .

5.8 Supplemental material

Calculation of J is equivalent to one minus the mean of the off-diagonal elements in the Pearson correlation matrix of all windows, multiplied by the number of windows (N). This means that the maximum of J is equal to N (all windows are completely uncorrelated, the correlation matrix is an identity matrix) and the minimum value for J is 0 when all windows are fully correlated (the correlation matrix is a unit matrix, the contents of all windows are perfectly correlated). See equation 6 for this equivalent definition (where Q_{ij} is the element on the row i and column j in the correlation matrix calculated between all windows, see equation 6).

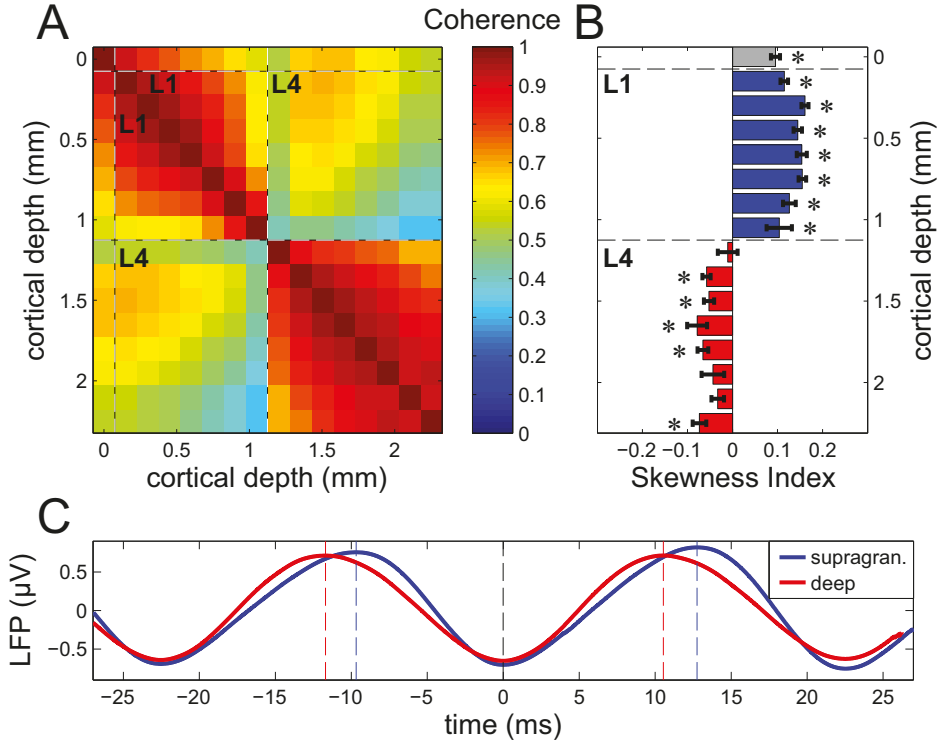
$$J = N * \left(1 - \frac{2 * \sum_{i=1}^N \sum_{j=i+1}^N Q_{ij}}{N * (N - 1)} \right) \quad (5.6)$$

$$Q_{ij} = \frac{\mathbf{z}_i \cdot \mathbf{z}_j}{L - 1} \quad (5.7)$$

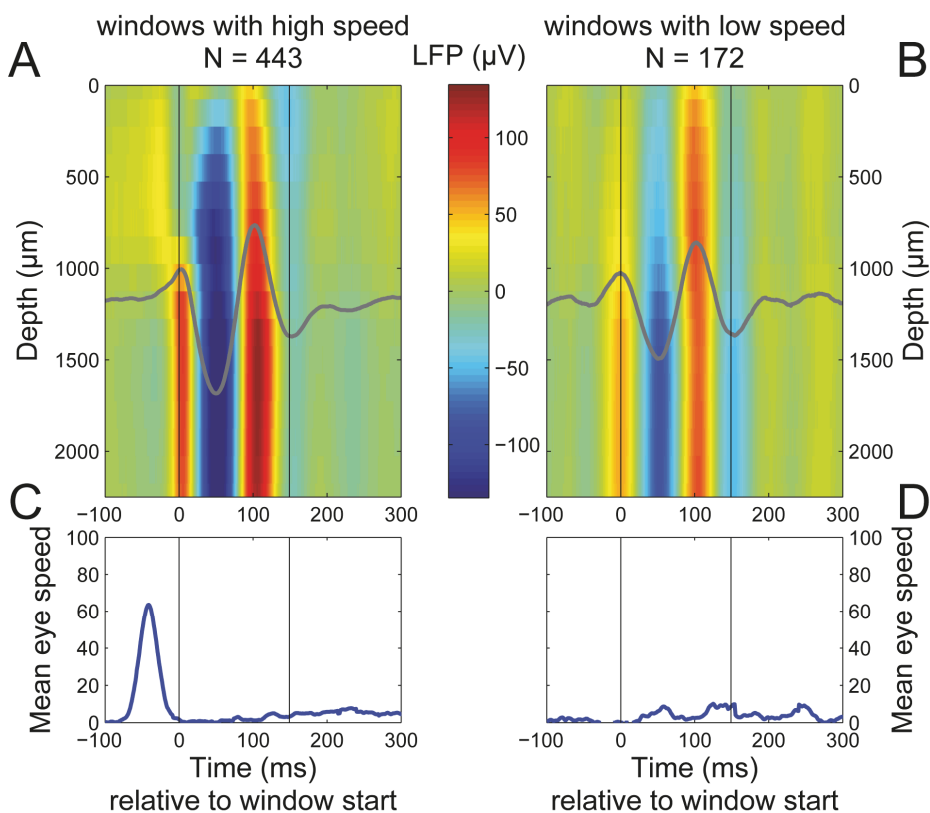


S 1. Detection of layer 4/5 boundary and corresponding gamma skewness shift. The position of the layer 4/5 boundary was taken as the position of the first sink (blue) – source (red) reversal in the CSD (panel B) shortly after stimulus onset (50-90 ms after stimulus onset, see black dashed lines). This position is indicated by a gray dashed line across all panels. Depth 0 corresponds to the top of the cortex, the location where the first negative visually evoked response (A) and first spiking response was observed (C). **(A)** Local field potential as a function of cortical depth after stimulus onset averaged across trials. Interpolated along the laminar axis using cubic spline interpolation. **(B)** The negative value

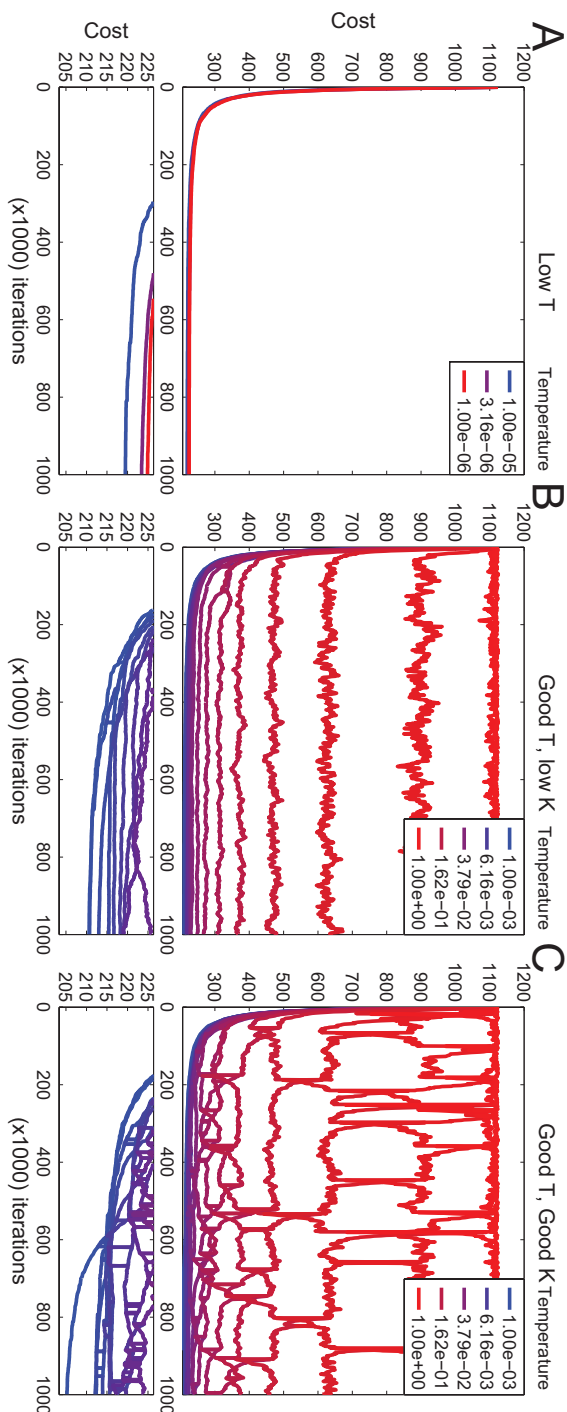
of the second derivative of A along the laminar axis (an estimate of the current source density, CSD. Blue color indicates sinks; red color indicates sources). **(C)** Heat map showing multi-unit activity.



S 2. Properties of stimulus induced gamma-band activity in LFP recordings in monkey V1. **(A)** Spectral coherence across cortical depth in the gamma band (40-50Hz). **(B-C)** Analogous to Figure 5-7B-C, but obtained by using PA with central frequency f_0 of 45 Hz with a bandwidth of $1/(2\pi\sigma) = 2$ Hz (eq. 5.5) instead of SWM.



S 3. Splitting up SWM windows based on eye velocity. The laminar LFP patterns shown in Figure 5-9B have been split up (A,B) by based on eye speed just before the start of the SWM window (C,D).

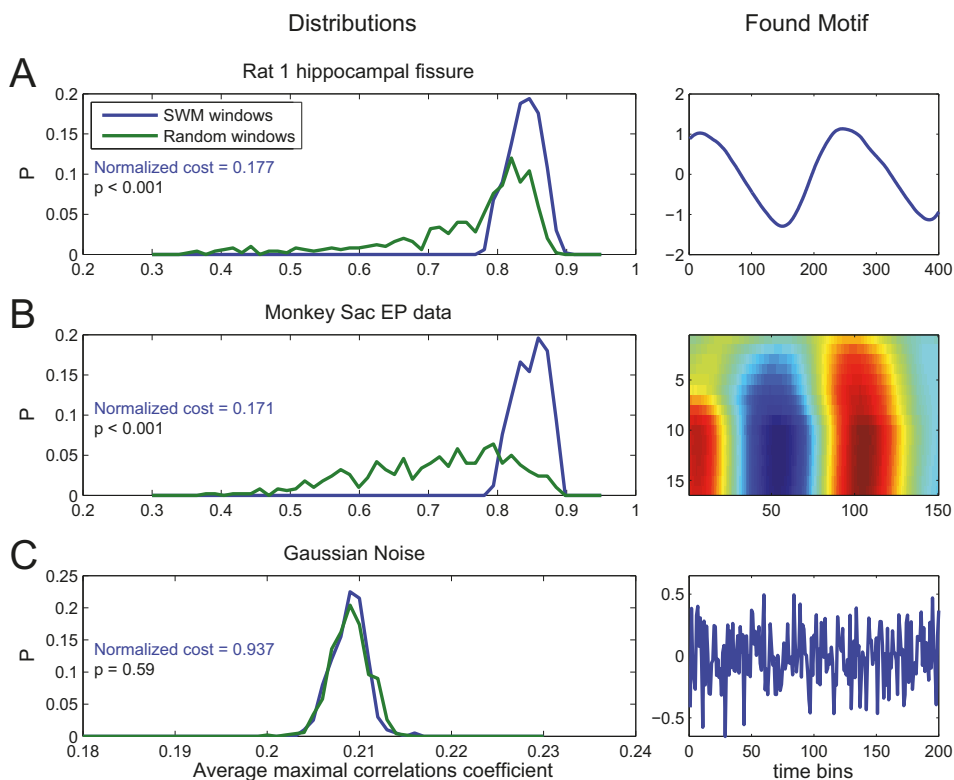


S 4. Examples of cost function trajectories.

Illustration how temperature parameters change the accuracy of SWM. Each panel (A-C) shows the cost function as a function of iteration number. Red colors indicate the cost of a high temperature state, whereas blue curves describe the cost trajectory of low temperature states (see legends). The top panels show the full trajectories, whereas the bottom panels show the cost value close to the minimum for easier comparison between the three different parameter sets. All three cases were performed on the same data set. **(A)** The amount of different temperatures is set low (3 different temperatures were used, see legend) and the individual temperatures are too low ($< 10^{-5}$) SWM will quickly converge to a minimum, but this will be a local one. **(B)** The amount of different temperatures (20) and their values is set well, spaced logarithmically between 1 and 10^{-3} . The highest temperature stays at the maximum cost value, whereas decreasing temperatures span the space between the maximum and the found minimum. However, the parameter that determines the probability of swapping temperatures between states (k in line 10 of Algorithm 2) is set too low causing this swapping to never happen. This makes the algorithm run independently for all 20 temperatures and in essence not use parallel tempering at all. **(C)**

Both temperatures (same values as in B) and k (200) are set properly. Parallel tempering is

in effect as can be witnessed by the jumps in the cost trajectories indicating swapping of states between all temperatures. The minimum found in this last case is therefore lowest of the three.



S 5 Examples of statistical testing of “meaningfulness” of found motifs. (Left) sampling distributions of mean maximal correlation coefficients with windows found by SWM (blue) and with random windows (green). A total of 500 random windows were used to generate the green distribution, whereas up to 500 windows found by SWM were used to generate the blue distribution (less if the number of windows was less than 500). The inset lists the normalized cost of the solution found by SWM, as well as the p-value of a Mann-Whitney U test, testing for the null-hypothesis that the blue and the green sampling distributions come from the sample population against the alternative that the blue distribution comes from a population with higher values. (Right) The motifs found by SWM. **(A)** The data recorded in the hippocampal fissure of rat 1 (see Figure 5-5A). **(B)** The saccade evoked potential in monkey V1 (see Figure 5-9B). **(C)** SWM applied to 20 trials of 3 seconds of Gaussian White noise. A total of 200 windows was used with a window length and guard of 200 ms.

Chapter 6. *General Discussion*

In this thesis we covered work investigating the mechanisms and functional interpretation of neuronal oscillations on the level of single neurons and networks of neurons. In this chapter we will summarize the main findings and thereby attempt to answer the questions raised in Chapter 1.

6.1 Summary

In Chapter 2 we investigated a model neuronal mechanism that generates phase-amplitude coupling (PAC) between alpha and gamma oscillations. The gamma rhythm produced by subsequent excitatory and inhibitory activity in the pyramidal cells and interneurons is periodically silenced by an inhibitory signal with alpha frequency. As a result, this gamma-band activity is nested within the alpha rhythm, generating PAC in the simulated LFP. Since the periodic alpha signal we use (thought to have a thalamic origin, see Chapter 3) is sinusoidal in shape, it has down-going (and up-going) flanks. This has a secondary effect: neuronal activity within the *duty cycle* imposed by the alpha rhythm is temporally sorted. The neurons with highest levels of excitation will fire early in the alpha cycle, whereas neurons with low excitation will fire later, or not at all. In this way, the alpha-gamma PAC is interpreted as a mechanism through which the cortex can segment and prioritize neural signals according to their “importance” (here taken as the level of excitation of the pyramidal cells involved).

In Chapter 3, we presented a model neuronal mechanism for the generation of the alpha rhythm in the thalamus. The model is based on experimental findings by Lorincz et al. [135] and builds on the *in silico* work by Vijayan and Kopell [127]. In this model a stable alpha rhythm is generated by two subsets of thalamo-cortical relay neurons firing in anti-phase. The “regular” thalamo-cortical relay cells (TCR) are inhibited by local interneurons that are periodically excited by the high-threshold bursting thalamo-cortical cells (HTC). The HTC cells are in turn inhibited by cells in the reticulate nucleus that receive input from the TCR cells. This loop of recurrent indirect inhibition makes the alpha rhythm stable, even when the HTC cells are perturbed. We have shown that this proposed mechanism for the thalamic alpha generator is able to produce an alpha rhythm both under an idling condition (i.e. when the TCR neurons receive no input to relay to the cortex) as well as under relay conditions, such that it can perform the temporal framing proposed by Lorincz et al. Besides this, the alpha generator circuitry was able to generate evoked responses similar to those measured experimentally. This suggests that the generation of alpha oscillations and visual evoked responses can be attributed to the same neuronal circuitry.

In Chapter 4 we discussed a mechanism that explains the delta-gamma PAC observed in monkey V1 that has been related to eye movements [41], [211].

Microsaccades are small involuntary eye movements that happen at a frequency of around 3 Hz in primates. When investigating the neuronal activity visible in the LFP locked to these microsaccades, two phases of activity can be distinguished. The first is a transient period in the first 100 ms directly following the saccade onset. This is characterized by a high-amplitude broad peak in the power spectrum. After this, a “sustained” period follows, in which a narrow-band gamma component is visible in the LFP. By way of model-based investigations, we showed that these two periods (transient and sustained) have different implications for neural processing in early visual cortex. The transient period is dominated by feed-forward processing upwards along the hierarchy of the visual cortex. In contrast, in the sustained period horizontal connections are much more important for determining the neural dynamics. This can be seen in a change in the receptive fields of the model neurons during this period.

The neuronal code in the spike trains of the model neurons in the two periods is also different: during the transient most information is carried by firing rate and firing latency. In contrast, during the sustained period, the level of synchrony as well as gamma phase difference are more important than firing rate.

Active sampling mechanisms similar to microsaccades also exist in other sensory modalities (such as rhythmic whisker movement and sniffing). Therefore, a similar mechanism that switches neuronal dynamics between feed-forward and recurrent processing, may generalize to other sensory modalities. Additionally, since the mechanism is marked by periodic transients, it may well be that these could be generated internally and as a result such a mechanism would be responsible for phase-amplitude coupling in other (non-sensory) brain areas.

In Chapter 5 we introduced a novel analysis method, called sliding window matching (SWM), for investigating signatures of neural activity in electrophysiological data. In the context of this thesis, it can be used to investigate the shape of neural oscillations in LFP, ECoG, MEG, or EEG recordings. It can also be used to detect recurring transients that occur at unknown time points in the data (such as the responses evoked by microsaccades discussed in Chapter 4). We have shown that SWM can detect non-sinusoidal properties of these waveforms, even when signal-to-noise ratio is low when more traditional methods fail to do so.

6.2 Discussion and outlook

6.2.1 Models and predictions

Most of the research presented in the previous chapters was done using simulations of model neural networks. In Chapter 1 I have made the case for the use of simulations studies, most importantly how they could guide future experiments (see Figure 1-1). In this section we can then assess whether the work in Chapter 2, Chapter 3 and Chapter 4 could lead to direct predictions. So I'd like to briefly cover some example predictions that can be tested experimentally, based on the insights that the model neural networks provide.

The model in Chapter 2 makes clear predictions on the firing order of pyramidal cells within an alpha cycle. An example experiment to test this would be to record activity from pyramidal cells in the visual cortex while modulating the "importance" of the stimulus in the receptive fields of these cells. This importance could be modulated by changing stimulus saliency (e.g. enhancing one stimulus contrast over another). It could also be achieved by modulating top-down signals by training the animal to perform some sort of attention task (e.g. having the animal covertly attend one stimulus over another). The model in Chapter 2 predicts that the pyramidal cells responding to the more "important" stimulus will fire earlier in the alpha cycle than those responding to the other stimulus.

The model mechanism in Chapter 3 ascribes an important role to the reticulate nucleus in the generation of the alpha rhythm in the thalamus. To test this hypothesis one could modulate activity in the reticulate nucleus (e.g. by electrical stimulation [330], tissue cooling [331], or optogenetics [332]–[334]) while recording the alpha activity in the LGN. Silencing the RTN should destabilize the ongoing alpha rhythm, whereas an excitatory pulse to the RTN may reset the alpha rhythm as did the simulated pulse to the TCR in Figure 3-6.

The most straightforward prediction in Chapter 4 is concerning the change of receptive fields in (early) visual cortex. The simulation results in Figure 4-6 predict that the receptive fields change between the transient and sustained period. One could test this prediction by mapping out the receptive fields of neurons in the two different periods. Secondly, one should take into account the type of stimulus, since Figure 4-6 predicts that the effective change of RF shape is strongest when the receptive field center is located near a border of a contrast change.

6.2.2 *Alpha oscillations*

Two of the preceding chapters have been on mechanisms involving alpha oscillations (Chapter 2 and Chapter 3). As mentioned in these chapters, and Chapter 1, activity in the alpha band has been suggested to reflect cortical idling [22], active inhibition [34], [145], and temporal segmentation [135], [186]. Chapter 2 suggests a cortical mechanism that unifies the latter two functions. In this mechanism a

periodic (sinusoidal) inhibitory signal can both temporally order the firing of local pyramidal cells as well as inhibit the least excited pyramidal cells from activating. In contrast to Chapter 2, the mechanism suggested in Chapter 3 focusses on the thalamic origin of alpha oscillations. In this model for the thalamus, alpha activity can be either a sign of idling (e.g. closing the eyes) or active inhibition, while at the same time providing temporal framing of the thalamic relay cells [135]. One missing link between these two model mechanism is the translation from thalamic to cortical alpha. In the thalamic case, the activity of the TCR cells is modulated with an alpha frequency. This would translate to a periodic excitatory signal to the cortical pyramidal cells, instead of the inhibitory signal in the mechanism of Chapter 2. On the other hand, there is the possibility that the periodic signal from the HTC cells is transmitted to the cortex. The HTC cells were identified as a subpopulation of the thalamic relay cells that exhibited different bursting dynamics [24], [117], [135]. This implies that these neurons also project to the cortex. A possibility here would be that these HTC neurons predominantly project to inhibitory neurons in the cortex, this would then translate to a periodic inhibitory signal to the cortical pyramidal cells that is roughly in antiphase with the periodic excitation from the HTC cells. This would unify both frameworks presented in Chapter 2 and Chapter 3. This idea calls for future work to investigate the possible cortical projections of the HTC cells.

Besides the feed-forward connections between the thalamic alpha generator and the cortex, there should also be a feed-back signal to the thalamus coming from pyramidal cells in layer 6 of the cortex [169]–[171], [189]–[191], [193]. As discussed in Chapter 3, cortical feedback can modulate the thalamic alpha oscillations. Secondly, alpha oscillations in the (visual) cortex could stabilize the thalamic oscillation, and vice versa. Future work should focus on the interplay of the thalamic and cortical alpha oscillations.

6.2.3 Phase-amplitude coupling and waveform shape

Another main theme in this thesis has been phase-amplitude coupling (PAC). In Chapter 2 we discussed a possible mechanism for functional alpha-gamma PAC in the occipital cortex, and the work in Chapter 4 investigated micro-saccade induced activity that leads to delta-gamma coupling.

As mentioned in Chapter 1, cross-frequency interactions, with PAC in particular have gathered a lot of interest recently [58]–[70]. The types of phase-amplitude coupling discussed in Chapter 2 and Chapter 4 concerns “real” phase-amplitude coupling, i.e. there is a gamma rhythm that is periodically modulated in strength throughout the cycle of a slower rhythm. However, as others have also pointed out

[119], [317], [335]–[337], most common analyses to detect PAC are sensitive to waveform shape. In other words: when the low-frequency rhythm has a non-sinusoidal waveform, its harmonics will show up as a “rhythm” whose amplitude is locked to a particular phase of the low-frequency rhythm. To disentangle these two cases, one could investigate the waveform shape for “non-sinusoidality”. We have shown that SWM, presented in Chapter 5, can be employed to detect this “non-sinusoidality” even when the ratio of signal-to-noise is low.

A recent review paper by Cole and Voytek [338] highlights the importance of the shape of neural oscillations, in particular to what extent they are not sinusoidal. They argued that the shape of the oscillation waveform not only has implications for measures of PAC, but that it in general may contain important information about the neural systems that generate them.

In future work, new methods such as SWM can help investigate waveform shapes and attempt to distinguish the different forms of cross-frequency interactions.

6.3 General conclusions

In this thesis we have studied candidate mechanisms for neuronal oscillations recorded in experimental settings using simulated neuronal networks. Besides these network simulations, we have introduced a new analysis method to better investigate the waveforms of oscillatory activity recorded in experimental settings and test hypotheses possibly informed by the model simulations.

Taking the findings above, can we answer the questions posed in Chapter 1?

The first question asked how occipital cortical alpha oscillations could help cortical processing of visual information on a neuronal level. Alpha oscillations could reflect a periodic inhibitory (or possibly excitatory as discussed above) modulation of activity in the cortical pyramidal cells. This periodic modulation can temporally order pyramidal activation based on saliency in their receptive field or top-down biases such as attention, in the extreme case, blocking the most unimportant pyramidal cells from firing completely.

The second research question asks how the alpha rhythm in the thalamus could be generated and modulated. Mutual inhibition between two subpopulation of thalamo-cortical relay cells, could lead to a stable alpha rhythm that can still be modulated in strength and phase by bottom-up and top-down signals.

The third question pertains to saccadic eye movements. What are their effects on oscillatory activity in visual cortex and what are their implications for neuronal processing? Saccadic eye movements cause transients in early visual cortex. These transients allow for rapid feed-forward processing of the novel information on the retina after the eye movement. After this initial transient, a stable local gamma

rhythm can emerge. This local gamma synchrony, while being slower than the rapid feed-forward transient, allows for contextualization and local computations of stimulus details.

Finally, we asked how waveforms in electrophysiological data could better be investigated. Methods such as SWM allow for better inspection of waveform shape, this is crucial for distinguishing different forms of phase-amplitude coupling. In general, in future work, investigating the details of waveforms in electrophysiological recordings may yield helpful insights in the neuronal mechanisms responsible for their generation.

Taken together, the work presented in this thesis has given us a better understanding of the possible mechanisms underlying the generation and function of alpha oscillations and phase-amplitude coupling in the visual cortex on a neuronal level. As such, the work in this thesis has contributed to “bridging the gap” between neuronal activity and electrophysiological recordings. The results presented in this thesis have yielded us with predictions that can guide us in the design of future experiments. The next step is to test these predictions experimentally. Based on the results from these experiments we can revise or update the mechanisms proposed in this thesis to bring us closer to closing the gap completely.

Bibliography

- [1] G. Deco, V. K. Jirsa, P. A. Robinson, M. Breakspear, and K. Friston, "The Dynamic Brain: From Spiking Neurons to Neural Masses and Cortical Fields," *PLoS Comput. Biol.*, vol. 4, no. 8, p. e1000092, Aug. 2008.
- [2] H. R. Wilson and J. D. Cowan, "Excitatory and Inhibitory Interactions in Localized Populations of Model Neurons," *Biophys. J.*, vol. 12, no. 1, pp. 1–24, Jan. 1972.
- [3] H. R. Wilson and J. D. Cowan, "A mathematical theory of the functional dynamics of cortical and thalamic nervous tissue," *Kybernetik*, vol. 13, no. 2, pp. 55–80, Sep. 1973.
- [4] R. L. Beurle, "Properties of a Mass of Cells Capable of Regenerating Pulses," *Philos. Trans. R. Soc. B Biol. Sci.*, vol. 240, no. 669, pp. 55–94, Aug. 1956.
- [5] R. Moran, D. a DA Pinotsis, and K. Friston, "Neural masses and fields in dynamic causal modeling.," *Front. Comput. Neurosci.*, vol. 7, no. May, pp. 1–12, Jan. 2013.
- [6] L. M. Harrison, O. David, and K. J. Friston, "Stochastic models of neuronal dynamics.," *Philos. Trans. R. Soc. Lond. B. Biol. Sci.*, vol. 360, no. 1457, pp. 1075–91, 2005.
- [7] W. Freeman, *Mass action in the nervous system: examination of the neurophysiological basis of adaptive behavior through the EEG*. New York: Academic Press, 1975.
- [8] R. B. Stein, "Some Models of Neuronal Variability," *Biophys. J.*, vol. 7, no. 1, pp. 37–68, Jan. 1967.
- [9] E. M. Izhikevich, "Simple model of spiking neurons," *IEEE Trans. Neural Networks*, vol. 14, no. 6, pp. 1569–1572, Nov. 2003.
- [10] A. L. Hodgkin and A. F. Huxley, "A quantitative description of membrane current and its application to conduction and excitation in nerve.," *J. Physiol.*, vol. 117, no. 4, pp. 500–44, Aug. 1952.
- [11] P. Dayan and L. Abbott, *Theoretical Neuroscience: Computational and Mathematical Modeling of Neural Systems*. The MIT Press, 2001.
- [12] M. London and M. Häusser, "Dendritic computation.," *Annu. Rev. Neurosci.*, vol. 28, no. 1, pp. 503–32, Jul. 2005.
- [13] D. Purves, *Neuroscience*, 3rd ed. Sunderland, Mass: Sinauer Associates, 2004.
- [14] S. Łęski, H. Lindén, T. Tetzlaff, K. H. Pettersen, and G. T. Einevoll, "Frequency dependence of signal power and spatial reach of the local field potential.," *PLoS Comput. Biol.*, vol. 9, no. 7, p. e1003137, Jul. 2013.
- [15] H. Lindén *et al.*, "Modeling the Spatial Reach of the LFP," *Neuron*, vol. 72, no. 5, pp. 859–872, Dec. 2011.
- [16] A. Destexhe and C. Bedard, "Local field potential," *Scholarpedia*, vol. 8, no. 8, p. 10713, 2013.
- [17] A. I. Mohammed, H. J. Gritton, H.-A. Tseng, M. E. Bucklin, Z. Yao, and X. Han, "An integrative approach for analyzing hundreds of neurons in task performing mice using wide-field calcium imaging," *Sci. Rep.*, vol. 6, no.

- August 2015, p. 20986, Feb. 2016.
- [18] A. Grinvald and R. Hildesheim, "VSDI: a new era in functional imaging of cortical dynamics.," *Nat. Rev. Neurosci.*, vol. 5, no. 11, pp. 874–85, Nov. 2004.
 - [19] D. Zecevic, W. Ross, and L. Cohen, "Voltage-sensitive dye," *Scholarpedia*, vol. 4, no. 3, p. 3355, 2009.
 - [20] G. Buzsáki and A. Draguhn, "Neuronal oscillations in cortical networks.," *Science*, vol. 304, no. 5679, pp. 1926–9, Jun. 2004.
 - [21] G. Buzsáki, *Rhythms of the brain*. Oxford New York: Oxford University Press, 2006.
 - [22] H. Berger, "Über das Elektroenkephalogramm des Menschen," *Arch. Psychiatr. Nervenkr.*, vol. 87, pp. 527–570, 1929.
 - [23] F. H. Lopes da Silva, T. H. van Lierop, C. F. Schrijer, and W. S. van Leeuwen, "Organization of thalamic and cortical alpha rhythms: spectra and coherences.," *Electroencephalogr. Clin. Neurophysiol.*, vol. 35, no. 6, pp. 627–39, Dec. 1973.
 - [24] S. W. Hughes and V. Crunelli, "Thalamic mechanisms of EEG alpha rhythms and their pathological implications.," *Neuroscientist*, vol. 11, no. 4, pp. 357–72, Aug. 2005.
 - [25] F. H. Lopes Da Silva and W. Storm Van Leeuwen, "The cortical source of the alpha rhythm," *Neurosci. Lett.*, vol. 6, no. 2–3, pp. 237–241, Nov. 1977.
 - [26] F. . Lopes da Silva, J. . Vos, J. Mooibroek, and A. van Rotterdam, "Relative contributions of intracortical and thalamo-cortical processes in the generation of alpha rhythms, revealed by partial coherence analysis," *Electroencephalogr. Clin. Neurophysiol.*, vol. 50, no. 5–6, pp. 449–456, Dec. 1980.
 - [27] S. Palva and J. M. Palva, "New vistas for α -frequency band oscillations," *Trends Neurosci.*, vol. 30, no. 4, pp. 150–158, Apr. 2007.
 - [28] E. D. Adrian and B. H. Matthews, "The interpretation of potential waves in the cortex.," *J. Physiol.*, vol. 81, no. 4, pp. 440–71, Jul. 1934.
 - [29] A. Bahramisharif, M. van Gerven, T. Heskes, and O. Jensen, "Covert attention allows for continuous control of brain-computer interfaces," *Eur. J. Neurosci.*, vol. 31, no. 8, pp. 1501–1508, Apr. 2010.
 - [30] B. F. Händel, T. Haarmeier, and O. Jensen, "Alpha oscillations correlate with the successful inhibition of unattended stimuli.," *J. Cogn. Neurosci.*, vol. 23, no. 9, pp. 2494–502, Sep. 2011.
 - [31] W. Klimesch, " α -band oscillations, attention, and controlled access to stored information.," *Trends Cogn. Sci.*, vol. 16, no. 12, pp. 606–17, Dec. 2012.
 - [32] O. Jensen, J. Gelfand, J. Kounios, and J. E. Lisman, "Oscillations in the alpha band (9–12 Hz) increase with memory load during retention in a short-term memory task.," *Cereb. Cortex*, vol. 12, no. 8, pp. 877–82, Aug. 2002.
 - [33] G. Pfurtscheller, "Induced Oscillations in the Alpha Band: Functional Meaning," *Epilepsia*, vol. 44, no. s12, pp. 2–8, Dec. 2003.
 - [34] W. Klimesch, P. Sauseng, and S. Hanslmayr, "EEG alpha oscillations: the inhibition-timing hypothesis.," *Brain Res. Rev.*, vol. 53, no. 1, pp. 63–88, Jan. 2007.
 - [35] O. Jensen, B. Gips, T. O. Bergmann, and M. Bonnefond, "Temporal coding

- organized by coupled alpha and gamma oscillations prioritize visual processing,” *Trends Neurosci.*, vol. 37, no. 7, pp. 357–69, Jul. 2014.
- [36] S. Haegens, V. Nácher, R. Luna, R. Romo, and O. Jensen, “ α -Oscillations in the monkey sensorimotor network influence discrimination performance by rhythmical inhibition of neuronal spiking,” *Proc. Natl. Acad. Sci. U. S. A.*, vol. 108, no. 48, pp. 19377–82, Nov. 2011.
- [37] P. Fries, D. Nikolić, and W. Singer, “The gamma cycle,” *Trends Neurosci.*, vol. 30, no. 7, pp. 309–16, Jul. 2007.
- [38] M. Bartos, I. Vida, and P. Jonas, “Synaptic mechanisms of synchronized gamma oscillations in inhibitory interneuron networks,” *Nat. Rev. Neurosci.*, vol. 8, no. 1, pp. 45–56, 2007.
- [39] P. Tiesinga and T. J. Sejnowski, “Cortical enlightenment: are attentional gamma oscillations driven by ING or PING?,” *Neuron*, vol. 63, no. 6, pp. 727–32, Sep. 2009.
- [40] M. J. Roberts *et al.*, “Robust gamma coherence between macaque V1 and V2 by dynamic frequency matching,” *Neuron*, vol. 78, no. 3, pp. 523–36, May 2013.
- [41] E. Lowet, M. J. Roberts, C. A. Bosman, P. Fries, and P. De Weerd, “Areas V1 and V2 show microsaccade-related 3-4-Hz covariation in gamma power and frequency,” *Eur. J. Neurosci.*, vol. 43, no. 10, pp. 1286–1296, May 2016.
- [42] E. Lowet, M. Roberts, A. Hadjipapas, A. Peter, J. van der Eerden, and P. De Weerd, “Input-Dependent Frequency Modulation of Cortical Gamma Oscillations Shapes Spatial Synchronization and Enables Phase Coding,” *PLOS Comput. Biol.*, vol. 11, no. 2, p. e1004072, Feb. 2015.
- [43] A. Hadjipapas, E. Lowet, M. J. Roberts, A. Peter, and P. De Weerd, “Parametric variation of gamma frequency and power with luminance contrast: A comparative study of human MEG and monkey LFP and spike responses,” *Neuroimage*, vol. 112, pp. 327–340, May 2015.
- [44] X. Jia, D. Xing, and A. Kohn, “No consistent relationship between gamma power and peak frequency in macaque primary visual cortex,” *J Neurosci*, vol. 33, no. 1, pp. 17–25, Jan. 2013.
- [45] S. Ray and J. H. R. Maunsell, “Differences in gamma frequencies across visual cortex restrict their possible use in computation,” *Neuron*, vol. 67, no. 5, pp. 885–96, Sep. 2010.
- [46] R. D. Traub, M. a Whittington, S. B. Colling, G. Buzsáki, and J. G. Jefferys, “Analysis of gamma rhythms in the rat hippocampus in vitro and in vivo,” *J. Physiol.*, vol. 493 (Pt 2), pp. 471–84, Jun. 1996.
- [47] C. von der Malsburg, “The Correlation Theory of Brain Function,” in *Models of Neural Networks: Temporal Aspects of Coding and Information Processing in Biological Systems*, E. Domany, J. L. van Hemmen, and K. Schulten, Eds. New York, NY: Springer New York, 1994, pp. 95–119.
- [48] S. Grossberg, “Adaptive pattern classification and universal recoding: II. Feedback, expectation, olfaction, illusions,” *Biol. Cybern.*, vol. 23, no. 4, pp. 187–202, Aug. 1976.
- [49] P. M. Milner, “A model for visual shape recognition,” *Psychol. Rev.*, vol. 81, no. 6, pp. 521–35, Nov. 1974.

- [50] W. Singer, "Neuronal synchrony: a versatile code for the definition of relations?," *Neuron*, vol. 24, no. 1, pp. 49–65, 111–25, Sep. 1999.
- [51] P. Fries, "A mechanism for cognitive dynamics: neuronal communication through neuronal coherence.," *Trends Cogn. Sci.*, vol. 9, no. 10, pp. 474–80, Oct. 2005.
- [52] F. Varela, J. P. Lachaux, E. Rodriguez, and J. Martinerie, "The brainweb: phase synchronization and large-scale integration.," *Nat. Rev. Neurosci.*, vol. 2, no. 4, pp. 229–239, 2001.
- [53] S. L. Bressler, R. Coppola, and R. Nakamura, "Episodic multiregional cortical coherence at multiple frequencies during visual task performance," *Nature*, vol. 366, no. 6451, pp. 153–156, Nov. 1993.
- [54] M. N. Havenith, S. Yu, J. Biederlack, N.-H. Chen, W. Singer, and D. Nikolić, "Synchrony makes neurons fire in sequence, and stimulus properties determine who is ahead.," *J. Neurosci.*, vol. 31, no. 23, pp. 8570–84, Jun. 2011.
- [55] Z. Nadasdy, "Information encoding and reconstruction from the phase of action potentials.," *Front. Syst. Neurosci.*, vol. 3, no. July, p. 6, Jan. 2009.
- [56] L. de Almeida, M. Idiart, and J. E. Lisman, "A second function of gamma frequency oscillations: an E%-max winner-take-all mechanism selects which cells fire.," *J. Neurosci.*, vol. 29, no. 23, pp. 7497–503, Jun. 2009.
- [57] M. S. Olufsen, M. A. Whittington, M. Camperi, and N. Kopell, "New roles for the gamma rhythm: population tuning and preprocessing for the Beta rhythm.," *J. Comput. Neurosci.*, vol. 14, no. 1, pp. 33–54.
- [58] O. Jensen and L. L. Colgin, "Cross-frequency coupling between neuronal oscillations.," *Trends Cogn. Sci.*, vol. 11, no. 7, pp. 267–9, Jul. 2007.
- [59] I. Soltesz and M. Deschênes, "Low- and high-frequency membrane potential oscillations during theta activity in CA1 and CA3 pyramidal neurons of the rat hippocampus under ketamine-xylazine anesthesia.," *J. Neurophysiol.*, vol. 70, no. 1, pp. 97–116, Jul. 1993.
- [60] a Bragin, G. Jandó, Z. Nadasdy, J. Hetke, K. Wise, and G. Buzsáki, "Gamma (40–100 Hz) oscillation in the hippocampus of the behaving rat.," *J. Neurosci.*, vol. 15, no. 1 Pt 1, pp. 47–60, Jan. 1995.
- [61] P. Lakatos, A. S. Shah, K. H. Knuth, I. Ulbert, G. Karmos, and C. E. Schroeder, "An oscillatory hierarchy controlling neuronal excitability and stimulus processing in the auditory cortex.," *J Neurophysiol*, vol. 94, no. 3, pp. 1904–1911, Sep. 2005.
- [62] R. T. Canolty *et al.*, "High gamma power is phase-locked to theta oscillations in human neocortex.," *Science*, vol. 313, no. 5793, pp. 1626–8, Sep. 2006.
- [63] F. Mormann *et al.*, "Phase/amplitude reset and theta-gamma interaction in the human medial temporal lobe during a continuous word recognition memory task," *Hippocampus*, vol. 15, no. 7, pp. 890–900, 2005.
- [64] B. Lega, J. Burke, J. Jacobs, and M. J. Kahana, "Slow-Theta-to-Gamma Phase-Amplitude Coupling in Human Hippocampus Supports the Formation of New Episodic Memories," *Cereb. Cortex*, vol. 26, no. 1, pp. 268–278, Jan. 2016.
- [65] J. López-Azcárate, M. J. Nicolás, I. Cordon, M. Alegre, M. Valencia, and J. Artieda, "Delta-mediated cross-frequency coupling organizes oscillatory activity across the rat cortico-basal ganglia network," *Front. Neural Circuits*,

- vol. 7, no. October, p. 155, 2013.
- [66] F. Roux, M. Wibral, W. Singer, J. Aru, and P. J. Uhlhaas, "The phase of thalamic alpha activity modulates cortical gamma-band activity: evidence from resting-state MEG recordings.," *J. Neurosci.*, vol. 33, no. 45, pp. 17827–35, Nov. 2013.
- [67] D. Osipova, D. Hermes, and O. Jensen, "Gamma power is phase-locked to posterior alpha activity.," *PLoS One*, vol. 3, no. 12, p. e3990, Jan. 2008.
- [68] R. T. Canolty and R. T. Knight, "The functional role of cross-frequency coupling.," *Trends Cogn. Sci.*, vol. 14, no. 11, pp. 506–15, Nov. 2010.
- [69] J. E. Lisman and O. Jensen, "The θ - γ neural code.," *Neuron*, vol. 77, no. 6, pp. 1002–16, Mar. 2013.
- [70] A. C. Heusser, D. Poeppel, Y. Ezzyat, and L. Davachi, "Episodic sequence memory is supported by a theta-gamma phase code.," *Nat. Neurosci.*, vol. 19, no. August, p. In Revision, 2016.
- [71] A. N. Landau and P. Fries, "Attention Samples Stimuli Rhythmically," *Curr. Biol.*, vol. 22, no. 11, pp. 1000–1004, Jun. 2012.
- [72] A. Bollimunta, J. Mo, C. E. Schroeder, and M. Ding, "Neuronal mechanisms and attentional modulation of corticothalamic α oscillations.," *J. Neurosci.*, vol. 31, no. 13, pp. 4935–4943, 2011.
- [73] A. C. Snyder, M. J. Morais, C. M. Willis, and M. A. Smith, "Global network influences on local functional connectivity," *Nat. Neurosci.*, vol. 18, no. 5, pp. 736–743, Mar. 2015.
- [74] R. VanRullen, B. Zoefel, and B. Ilhan, "On the cyclic nature of perception in vision versus audition," *Philos. Trans. R. Soc. B Biol. Sci.*, vol. 369, no. 1641, pp. 20130214–20130214, Mar. 2014.
- [75] E. Spaak, M. Bonnefond, A. Maier, D. a Leopold, and O. Jensen, "Layer-specific entrainment of γ -band neural activity by the α rhythm in monkey visual cortex.," *Curr. Biol.*, vol. 22, no. 24, pp. 2313–8, Dec. 2012.
- [76] B. L. Foster and J. Parvizi, "Resting oscillations and cross-frequency coupling in the human posteromedial cortex.," *Neuroimage*, vol. 60, no. 1, pp. 384–91, Mar. 2012.
- [77] Y. B. Saalmann, M. a Pinsk, L. Wang, X. Li, and S. Kastner, "The pulvinar regulates information transmission between cortical areas based on attention demands.," *Science*, vol. 337, no. 6095, pp. 753–6, Aug. 2012.
- [78] W. Singer and C. M. Gray, "Visual Feature Integration and the Temporal Correlation Hypothesis," *Annu. Rev. Neurosci.*, vol. 18, no. 1, pp. 555–586, Mar. 1995.
- [79] A. K. Engel and W. Singer, "Temporal binding and the neural correlates of sensory awareness," *Trends Cogn. Sci.*, vol. 5, no. 1, pp. 16–25, 2001.
- [80] T. Miconi and R. VanRullen, "The Gamma Slideshow: Object-Based Perceptual Cycles in a Model of the Visual Cortex," *Front. Hum. Neurosci.*, vol. 4, no. November, p. 205, 2010.
- [81] S. Panzeri, J. H. Macke, J. Gross, and C. Kayser, "Neural population coding: combining insights from microscopic and mass signals," *Trends Cogn. Sci.*, vol. 19, no. 3, pp. 162–172, 2015.
- [82] J. O'Keefe and M. L. Recce, "Phase relationship between hippocampal place

- units and the EEG theta rhythm.," *Hippocampus*, vol. 3, no. 3, pp. 317–30, Jul. 1993.
- [83] O. Jensen and J. E. Lisman, "Position reconstruction from an ensemble of hippocampal place cells: contribution of theta phase coding.," *J. Neurophysiol.*, vol. 83, no. 5, pp. 2602–9, May 2000.
- [84] C. Kayser, M. a. Montemurro, N. K. Logothetis, and S. Panzeri, "Spike-Phase Coding Boosts and Stabilizes Information Carried by Spatial and Temporal Spike Patterns," *Neuron*, vol. 61, no. 4, pp. 597–608, 2009.
- [85] L. L. Colgin *et al.*, "Frequency of gamma oscillations routes flow of information in the hippocampus.," *Nature*, vol. 462, no. 7271, pp. 353–7, Nov. 2009.
- [86] M. a Belluscio, K. Mizuseki, R. Schmidt, R. Kempter, and G. Buzsáki, "Cross-frequency phase-phase coupling between θ and γ oscillations in the hippocampus.," *J. Neurosci.*, vol. 32, no. 2, pp. 423–35, Jan. 2012.
- [87] A. B. L. Tort, R. W. Komorowski, J. R. Manns, N. J. Kopell, and H. Eichenbaum, "Theta-gamma coupling increases during the learning of item-context associations.," *Proc. Natl. Acad. Sci. U. S. A.*, vol. 106, no. 49, pp. 20942–7, Dec. 2009.
- [88] A. Hyafil, L. Fontolan, C. Kabdebon, B. Gutkin, and A.-L. Giraud, "Speech encoding by coupled cortical theta and gamma oscillations," *Elife*, vol. 4, pp. 1–23, May 2015.
- [89] J. Huxter, N. Burgess, and J. O'Keefe, "Independent rate and temporal coding in hippocampal pyramidal cells.," *Nature*, vol. 425, no. 6960, pp. 828–832, 2003.
- [90] J. R. Huxter, T. J. Senior, K. Allen, and J. Csicsvari, "Theta phase-specific codes for two-dimensional position, trajectory and heading in the hippocampus.," *Nat. Neurosci.*, vol. 11, no. 5, pp. 587–94, May 2008.
- [91] H. Hirase, A. Czurkó, J. Csicsvari, and G. Buzsáki, "Firing rate and theta-phase coding by hippocampal pyramidal neurons during 'space clamping'.," *Eur. J. Neurosci.*, vol. 11, no. 12, pp. 4373–80, Dec. 1999.
- [92] O. Jensen, "Information Transfer Between Rhythmically Coupled Networks: Reading the Hippocampal Phase Code," *Neural Comput.*, vol. 13, no. 12, pp. 2743–2761, Dec. 2001.
- [93] E. Hairer and G. Wanner, *Solving ordinary differential equations II. Stiff and differential-algebraic problems*, vol. 1. Springer-Verlag, Berlin, 1991.
- [94] M. Pospischil *et al.*, "Minimal Hodgkin-Huxley type models for different classes of cortical and thalamic neurons.," *Biol. Cybern.*, vol. 99, no. 4–5, pp. 427–41, Nov. 2008.
- [95] O. Jensen, P. Goel, N. Kopell, M. Pohja, R. Hari, and B. Ermentrout, "On the human sensorimotor-cortex beta rhythm: sources and modeling.," *Neuroimage*, vol. 26, no. 2, pp. 347–55, Jun. 2005.
- [96] W. E. Vinje and J. L. Gallant, "Sparse coding and decorrelation in primary visual cortex during natural vision.," *Science*, vol. 287, no. 5456, pp. 1273–6, Feb. 2000.
- [97] J. J. Knierim and D. C. van Essen, "Neuronal responses to static texture patterns in area V1 of the alert macaque monkey.," *J. Neurophysiol.*, vol. 67,

- no. 4, pp. 961–80, Apr. 1992.
- [98] J. N. Mercer, C. S. Chan, T. Tkatch, J. Held, and D. J. Surmeier, “Nav1.6 sodium channels are critical to pacemaking and fast spiking in globus pallidus neurons,” *J. Neurosci.*, vol. 27, no. 49, pp. 13552–13566, 2007.
- [99] D. Curtis and J. Eccles, “The time courses of excitatory and inhibitory synaptic actions,” *J. Physiol.*, vol. 145, no. 3, pp. 529–546, Mar. 1959.
- [100] G. Buzsáki and X.-J. Wang, “Mechanisms of gamma oscillations,” *Annu. Rev. Neurosci.*, vol. 35, pp. 203–25, Jan. 2012.
- [101] M. a Whittington, M. O. Cunningham, F. E. N. LeBeau, C. Racca, and R. D. Traub, “Multiple origins of the cortical γ rhythm,” *Dev. Neurobiol.*, vol. 71, no. 1, pp. 92–106, Jan. 2011.
- [102] D. Lozano-Soldevilla, N. ter Huurne, R. Cools, and O. Jensen, “GABAergic Modulation of Visual Gamma and Alpha Oscillations and Its Consequences for Working Memory Performance,” *Curr. Biol.*, vol. 24, no. 24, pp. 2878–2887, 2014.
- [103] M. Vinck, T. Womelsdorf, E. a Buffalo, R. Desimone, and P. Fries, “Attentional Modulation of Cell-Class-Specific Gamma-Band Synchronization in Awake Monkey Area V4,” *Neuron*, vol. 80, no. 4, pp. 1077–1089, 2013.
- [104] D. C. Somers, S. B. Nelson, and M. Sur, “An emergent model of orientation selectivity in cat visual cortical simple cells,” *J. Neurosci.*, vol. 15, no. 8, pp. 5448–65, Aug. 1995.
- [105] P. Buzás, K. Kovács, A. S. Ferecskó, J. M. L. Budd, U. T. Eysel, and Z. F. Kisvárday, “Model-based analysis of excitatory lateral connections in the visual cortex,” *J. Comp. Neurol.*, vol. 499, no. 6, pp. 861–81, Dec. 2006.
- [106] W. H. Bosking, Y. Zhang, B. Schofield, and D. Fitzpatrick, “Orientation Selectivity and the Arrangement of Horizontal Connections in Tree Shrew Striate Cortex,” *J. Neurosci.*, vol. 17, no. 6, pp. 2112–2127, Mar. 1997.
- [107] B. Hille, *Ion Channels of Excitable Membranes*, 2nd ed. Sinauer Associates, 1992.
- [108] G. R. Holt and C. Koch, “Electrical interactions via the extracellular potential near cell bodies,” *J. Comput. Neurosci.*, vol. 6, no. 2, pp. 169–84, 1999.
- [109] M. W. Reimann, C. a Anastassiou, R. Perin, S. L. Hill, H. Markram, and C. Koch, “A biophysically detailed model of neocortical local field potentials predicts the critical role of active membrane currents,” *Neuron*, vol. 79, no. 2, pp. 375–90, Jul. 2013.
- [110] I. S. Gradshteyn and I. M. Ryzhik, *Table of Integrals, Series, and Products*, 7th ed. Academic Press, 2007.
- [111] W. H. Press, S. A. Teukolsky, W. T. Vetterling, and B. P. Flannery, *Numerical Recipes 3rd Edition: The Art of Scientific Computing*, 3rd ed. Cambridge University Press, 2007.
- [112] A. Mazzoni, H. Lindén, H. Cuntz, A. Lansner, S. Panzeri, and G. T. Einevoll, “Computing the Local Field Potential (LFP) from Integrate-and-Fire Network Models,” *PLoS Comput. Biol.*, vol. 11, no. 12, p. e1004584, Dec. 2015.
- [113] A. B. L. Tort, R. Komorowski, H. Eichenbaum, and N. Kopell, “Measuring phase-amplitude coupling between neuronal oscillations of different frequencies,” *J. Neurophysiol.*, vol. 104, no. 2, pp. 1195–210, Aug. 2010.

- [114] J. Hartigan and M. Wong, "Algorithm AS 136: A k-means clustering algorithm," *Appl. Stat.*, vol. 28, no. 1, pp. 100–108, 1979.
- [115] P. J. Rousseeuw, "Silhouettes: A graphical aid to the interpretation and validation of cluster analysis," *J. Comput. Appl. Math.*, vol. 20, pp. 53–65, Nov. 1987.
- [116] B. Efron, "Bootstrap Methods: Another Look at the Jackknife," *Ann. Stat.*, vol. 7, no. 1, pp. 1–26, Jan. 1979.
- [117] S. W. Hughes *et al.*, "Synchronized oscillations at alpha and theta frequencies in the lateral geniculate nucleus.," *Neuron*, vol. 42, no. 2, pp. 253–68, Apr. 2004.
- [118] Y. B. Saalman and S. Kastner, "Cognitive and perceptual functions of the visual thalamus.," *Neuron*, vol. 71, no. 2, pp. 209–23, Jul. 2011.
- [119] J. Aru *et al.*, "Untangling cross-frequency coupling in neuroscience.," *Curr. Opin. Neurobiol.*, vol. 31, pp. 51–61, 2014.
- [120] H. Lee, G. V. Simpson, N. K. Logothetis, and G. Rainer, "Phase locking of single neuron activity to theta oscillations during working memory in monkey extrastriate visual cortex," *Neuron*, vol. 45, no. 1, pp. 147–156, 2005.
- [121] M. A. Montemurro, M. J. Rasch, Y. Murayama, N. K. Logothetis, and S. Panzeri, "Phase-of-Firing Coding of Natural Visual Stimuli in Primary Visual Cortex," *Curr. Biol.*, vol. 18, no. 5, pp. 375–380, Mar. 2008.
- [122] H. K. Turesson, N. K. Logothetis, and K. L. Hoffman, "Category-selective phase coding in the superior temporal sulcus.," *Proc. Natl. Acad. Sci. U. S. A.*, vol. 109, no. 47, pp. 19438–43, 2012.
- [123] M. Vinck *et al.*, "Gamma-phase shifting in awake monkey visual cortex.," *J. Neurosci.*, vol. 30, no. 4, pp. 1250–1257, Jan. 2010.
- [124] M. Siegel, M. R. Warden, and E. K. Miller, "Phase-dependent neuronal coding of objects in short-term memory.," *Proc. Natl. Acad. Sci. U. S. A.*, vol. 106, no. 50, pp. 21341–21346, 2009.
- [125] D. Hubel and T. Wiesel, "Receptive fields of single neurones in the cat's striate cortex.," *J. Physiol.*, vol. 148, no. Pt 12, pp. 574–91, Oct. 1959.
- [126] D. Hubel and T. Wiesel, "Receptive fields, binocular interaction and functional architecture in the cat's visual cortex.," *J. Physiol.*, vol. 160, pp. 106–54, Jan. 1962.
- [127] S. Vijayan and N. J. Kopell, "Thalamic model of awake alpha oscillations and implications for stimulus processing.," *Proc. Natl. Acad. Sci. U. S. A.*, vol. 109, no. 45, pp. 18553–8, Nov. 2012.
- [128] G. Pfurtscheller and F. H. Lopes da Silva, "Event-related EEG/MEG synchronization and desynchronization: basic principles.," *Clin. Neurophysiol.*, vol. 110, no. 11, pp. 1842–57, Nov. 1999.
- [129] M. S. Worden, J. J. Foxe, N. Wang, and G. V Simpson, "Anticipatory biasing of visuospatial attention indexed by retinotopically specific alpha-band electroencephalography increases over occipital cortex.," *J. Neurosci.*, vol. 20, no. 6, p. RC63, 2000.
- [130] N. Hoogenboom, J.-M. Schoffelen, R. Oostenveld, L. M. Parkes, and P. Fries, "Localizing human visual gamma-band activity in frequency, time and space.," *Neuroimage*, vol. 29, no. 3, pp. 764–73, Feb. 2006.

- [131] R. Scheeringa *et al.*, “Neuronal dynamics underlying high- and low-frequency EEG oscillations contribute independently to the human BOLD signal,” *Neuron*, vol. 69, no. 3, pp. 572–83, Feb. 2011.
- [132] J. Gross, J. Kujala, M. Hamalainen, L. Timmermann, A. Schnitzler, and R. Salmelin, “Dynamic imaging of coherent sources: Studying neural interactions in the human brain,” *Proc. Natl. Acad. Sci. U. S. A.*, vol. 98, no. 2, pp. 694–699, Jan. 2001.
- [133] S. Ray and J. H. R. Maunsell, “Different origins of gamma rhythm and high-gamma activity in macaque visual cortex,” *PLoS Biol.*, vol. 9, no. 4, p. e1000610, Apr. 2011.
- [134] X.-J. Wang, “Neurophysiological and Computational Principles of Cortical Rhythms in Cognition,” *Physiol. Rev.*, vol. 90, no. 3, pp. 1195–1268, Jul. 2010.
- [135] M. L. Lorincz, K. a Kékesi, G. Juhász, V. Crunelli, and S. W. Hughes, “Temporal framing of thalamic relay-mode firing by phasic inhibition during the alpha rhythm,” *Neuron*, vol. 63, no. 5, pp. 683–96, Sep. 2009.
- [136] M. R. Mehta, A. K. Lee, and M. A. Wilson, “Role of experience and oscillations in transforming a rate code into a temporal code,” *Nature*, vol. 417, no. 6890, pp. 741–6, Jun. 2002.
- [137] M. V Tsodyks, W. E. Skaggs, T. J. Sejnowski, and B. L. McNaughton, “Population dynamics and theta rhythm phase precession of hippocampal place cell firing: a spiking neuron model,” *Hippocampus*, vol. 6, no. 3, pp. 271–80, 1996.
- [138] O. Jensen and J. E. Lisman, “Hippocampal CA3 region predicts memory sequences: accounting for the phase precession of place cells,” *Learn. Mem.*, vol. 3, no. 2–3, pp. 279–287, Jan. 1996.
- [139] M. J. Jutras, P. Fries, and E. a Buffalo, “Oscillatory activity in the monkey hippocampus during visual exploration and memory formation,” *Proc. Natl. Acad. Sci.*, vol. 110, no. 32, pp. 13144–13149, Aug. 2013.
- [140] A. J. Watrous, D. J. Lee, A. Izadi, G. G. Gurkoff, K. Shahlaie, and A. D. Ekstrom, “A comparative study of human and rat hippocampal low-frequency oscillations during spatial navigation,” *Hippocampus*, vol. 23, no. 8, pp. 656–661, Aug. 2013.
- [141] P. B. Sederberg, M. J. Kahana, M. W. Howard, E. J. Donner, and J. R. Madsen, “Theta and gamma oscillations during encoding predict subsequent recall,” *J. Neurosci.*, vol. 23, no. 34, pp. 10809–14, Nov. 2003.
- [142] N. Axmacher, M. M. Henseler, O. Jensen, I. Weinreich, C. E. Elger, and J. Fell, “Cross-frequency coupling supports multi-item working memory in the human hippocampus,” *Proc. Natl. Acad. Sci.*, vol. 107, no. 7, pp. 3228–3233, Feb. 2010.
- [143] R. Efron, “The minimum duration of a perception,” *Neuropsychologia*, vol. 8, no. 1, pp. 57–63, Jan. 1970.
- [144] G. Buzsáki, P. Rappelsberger, and L. Kellényi, “Depth profiles of hippocampal rhythmic slow activity (‘theta rhythm’) depend on behaviour,” *Electroencephalogr. Clin. Neurophysiol.*, vol. 61, no. 1, pp. 77–88, Jul. 1985.
- [145] O. Jensen and A. Mazaheri, “Shaping functional architecture by oscillatory alpha activity: gating by inhibition,” *Front. Hum. Neurosci.*, vol. 4, no.

- November, p. 186, Jan. 2010.
- [146] J. J. Foxe and A. C. Snyder, "The role of alpha-band brain oscillations as a sensory suppression mechanism during selective attention," *Front. Psychol.*, vol. 2, no. JUL, pp. 1–13, 2011.
 - [147] C. A. Bosman, T. Womelsdorf, R. Desimone, and P. Fries, "A microsaccadic rhythm modulates gamma-band synchronization and behavior.," *J. Neurosci.*, vol. 29, no. 30, pp. 9471–80, Jul. 2009.
 - [148] J. Ito, P. Maldonado, W. Singer, and S. Grün, "Saccade-related modulations of neuronal excitability support synchrony of visually elicited spikes.," *Cereb. Cortex*, vol. 21, no. 11, pp. 2482–97, Nov. 2011.
 - [149] C. Rajkai, P. Lakatos, C.-M. Chen, Z. Pincze, G. Karmos, and C. E. Schroeder, "Transient cortical excitation at the onset of visual fixation.," *Cereb. Cortex*, vol. 18, no. 1, pp. 200–9, Jan. 2008.
 - [150] P. Andersen and S. A. Andersson, *Physiological basis of the alpha rhythm*, vol. 1. Plenum Publishing Corporation, 1968.
 - [151] A. Bollimunta, Y. Chen, C. E. Schroeder, and M. Ding, "Neuronal mechanisms of cortical alpha oscillations in awake-behaving macaques.," *J. Neurosci.*, vol. 28, no. 40, pp. 9976–88, Oct. 2008.
 - [152] A. Viriyopase, R.-M. Memmesheimer, and S. Gielen, "Cooperation and competition of gamma oscillation mechanisms.," *J. Neurophysiol.*, vol. 116, no. 2, pp. 232–51, Aug. 2016.
 - [153] S. W. Hughes *et al.*, "Thalamic Gap Junctions Control Local Neuronal Synchrony and Influence Macroscopic Oscillation Amplitude during EEG Alpha Rhythms.," *Front. Psychol.*, vol. 2, no. August, p. 193, Jan. 2011.
 - [154] S. Ching, A. Cimenser, P. L. Purdon, E. N. Brown, and N. J. Kopell, "Thalamocortical model for a propofol-induced alpha-rhythm associated with loss of consciousness.," *Proc. Natl. Acad. Sci. U. S. A.*, vol. 107, no. 52, pp. 22665–70, Dec. 2010.
 - [155] M. L. Lorincz, V. Crunelli, and S. W. Hughes, "Cellular Dynamics of Cholinergically Induced (8–13 Hz) Rhythms in Sensory Thalamic Nuclei In Vitro," *J. Neurosci.*, vol. 28, no. 3, pp. 660–671, Jan. 2008.
 - [156] A. A. Fingelkurts and A. A. Fingelkurts, "Timing in cognition and EEG brain dynamics: discreteness versus continuity," *Cogn. Process.*, vol. 7, no. 3, pp. 135–162, Sep. 2006.
 - [157] R. VanRullen, "Perceptual Cycles," *Trends Cogn. Sci.*, vol. 20, no. 10, pp. 723–735, Oct. 2016.
 - [158] B. Gips, J. P. J. M. van der Eerden, and O. Jensen, "A biologically plausible mechanism for neuronal coding organized by the phase of alpha oscillations.," *Eur. J. Neurosci.*, vol. 44, no. 4, pp. 2147–61, Aug. 2016.
 - [159] G. Buzsáki, "The thalamic clock: Emergent network properties," *Neuroscience*, vol. 41, no. 2–3, pp. 351–364, Jan. 1991.
 - [160] T. Bal and D. A. McCormick, "Mechanisms of oscillatory activity in guinea-pig nucleus reticularis thalami in vitro: a mammalian pacemaker.," *J. Physiol.*, vol. 468, pp. 669–91, Aug. 1993.
 - [161] R. Hindriks and M. J. A. M. van Putten, "Thalamo-cortical mechanisms underlying changes in amplitude and frequency of human alpha

- oscillations," *Neuroimage*, vol. 70, pp. 150–163, Apr. 2013.
- [162] M. A. Long, "Small Clusters of Electrically Coupled Neurons Generate Synchronous Rhythms in the Thalamic Reticular Nucleus," *J. Neurosci.*, vol. 24, no. 2, pp. 341–349, Jan. 2004.
- [163] K. G. Thompson, "Neuronal Basis of Covert Spatial Attention in the Frontal Eye Field," *J. Neurosci.*, vol. 25, no. 41, pp. 9479–9487, Oct. 2005.
- [164] T. Moore and M. Fallah, "Microstimulation of the frontal eye field and its effects on covert spatial attention.," *J. Neurophysiol.*, vol. 91, no. 1, pp. 152–62, Jan. 2004.
- [165] S. Yantis *et al.*, "Transient neural activity in human parietal cortex during spatial attention shifts," *Nat. Neurosci.*, vol. 5, no. 10, pp. 995–1002, Sep. 2002.
- [166] M. Corbetta, G. L. Shulman, F. M. Miezin, and S. E. Petersen, "Superior parietal cortex activation during spatial attention shifts and visual feature conjunction.," *Science*, vol. 270, no. 5237, pp. 802–5, Nov. 1995.
- [167] J. R. Dormand and P. J. Prince, "A family of embedded Runge-Kutta formulae," *J. Comput. Appl. Math.*, vol. 6, no. 1, pp. 19–26, Mar. 1980.
- [168] A. Destexhe, T. Bal, D. A. McCormick, and T. J. Sejnowski, "Ionic mechanisms underlying synchronized oscillations and propagating waves in a model of ferret thalamic slices.," *J. Neurophysiol.*, vol. 76, no. 3, pp. 2049–70, Sep. 1996.
- [169] S. R. Crandall, S. J. Cruikshank, B. W. Connors, S. R. Crandall, S. J. Cruikshank, and B. W. Connors, "A Corticothalamic Switch: Controlling the Thalamus with Dynamic Synapses," *Neuron*, vol. 86, no. 3, pp. 1–15, 2015.
- [170] A. M. Thomson, "Neocortical layer 6, a review.," *Front. Neuroanat.*, vol. 4, no. March, p. 13, 2010.
- [171] F. Crick, "Function of the thalamic reticular complex: the searchlight hypothesis.," *Proc. Natl. Acad. Sci. U. S. A.*, vol. 81, no. 14, pp. 4586–90, Jul. 1984.
- [172] R. VanRullen and J. S. P. Macdonald, "Perceptual Echoes at 10 Hz in the Human Brain," *Curr. Biol.*, vol. 22, no. 11, pp. 995–999, Jun. 2012.
- [173] E. C. Lalor, B. A. Pearlmutter, R. B. Reilly, G. McDarby, and J. J. Foxe, "The VESPA: A method for the rapid estimation of a visual evoked potential," *Neuroimage*, vol. 32, no. 4, pp. 1549–1561, Oct. 2006.
- [174] P. Welch, "The use of fast Fourier transform for the estimation of power spectra: A method based on time averaging over short, modified periodograms," *IEEE Trans. Audio Electroacoust.*, vol. 15, no. 2, pp. 70–73, Jun. 1967.
- [175] R. Polge and E. Mitchell, "Impulse Response Determination by Cross Correlation," *IEEE Trans. Aerosp. Electron. Syst.*, vol. AES-6, no. 1, pp. 91–97, Jan. 1970.
- [176] K. McAlonan, J. Cavanaugh, and R. H. Wurtz, "Guarding the gateway to cortex with attention in visual thalamus," *Nature*, vol. 456, no. 7220, pp. 391–394, Nov. 2008.
- [177] X. J. Wang, "Multiple dynamical modes of thalamic relay neurons: rhythmic bursting and intermittent phase-locking," *Neuroscience*, vol. 59, no. 1, pp. 21–31, 1994.

- [178] S. M. Sherman, "Tonic and burst firing: dual modes of thalamocortical relay," *Trends Neurosci.*, vol. 24, no. 2, pp. 122–126, Feb. 2001.
- [179] J. J. Zhu, D. J. Uhrich, and W. W. Lytton, "Burst firing in identified rat geniculate interneurons.," *Neuroscience*, vol. 91, no. 4, pp. 1445–60, Jan. 1999.
- [180] D. A. McCormick and H. R. Feeseer, "Functional implications of burst firing and single spike activity in lateral geniculate relay neurons," *Neuroscience*, vol. 39, no. 1, pp. 103–113, Jan. 1990.
- [181] A. M. Bastos, F. Briggs, H. J. Alitto, G. R. Mangun, and W. M. Usrey, "Simultaneous Recordings from the Primary Visual Cortex and Lateral Geniculate Nucleus Reveal Rhythmic Interactions and a Cortical Source for Gamma-Band Oscillations," *J. Neurosci.*, vol. 34, no. 22, pp. 7639–7644, 2014.
- [182] H. Jahnsen and R. Llinás, "Electrophysiological properties of guinea-pig thalamic neurones: an in vitro study.," *J. Physiol.*, vol. 349, pp. 205–26, Apr. 1984.
- [183] S. Makeig *et al.*, "Dynamic brain sources of visual evoked responses.," *Science*, vol. 295, no. 5555, pp. 690–4, Jan. 2002.
- [184] J. Cui, W. Wong, and S. Mann, "Time-frequency analysis of visual evoked potentials by means of matching pursuit with chirplet atoms.," *Conf. Proc. ... Annu. Int. Conf. IEEE Eng. Med. Biol. Soc. IEEE Eng. Med. Biol. Soc. Annu. Conf.*, vol. 1, pp. 267–70, 2004.
- [185] P. a Rhodes and R. Llinás, "A model of thalamocortical relay cells.," *J. Physiol.*, vol. 565, no. Pt 3, pp. 765–81, Jun. 2005.
- [186] O. Jensen, B. Gips, T. O. Bergmann, and M. Bonnefond, "Temporal coding organized by coupled alpha and gamma oscillations prioritize visual processing," *Trends Neurosci.*, vol. 37, no. 7, 2014.
- [187] D. a McCormick and J. R. Huguenard, "A model of the electrophysiological properties of thalamocortical relay neurons.," *J. Neurophysiol.*, vol. 68, no. 4, pp. 1384–1400, 1992.
- [188] F. Sala and A. Hernández-Cruz, "Calcium diffusion modeling in a spherical neuron. Relevance of buffering properties.," *Biophys. J.*, vol. 57, no. 2, pp. 313–24, 1990.
- [189] A. M. Sillito and H. E. Jones, "Corticothalamic interactions in the transfer of visual information.," *Philos. Trans. R. Soc. Lond. B. Biol. Sci.*, vol. 357, no. 1428, pp. 1739–52, Dec. 2002.
- [190] J. Cudeiro and A. M. Sillito, "Looking back: corticothalamic feedback and early visual processing.," *Trends Neurosci.*, vol. 29, no. 6, pp. 298–306, Jun. 2006.
- [191] H. J. Alitto and W. M. Usrey, "Dissecting the Dynamics of Corticothalamic Feedback," *Neuron*, vol. 86, no. 3, pp. 605–607, 2015.
- [192] F. H. Lopes da Silva, J. P. Pijn, D. Velis, and P. C. Nijssen, "Alpha rhythms: noise, dynamics and models.," *Int. J. Psychophysiol.*, vol. 26, no. 1–3, pp. 237–49, Jun. 1997.
- [193] H. J. Alitto and W. M. Usrey, "Corticothalamic feedback and sensory processing," *Curr. Opin. Neurobiol.*, vol. 13, no. Figure 2, pp. 440–445, 2003.
- [194] D. Pinault, "The thalamic reticular nucleus: structure, function and concept.," *Brain Res. Brain Res. Rev.*, vol. 46, no. 1, pp. 1–31, Aug. 2004.

- [195] B. M. Sayers, H. A. Beagley, and W. R. Henshall, "The mechanism of auditory evoked EEG responses.," *Nature*, vol. 247, no. 5441, pp. 481–3, Feb. 1974.
- [196] S. Hanslmayr *et al.*, "Alpha phase reset contributes to the generation of ERPs.," *Cereb. Cortex*, vol. 17, no. 1, pp. 1–8, Jan. 2007.
- [197] A. Mazaheri and O. Jensen, "Posterior alpha activity is not phase-reset by visual stimuli.," *Proc. Natl. Acad. Sci. U. S. A.*, vol. 103, no. 8, pp. 2948–52, Feb. 2006.
- [198] D. Kleinfeld, E. Ahissar, and M. E. Diamond, "Active sensation: insights from the rodent vibrissa sensorimotor system.," *Curr. Opin. Neurobiol.*, vol. 16, no. 4, pp. 435–44, Aug. 2006.
- [199] M. Wachowiak, "All in a Sniff: Olfaction as a Model for Active Sensing," *Neuron*, vol. 71, no. 6, pp. 962–73, Sep. 2011.
- [200] C. E. Schroeder, D. A. Wilson, T. Radman, H. Scharfman, and P. Lakatos, "Dynamics of Active Sensing and perceptual selection.," *Curr. Opin. Neurobiol.*, vol. 20, no. 2, pp. 172–6, Apr. 2010.
- [201] I. Kagan and Z. M. Hafed, "Active Vision: Microsaccades Direct the Eye to Where It Matters Most," *Curr. Biol.*, vol. 23, no. 17, pp. R712–R714, Sep. 2013.
- [202] S. Martinez-Conde, J. Otero-Millan, and S. L. Macknik, "The impact of microsaccades on vision: towards a unified theory of saccadic function," *Nat. Rev. Neurosci.*, vol. 14, no. 2, pp. 83–96, Jan. 2013.
- [203] J. Otero-Millan, X. G. Troncoso, S. L. Macknik, I. Serrano-Pedraza, and S. Martinez-Conde, "Saccades and microsaccades during visual fixation, exploration, and search: Foundations for a common saccadic generator," *J. Vis.*, vol. 8, no. 14, pp. 21–21, Dec. 2008.
- [204] S. Martinez-Conde, S. L. Macknik, X. G. Troncoso, and D. H. Hubel, "Microsaccades: a neurophysiological analysis," *Trends Neurosci.*, vol. 32, no. 9, pp. 463–475, Sep. 2009.
- [205] M. Rolf, "Microsaccades: small steps on a long way.," *Vision Res.*, vol. 49, no. 20, pp. 2415–41, Oct. 2009.
- [206] L. Melloni, C. M. Schwiedrzik, E. Rodriguez, and W. Singer, "(Micro)Saccades, corollary activity and cortical oscillations," *Trends Cogn. Sci.*, vol. 13, no. 6, pp. 239–245, Jun. 2009.
- [207] J. B. Reppas, W. M. Usrey, and R. C. Reid, "Saccadic eye movements modulate visual responses in the lateral geniculate nucleus.," *Neuron*, vol. 35, no. 5, pp. 961–74, Aug. 2002.
- [208] D. A. Leopold and N. K. Logothetis, "Microsaccades differentially modulate neural activity in the striate and extrastriate visual cortex," *Exp. Brain Res.*, vol. 123, no. 3, pp. 341–345, Nov. 1998.
- [209] S. Martinez-Conde, S. L. Macknik, and D. H. Hubel, "Microsaccadic eye movements and firing of single cells in the striate cortex of macaque monkeys.," *Nat. Neurosci.*, vol. 3, no. 3, pp. 251–8, Mar. 2000.
- [210] S. Martinez-Conde, S. L. Macknik, and D. H. Hubel, "The function of bursts of spikes during visual fixation in the awake primate lateral geniculate nucleus and primary visual cortex.," *Proc. Natl. Acad. Sci. U. S. A.*, vol. 99, no. 21, pp. 13920–5, Oct. 2002.
- [211] J. Ito, P. Maldonado, and S. Grün, "Cross-frequency interaction of the eye-

- movement related LFP signals in V1 of freely viewing monkeys.," *Front. Syst. Neurosci.*, vol. 7, p. 1, Jan. 2013.
- [212] E. Lowet, M. J. Roberts, A. Peter, B. Gips, and P. De Weerd, "Neuronal gamma-band synchronization regulated by instantaneous modulations of the oscillation frequency," *bioRxiv*, 2016.
- [213] M. Poletti, C. Listorti, and M. Rucci, "Microscopic Eye Movements Compensate for Nonhomogeneous Vision within the Fovea," *Curr. Biol.*, vol. 23, no. 17, pp. 1691–1695, Sep. 2013.
- [214] R. Engbert and R. Kliegl, "Microsaccades uncover the orientation of covert attention," *Vision Res.*, vol. 43, pp. 1035–1045, 2003.
- [215] R. Engbert, "Microsaccades: a microcosm for research on oculomotor control, attention, and visual perception," in *Progress in Brain Research*, vol. 154, no. SUPPL. A, 2006, pp. 177–192.
- [216] H. Collewijn and E. Kowler, "The significance of microsaccades for vision and oculomotor control," *J. Vis.*, vol. 8, no. 14, pp. 20–20, Dec. 2008.
- [217] M. Stokes and E. Spaak, "The Importance of Single-Trial Analyses in Cognitive Neuroscience," *Trends Cogn. Sci.*, vol. 20, no. 7, pp. 483–486, Jul. 2016.
- [218] J. Ito, P. Maldonado, and S. Gruen, "Cross-frequency coupling of eye-movement related LFP activities of freely viewing monkeys," *BMC Neuroscience*, vol. 12, p. P132, 2011.
- [219] E. Florin and S. Baillet, "The brain's resting-state activity is shaped by synchronized cross-frequency coupling of neural oscillations," *Neuroimage*, vol. 111, pp. 26–35, May 2015.
- [220] I. C. Fiebelkorn, Y. B. Saalman, and S. Kastner, "Rhythmic sampling within and between objects despite sustained attention at a cued location.," *Curr. Biol.*, vol. 23, no. 24, pp. 2553–8, Dec. 2013.
- [221] A. Landau and P. Fries, "Detection performance is modulated at a low-theta selection rhythm.," *J. Vis.*, vol. 11, no. 11, pp. 170–170, Sep. 2011.
- [222] M. C. Morrone, A. Tomassini, M. Jacono, D. Spinelli, and G. Sandini, "Rhythmic Oscillations of Visual Contrast Sensitivity Triggered by Voluntary Action and their Link to Perceived Time Compression," *Procedia - Soc. Behav. Sci.*, vol. 126, pp. 98–99, Mar. 2014.
- [223] T. Masquelier, G. Portelli, and P. Kornprobst, "Microsaccades enable efficient synchrony-based coding in the retina: a simulation study.," *Sci. Rep.*, vol. 6, p. 24086, 2016.
- [224] C. A. Bosman *et al.*, "Attentional Stimulus Selection through Selective Synchronization between Monkey Visual Areas," *Neuron*, vol. 75, no. 5, pp. 875–888, Sep. 2012.
- [225] S. Thorpe, A. Delorme, and R. Van Rullen, "Spike-based strategies for rapid processing," *Neural Networks*, vol. 14, pp. 715–725, 2001.
- [226] P. Maldonado, C. Babul, W. Singer, E. Rodriguez, D. Berger, and S. Grün, "Synchronization of neuronal responses in primary visual cortex of monkeys viewing natural images.," *J. Neurophysiol.*, vol. 100, no. 3, pp. 1523–32, 2008.
- [227] N. Brunet *et al.*, "Visual Cortical Gamma-Band Activity During Free Viewing of Natural Images.," *Cereb. Cortex*, pp. 1–9, Oct. 2013.
- [228] N. Kopell and G. B. Ermentrout, "Chapter 1 Mechanisms of phase-locking and

- frequency control in pairs of coupled neural oscillators," *Handb. Dyn. Syst.*, vol. 2, pp. 3–54, 2002.
- [229] E. M. Izhikevich, *Dynamical Systems in Neuroscience: The Geometry of Excitability and Bursting*, vol. 25, no. 1, 2007.
- [230] A. Pikovsky, M. Rosenblum, J. Kurths, and R. C. Hilborn, "Synchronization: A Universal Concept in Nonlinear Science," *Am. J. Phys.*, vol. 70, no. 6, p. 655, 2002.
- [231] V. A. F. Lamme and P. R. Roelfsema, "The distinct modes of vision offered by feedforward and recurrent processing," *Trends Neurosci.*, vol. 23, pp. 571–579, 2000.
- [232] T. Womelsdorf *et al.*, "Modulation of neuronal interactions through neuronal synchronization.," *Science*, vol. 316, pp. 1609–1612, 2007.
- [233] P. L. Boyland, "Bifurcations of circle maps: Arnol'd tongues, bistability and rotation intervals," *Commun. Math. Phys.*, vol. 106, no. 3, pp. 353–381, Sep. 1986.
- [234] A. Kepecs, "The Sniff as a Unit of Olfactory Processing," *Chem. Senses*, vol. 31, no. 2, pp. 167–179, Dec. 2005.
- [235] A. N. Landau and P. Fries, "Attention Samples Stimuli Rhythmically.," *Curr. Biol.*, vol. 22, no. 11, Jun. 2012.
- [236] C. C. H. Petersen, "Cortical Control of Whisker Movement," *Annu. Rev. Neurosci.*, vol. 37, no. 1, pp. 183–203, Jul. 2014.
- [237] D. Martin, C. Fowlkes, D. Tal, and J. Malik, "A database of human segmented natural images and its application to evaluating segmentation algorithms and measuring ecological statistics," *Proc. Eighth IEEE Int. Conf. Comput. Vision. ICCV 2001*, vol. 2, 2001.
- [238] J. P. Lachaux, E. Rodriguez, J. Martinerie, and F. J. Varela, "Measuring phase synchrony in brain signals.," *Hum. Brain Mapp.*, vol. 8, no. 4, pp. 194–208, 1999.
- [239] D. L. Ringach, R. M. Shapley, and M. J. Hawken, "Orientation selectivity in macaque V1: diversity and laminar dependence.," *J. Neurosci.*, vol. 22, no. 13, pp. 5639–51, Jul. 2002.
- [240] E. Lowet, M. Roberts, A. Peter, B. Gips, and P. De Weerd, "Synchronization principles of gamma rhythms in monkey visual cortex," *bioRxiv*, 2016.
- [241] J. B. Swettenham, S. D. Muthukumaraswamy, and K. D. Singh, "Spectral properties of induced and evoked gamma oscillations in human early visual cortex to moving and stationary stimuli.," *J. Neurophysiol.*, vol. 102, pp. 1241–1253, 2009.
- [242] S. P. Burns, D. Xing, M. J. Shelley, and R. M. Shapley, "Searching for autocohereance in the cortical network with a time-frequency analysis of the local field potential.," *J. Neurosci.*, vol. 30, no. 11, pp. 4033–47, Mar. 2010.
- [243] S. P. Burns, D. Xing, and R. M. Shapley, "Is gamma-band activity in the local field potential of V1 cortex a 'clock' or filtered noise?," *J. Neurosci.*, vol. 31, no. 26, pp. 9658–64, Jun. 2011.
- [244] M. Lundqvist, J. Rose, P. Herman, S. L. Brincat, T. J. Buschman, and E. K. Miller, "Gamma and Beta Bursts Underlie Working Memory," *Neuron*, vol. 90, no. 1, pp. 152–164, 2016.

- [245] O. David, J. M. Kilner, and K. J. Friston, "Mechanisms of evoked and induced responses in MEG/EEG," *Neuroimage*, vol. 31, no. 4, pp. 1580–1591, 2006.
- [246] C. Pantev, "Evoked and induced gamma band activity of the human cortex," *Brain Topogr.*, vol. 7, no. 321–33, pp. 321–330, 1995.
- [247] C. Tallon-Baudry, A. Kreiter, and O. Bertrand, "Sustained and transient oscillatory responses in the gamma and beta bands in a visual short-term memory task in humans.," *Vis. Neurosci.*, vol. 16, no. 3, pp. 449–59, May 1999.
- [248] C. Tallon-Baudry, "The roles of gamma-band oscillatory synchrony in human visual cognition," *Front. Biosci.*, vol. Volume, no. 14, p. 321, 2009.
- [249] L. Melloni, C. Molina, M. Pena, D. Torres, W. Singer, and E. Rodriguez, "Synchronization of Neural Activity across Cortical Areas Correlates with Conscious Perception," *J. Neurosci.*, vol. 27, no. 11, pp. 2858–2865, Mar. 2007.
- [250] D. A. Jeffreys, "Evoked Potential Studies of Face and Object Processing," *Vis. cogn.*, vol. 3, no. 1, pp. 1–38, Mar. 1996.
- [251] G. Sclar, J. H. Maunsell, and P. Lennie, "Coding of image contrast in central visual pathways of the macaque monkey.," *Vis. Res.*, vol. 30, no. 1, pp. 1–10, 1990.
- [252] D. Contreras and L. Palmer, "Response to Contrast of Electrophysiologically Defined Cell Classes in Primary Visual Cortex," *J. Neurosci.*, vol. 23, no. 17, pp. 6936–6945, Jul. 2003.
- [253] J. Schadow *et al.*, "Stimulus intensity affects early sensory processing: visual contrast modulates evoked gamma-band activity in human EEG.," *Int. J. Psychophysiol.*, vol. 66, no. 1, pp. 28–36, Oct. 2007.
- [254] T. Masquelier, E. Hugues, G. Deco, and S. J. Thorpe, "Oscillations, Phase-of-Firing Coding, and Spike Timing-Dependent Plasticity: An Efficient Learning Scheme," *J. Neurosci.*, vol. 29, no. 43, pp. 13484–13493, Oct. 2009.
- [255] P. Fries, "Rhythms for Cognition: Communication through Coherence," *Neuron*, vol. 88, no. 1. 2015.
- [256] X. Jia, M. A. Smith, and A. Kohn, "Stimulus Selectivity and Spatial Coherence of Gamma Components of the Local Field Potential," *J. Neurosci.*, vol. 31, no. 25, pp. 9390–9403, Jun. 2011.
- [257] B. J. A. Palanca and G. C. DeAngelis, "Does Neuronal Synchrony Underlie Visual Feature Grouping?," *Neuron*, vol. 46, no. 2, pp. 333–346, Apr. 2005.
- [258] R. Eckhorn, A. Bruns, M. Saam, A. Gail, A. Gabriel, and H. J. Brinksmeier, "Flexible cortical gamma-band correlations suggest neural principles of visual processing," *Vis. cogn.*, vol. 8, no. 3–5, pp. 519–530, Jun. 2001.
- [259] D. Hermes, K. J. Miller, B. A. Wandell, and J. Winawer, "Stimulus Dependence of Gamma Oscillations in Human Visual Cortex," *Cereb. Cortex*, vol. 25, no. 9, pp. 2951–2959, Sep. 2015.
- [260] E. Izhikevich and Y. Kuramoto, "Weakly coupled oscillators," *Encycl. Math. Phys.*, pp. 48–53, 2006.
- [261] T. Akam, I. Oren, L. Mantoan, E. Ferenczi, and D. Kullmann, "Oscillatory dynamics in the hippocampus support dentate gyrus-CA3 coupling.," *Nat. Neurosci.*, no. November 2011, pp. 1–9, 2012.
- [262] L. Bai, X. Huang, Q. Yang, and J.-Y. Wu, "Spatiotemporal patterns of an evoked network oscillation in neocortical slices: coupled local oscillators.," *J.*

- Neurophysiol.*, vol. 96, no. 5, pp. 2528–38, Nov. 2006.
- [263] G. B. Ermentrout and D. Kleinfeld, “Traveling electrical waves in cortex: insights from phase dynamics and speculation on a computational role,” *Neuron*, vol. 29, no. 1, pp. 33–44, Jan. 2001.
- [264] M. Besserve, S. C. Lowe, N. K. Logothetis, B. Schoelkopf, and S. Panzeri, “Shifts of Gamma Phase across Primary Visual Cortical Sites Reflect Dynamic Stimulus-Modulated Information Transfer,” *PLoS Biol.*, vol. 13, no. 9, 2015.
- [265] B. Pakkenberg *et al.*, “Aging and the human neocortex,” *Exp. Gerontol.*, vol. 38, no. 1–2, pp. 95–99, 2003.
- [266] A. Schüz and G. Palm, “Density of neurons and synapses in the cerebral cortex of the mouse,” *J. Comp. Neurol.*, vol. 286, no. 4, pp. 442–455, Aug. 1989.
- [267] G. T. Buračas, A. M. Zador, M. R. DeWeese, and T. D. Albright, “Efficient Discrimination of Temporal Patterns by Motion-Sensitive Neurons in Primate Visual Cortex,” *Neuron*, vol. 20, no. 5, pp. 959–969, May 1998.
- [268] P. Reinagel and R. C. Reid, “Temporal coding of visual information in the thalamus,” *J. Neurosci.*, vol. 20, no. 14, pp. 5392–400, Jul. 2000.
- [269] R. Guyonneau, R. Vanrullen, and S. J. Thorpe, “Temporal codes and sparse representations: a key to understanding rapid processing in the visual system,” *J. Physiol. Paris*, vol. 98, no. 4–6, pp. 487–97, Jul. 2004.
- [270] N. Caporale and Y. Dan, “Spike timing-dependent plasticity: a Hebbian learning rule,” *Annu. Rev. Neurosci.*, vol. 31, pp. 25–46, 2008.
- [271] H. Markram, J. Lübke, M. Frotscher, and B. Sakmann, “Regulation of synaptic efficacy by coincidence of postsynaptic APs and EPSPs,” *Science*, vol. 275, no. 5297, pp. 213–5, Jan. 1997.
- [272] W. B. Levy and O. Steward, “Temporal contiguity requirements for long-term associative potentiation/depression in the hippocampus,” *Neuroscience*, vol. 8, no. 4, pp. 791–797, Apr. 1983.
- [273] R. M. Bruno and B. Sakmann, “Cortex is driven by weak but synchronously active thalamocortical synapses,” *Science*, vol. 312, no. 5780, pp. 1622–7, Jun. 2006.
- [274] X. Jia, S. Tanabe, and A. Kohn, “Gamma and the Coordination of Spiking Activity in Early Visual Cortex,” *Neuron*, vol. 77, no. 4, pp. 762–774, Feb. 2013.
- [275] D. M. Schneider and S. M. N. Woolley, “Extra-Classical Tuning Predicts Stimulus-Dependent Receptive Fields in Auditory Neurons,” *J. Neurosci.*, vol. 31, no. 33, pp. 11867–11878, Aug. 2011.
- [276] J. Fournier, C. Monier, M. Pananceau, and Y. Frégnac, “Adaptation of the simple or complex nature of V1 receptive fields to visual statistics,” *Nat. Neurosci.*, vol. 14, no. 8, pp. 1053–1060, Jul. 2011.
- [277] M. W. Self, T. van Kerkoerle, H. Supèr, and P. R. Roelfsema, “Distinct Roles of the Cortical Layers of Area V1 in Figure-Ground Segregation,” *Curr. Biol.*, pp. 1–9, Oct. 2013.
- [278] J. Cavanaugh, R. A. Berman, W. M. Joiner, and R. H. Wurtz, “Saccadic Corollary Discharge Underlies Stable Visual Perception,” *J. Neurosci.*, vol. 36, no. 1, pp. 31–42, Jan. 2016.
- [279] Z. M. Hafed, “Alteration of visual perception prior to microsaccades,”

- Neuron*, vol. 77, no. 4, pp. 775–86, Feb. 2013.
- [280] M. V Sanchez-Vives, L. G. Nowak, and D. a McCormick, “Cellular mechanisms of long-lasting adaptation in visual cortical neurons in vitro.,” *J. Neurosci.*, vol. 20, no. 11, pp. 4286–99, Jun. 2000.
- [281] M. V Sanchez-Vives, L. G. Nowak, and D. A. McCormick, “Membrane mechanisms underlying contrast adaptation in cat area 17 in vivo.,” *J. Neurosci.*, vol. 20, no. 11, pp. 4267–85, Jun. 2000.
- [282] A. M. Bastos, W. M. Usrey, R. a Adams, G. R. Mangun, P. Fries, and K. J. Friston, “Canonical microcircuits for predictive coding.,” *Neuron*, vol. 76, no. 4, pp. 695–711, Nov. 2012.
- [283] A. M. Bastos *et al.*, “Visual Areas Exert Feedforward and Feedback Influences through Distinct Frequency Channels,” *Neuron*, pp. 390–401, 2014.
- [284] B. Scholl, A. Y. Y. Tan, J. Corey, and N. J. Priebe, “Emergence of Orientation Selectivity in the Mammalian Visual Pathway,” *J. Neurosci.*, vol. 33, no. 26, pp. 10616–10624, Jun. 2013.
- [285] X. Zhao, H. Chen, X. Liu, and J. Cang, “Orientation-selective Responses in the Mouse Lateral Geniculate Nucleus,” *J. Neurosci.*, vol. 33, no. 31, pp. 12751–12763, Jul. 2013.
- [286] P. Antinucci, F. Abbas, and P. R. Hunter, “Orientation Selectivity in the Retina: ON Cell Types and Mechanisms,” *J. Neurosci.*, vol. 36, no. 31, pp. 8064–8066, Aug. 2016.
- [287] C. E. Schroeder and P. Lakatos, “Low-frequency neuronal oscillations as instruments of sensory selection,” *Trends Neurosci.*, vol. 32, no. 1, pp. 9–18, Jan. 2009.
- [288] A. Mazaheri and O. Jensen, “Asymmetric amplitude modulations of brain oscillations generate slow evoked responses.,” *J. Neurosci.*, vol. 28, no. 31, pp. 7781–7787, 2008.
- [289] E. Sejdić, I. Djurović, and J. Jiang, “Time–frequency feature representation using energy concentration: An overview of recent advances,” *Digit. Signal Process.*, vol. 19, no. 1, pp. 153–183, Jan. 2009.
- [290] R. Lyons, “dsp tips & tricks - the sliding DFT,” *IEEE Signal Process. Mag.*, vol. 20, no. 2, pp. 74–80, Mar. 2003.
- [291] M. Le Van Quyen *et al.*, “Comparison of Hilbert transform and wavelet methods for the analysis of neuronal synchrony.,” *J. Neurosci. Methods*, vol. 111, pp. 83–98, 2001.
- [292] N. E. Huang *et al.*, “The empirical mode decomposition and the Hilbert spectrum for nonlinear and non-stationary time series analysis,” *Proc. R. Soc. A Math. Phys. Eng. Sci.*, vol. 454, no. 1971, pp. 903–995, Mar. 1998.
- [293] N. E. Huang, “Introduction to the Hilbert-Huang Transform and its related mathematical problems,” *Hilbert-Huang Transform Its Appl.*, pp. 1–26, 2005.
- [294] P. Flandrin, G. Rilling, and P. Goncalves, “Empirical Mode Decomposition as a Filter Bank,” *IEEE Signal Process. Lett.*, vol. 11, no. 2, pp. 112–114, Feb. 2004.
- [295] R. Vautard and M. Ghil, “Singular spectrum analysis in nonlinear dynamics, with applications to paleoclimatic time series,” *Phys. D Nonlinear Phenom.*, vol. 35, no. 3, pp. 395–424, May 1989.

- [296] R. Vautard, P. Yiou, and M. Ghil, "Singular-spectrum analysis: A toolkit for short, noisy chaotic signals," *Phys. D Nonlinear Phenom.*, vol. 58, no. 1–4, pp. 95–126, Sep. 1992.
- [297] M. Ghil, "Advanced spectral methods for climatic time series," *Rev. Geophys.*, vol. 40, no. 1, p. 1003, 2002.
- [298] P. Bonizzi *et al.*, "Singular spectrum analysis improves analysis of local field potentials from macaque V1 in active fixation task," in *2012 Annual International Conference of the IEEE Engineering in Medicine and Biology Society*, 2012, vol. 2012, pp. 2945–2948.
- [299] P. Bonizzi, J. M. H. Karel, O. Meste, and R. L. M. Peeters, "Singular spectrum decomposition: A new method for time series decomposition," *Adv. Adapt. Data Anal.*, vol. 6, no. 4, p. 1450011, Oct. 2014.
- [300] S. G. Mallat and Zhifeng Zhang, "Matching pursuits with time-frequency dictionaries," *IEEE Trans. Signal Process.*, vol. 41, no. 12, pp. 3397–3415, 1993.
- [301] N. Metropolis, A. W. Rosenbluth, M. N. Rosenbluth, A. H. Teller, and E. Teller, "Equation of State Calculations by Fast Computing Machines," *J. Chem. Phys.*, vol. 21, no. 1953, pp. 1087–1092, 1953.
- [302] W. K. Hastings, "Monte carlo sampling methods using Markov chains and their applications," *Biometrika*, vol. 57, pp. 97–109, 1970.
- [303] C. Andrieu, N. De Freitas, A. Doucet, and M. I. Jordan, "An introduction to MCMC for machine learning," *Mach. Learn.*, vol. 50, no. 1–2, pp. 5–43, 2003.
- [304] B. P. Carlin and S. Chib, "Bayesian Model Choice via Markov Chain Monte Carlo Methods," *J. R. Stat. Soc. Ser. B*, vol. 57, no. 3, pp. 473–484, 1995.
- [305] D. Frenkel and B. Smit, *Understanding molecular simulation: from algorithms to applications*. Academic Press, 2001.
- [306] S. Kirkpatrick, C. D. Gelatt, and M. P. Vecchi, "Optimization by simulated annealing," *Science*, vol. 220, no. 4598, pp. 671–80, May 1983.
- [307] T. van Kerkoerle *et al.*, "Alpha and gamma oscillations characterize feedback and feedforward processing in monkey visual cortex," *Proc. Natl. Acad. Sci.*, vol. 111, no. 40, pp. 14332–14341, 2014.
- [308] N. Delprat, B. Escudié, P. Guillemain, R. Kronland-Martinet, P. Tchamitchian, and B. Torrèsani, "Asymptotic wavelet and Gabor analysis: Extraction of instantaneous frequencies," *Inf. Theory, IEEE Trans.*, vol. 38, no. 2, pp. 644–664, 1992.
- [309] K. J. Miller, L. B. Sorensen, J. G. Ojemann, and M. den Nijs, "Power-law scaling in the brain surface electric potential," *PLoS Comput. Biol.*, vol. 5, no. 12, p. e1000609, Dec. 2009.
- [310] D. Gilden, T. Thornton, and M. Mallon, "1/f noise in human cognition," *Science (80-.)*, vol. 267, no. 5205, pp. 1837–1839, Mar. 1995.
- [311] D. L. Gilden, "Cognitive emissions of 1/f noise," *Psychol. Rev.*, vol. 108, no. 1, pp. 33–56, 2001.
- [312] J. Henrie and R. Shapley, "LFP power spectra in V1 cortex: the graded effect of stimulus contrast," *J. Neurophysiol.*, pp. 479–490, 2005.
- [313] G. Baranauskas *et al.*, "Origins of 1/f² scaling in the power spectrum of intracortical local field potential," *J. Neurophysiol.*, vol. 107, no. 3, pp. 984–

- 94, Feb. 2012.
- [314] K. W. Bieri, K. N. Bobbitt, and L. L. Colgin, “Slow and Fast Gamma Rhythms Coordinate Different Spatial Coding Modes in Hippocampal Place Cells,” *Neuron*, vol. 82, no. 3, pp. 670–681, May 2014.
 - [315] C. Zheng and L. L. Colgin, “Beta and Gamma Rhythms Go with the Flow,” *Neuron*, vol. 85, no. 2, pp. 236–237, Jan. 2015.
 - [316] R. Scheffer-Teixeira and A. B. Tort, “Lack of evidence for cross-frequency phase-phase coupling between theta and gamma oscillations in the hippocampus,” Mar. 2016.
 - [317] D. Lozano-Soldevilla, N. ter Huurne, and R. Oostenveld, “Neuronal Oscillations with Non-sinusoidal Morphology Produce Spurious Phase-to-Amplitude Coupling and Directionality,” *Front. Comput. Neurosci.*, vol. 10, no. August, pp. 1–17, Aug. 2016.
 - [318] A. Maier, G. K. Adams, C. Aura, and D. a Leopold, “Distinct superficial and deep laminar domains of activity in the visual cortex during rest and stimulation.,” *Front. Syst. Neurosci.*, vol. 4, no. August, pp. 1–11, Jan. 2010.
 - [319] K. H. Pettersen, A. Devor, I. Ulbert, A. M. Dale, and G. T. Einevoll, “Current-source density estimation based on inversion of electrostatic forward solution: effects of finite extent of neuronal activity and conductivity discontinuities.,” *J. Neurosci. Methods*, vol. 154, no. 1–2, pp. 116–33, Jun. 2006.
 - [320] M. Ainsworth *et al.*, “Dual Gamma Rhythm Generators Control Interlaminar Synchrony in Auditory Cortex,” *J. Neurosci.*, vol. 31, no. 47, pp. 17040–17051, Nov. 2011.
 - [321] D. Xing, C.-I. Yeh, S. Burns, and R. M. Shapley, “Laminar analysis of visually evoked activity in the primary visual cortex.,” *Proc. Natl. Acad. Sci. U. S. A.*, vol. 109, pp. 13871–6, 2012.
 - [322] R. Brunelli, *Template Matching Techniques in Computer Vision: Theory and Practice*. Wiley Publishing, 2009.
 - [323] Y. Li, Z. Ma, W. Lu, and Y. Li, “Automatic removal of the eye blink artifact from EEG using an ICA-based template matching approach,” *Physiol. Meas.*, vol. 27, no. 4, p. 425, 2006.
 - [324] C. D. Woody, “Characterization of an adaptive filter for the analysis of variable latency neuroelectric signals,” *Med. Biol. Eng.*, vol. 5, pp. 539–554, 1967.
 - [325] M. Ahmadi and R. Quian Quiroga, “Automatic denoising of single-trial evoked potentials,” *Neuroimage*, vol. 66, pp. 672–680, Feb. 2013.
 - [326] L. De Gennaro and M. Ferrara, “Sleep spindles: An overview,” *Sleep Medicine Reviews*, vol. 7, no. 5, pp. 423–440, 2003.
 - [327] G. Buzsáki, “Hippocampal sharp waves: Their origin and significance,” *Brain Res.*, vol. 398, no. 2, pp. 242–252, Nov. 1986.
 - [328] M. de Curtis, J. G. R. Jefferys, and M. Avoli, “Interictal Epileptiform Discharges in Partial Epilepsy: Complex Neurobiological Mechanisms Based on Experimental and Clinical Evidence,” in *Jasper’s Basic Mechanisms of the Epilepsies*, 2012.
 - [329] S. J. Harrison *et al.*, “Large-scale Probabilistic Functional Modes from resting

- state fMRI," *Neuroimage*, vol. 109, pp. 217–231, Apr. 2015.
- [330] W. Penfield and H. Jasper, *Epilepsy and the Functional Anatomy of the Human Brain*. Little Brown & Co, 1954.
- [331] B. Coomber *et al.*, "Cortical inactivation by cooling in small animals.," *Front. Syst. Neurosci.*, vol. 5, no. June, p. 53, 2011.
- [332] K. Deisseroth, "Optogenetics," *Nat. Methods*, vol. 8, no. 1, pp. 26–29, Jan. 2011.
- [333] L. Fenno, O. Yizhar, and K. Deisseroth, "The development and application of optogenetics.," *Annu. Rev. Neurosci.*, vol. 34, pp. 389–412, 2011.
- [334] O. Yizhar, L. E. Fenno, T. J. Davidson, M. Mogri, and K. Deisseroth, "Optogenetics in Neural Systems," *Neuron*, vol. 71, no. 1, pp. 9–34, Jul. 2011.
- [335] M. A. Kramer, A. B. L. Tort, and N. J. Kopell, "Sharp edge artifacts and spurious coupling in EEG frequency comodulation measures," *J. Neurosci. Methods*, vol. 170, no. 2, pp. 352–357, May 2008.
- [336] E. M. Gerber, B. Sadeh, A. Ward, R. T. Knight, and L. Y. Deouell, "Periodic Non-Sinusoidal Activity Can Produce Cross-Frequency Coupling in Cortical Signals in the Absence of Functional Interaction Between Neural Sources," *bioRxiv*, pp. 1–33, 2016.
- [337] A. P. Vaz, R. B. Yaffe, J. H. Wittig, S. K. Inati, and K. A. Zaghloul, "Dual origins of measured phase-amplitude coupling reveal distinct neural mechanisms underlying episodic memory in the human cortex," *Neuroimage*, vol. 148, pp. 148–159, Mar. 2017.
- [338] S. R. Cole and B. Voytek, "Brain Oscillations and the Importance of Waveform Shape.," *Trends Cogn. Sci.*, vol. 21, no. 2, pp. 137–149, Jan. 2017.
- [339] M. E. Raichle, "A brief history of human brain mapping.," *Trends Neurosci.*, vol. 32, no. 2, pp. 118–26, Feb. 2009.
- [340] S. Ogawa, T. M. Lee, A. R. Kay, and D. W. Tank, "Brain magnetic resonance imaging with contrast dependent on blood oxygenation.," *Proc. Natl. Acad. Sci. U. S. A.*, vol. 87, no. 24, pp. 9868–72, Dec. 1990.
- [341] A. T. Gullledge and G. J. Stuart, "Excitatory actions of GABA in the cortex.," *Neuron*, vol. 37, no. 2, pp. 299–309, Jan. 2003.
- [342] B. E. Alger and R. A. Nicoll, "GABA-mediated biphasic inhibitory responses in hippocampus.," *Nature*, vol. 281, no. 5729, pp. 315–7, Sep. 1979.
- [343] P. Andersen, R. Dingledine, L. Gjerstad, I. A. Langmoen, and A. M. Laursen, "Two different responses of hippocampal pyramidal cells to application of gamma-amino butyric acid.," *J. Physiol.*, vol. 305, pp. 279–96, Aug. 1980.
- [344] P. Fries, "Neuronal Gamma-Band Synchronization as a Fundamental Process in Cortical Computation," *Annu. Rev. Neurosci.*, vol. 32, no. 1, pp. 209–224, Jun. 2009.

Nederlandse samenvatting

Neuronen (hersencellen) zijn de basiseenheid van de hersenen. Door elektrische signalen uit te wisselen kunnen neuronen met elkaar communiceren, en de werking van onze hersenen is afhankelijk van deze communicatie. Om deze reden is het een goed idee om de elektrische signalen in de hersenen te meten wanneer we de werking van de hersenen willen onderzoeken.

De elektromagnetische signalen kunnen van buitenaf gemeten worden met behulp van elektro-encefalografie (EEG) of magneto-encefalografie (MEG). In het geval van celculturen in een petrischaal, proefdieronderzoek, en zelfs in sommige klinische onderzoeken is het mogelijk om elektrodes direct in het hersenweefsel te steken om zo de *local field potential* (LFP) te meten.

Het werk gepresenteerd in dit proefschrift is hoofdzakelijk theoretisch. Hiermee bedoel ik dat alle experimenten *in silico* uitgevoerd zijn. Dit wil zeggen dat er geen levende cellen bij de metingen betrokken waren, maar dat alles met behulp van een computer gesimuleerd is. Dit heeft als grote voordeel dat we totale controle hebben over het gesimuleerde hersenweefsel.

De neurale code die in de hersenen door de neuronen verwerkt en gecommuniceerd wordt is voornamelijk terug te vinden in de spatio-temporele patronen van de actiepotentialen. Actiepotentialen zijn elektrische pulsen die uitgezonden worden door een neuron om te communiceren met andere neuronen. Het meten van de LFP is echter experimenteel een stuk gemakkelijker dan het vastleggen van actiepotentialen van veel afzonderlijke neuronen tegelijkertijd. Daarom is de LFP, naast de actiepotentialen van de gesimuleerde neuronen, ook een belangrijke uitkomst van onze simulaties.

Een van de hoofdonderwerpen in dit proefschrift is het bestaan van *oscillaties* in de activiteit van de neuronen (en dus ook in de LFP). Deze oscillaties kunnen ook gemeten worden met de eerdergenoemde MEG- en EEG-meettechnieken.

In hoofdstuk 2 heb ik een neuronaal mechanisme onderzocht dat koppeling tussen de fase van alfa oscillaties (~10 Hz) en de amplitude van gamma oscillaties (30-80 Hz) kan veroorzaken.

Dit wordt ook wel *phase-amplitude coupling* of PAC genoemd. Het gamma ritme werd geproduceerd door de achtereenvolgende activatie van excitatoire en inhibitoire

hersencellen^{##}. Dit ritme werd periodiek stilgelegd door een inhibitorisch signaal met alfa-frequentie. Dit had als resultaat dat de amplitude van gamma activiteit in het gesimuleerde netwerk dus ook met een gammafrequentie werd gemoduleerd, leidend tot PAC in de gesimuleerde LFP. Omdat de periodieke alfa-inhibitie (die waarschijnlijk uit de thalamus komt, zie hoofdstuk 3) sinus-vormig is, heeft dit ook een tweede effect naast het genereren van PAC: de activiteit van neuronen binnen de *duty cycle* opgelegd door de alfa-inhibitie wordt temporeel geordend. De neuronen in de cortex die het sterkst geëxciteerd worden zullen het eerst in de alfa-periode vuren. Neuronen die minder sterk worden geëxciteerd vuren hierna, of zelfs helemaal niet. Op deze manier kan de PAC tussen alfa en gamma geïnterpreteerd worden als een mechanisme waarmee de cortex neurale signalen kan prioriteren op basis van hun “belang” (dit belang is hier dan vertaald in het niveau van excitatie van de hersencellen in kwestie).

In hoofdstuk 3, heb ik een model gepresenteerd voor het netwerk van neuronen dat het alfa-ritme genereert in de thalamus. Het model is gebaseerd op experimentele bevindingen van Lorincz et al. [135] en het model heeft het *in silico* werk van Vijayan en Kopell [127] als basis. In dit modelmechanisme wordt een stabiel alfaritme gegenereerd door twee subpopulaties van *relay*-cellen (cellen in de thalamus die signalen doorsturen naar de cortex) die in om-en-om (in tegenfase) activeren. De “normale” *thalamo-cortical relay* (TCR) neuronen worden geïnhibeerd door lokale interneuronen die periodiek aangestuurd worden door *high-threshold bursting* TCR-cellen (HTC). De HTC-cellen worden op hun beurt geïnhibeerd door cellen in de *reticular nucleus* die aangestuurd worden door de TCR-cellen, om zo de cirkel te sluiten. Deze lus van wederzijdse inhibitie zorgt voor een stabiel alfa-ritme, zelfs als de HTC-populatie verstoord wordt. Ik heb laten zien dat dit voorgestelde mechanisme alfa-oscillaties kan genereren als de thalamus “werkloos” is (als de relay-cellen geen signalen binnenkrijgen om door te sturen naar de cortex). Het modelnetwerk kan ook alfa genereren als het juist *wel* signalen doorstuurt, zodat het *temporal framing* kan uitvoeren zoals Lorincz et al. voorstellen in hun werk. Hiernaast heb ik laten zien dat het modelnetwerk ook *evoked responses* kan genereren (een karakteristiek patroon in de LFP als gevolg van het presenteren van een stimulus aan de proefpersoon/dier) vergelijkbaar met experimentele metingen. Dit maakt het aannemelijk dat het genereren van zowel alfa-oscillaties als *evoked responses* door dezelfde (circuits van) neuronen in de thalamus wordt volbracht.

^{##} Het verschil tussen excitatoire en inhibitorische cellen zit hem in het effect dat de actiepotentialen van de neuronen hebben. Kort gezegd zorgen excitatoire cellen voor een vergoting van de kans dat het ontvangende neuron een actiepotentiaal genereert, terwijl een inhibitorisch neuron deze kans juist verkleint.

In hoofdstuk 4 heb ik een mechanisme besproken dat de PAC verklaart tussen delta- en gamma-activiteit die wordt gemeten in primaire visuele cortex (V1) van apen wanneer zij saccades maken [41], [211]. Microsaccades zijn snelle, korte, onbewuste oogbewegingen die de aap ongeveer drie keer per seconde maakt. In de LFP in V1 zijn twee fases van verschillende activiteit te zien elke keer als de aap een microsaccade maakt. De eerste kortstondige fase is te zien in de eerste 100 ms na het begin van de microsaccade. De eerste fase wordt gekenmerkt door activiteit met een breedbandig spectrum. Hierna volgt de “lange” periode die pas eindigt bij het begin van de volgende oogbeweging. Gedurende deze “lange” periode is er smalbandige gamma activiteit te zien (30-50 Hz) in de LFP. Door onze modelstudies heb ik laten zien dat deze twee periodes (de “kortstondige” en de “lange”) verschillende consequenties hebben voor het verwerken van neurale signalen in de visuele cortex. De kortstondige periode wordt gedomineerd door *feed-forward* verwerking waarbij alle neurale transformaties en andere verwerking van neurale signalen worden gedaan op basis van de synapsen langs de hiërarchie van het visuele systeem (bijvoorbeeld de synapsen tussen de retina en de thalamus, en vervolgens de synapsen tussen thalamus en V1, etc.). Daarentegen zijn de horizontale connecties (de synapsen *binnen* de niveaus van de visuele hiërarchie (bijvoorbeeld synapsen van neuronen in V1 met elkaar) veel belangrijker voor de neurale dynamica in de lange fase die de kortstondige fase opvolgt. Dit is dan ook terug te zien in een verandering van de receptieve velden van de gemodelleerde neuronen in deze tweede periode.

De neurale code in de actiepotentialen van de gesimuleerde neuronen in de twee periodes is ook verschillend: gedurende de kortstondige periode wordt de meeste informatie overgebracht door de vuurfrequentie en het vuurtijdstip van de neuronen. Dit verandert in de lange periode, hier is de gamma-synchronisatie en de fase van het gamma ritme waarin gevuurd wordt van groter belang dan de individuele vuurfrequentie van de neuronen.

Mechanismes om periodiek de omgeving waar te nemen en te exploreren vergelijkbaar met microsaccades bestaan ook in andere sensorische modaliteiten (zoals ritmische beweging van snorharen en periodieke snuiven voor het waarnemen van geuren). Dit maakt het waarschijnlijk dat ook in andere sensorische hersengebieden de neurale dynamica op vergelijkbare manier kunnen schakelen tussen *feed-forward* en horizontale verwerking van signalen. Daarbij komt dat het periodieke karakter van deze activiteit veel overeenkomsten heeft met “intrinsieke” neurale oscillaties (zoals de alfa-oscillaties in hoofdstukken 2 en 3). Dit zou betekenen dat een periodieke wisseling tussen vergelijkbare *feed-forward* en

horizontale informatieverwerking ook mogelijk is in andere, niet-sensorische, hersengebieden.

In hoofdstuk 5 heb ik een nieuwe methode geïntroduceerd hoofdzakelijk bedoeld voor de analyse van elektrofysiologische data. Deze methode heet *Sliding Window Matching* (SWM). SWM is een methode die automatisch terugkerende patronen kan ontdekken in meetgegevens. Op deze manier kan SWM toegepast worden op elektrofysiologische meetgegevens om zo bepaalde terugkerende patronen in de neurale activiteit op te sporen. In de context van dit proefschrift kan SWM gebruikt worden om de vorm van neurale oscillaties in LFP-, ECoG-, MEG-, of EEG-metingen te bestuderen. Daarnaast kan het gebruikt worden om terugkerende kortstondige activiteit te detecteren wanneer de tijdstippen waarop deze gebeuren niet bekend zijn (zoals de *evoked responses* die gepaard gaan met de microsaccades in hoofdstuk 4). Ik heb laten zien dat SWM de vorm niet-sinusoidale oscillaties getrouw in een ruzig signaal kan terugvinden, terwijl andere, meer traditionele methodes, hier niet in slagen.

In dit proefschrift heb ik laten zien dat het mogelijk is om, met behulp van simulaties en nieuwe methodiek, meer inzicht te krijgen in de functie en de organisatie van de netwerken van neuronen die de elektrofysiologische signalen produceren die meetbaar zijn. De resultaten in dit proefschrift geven ons een beter idee hoe alfa-oscillaties gegenereerd kunnen worden in de thalamus, en hoe alfa-oscillaties en *phase-amplitude coupling* de verwerking van informatie in de visuele cortex kunnen beïnvloeden. De volgende stap zal zijn om de voorspellingen die voortkomen uit de simulaties te vertalen naar experimenteel onderzoek, om zo de theoretische modellen uit dit proefschrift te testen en vervolgens te herzien of aan te passen. Op deze manier komen we een stap dichterbij het begrijpen van de neurale activiteit in de visuele cortex.

Author publications

Published work

- O. Jensen, **B. Gips**, T. O. Bergmann, and M. Bonnefond, “Temporal coding organized by coupled alpha and gamma oscillations prioritize visual processing,” *Trends Neurosci.*, vol. 37, no. 7, pp. 357–69, Jul. 2014.
- **B. Gips**, J. P. J. M. van der Eerden, and O. Jensen, “A Biologically Plausible Mechanism for Neuronal Coding Organized by the Phase of Alpha Oscillations,” *Eur. J. Neurosci.*, Jun. 2016.
- **B. Gips**, A. Bahramisharif, E. Lowet, M. J. Roberts, P. de Weerd, O. Jensen, and J. van der Eerden, “Discovering recurring patterns in electrophysiological recordings,” *J. Neurosci. Methods*, vol. 275, pp. 66–79, Jan. 2017.

In preparation

- E. Lowet, M. J. Roberts, A. Peter, **B. Gips**, and P. De Weerd, “A quantitative theory of gamma synchronization in macaque V1”
- E. Lowet, **B. Gips**, M. J. Roberts, P. De Weerd, O. Jensen, and J. P. J. M. van der Eerden, “Microsaccade-rhythmic 3-4Hz modulation of synchronization and coding in early visual cortex,”
- **B. Gips**, O. Jensen, and J. P. J. M. van der Eerden, “A model mechanism for the generation of thalamic alpha oscillations,”

Curriculum Vitae

Bart Cornelis Ivo Gips was born on 8 August 1989 in Amsterdam. He attended high school at the Stedelijk Gymnasium Nijmegen and graduated in 2007. After his high school graduation, Bart enrolled in the Natural Science bachelor programme of the Radboud University in Nijmegen. In 2010 he completed his bachelor's thesis under supervision of Dr. Marc van Wanrooij at professor John van Opstal's biophysics department on the plasticity of the human auditory system. After obtaining his BSc degree in biophysics with the *judicium bene meritum*, Bart enrolled in the new computational neuroscience track of the master's programme of Cognitive Neuroscience at the Donders Institute. In the second year of the Master's programme, Bart joined professor Paul Tiesinga's Neuroinformatics lab at the Radboud University for a Master's internship. Here Bart worked on model for orientation and direction selectivity in the primary visual cortex. This model could account for a visual illusion occurring when moving dots change their direction of motion. After submitting his thesis, Bart graduated from the Cognitive Neuroscience master's programme with the *bene meritum* *judicium*.

After completing his degree, Bart joined professor Jan van der Eerden at the Donders Centre for Cognitive Neuroimaging in Nijmegen on his project called *Bridging the gap between neuronal activity and neuroimaging*. Together with professor Ole Jensen and professor Van der Eerden, Bart performed the work presented in this thesis.

Acknowledgements

First I would like to thank my main supervisors: Jan van der Eerden and Ole Jensen. Without them this whole project would have been impossible. Thanks Ole, for accepting me in your already large research group. The meetings Jan and I had with you were essential to the progress of the whole project. Thanks Jan, for giving me the opportunity to work with you every day. Every PhD student should envy me for working with a supervisor as invested as you were. At the same time, you gave me the room to figure out most of the problems we encountered by myself. It has been fantastic to work with you, and I will miss our daily cup of coffee in the morning.

I would like to thank the roommates I had during my years at the DCCN. Thanks to the ladies in our pre-renovation office on the top floor: Mieke, Elexa, Ilke, Madelon and Kim. Your conversations on sports, diets and Kim's love life forced me to quickly adapt to the psychologist-dominated DCCN, coming from the mostly male world of the science faculty. I also want to thank the roommates that followed after the renovation: Stephanie, Simon and Peter. Our office has always been a great environment to work in, with just the right balance between banter and quiet work time.

I want to thank the people of both Ole's neuronal oscillations group and David's MR techniques group. It is great how I, as this strange person that only played around with simulated neural networks, have been accepted in both your groups. All of you made the DCCN a great place to work both socially and intellectually.

I especially would like to thank the people I cooperated with on scientific projects throughout my stay at the DCCN: Ali, Eric, Mark, Peter, and Tzvetan.

I would like to thank Betty and Mora, of course for the good food, but mainly for their company and their persistence on trying to teach me Italian.

I of course want to thank Ceci. We had some of the greatest times together that I will never forget. I hope we can stay in touch.

I want to thank my paranymphs: Daan and Nicco. I am incredibly lucky to have a brother like Daan, who is not only my brother but also my best friend. Also, I am super grateful to have met this strange Italian guy who, despite the fact that I had only known him for a few days, immediately invited me to join him to travel with

him to Firenze to celebrate his Bachelor's degree. I can always count on either of you if we need to talk about the things that are bothering me (or you, or us), be they good or bad. Both of you are the best.

I would like to thank the CNS girly gang: Ashley (as his name suggests, part of the girly gang), Emma, Johanne, Lianne, Martine, Suus. We found our origins in Café Samson on Tuesday evenings, this has now more-or-less switched to Fridays. But that does not matter; the recipe has stayed the same. Unwinding together over a couple of drinks with you has always been somewhat of a zenith of the week for me. Of course the girly gang has expanded a bit over time, it even gained some more Y-chromosomes. Thanks Dan, Lisa, Maarten, Rick and Staudigl for bravely supporting our Cultuurcafé habits.

I would like to thank the people at the Paul Tiesinga's Neuroinformatics department where I conducted my Master's internship. I still have fond memories of the year that I worked there with you.

I have interacted with many other fantastic people at the different centres of the Donders Institute throughout the last years. I may not have mentioned you here explicitly, but you should know that you, of course, also have my thanks.

Finally, I want to thank my mates from Zorrow: Han, Jorg, Louis, Mark and Remi. I have known you all since the start of my time at university (before I was even interested in Neuroscience). Regardless, the Wednesday evenings together remained a staple, despite each of us finishing our degree and moving on to different jobs. I hope we can manage to keep it going much longer, if perhaps no longer every Wednesday evening.

Donders Graduate School for Cognitive Neuroscience

For a successful research Institute, it is vital to train the next generation of young scientists. To achieve this goal, the Donders Institute for Brain, Cognition and Behaviour established the Donders Graduate School for Cognitive Neuroscience (DGCN), which was officially recognised as a national graduate school in 2009. The Graduate School covers training at both Master's and PhD level and provides an excellent educational context fully aligned with the research programme of the Donders Institute.

The school successfully attracts highly talented national and international students in biology, physics, psycholinguistics, psychology, behavioral science, medicine and related disciplines. Selective admission and assessment centers guarantee the enrolment of the best and most motivated students.

The DGCN tracks the career of PhD graduates carefully. More than 50% of PhD alumni show a continuation in academia with postdoc positions at top institutes worldwide, e.g. Stanford University, University of Oxford, University of Cambridge, UCL London, MPI Leipzig, Hanyang University in South Korea, NTNU Norway, University of Illinois, North Western University, Northeastern University in Boston, ETH Zürich, University of Vienna etc. Positions outside academia spread among the following sectors: specialists in a medical environment, mainly in genetics, geriatrics, psychiatry and neurology. Specialists in a psychological environment, e.g. as specialist in neuropsychology, psychological diagnostics or therapy. Positions in higher education as coordinators or lecturers. A smaller percentage enters business as research consultants, analysts or head of research and development. Fewer graduates stay in a research environment as lab coordinators, technical support or policy advisors. Upcoming possibilities are positions in the IT sector and management position in pharmaceutical industry. In general, the PhDs graduates almost invariably continue with high-quality positions that play an important role in our knowledge economy.

For more information on the DGCN as well as past and upcoming defenses please visit:

<http://www.ru.nl/donders/graduate-school/phd/>